Defence Research and Recherche et développement
Development Canada pour la défense Canada

DEFENCE R&D DÉFENSE

Submarine Structure Modeling and Analysis for Life-Cycle Management

Phase 2 Final Report

Lei Jiang
John Wallace
Martec Limited

Prepared by:
Martec Limited
Suite 400, 1888 Brunswick Street
Halifax, Nova Scotia B3J 3J8

Defence R&D Canada – Atlantic

Contract Report
DRDC Atlantic CR 2007-329
February 2008

Canada

This page intentionally left blank.

Submarine Structure Modeling and Analysis for Life-Cycle Management

Phase 2 Final Report

Lei Jiang
John Wallace
Martec Limited

Prepared By:
Martec Limited
1888 Brunswick Street, Suite 400
Halifax, Nova Scotia B3J 3J8

The scientific or technical validity of this Contract Report is entirely the responsibility of the Contractor and the contents do not necessarily have the approval or endorsement of Defence R&D Canada.

Defence R&D Canada – Atlantic

Principal Author

Original signed by Lei Jiang

Lei Jiang

Martec Limited

Approved by

Original signed by Neil Pegg

Neil G. Pegg

Head, Warship Performance

Approved for release by

Original signed by Leon Cheng

Leon Cheng

Chair, DRP

Abstract

This report presents results from the nonlinear structural analyses of six cylinder specimens in order to provide validation of the finite element methods of predicting collapse pressures and post collapse behaviour of stiffened cylindrical shells. The six cylinder specimens considered in the present study included a non-corroded short cylinder, two short cylinders with simulated center corrosion, a non-corroded long cylinder, a long cylinder with simulated corrosion in flange and a long cylinder with penetrations. The nonlinear calculations were performed using the VAST finite element (FE) code. In these nonlinear analyses, convergence studies were first conducted to determine the adequate mesh sizes for capturing nonlinear collapse behaviour of cylinders of different geometry. Other factors affecting the nonlinear responses of cylinders, such as material properties, geometric imperfections, boundary conditions, specimen's self weight and some meshing details, were also considered. In order to facilitate direct comparison between measured and predicted strain histories, a FORTRAN program was developed to automatically extract load-strain histories at all strain gauge locations from the FE solutions. FE meshes were produced using SubSAS, a submarine structural analysis program developed for DRDC Atlantic and the UK MoD. Tools for incorporating tapered regions and simulated corrosion were under development in SubSAS at the time of writing, and so specialized FORTRAN programs were written to incorporate these features into the FE models, and to generate shell element meshes for plate junctions that do not contain material overlaps. Very good agreement is obtained between the numerical and experimental results, indicating that the modeling approach and numerical analysis procedures described herein are capable of predicting the collapse behaviour of corroded stiffened cylindrical shells.

Résumé

Le présent rapport présente les résultats d'analyses de structure non linéaires menées sur six éprouvettes cylindriques dans le but de valider les méthodes par éléments finis utilisées pour prédire les pressions d'écrasement et le comportement post-écrasement des coques cylindriques renforcées. Les six éprouvettes cylindriques en question étaient un cylindre court non corrodé, deux cylindres courts à corrosion simulée au centre, un cylindre long non corrodé, un cylindre long à corrosion simulée aux brides, ainsi qu'un cylindre long à corrosion pénétrante. Les calculs non linéaires ont été effectués à l'aide du code d'éléments finis VAST. Dans ces analyses non linéaires, des études de convergence ont d'abord été menées pour déterminer la taille des maillages apte à représenter le comportement d'écrasement non linéaire de cylindres présentant des géométries différentes. D'autres facteurs susceptibles de modifier les réponses non linéaires des cylindres, comme les propriétés des matériaux, les imperfections géométriques, les conditions limites, le poids propre des éprouvettes et certains détails de maillage, ont aussi été pris en considération. Pour qu'il soit plus facile de comparer directement l'évolution des contraintes mesurées avec l'évolution des contraintes prédites, un programme FORTRAN a été mis au point pour automatiquement extraire des solutions par éléments finis l'évolution des contraintes sous charge à tous les emplacements de jauges extensométriques. Un certain nombre d'autres programmes FORTRAN ont également été mis au point pour incorporer dans les modèles par éléments finis certaines caractéristiques telles que zones coniques et corrosions simulées, et pour générer des maillages d'éléments spéciaux de coque pour le cas de la jonction de plaque qui ne contiennent pas de chevauchements de matière. Une très bonne concordance est obtenue entre les résultats numériques et expérimentaux, ce qui indique que le programme VAST est capable de prédire le comportement d'écrasement non linéaire de coques cylindriques renforcées par raidisseurs corrodées.

This page intentionally left blank.

Executive summary

Submarine Structure Modeling and Analysis for Life-Cycle Management: Phase 2 Final Report

Jiang, L.; Wallace, J.; DRDC Atlantic CR 2007-329; Defence R&D Canada – Atlantic; February 2008.

Background: DRDC Atlantic, in partnership with the United Kingdom Ministry of Defence, has funded the development of SubSAS (Submarine Structural Analysis Suite), a specialized software tool for both design-level and finite element analysis (FEA) of submarine structures. DRDC Atlantic and the Netherlands Ministry of Defence have performed a series of cylinder collapse tests to determine the effects of corrosion damage (thinning) on the structural performance of submarine pressure hull compartments. Numerical analyses of these controlled experimental collapse tests are required in order to validate previous and future structural assessments.

Results: Martec Limited was contracted by DRDC Atlantic to undertake structural analyses of the experimental collapse specimens. The work performed under Phase 2 of contract no. W7707-063569 is summarized in this document, including: 1) nonlinear FE collapse analyses of six small-scale aluminium pressure hull models, 2) comparison of various FE modeling methods used in those analyses, and 3) comparison of the FE predictions with the experimental results.

Significance: The FE and experimental results showed very good agreement, indicating that the SubSAS modeling and FE analysis methods described herein are capable of predicting nonlinear collapse behaviour of pressure hull structures with and without corrosion thinning. This validation is important as SubSAS is used to perform strength assessments of real submarines and for modeling the effects of through-life corrosion damage.

Sommaire

Submarine Structure Modeling and Analysis for Life-Cycle Management: Phase 2 Final Report

Contexte : RDDC Atlantique, en partenariat avec le ministère de la Défense du Royaume-Uni, a financé le développement d'une suite de programmes d'analyse de la structure des sous-marins nommée SubSAS (Submarine Structural Analysis Suite), outil logiciel spécialisé destiné à la fois à la conception et à l'analyse par éléments finis des structures de sous-marins. RDDC Atlantique et le ministère de la Défense des Pays-Bas ont effectué une série d'essais d'écrasement de cylindres pour déterminer les effets des dommages par corrosion (amincissements) sur la performance de la structure des compartiments constitutifs de la coque épaisse des sous-marins. Des analyses numériques de ces essais d'écrasement expérimentaux contrôlés s'imposent pour valider les évaluations antérieures et futures.

Résultats : Martec Limited a été engagé par contrat par RDDC Atlantique pour entreprendre des analyses de la structure des éprouvettes expérimentales soumises aux tests d'écrasement. Le travail réalisé dans la Phase 2 du marché numéro W7707-063569 est résumé dans le présent document, y compris : 1) les analyses d'écrasement par la méthode par éléments finis (EF) non linéaire de six modèles à petite échelle de coques épaisses en aluminium, 2) la comparaison des diverses méthodes de modélisation par EF utilisées dans ces analyses, et 3) la comparaison des prédictions par EF avec les résultats expérimentaux.

Portée : Les prédictions par EF et les résultats expérimentaux ont présenté une très bonne concordance, indiquant que les méthodes de modélisation SubSAS et le programme VAST d'analyse par EF sont capables de prédire le comportement d'écrasement non linéaire de la structure des coques épaisses avec et sans dommages par corrosion. Cette validation est importante car le logiciel SubSAS est utilisé pour calculer la résistance de sous-marins réels et pour modéliser les effets de dommages par corrosion sur l'ensemble de leur cycle de vie.

Smart Solutions for Engineering,
Science and Computing

Submarine Structure Modeling and Analysis for Life-Cycle Management

Phase 2 – Final Report

Martec Technical Report # TR-07-59 r3

May 2008

Prepared for:

DRDC Atlantic
9 Grove Street
Dartmouth, NS
B2Y 3Z7

REVISION CONTROL

REVISION	REVISION DATE
TR-07-59	October, 2007
TR-07-59 revision 1	December, 2007
TR-07-59 revision 2	March, 2008
TR-07-59 revision 3	May, 2008

SIGNATURE PAGE

Submarine Structure Modeling and Analysis for Life-Cycle Management

Phase 2 - Final Report

Technical Report # TR-07-59 r3
May 2007

Prepared by: _____ **Date:** May 26, 08
Lei Jiang
Senior Research Engineer

Prepared by: _____ **Date:** May 28, 2008
John Wallace
Senior Research Engineer
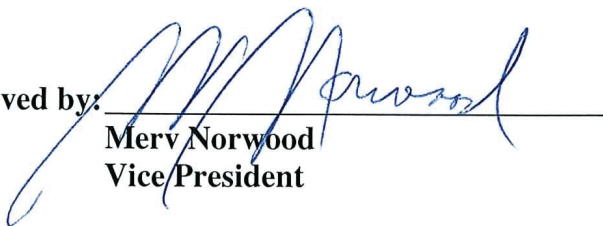
Reviewed by: _____ **Date:** 26 May 2808
Merv Norwood
Vice President

Approved by: _____ **Date:** 26 May 2008
Merv Norwood
Vice President

This page intentionally left blank.

TABLE OF CONTENTS

LIST OF FIGURES

LIST OF TABLES

This page intentionally left blank.

1.0 INTRODUCTION

This report provides a summary of the work performed under Phase 2 of a three phase project entitled "Submarine Structure Modeling and Analysis for LCM", Public Works and Government Services Canada (PWGSC) Contract Number W7707-6-3569, File Number HAL-6-60817. The objective of this phase is to validate structural strength analysis and corrosion modeling procedures provided in the SubSAS program through comparison of the predicted and measured nonlinear collapse behaviour of six cylindrical specimens with and without corrosions.

The cylinder specimens considered in the present study (six in total) included a non-corroded short cylinder, two short cylinders with simulated center corrosion, a non-corroded long cylinder, a long cylinder with simulated corrosion in flange and a long cylinder with penetrations [1]. The first five cylinders were stiffened with external T-bars, whereas the last cylinder was stiffened by flat bar stiffeners. Before the experiments in which these cylinders were pressurized to collapse, all specimens were measured thoroughly for geometric imperfections, thickness variations and material properties, and selected specimens were instrumented with strain gauges at appropriate locations. Corrosion was simulated by removing material from either the shell or stiffeners, and thus the effects of reduced shell thickness or stiffener area was studied in isolation from any possible material degradation due to corrosion. An extensive study of these cylinder models was performed in Phase I of this contract using submarine design formulas (SDF) and linear finite element techniques [2]. In the present phase, nonlinear finite element analyses of these cylinders were carried out.

The nonlinear calculations presented in this report were performed using the VAST finite element code, which is the solver engine incorporated into the SubSAS program. In these nonlinear analyses, convergence studies were first conducted to determine the adequate meshes for capturing nonlinear collapse behaviour of cylinders of different geometric configurations. All of these finite element models were initially created by using SubSAS and then modified by specially developed FORTRAN programs if required. The measured out-of-circularities and thickness variations were included in these models using Fourier representations in the circumferential direction and spline functions along the length of the models. To investigate the effect of material properties, nonlinear solutions were obtained for each cylinder specimen using three different material models, including bilinear perfectly plastic, bilinear strain hardening and multi-linear stress-strain properties. The material test data in the circumferential direction were utilized in most of the nonlinear analyses, but the axial test data were considered for the long cylinder model. Other factors affecting the nonlinear responses of the stiffened cylinders, such as boundary conditions, self-weight and meshing details at shell-shell junctions, were also investigated. In order to facilitate direct comparison of measured and computed strain-pressure histories, a FORTRAN program was developed to automatically extract strain histories at all strain gauge locations from the finite element stress/strain files. A number of other FORTRAN programs were also developed to incorporate certain features into the finite element models, such as tapered regions, simulated corrosions, and to generate special shell element meshes for plate junction that do not contain material overlaps.

Details on the generation of finite element models for nonlinear analyses of the experimental cylinders are presented in the next chapter. Chapter 3 contains a comprehensive description of the numerical solutions. Conclusions and recommendations for future work are presented in Chapter 4.

2.0   FINITE ELEMENT MODEL OF THE EXPERIMENTAL CYLINDERS

As part of an effort to understand the effect of corrosion on the strength of submarine pressure hulls, a joint experimental research program involving DRDC Atlantic and the Ministry of Defence of the Netherlands has been undertaken. This program involved the fabrication, testing and analyses of several small-scale aluminium ring-stiffened cylinders. It also involved a study into the effects of corrosion on the collapse behaviour of submarine pressure hulls. In those studies, corrosion effects were simulated by removing material from some of the test cylinders. The experiments provided valuable data for validation of the nonlinear finite element analysis capabilities in the SubSAS program for predicting plastic collapse and post-collapse behaviour of stiffened cylinders with and without corrosion.

The current phase of the contract included numerical modelling of six experimental cylinders. The various issues related to the generation of finite element models are addressed in this chapter.

2.1   NOMINAL CYLINDER GEOMETRY

A complete description of the cylinders, along with descriptions of the experimental tests and results can be found in a report by MacKay [1]. Three different nominal cylinder geometries were considered, as will be explained below. The first group included three "short" cylinders, which were designed to fail as a result of interframe collapse. Stiffener spacing and sizes were designed to promote failure in the central bay. The basic geometry of short cylinders is shown in Figure 2.1. Among these short cylinders, two of them included simulated corrosion on the cylinder wall. This took the form of a square patch (34 mm × 34 mm) of uniformly reduced thickness. In the corroded patch, the shell thickness was reduced by 25% as indicated in Figure 2.2.

The second cylinder geometry had the same inner radius as the first cylinder geometry and it had a similar wall thickness. However, this second group of cylinders were longer than the first group (510mm vs. 300mm) and contained significantly smaller stiffeners. These "long" cylinders, as shown in Figure 2.3, were designed to fail by way of overall collapse based on the submarine design formulas. One of the long cylinders included simulated corrosion of the flanges as shown in Figure 2.4. This corrosion was imposed on two flanges, Frames #4 and #5, and at only one circumferential location. The simulated corrosion was designed to precipitate buckling through first yielding in the stiffener flanges.

The final cylinder, which had roughly similar overall dimensions as the previously mentioned long cylinders, was also designed to fail by overall collapse. Stiffeners had a different shape and size than those of the long cylinder but, as in the case of the long cylinders, were relatively modest in size. The other unique and significant feature of this cylinder was the addition of two reinforced circular penetrations, as shown in Figure 2.5. These penetrations were located on opposite sides of the cylinder and were staggered longitudinally. The first penetration (A) was centred between two stiffeners whereas the centre of the second penetration (B) was aligned with one of the stiffeners. The sizes of the two penetrations were the same, as were the size and shapes of the penetration reinforcements.

The nominal dimensions were utilized to generate the basic finite element meshes using SubSAS. These basic meshes were then modified, through SubSAS or the specially developed FORTRAN codes, to include other geometric features as outlined in the following sections.

2.2   GEOMETRIC IMPERFECTIONS

Due to manufacturing procedures, the fabricated cylinders were not perfectly cylindrical in shape. Such geometric imperfections can have a significant influence on the maximum external pressure that a cylinder can withstand. Hence, accurate numerical analyses require accurate descriptions of the cylinder's shape including any out-of-circularities.

Before the experiments, each cylinder was measured for out-of-circularities (OOC's) and these measurements, which are included in Reference [1], were supplied by the Scientific Authority.

In order to impose similar OOC's on the numerical models, the discretely measured OOC's had to be transformed to a continuous map which was made up of a combination of Fourier series and spline curves. The Fourier series were generated by way of discrete Fourier transformations (DFT) which convert discrete radial measurements at each longitudinal location to a series of harmonics in the circumferential direction. The resulting Fourier series is as follows:

$$R_\theta = b_0 + \sum_{n=1}^{\infty} \left\{ a_n \sin(n\theta) + b_n \cos(n\theta) \right\}$$

$$= b_0 + \sum_{n=1}^{\infty} A_n \cos(n\theta - \phi_n)$$

where $A_n = \sqrt{a_n^2 + b_n^2}$ and $\phi_n = \tan^{-1}\left(\dfrac{a_n}{b_n}\right)$.

For a series of evenly spaced points, the coefficients a_n and b_n can be computed for values of n up to *N/2* by the following equation:

$$b_0 = \frac{1}{N} \sum_{i=0}^{N-1} R_\theta \,,\; a_n = \frac{2}{N} \sum_{i=0}^{N-1} R_\theta \sin(n\theta_i),\; b_n = \frac{2}{N} \sum_{i=0}^{N-1} R_\theta \cos(n\theta_i)$$

where $\theta_i = 2\pi\left(\dfrac{i}{N}\right)$.

The terms of the Fourier series represent different harmonic mode shapes, starting at mode 0 which is a constant value and is sometimes referred to as the breathing mode. Mode 1 represents an offset from the axis of rotation. Subsequent terms represent harmonics 2 to *N/2*. Since Fourier transformations require at least two measurement points per sine wave, the maximum harmonic number is half of the number of measurement points. For each cylinder, 36 measurements were taken around the circumference of the cylinder at each stiffener location as well as at mid-bay locations. As a result, at each longitudinal location, the highest harmonic that could be extracted from the measurements was 18. All measurements were taken from the outside of the cylinder. Hence, measurements at stiffener locations provide radial measurements to the outside of each stiffener flange, while mid-bay measurements provide radial measurements to the outside face of the cylinder wall.

It is important to note that the coefficients of the first two harmonic modes, Mode 0 and Mode 1, which represent an average radius value and an offset from the true axis of rotation, were functions of the experimental measurement procedure and not part of the actual out-of-circularities. Hence, these terms were ignored. The summation of the remaining harmonics represented the radial eccentricity, that is, the OOC's at each longitudinal location of measurement. In generating finite element models of the cylinders SubSAS computed the Fourier coefficients from the original measured data points, performed interpolation axially using spline functions and superimposed the OOC values from Mode 2 to Mode $N/2$ onto the nodal coordinates of the "geometrically perfect" finite element models.

Measured out-of-circularities, taken on the top of flanges or on the outside surface of the shell, needed to be converted to shell mid-surface, as was required for the numerical analyses. However, this data conversion required a subtraction of a constant from the originally measured radii, this resulted in a change of the average radius (zero-th harmonic), but not the coefficients of the higher Fourier components. As a result, the original measured data were directly utilized in the SubSAS to define out-of-circularities.

In order to verify the Fourier analysis routines implemented in the SubSAS program, a FORTRAN code was also developed to perform the same calculations. The Fourier coefficients computed by SubSAS and the FORTRAN program were compared against each other and with those given in Reference [1]. Exact agreement between all three sets of solutions was obtained.

2.3   CYLINDER THICKNESS MEASUREMENTS

MacKay [1] reported that variations in cylinder wall thicknesses around the circumference in the centre bay of each experimental cylinder were deduced from radial measurements on the outside and inside walls of each cylinder. Mean thicknesses in the central bay of the short and long cylinders are summarized in Table 2.1.

Measurements were taken at 10° intervals. As these data only described thickness variation in the circumferential direction at a single axial location, assumptions had to be made on the variation of cylinder wall thicknesses along the axial direction. SubSAS uses a Voronoi tessellation algorithm to assign thickness values to elements based on an unstructured cluster of points of known thickness [2]. For each of the experimental cylinders, points were specified at the two ends of the centre bay. The result was a group of elements for which thicknesses varied circumferentially according to the measured values and were constant along the axial direction, where a uniform thickness was applied to each element. In all other areas of the cylinder between the thickened ends, a constant thickness value equal to the average measured thickness was used.

2.4   MATERIAL PROPERTIES

The short and long cylinders were fabricated from 6082-T6 aluminium tubing and the penetration model was fabricated from 6061-T6 aluminium alloy.

Non-linear material properties used in all numerical analyses described in this report were based on experimental material tests supplied by the Scientific Authority [1,3]. Some of these properties

came from experimental tests performed by Schielab b.v. in Rotterdam [1], while others were based on tests performed by TNO [3].

The multi-linear properties utilized for the short and long cylinders were based on test results from TNO on AL 6082-T6 tubing [3] as shown in Figures 2.6 and 2.7. These test data indicated that the material was anisotropic because both the stiffness and yield strength in the axial direction was higher than that in the circumferential direction. In order to use these results to define multi-linear stress-strain properties for nonlinear finite element analyses, the basic TNO data had to be shifted to account for an initial offset observed in all six sets of measurements. The strain offset for each curve was determined by extrapolating from the third non-zero point (stress of roughly 90 MPa) back to zero stress and then shifting the curve so that it past through the origin. The resulting strain offsets are given in Table 2.2.

The corrected axial and circumferential stress-strain curves are given in Figures 2.8 and 2.9. These curves show less variation between the three tests than did the original data, as shown in Figures 2.6 and 2.7. The averaged multi-linear stress-strain curves from the TNO experiments are compared with the bilinear stress-strain curves generated using material properties from the tests by Schielab b.v. [1] in Figures 2.10 and 2.11. Each figure includes two bilinear curves. One uses a strain hardening modulus of 1,400 MPa, as suggested in Reference [1]. This same value was used for both the axial and circumferential directions. The other bilinear curve in each figure represents a perfectly plastic condition, where a zero hardening modulus is assumed. The elastic modulus and yield stress of this material were also extracted from the TNO test data and are compared with the test data from Schielab b.v. in Table 2.3. In this data extraction process, a 0.2% offset was applied to the multi-linear curves obtained from the TNO test data. Poisson's ratio for AL 6082-T6 was set to 0.3 in nonlinear analyses for all short and long cylinders.

The complete material test curves for 6061-T6 were not available. MacKay [1] reported that the elastic modulus is 71000 MPa, the yield stress is 250 MPa and Poisson's ratio value is 0.32. These material properties were utilized in the present analyses of the penetration cylinder.

2.5   EXPERIMENTAL TEST CONFIGURATION

In the experimental tests, each cylinder was fitted with relatively massive steel endcaps, which provided a seal against the external pressurized fluid and also contributed to the rigidity of the thickened ends of each cylinder [1]. The connection detail between an endcap and the end region of a typical cylinder is depicted in Figure 2.12. Twelve bolts, evenly spaced around each end of each cylinder, clamped the endcaps to the cylinders. This connection detail will be used to define boundary conditions later in this report.

After being fitted and instrumented, each cylinder was lowered into the test tank as shown in Figure 2.13 and an external pressure was applied. A complete load-response history of each tested cylinder was recorded using the procedure detailed in Reference [1].

2.6   FINITE ELEMENT MODEL GENERATION

As in the previous phase of the present contract [2], all finite element models of the cylinders were generated by the SubSAS program. This program was developed by Martec Limited under contract

to DRDC-Atlantic. It was designed to aid in the generation of finite element models of submarine structures, including stiffened pressure hulls and internal structures. In the present study, all finite element models were constructed using the 4-noded quadrilateral shell element (IEC5) in the VAST finite element program. This 4-noded shell element is one of the most commonly used element type in VAST for characterizing plastic buckling of thin-walled structures. This element was derived based on the degenerated isoparametric solid element formulation. The shear locking problem, which is common to this type of shell elements, was removed by using the method of mixed interpolation of transverse shear components (MITC4). The geometric nonlinear capability in this element was developed using a consistent co-rotational formulation, which is capable of handling arbitrarily large displacements and rotations.

In the present nonlinear finite element analyses, the following features were included:

- external ring stiffeners with Tee and flat-bar cross-sections,
- circular penetrations and penetration reinforcements,
- out-of-circularities,
- variations in thickness over the surface of the model,
- boundary conditions, and
- external pressure loads.

SubSAS was not capable of including the simulated corrosion on the short and long cylinder models at the present time, so it had to be introduced outside SubSAS. The nonlinear material properties were also introduced outside SubSAS. These were accomplished by way of computer programs specially developed for this work.

2.6.1   Applied Loads

The pressure loads applied to the cylinder finite element model included external pressure on the cylinder wall and concentrated axial forces at one end of the cylinders which was permitted to move in the axial direction. These concentrated axial forces were due to pressure loads acting on the endcaps and are displayed in Figure 2.14. No loads were applied to the flange and web of the stiffeners since both sides of these components were exposed to the same external pressure. Although the definition of the pressure loads on the cylinder wall was relatively straightforward, some special considerations were required to ensure that the equivalent end forces were properly defined.

In an actual experimental cylinder, as shown in Figure 2.15, the total end load was equal to the total pressure load on the endcap, which had a radius equal to the outer radius of the cylinder wall at the cylinder end. However, in the finite element models of the 4-noded quadrilateral shell elements, concentrated loads were applied to nodes which were located on the mid-surface and pressure loads were also applied to the mid-surface geometry as indicated in Figure 2.15. To be consistent with the finite element model, SubSAS utilized the mid-surface geometry of the end shell to calculate the end loads. This raised the question of whether the end loads should be calculated based on the full radius of the endcap or the mid-surface radius of the end section of the cylinder.

In order to answer this question, the axial stresses in the center section of a short cylinder were estimated using both the actual and mid-surface geometries. These calculations were based on a static equilibrium requirement, which suggested that over an arbitrary cross-section through the

thin-walled portion of a cylinder, the axial end load was balanced by the axial stress in the cylinder wall and the axial component of the pressure acting on the tapered portion of the cylinder, as displayed in Figure 2.15. In the case of the physical model, as shown in Figure 2.15a, the computed axial stress in the centre portion of the cylinder was 22.75 MPa. For the finite element model, where both the end load and the pressure acting on the tapered region were based on mid-surface geometry (see Figure 2.15b), the calculated axial stress was 22.25 MPa. This value was less than the value from the physical model by 2%. However, if the physical dimensions of the endcap were utilized to calculate the end load in finite element models, the calculated axial stress was 25.52 MPa, which was larger than the physical model value by 12%. These basic considerations justified the treatment of endcap loads in the SubSAS program, where all the calculations were based on the mid-surface geometry, which was consistent with the shell finite element models.

2.6.2   Simulated Corrosion

Modelling the reduced thickness in the simulated corrosion area of the two corroded short cylinder models involved use of the newly implemented shell thickness offset feature in VAST. This feature allows the nodes of a four-noded shell element to be offset from the mid-surface along the thickness direction. The amount of offset is defined by the parametric coordinate, such that values range from –1.0 to +1.0 represent cases where the nodes are positioned on the lower and upper surfaces, respectively.

In finite element models for the corroded cylinders, all nodes remained in the mid-surface of the non-corroded cylinder. Since the inside wall of the cylinders had a radius of 110mm and the nominal wall thickness of cylinders, excluding the thickened ends, was 2.5 mm all shell nodes in the thin-walled portion of the model (including the corroded patch) had a nominal radius of 111.25 mm. As illustrated in Figure 2.16, all material removed from the corrosion patch was taken from the outside of each cylinder. This meant that elements in each corroded patch had a nominal offset of 0.333. The actual offsets used in the finite element models were based on measured shell thicknesses. Application of the simulated corrosion patch to a non-corroded finite element model involved adjustment of the shell thickness and node offset parameter for elements in the corroded area. In the present work, this was done through a special purpose FORTRAN program. A typical finite element model with the corrosion patch is displayed in Figure 2.17.

The "dog-bone" shaped flange corrosion in the long cylinders was also introduced into the non-corroded model through a special purpose program. A typical model with the flange corrosion is given in Figure 2.18.

2.6.3   Boundary Conditions

The degree of fixity at the ends of the cylinders was a matter of interest in the present study. As the treatment of boundary conditions could have a noticeable effect on the nonlinear finite element solutions, various boundary conditions were considered in the present work.

The default boundary conditions used in all SubSAS models (Boundary Condition I) are displayed in Figure 2.19, in which one end of the cylinder was fully clamped, whereas the other end was also fully constrained except the axial translation. This arrangement allowed axial end loads to be applied to the model. These boundary conditions were justified by the fact that the bending stiffness of the end region of the cylinder was significantly higher than that of the center section

(due to increased shell thickness and the endcap support), such that the rotations at the ends were negligible.

In order to investigate the effect of rotational constraints at the cylinder ends, two other types of boundary conditions were considered for the long cylinder. In Boundary Condition II, as shown in Figure 2.20, simply support boundary conditions were applied at the inner edges of the endcaps to simulate shell-endcap interactions. The axial translation was constrained at one end, allowing the axial end forces to be applied to the other end. The Boundary Condition III is displayed in Figure 2.21, where simply supported conditions were utilized to simulate not only the shell-endcap interactions at the inner edges of the endcaps, but also the bolt connections which tied the endcaps to the cylinder. The axial translation was still fixed at one end, similar to the other boundary conditions.

It should be noted that in all the three boundary conditions presented above, the axial end loads were applied uniformly at one end of the model, but the compatibility of the axial displacement was not enforced over the end section. The consequence of this treatment was that the initially planar end section might not be planar after deformation. In order to test the significance of this assumption, an additional boundary condition was considered, in which one end of the cylinder was fully constrained as in Boundary Condition I, but the other end was constrained through rigid links, which related the translations and rotations of all the nodes in the end section at the motions of a master node at the center of the end section. This master node was not a physical node in the finite element model, but introduced solely for the purpose of applying the rigid links. These rigid links ensured that the end section be planar, although the nodes in this section could translate and rotate together. The last boundary condition type is referred as Boundary Condition IV in the later part of this report.

2.7   EXTRACTION OF PRESSURE-STRAIN HISTORY

One of the major requirements of the present work was to compare the numerically predicted and experimentally measured pressure-strain histories at selected locations on the cylinders where the strain gauges were installed. This required post-processing of the nonlinear finite element results. Although a stress post-processing capability was already available in Trident FEA for nonlinear analyses using 4-noded quad shell elements, this capability has a few limitations that limited its usefulness for the present application. First of all, the current version of Trident FEA can only display the stresses and plastic strain, but not the total strain as required in the present work. Second, the generation of pressure-strain histories for a large number of points would be time consuming because it requires selection of the appropriate points one by one from the complicated three-dimension shell element model.

To resolve these difficulties, a special purpose FORTRAN program, named StrainExtractor, was developed in the present work to automatically extract strain results at all strain gauge locations. From the basic constitutive relation for elastic-plastic deformation as

$$\boldsymbol{\sigma} = \boldsymbol{D}\left(\boldsymbol{\varepsilon} - \boldsymbol{\varepsilon}^{P}\right)$$

where $\boldsymbol{\sigma}$, $\boldsymbol{D}$, $\boldsymbol{\varepsilon}$, $\boldsymbol{\varepsilon}^{P}$ denote stresses, elasticity matrix, total strains and plastic strains, respectively.

The total strains were computed from the current stresses and plastic strains as

$$\boldsymbol{\varepsilon} = \boldsymbol{D}^{-1}\boldsymbol{\sigma} + \boldsymbol{\varepsilon}^{P}.$$

This relation is valid for both elastic and elastic-plastic deformations.

In most of the finite element models utilized in the present study, the element edges were parallel to either the axial or circumferential directions of the stiffened cylinder. This made the extraction of the axial and circumferential stress and strain components straightforward. However, for the penetration model, the mesh layout became quite irregular near the cylinder-penetration junctions. In this case, element local coordinate system axes were not aligned with the strain gauges and local FE strains had to be transformed in order to obtain strain values in the desired direction. Strain along desired direction $\boldsymbol{v}$ is computed as follows:

$$\tilde{\varepsilon} = \begin{bmatrix} l^2 & m^2 & lm & mn & nl \end{bmatrix} \begin{bmatrix} \varepsilon_{xx} \\ \varepsilon_{yy} \\ \gamma_{xy} \\ \gamma_{yz} \\ \gamma_{zx} \end{bmatrix}$$

where $l = \boldsymbol{e}_1^T \boldsymbol{v}$, $m = \boldsymbol{e}_2^T \boldsymbol{v}$, $n = \boldsymbol{e}_3^T \boldsymbol{v}$ are components of the direction cosine for the desired direction
measured in the element local system,
$\boldsymbol{e}_1, \boldsymbol{e}_2, \boldsymbol{e}_3$ are the element local axes, and
$\varepsilon_{xx}, \dots \gamma_{zx}$ denote the strain components in the element local coordinate system.

The strain gauge locations implemented in the StrainExtractor program for the short cylinders, the long cylinders and the penetration cylinder are summarized in Tables 2.4-2.6, respectively. These included all the strain gauge locations given in Reference [1]. During the development of this special purpose program, it was assumed that the finite element models for all cylinders were arranged in modules. A "module", as defined by Trident FEA, is group of elements that can be isolated from the remainder of a Trident FEA model for purposes of manipulating or modifying all elements in the module in a single operation. For the short and long cylinders, all shell elements were grouped into five modules as shown in Figures 2.23 and 2.24, where Module 1 contained elements for the thicker cylinder walls at both ends, Module 2 contained elements for the tapered regions, Module 3 was for the thinner cylinder wall in the center section, Module 4 contained the webs of all stiffeners and Module 5 contained flanges of all stiffeners. For the finite element model of the penetration cylinder, the shell elements were arranged in six modules, where the cylinder wall was represented by Module 1, the flat bar stiffeners by Module 2. Each of the penetrations was represented by two modules, one for the portion outside the cylinder wall and the other for the portion inside the cylinder wall, as shown in Figure 2.25. The module numbers for strain gauge locations are shown in Tables 2.4-2.6, where positive and negative numbers indicated that strain gauges were on the upper and lower surfaces of the corresponding shell elements.

The axial locations given in Tables 2.4-2.6 were measured from the end of the cylinder at which the axial load was applied, i.e. the end at which the value of global coordinate X is a minimum. For the short and long cylinder models, the circumferential angles were measured clockwise from the positive Z direction. This convention of angle definition was consistent with that used for

description of circumferential variation of shell thicknesses and out-of-circularities. However, for the penetration model, the circumferential angle was measured clockwise from the position Y direction.

For uniaxial strain gauges, the desired strain component must be defined at each strain gauge location. This was achieved by using a strain component flag, where values of 1 and 2 indicated axial and circumferential strains, respectively. This flag is included in Tables 2.4-2.6. Since for most of the models the x-axis of the element local system was in either the axial or the circumferential directions, the determination of these strain components was straightforward. The extraction of strain histories at the locations of strain rosettes on the inner wall of penetrations was relatively more complicated due to the irregular mesh layout in those areas. In this case, following the identification of the appropriate element, the complete set of strain components were first extracted in the element local system and then transformed into the desired direction using the strain transformation formula given above. The strain values in the vertical direction and $\pm 60^O$ and 180° from the vertical direction were calculated. The strain rosettes were indicated by a value of strain component flag of 3, as indicated in Table 2.6.

Output from the StrainExtractor program was a group of text files, one for each of the strain gauges specified in Tables 2.4-2.6. Each text file contained 6 columns of data, including the load parameter, strains at the four numerical integration points in the identified element and close to the appropriate surface and the average of the four strain values. For all strain history results given in this report, the average strain values were utilized.

Table 2.1: Measured Average Shell Thickness

Specimen	Shell Thickness (mm)			
	Un-corroded area		Corroded area	
	Ideal	Measured	Ideal	Measured
L300-No2	2.5	2.486		
L300-No3	2.5	2.477	1.875	1.870
L300-No4	2.5	2.544	1.875	1.904
L510-No1	3.0	3.052		
L510-No2	3.0	2.972		

Table 2.2: Calculated Strain Offsets.

Axial Coupons		Circumferential Coupons	
Specimen #	Strain offset (%)	Specimen #	Strain offset (%)
1	0.007864	1	0.004796
2	0.001876	2	0.005173
3	0.009722	3	0.012679

Table 2.3: Comparison of Material Properties from Schielab and TNO Tests

	Axial Properties		Circumferential Properties	
	Elastic Modulus (MPa)	Yield Stress (MPa)	Elastic Modulus (MPa)	Yield Stress (MPa)
Bilinear	71,350.0	302.4	71,350.0	272.3
Multi-linear	72,903.0	310.9	72,498.3	273.9

Table 2.4: Locations for Strain History Extraction for the Short Cylinders

Strain Gauge #	Axial Location (mm)	Circumferential Angle (°)	Module # in FE Model	Strain Component
1	125.0	0.0	5	2
2	125.0	10.0	5	2
3	125.0	45.0	5	2
4	125.0	90.0	5	2
5	125.0	180.0	5	2
6	125.0	270.0	5	2
7	125.0	315.0	5	2
8	125.0	350.0	5	2
9	175.0	0.0	5	2
10	175.0	10.0	5	2
11	175.0	45.0	5	2
12	175.0	90.0	5	2
13	175.0	180.0	5	2
14	175.0	270.0	5	2
15	175.0	315.0	5	2
16	175.0	350.0	5	2
17	150.0	0.0	3	1
18	150.0	90.0	3	1
19	150.0	180.0	3	1
20	150.0	270.0	3	1
21	150.0	0.0	3	2
22	150.0	90.0	3	2
23	150.0	180.0	3	2
24	150.0	270.0	3	2
25	129.0	0.0	3	2
26	129.0	90.0	3	2
27	129.0	180.0	3	2
28	129.0	270.0	3	2
29	171.0	0.0	3	2
30	171.0	90.0	3	2
31	171.0	180.0	3	2
32	171.0	270.0	3	2
33	150.0	0.0	-3	1
34	150.0	10.0	-3	1
35	150.0	45.0	-3	1
36	150.0	90.0	-3	1
37	150.0	180.0	-3	1
38	150.0	270.0	-3	1
39	150.0	315.0	-3	1
40	150.0	350.0	-3	1
41	150.0	0.0	-3	2
42	150.0	10.0	-3	2
43	150.0	45.0	-3	2
44	150.0	90.0	-3	2
45	150.0	180.0	-3	2
46	150.0	270.0	-3	2
47	150.0	315.0	-3	2
48	150.0	350.0	-3	2

Table 2.5: Locations for Strain History Extraction for the Long Cylinders

Strain Gauge #	Axial Location (mm)	Circumferential Angle (°)	Module # in FE Model	Strain Component
1	230.0	0.0	5	2
2	230.0	30.0	5	2
3	230.0	60.0	5	2
4	230.0	90.0	5	2
5	230.0	120.0	5	2
6	230.0	150.0	5	2
7	230.0	180.0	5	2
8	230.0	210.0	5	2
9	230.0	240.0	5	2
10	230.0	270.0	5	2
11	230.0	300.0	5	2
12	230.0	330.0	5	2
13	280.0	0.0	5	2
14	280.0	30.0	5	2
15	280.0	60.0	5	2
16	280.0	90.0	5	2
17	280.0	120.0	5	2
18	280.0	150.0	5	2
19	280.0	180.0	5	2
20	280.0	210.0	5	2
21	280.0	240.0	5	2
22	280.0	270.0	5	2
23	280.0	300.0	5	2
24	280.0	330.0	5	2
25	255.0	0.0	3	1
26	255.0	60.0	3	1
27	255.0	120.0	3	1
28	255.0	180.0	3	1
29	255.0	240.0	3	1
30	255.0	300.0	3	1
31	255.0	0.0	3	2
32	255.0	60.0	3	2
33	255.0	120.0	3	2
34	255.0	180.0	3	2
35	255.0	240.0	3	2
36	255.0	300.0	3	2
37	105.0	0.0	3	1
38	105.0	60.0	3	1
39	105.0	120.0	3	1
40	105.0	180.0	3	1
41	105.0	240.0	3	1
42	105.0	300.0	3	1
43	405.0	0.0	3	1
44	405.0	60.0	3	1
45	405.0	120.0	3	1
46	405.0	180.0	3	1
47	405.0	240.0	3	1
48	405.0	300.0	3	1

Table 2.5 (Cont'd): Locations for Strain History Extraction for the Long Cylinders

Strain Gauge #	Axial Location (mm)	Circumferential Angle (°)	Module # in FE Model	Strain Component
49	255.0	0.0	-3	1
50	255.0	60.0	-3	1
51	255.0	120.0	-3	1
52	255.0	180.0	-3	1
53	255.0	240.0	-3	1
54	255.0	300.0	-3	1
55	255.0	0.0	-3	2
56	255.0	60.0	-3	2
57	255.0	120.0	-3	2
58	255.0	180.0	-3	2
59	255.0	240.0	-3	2
60	255.0	300.0	-3	2

Table 2.6: Locations for Strain History Extraction for the Penetration Cylinder

(a) Uni-Axial Strain Gauges on Stiffeners

Strain Gauge #	Axial Loc. (mm)	Circum. Angle (^{o})	Radius (mm)	Module # in FE Model	Strain Component
1	260.0	0.0	120.7	2	2
2	260.0	20.0	120.7	2	2
3	260.0	40.0	120.7	2	2
4	260.0	60.0	120.7	2	2
5	260.0	80.0	120.7	2	2
6	260.0	100.0	120.7	2	2
7	260.0	120.0	120.7	2	2
8	260.0	140.0	120.7	2	2
9	260.0	160.0	120.7	2	2
10	260.0	180.0	120.7	2	2
11	260.0	200.0	120.7	2	2
12	260.0	220.0	120.7	2	2
13	260.0	240.0	120.7	2	2
14	260.0	260.0	120.7	2	2
15	260.0	280.0	120.7	2	2
16	260.0	300.0	120.7	2	2
17	260.0	320.0	120.7	2	2
18	260.0	340.0	120.7	2	2
19	180.0	15.0	120.7	2	2
20	180.0	315.0	120.7	2	2
21	220.0	15.0	120.7	2	2
22	220.0	315.0	120.7	2	2
23	340.0	165.0	120.7	2	2
24	340.0	195.0	120.7	2	2

(b) Strain rosettes on inner wall of Penetration A

Strain Gauge #	X (mm)	Y (mm)	Z (mm)	Module # in FE Model	Strain Component
25	172.50	111.35	0.0	5	3
26	180.55	109.64	-19.45	5	3
27	200.00	107.90	-27.50	5	3
28	172.50	111.35	0.0	6	3
29	180.55	109.64	-19.45	6	3
30	200.00	107.90	-27.50	6	3

(c) Strain rosettes on inner wall of Penetration B

Strain Gauge #	X (mm)	Y (mm)	Z (mm)	Module # in FE Model	Strain Component
31	312.50	-111.35	0.0	3	3
32	320.55	-109.64	-19.45	3	3
33	340.00	-107.90	-27.50	3	3
34	312.50	-111.35	0.0	4	3
35	320.55	-109.64	-19.45	4	3
36	340.00	-107.90	-27.50	4	3
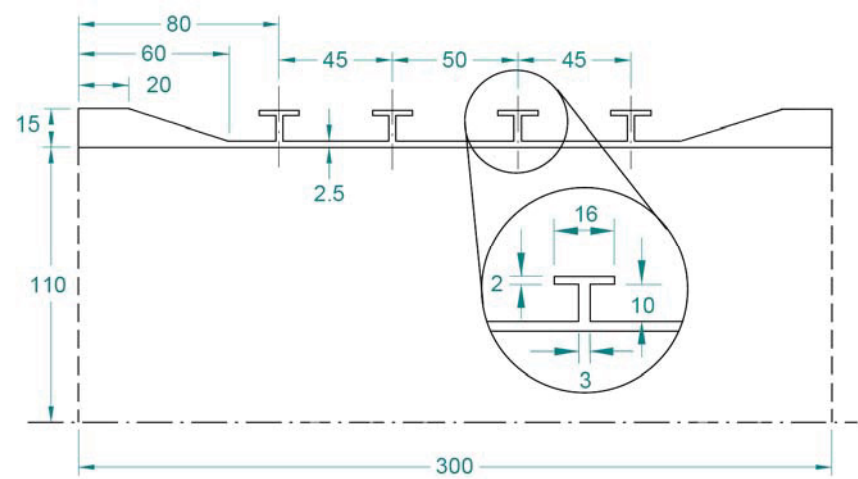
Figure 2.1: Nominal Geometry of Short Cylinder (mm).
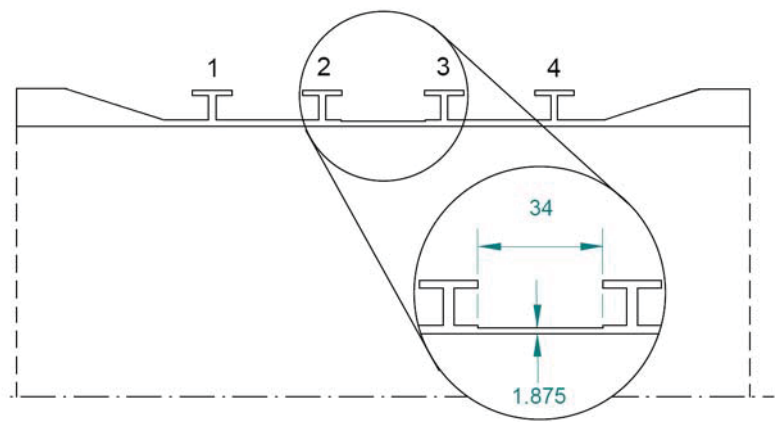
Figure 2.2: Short Cylinder with Simulated Corrosion (mm).
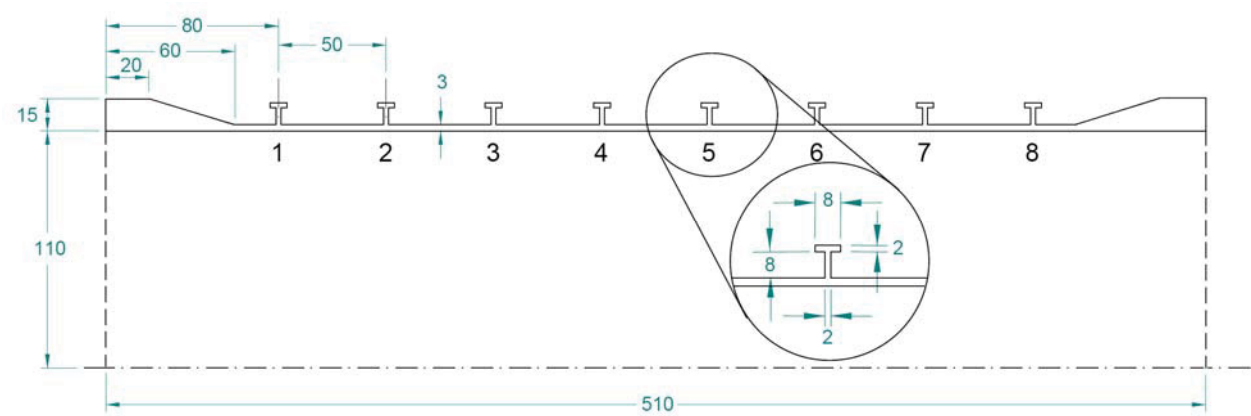
Figure 2.3: Nominal Geometry of Long Cylinder (mm).
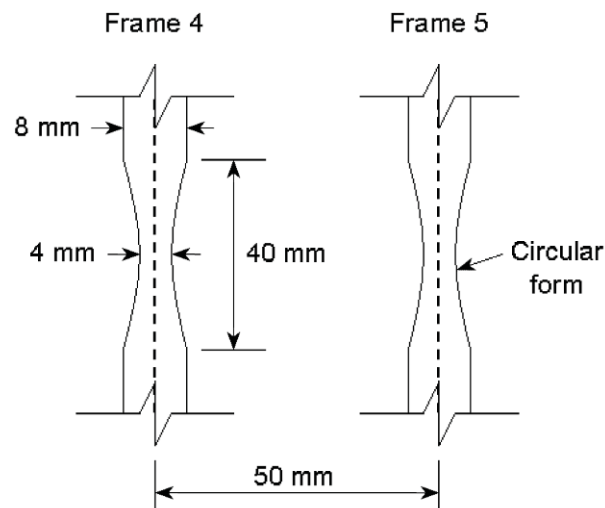
Figure 2.4: Long Cylinder Simulated Flange Corrosion.
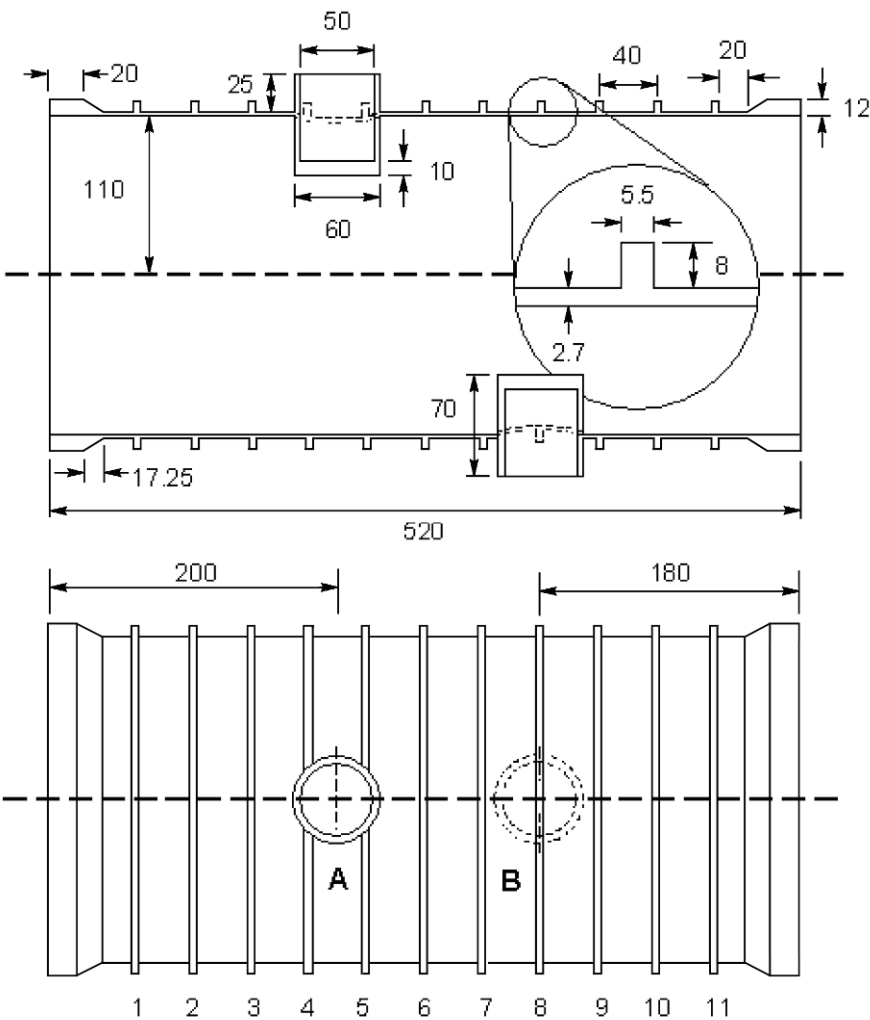
Figure 2.5: Nominal Geometry of Cylinder with Penetrations (mm).
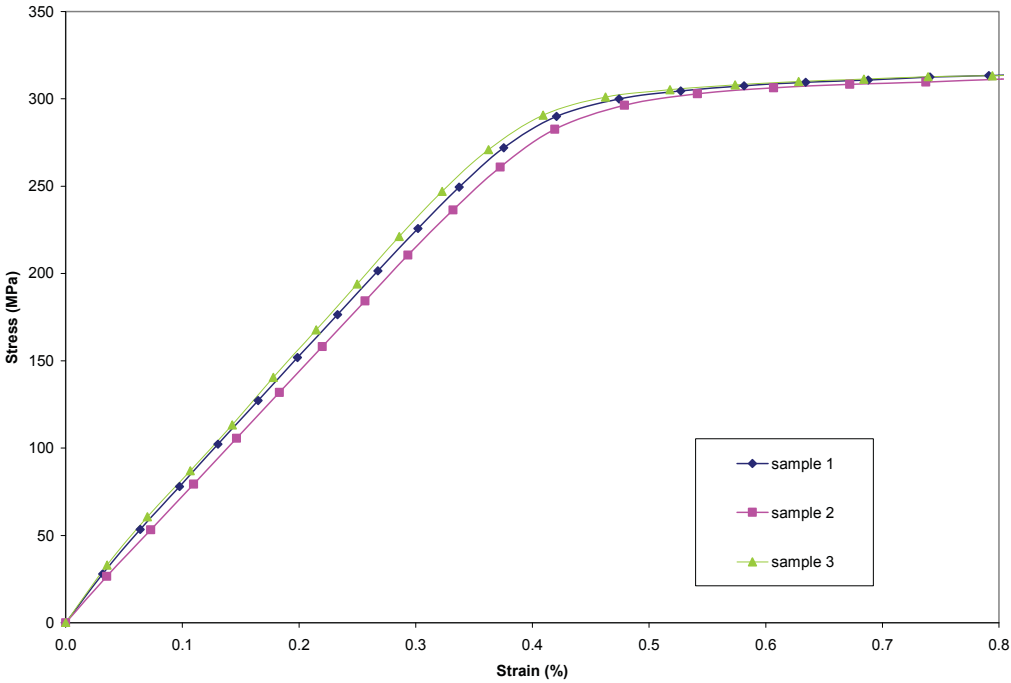
Figure 2.6: Original Experimental Data from TNO for Axial Stress-Strain Properties.
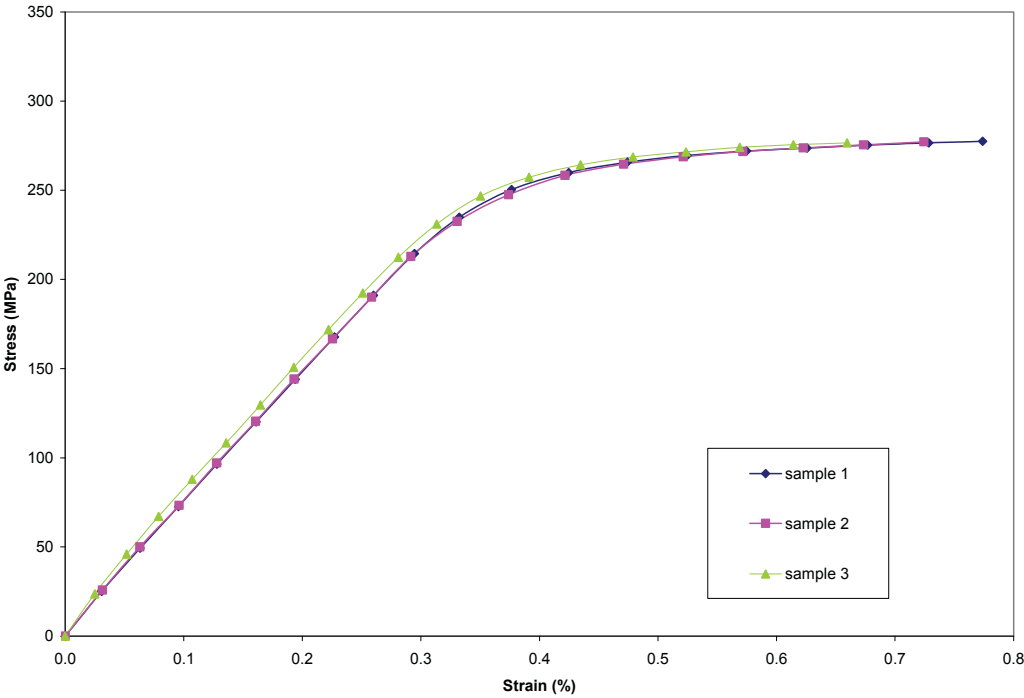
Figure 2.7: Original Experimental Data from TNO for Circumferential Stress-Strain Properties.
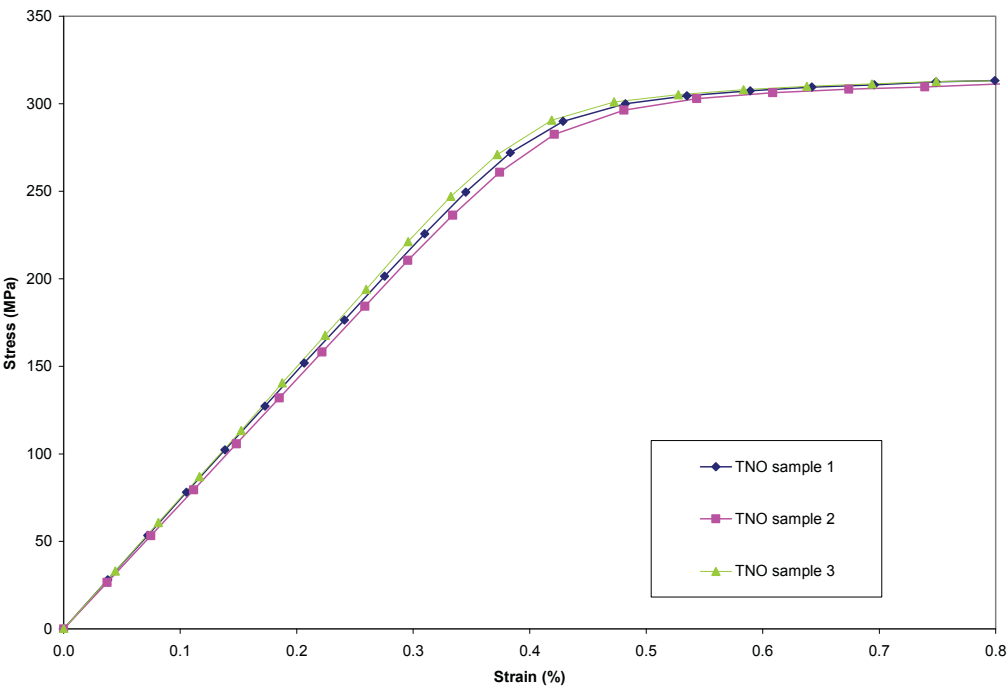
Figure 2.8: Corrected TNO Experimental Data for Axial Stress-Strain Properties.
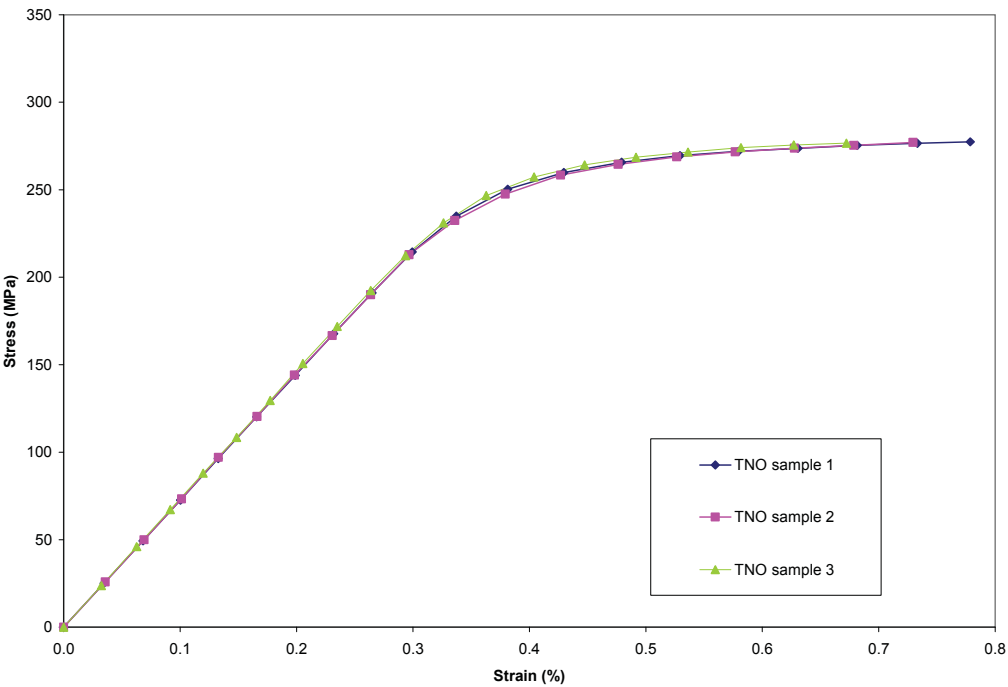
Figure 2.9: Corrected TNO Experimental Data for Circumferential Stress-Strain Properties.
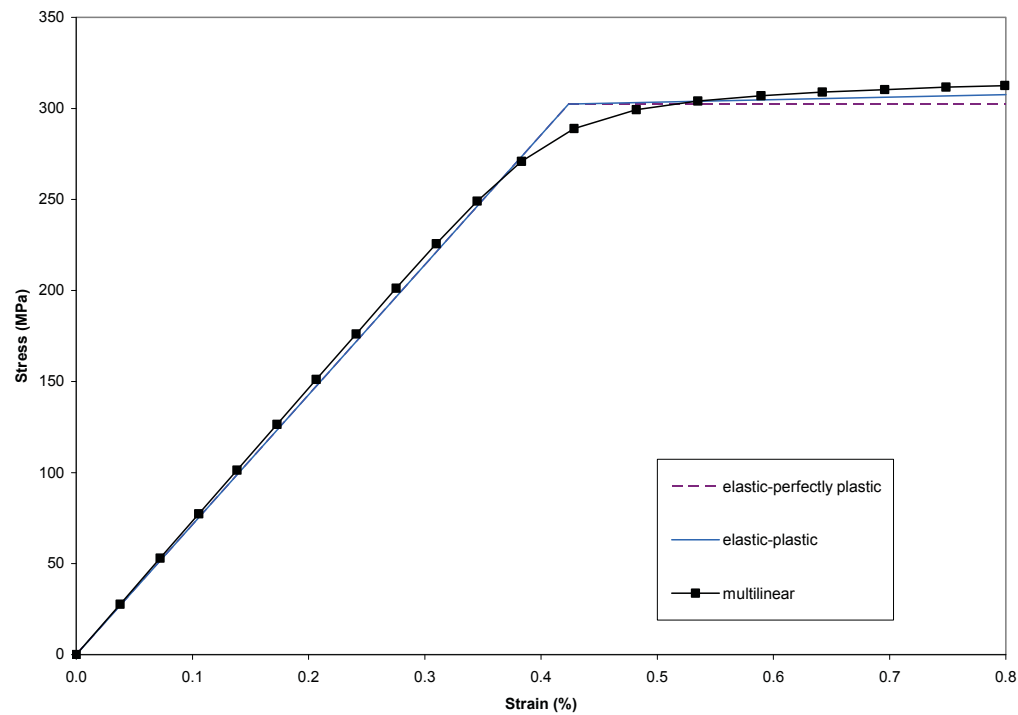
Figure 2.10: Comparison of Bilinear and Averaged Multi-linear Stress-Strain Properties in the Axial Direction.
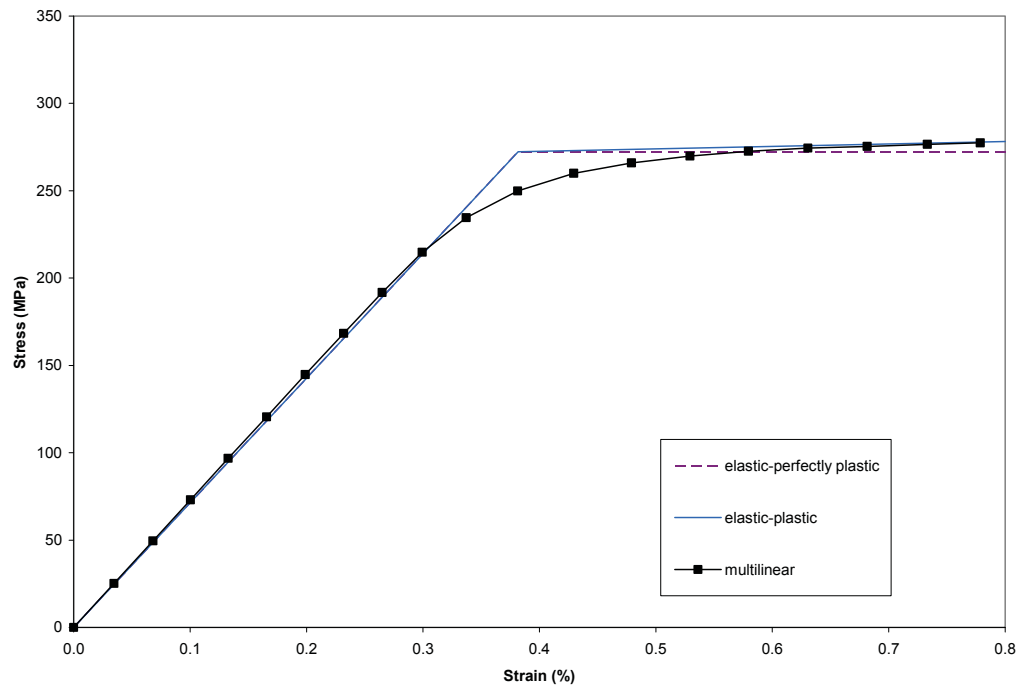
Figure 2.11: Comparison of Bilinear and Averaged Multi-linear Stress-Strain Properties in the Circumferential Direction.
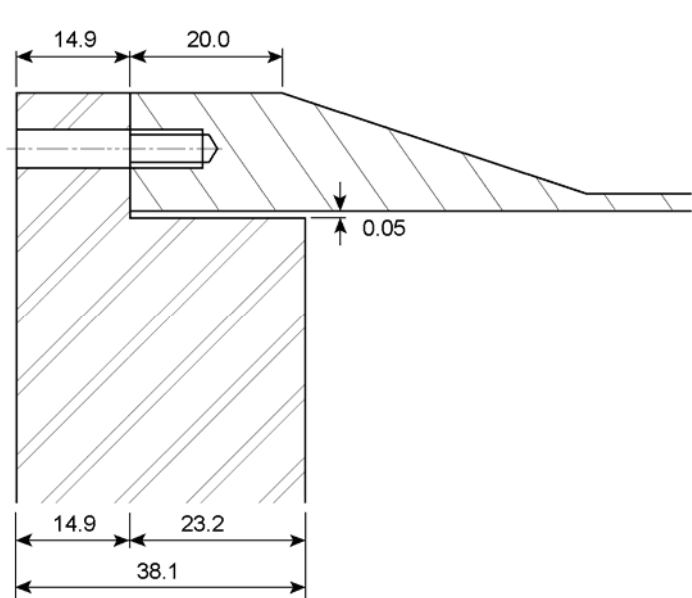
Figure 2.12: Endcap Connection Detail (mm).
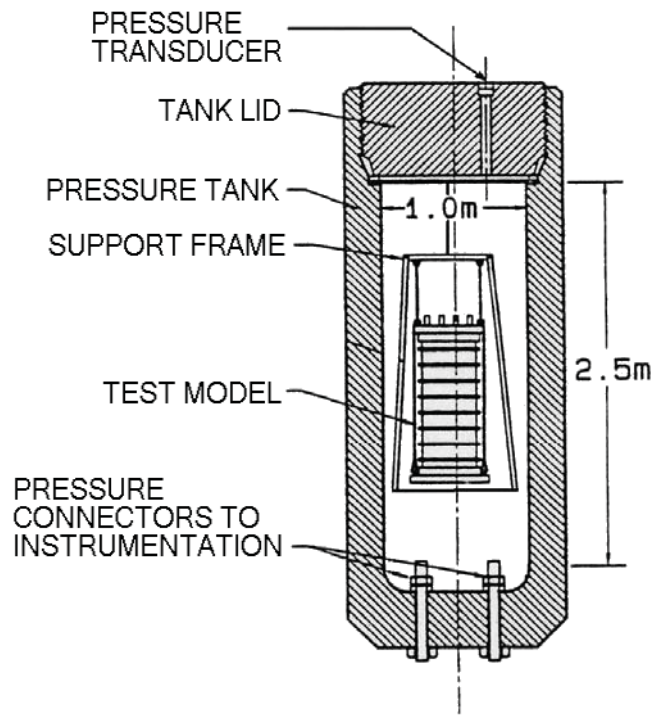
Figure 2.13 Experimental Test Setup
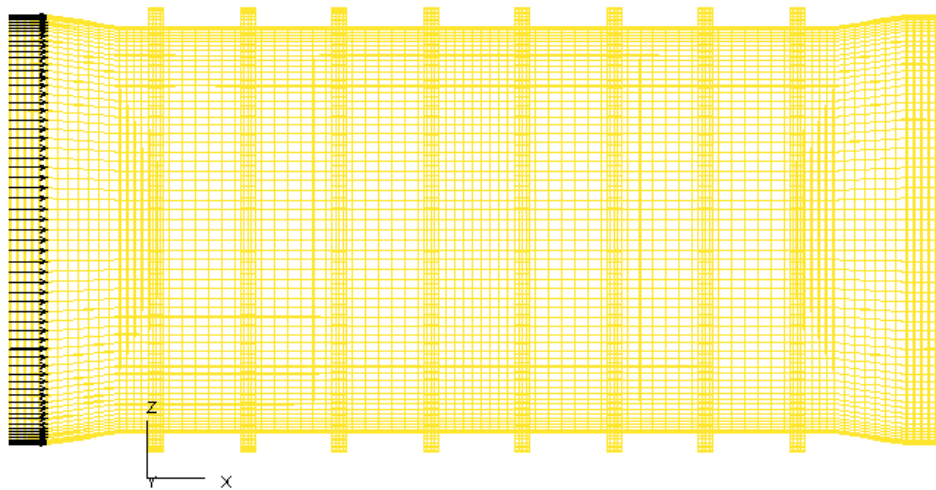
Force Resultant; Load Case   1:
STATIC LOAD ANALYSIS: CASE NUMBER   1

Figure 2.14: Concentrated Forces Acting at One End of the Finite Element Model at Which Axial Movement is not Constrained.
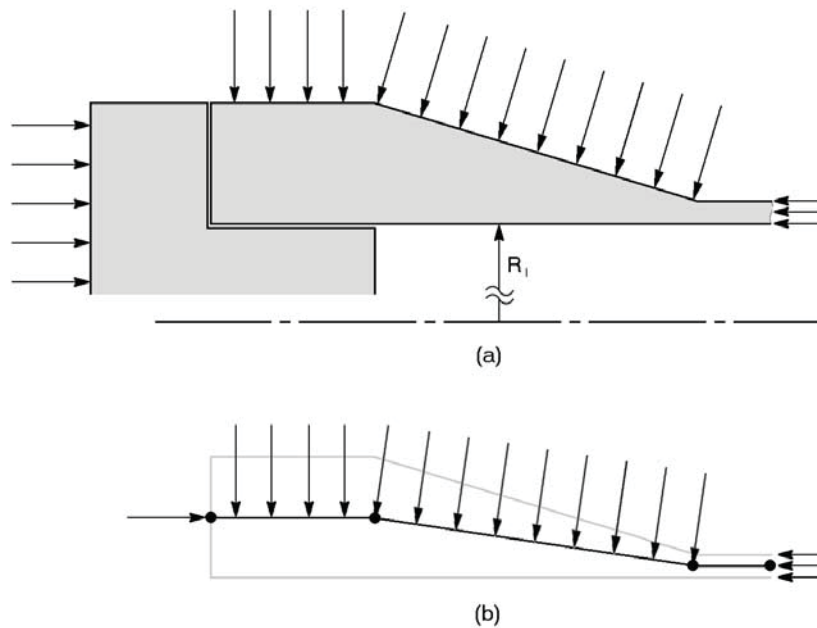
Figure 2.15: Longitudinal Loads on Physical Cylinder Configuration (a) and Finite Element Model (b)

$$offset = \frac{t - t_c}{t_c} = \frac{2.5 - 1.875}{1.875} = 0.333$$
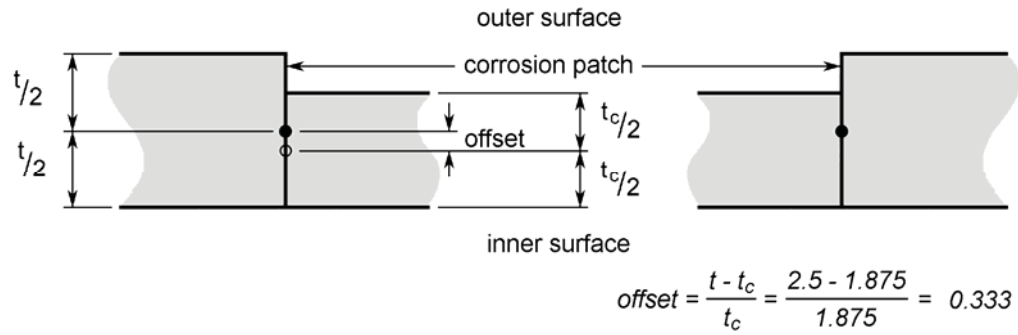
Figure 2.16: Element Offsets for Short Cylinder Corrosion Patch.
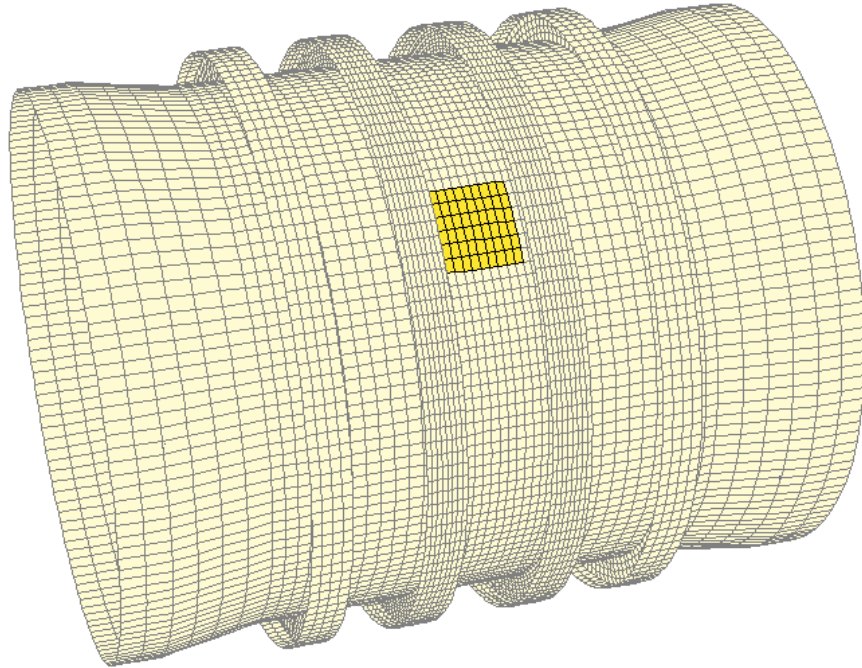
Figure 2.17: Sample Finite Element Model of Short Cylinder Including Corrosion.
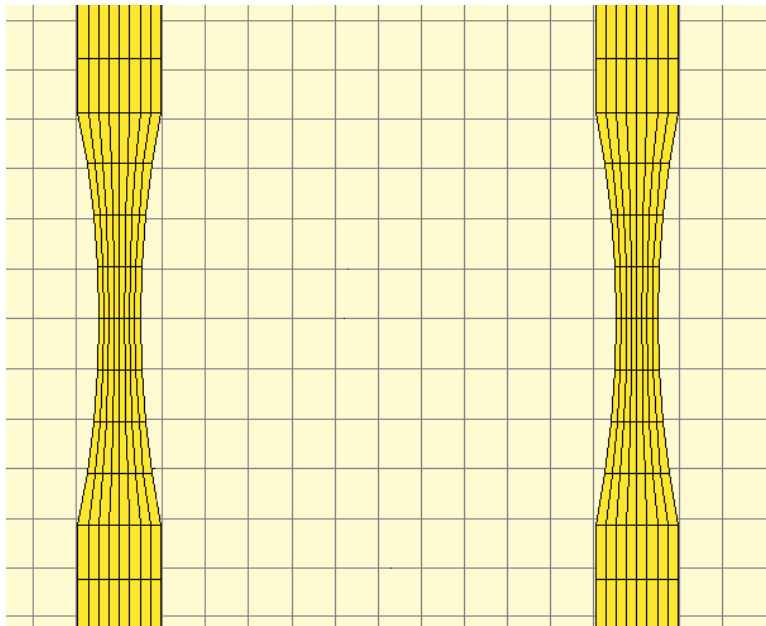
Figure 2.18: Detail of Finite Element Model of Long Cylinder with Simulated Flange Corrosion.

$v = w = 0$

$\theta_X = \theta_Y = \theta_Z = 0$

$u = v = w = 0$

$\theta_X = \theta_Y = \theta_Z = 0$
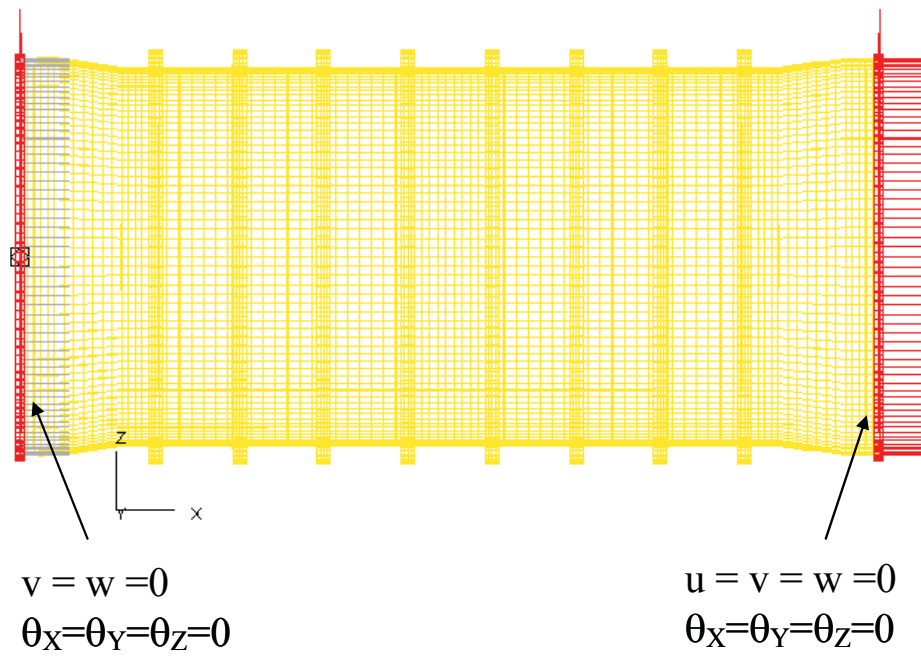
Figure 2.19: Boundary Condition I-Clamped at Both Ends.

$v = w = 0$

$v = w = 0$ $u = 0$
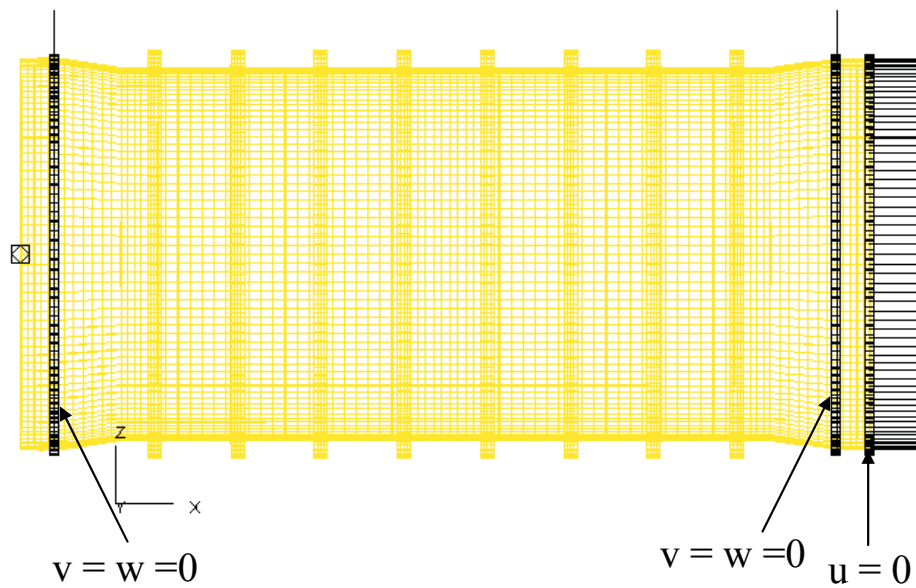
Figure 2.20: Boundary Condition II-Pinned Along the Edge of Endcap.

v = w =0

v = w =0

u = v = w =0
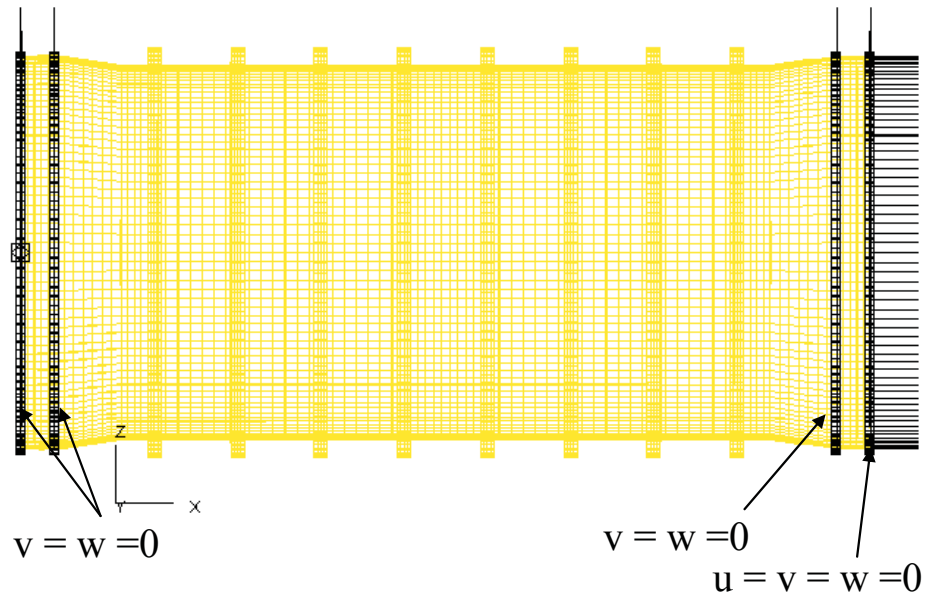
Figure 2.21: Boundary Condition III - Pinned Along Edge of Endcap and Bolt Connections.

Rigid links

u = v = w =0

$\theta_X=\theta_Y=\theta_Z=0$
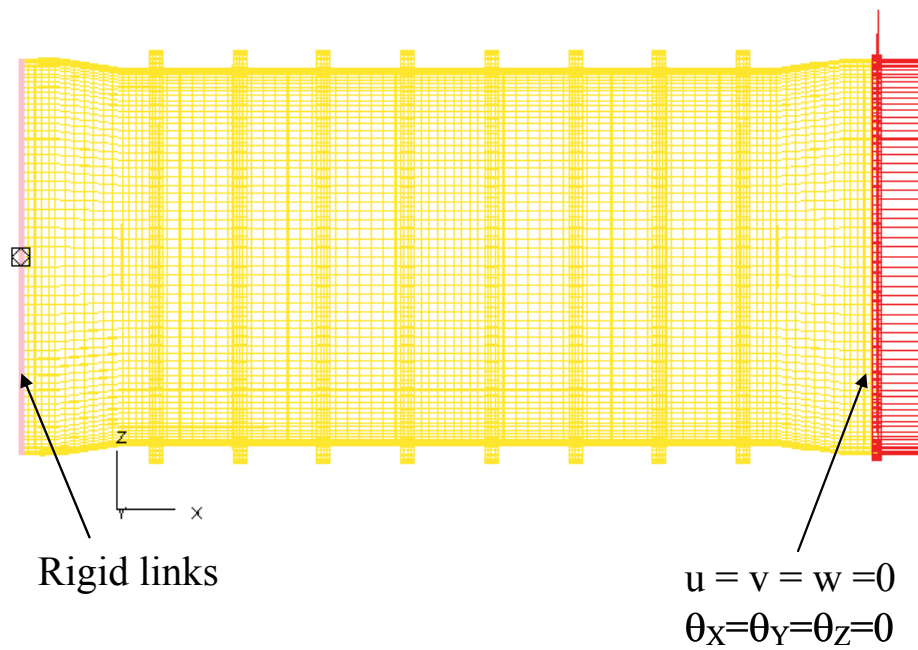
Figure 2.22: Boundary Condition IV -Clamped at One End and Rigid Link at the Other End.
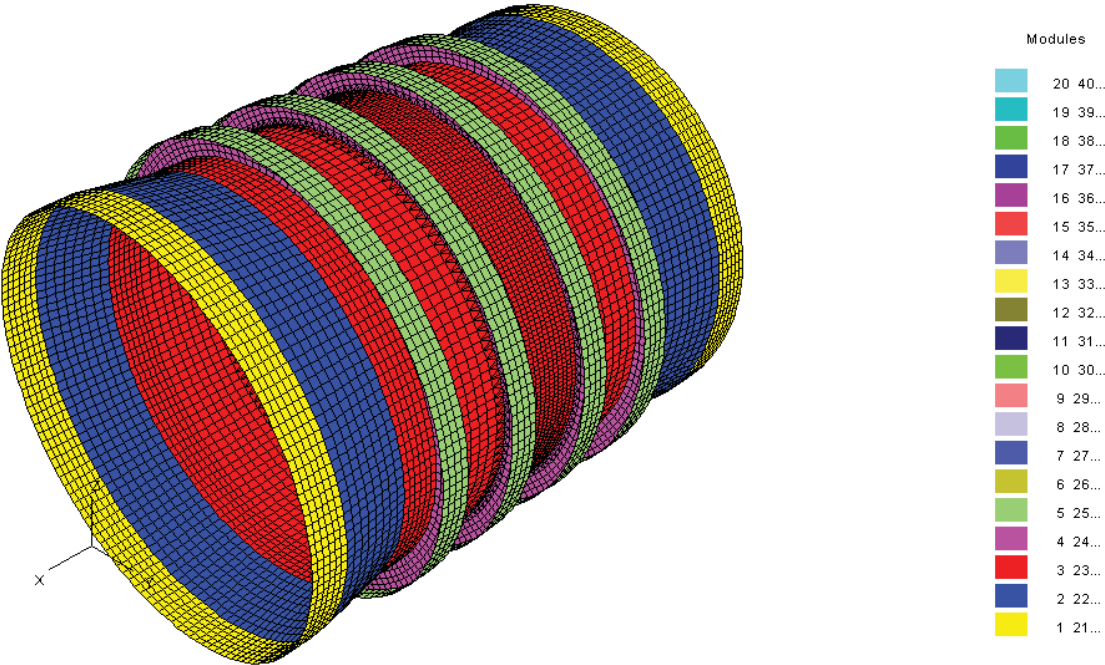
Figure 2.23: Module Definition in Finite Element Model for Short Cylinder.
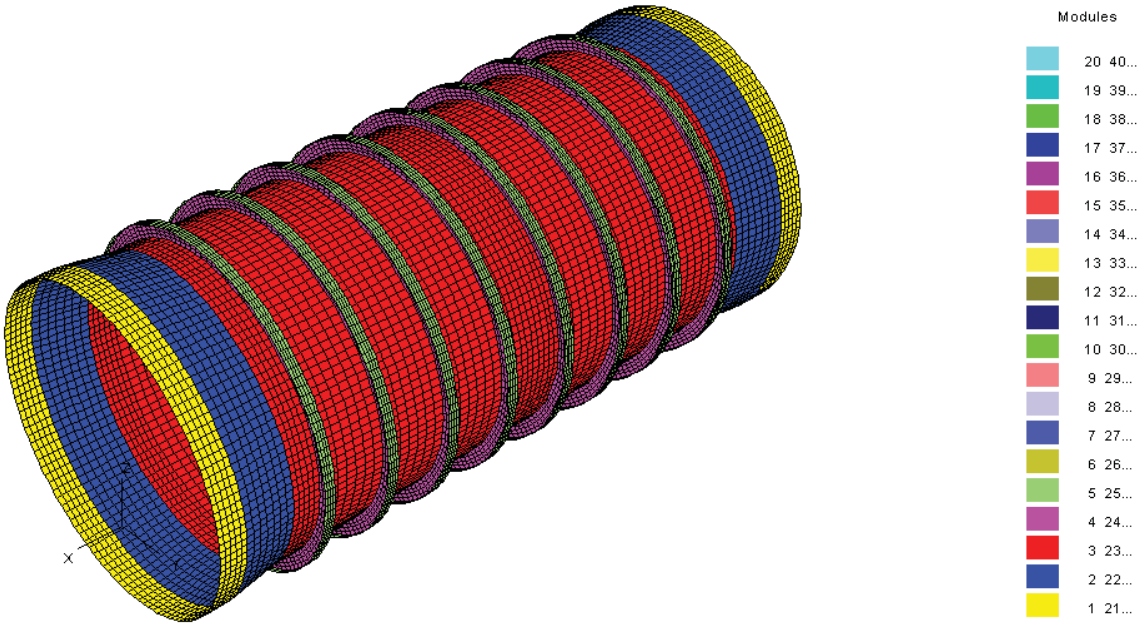
Figure 2.24: Module Definition in Finite Element Model for Long Cylinder.
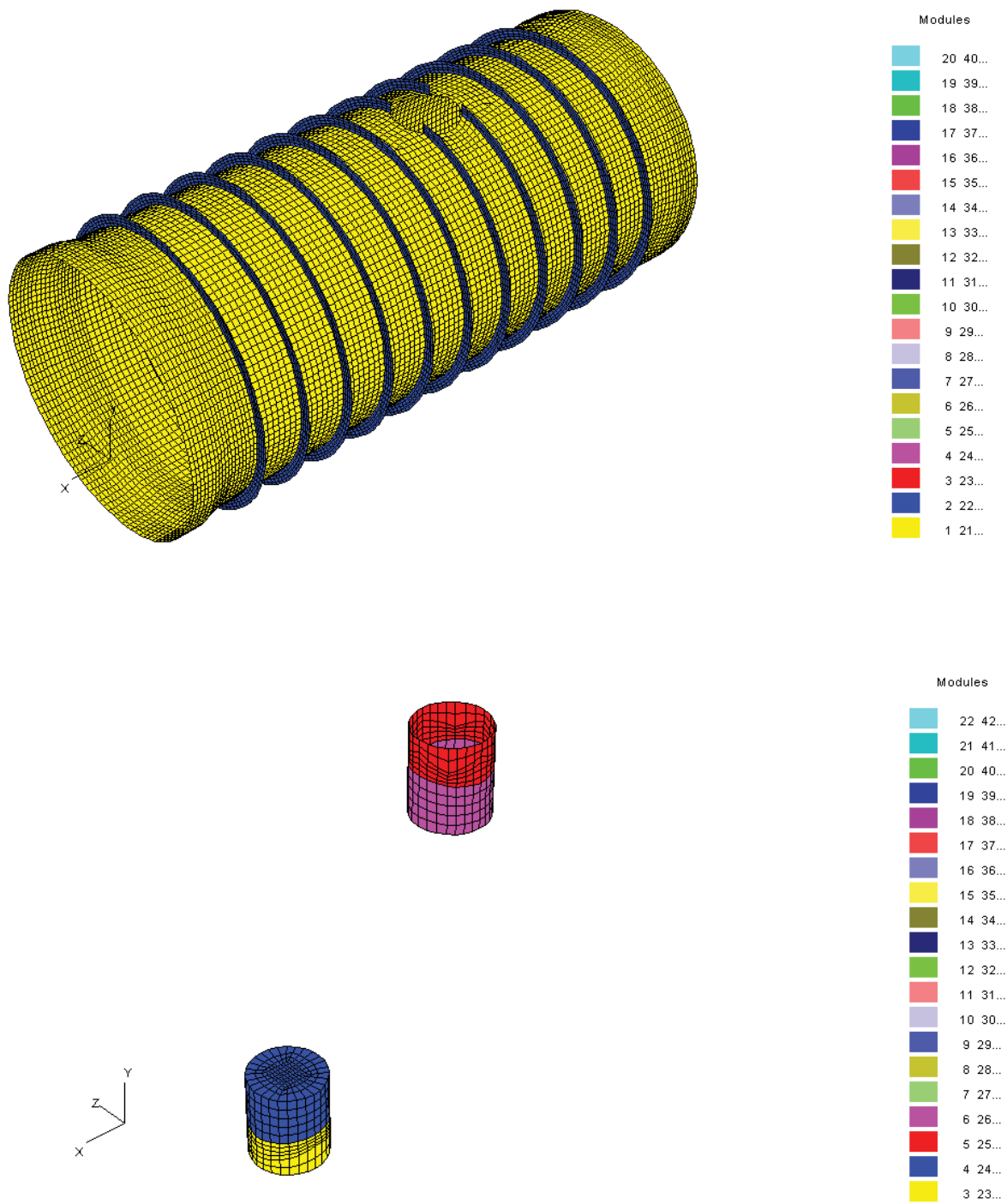
Figure 2.25: Module Definition in Finite Element Model for Cylinder with Penetration.

3.0   NON-LINEAR FINITE ELEMENT RESULTS

In the previous chapter, we described development of three-dimensional finite element models of the six experimental cylinders summarized in Table 3.1. These finite element models were created using the SubSAS program and the 4-noded nonlinear quadrilateral shell element was utilized in all the models. Measured thickness variations and out-of-circularities in axial and circumferential directions were incorporated into these finite element models. The simulated corrosion patch in the short cylinders and flange reduction in the long cylinders were both introduced using special FORTRAN programs developed for these purposes.

All nonlinear analyses were performed using the VAST finite element program, which provided both geometrically and materially nonlinear capabilities. In the analyses of the short and long cylinder models, convergence studies were first conducted to investigate the effect of the level of finite element mesh refinement on the nonlinear solutions and to determine the minimum mesh that was required to capture the highly nonlinear behaviour of the cylinders in the post-collapse regime. Due to complications in model generation for the cylinder with penetrations, the finite element mesh used for nonlinear analyses was selected based on the convergence studies for linear analyses performed in Phase 1 of the present contract [2].

Following the convergence study, the effect of nonlinear material models on the numerical solutions was investigated. Three material models were considered to represent the constitutive relations for elastic-plastic deformations during the nonlinear loading process. These included an elastic-perfectly plastic material property, a bilinear material property with isotropic or kinematic strain hardening, and the most general multi-linear stress-strain property directly extracted from the experimentally obtained stress-strain curves. The multi-linear material property was treated using the overlay model, which was proved to be highly accurate for both loading and unloading. The material constants required in all three models were determined from the material test data in the circumferential direction as given in Figure 2.11. For the cylinder with penetrations, nonlinear solution was only obtained using the elastic-perfectly-plastic material model.

In order to obtain the post-collapse response, the orthogonal trajectory solution procedure was employed in the present nonlinear analyses. This solution technique involves a constraint equation similar to the one used in the constant arc-length method, but eliminates the requirement for solving quadratic algebraic equations. For this reason, the orthogonal trajectory method is more robust than the classical arc-length method in most situations. Upon successful completion of the nonlinear runs, detailed comparisons of computed and measured pressure-strain histories were performed whenever the strain gauge measurements were available.

In addition, the effects of a number of other factors on the nonlinear solutions were also explored. These included thickness variations, boundary conditions, self-weight of cylinder and endcap, and material overlap at the plate junctions in the finite element model. These studies were all based on the behaviour of the non-corroded long cylinder L510-No1.

For highly nonlinear finite element analyses, such as the plastic collapse of nearly-perfect stiffened cylinders as considered in the present work, numerical stability of the numerical solutions could be improved by superimposing a linear buckling mode shape onto the initial finite element model as geometric imperfection. However, the predicted nonlinear behaviour could be sensitive to the magnitude of the superimposed imperfections. In this contract, a parametric study was also carried

out for the cylinder with penetrations to investigate the sensitivity of the nonlinear solutions to the amplitude of the added imperfections.

Numerical solutions from all these analyses are presented below in detail.

3.1   FIRST SHORT CYLINDER (L300-No2)

3.1.1   Convergence Study

In order to determine the minimum level of mesh refinement required to obtain accurate nonlinear solutions for the short cylinders, four finite element models were first created for the non-corroded short cylinder L300-No2. The 4-noded quadrilateral shell element was utilized in these models as shown in Figures 3.1-3.4, and the meshing parameters are summarized in Table 3.2. All models were generated using the SubSAS program, with which both the measured circumferential thickness variation and measured out-of-circularities in both directions were included. Since thickness measurements were available only at the centre of the central bay, the measured thicknesses were applied uniformly over the central bay as indicated in Figure 3.5. For all other portions of the cylindrical wall between the tapered ends, the average thickness value was used. In this convergence study, bilinear material property based on material testing in the circumferential direction was employed and the isotropic hardening model was used to take into account the effect of strain hardening. The clamped boundary conditions (BC I as shown in Figure 2.19) were used in these studies.

The deformed configurations of the short cylinder predicted by VAST using different meshes are presented in Figures 3.6-3.17. These results indicate that interframe collapse occurred at the central bay for all four meshes, as shown in Figures 3.8, 3.12 and 3.15. This failure mode was consistent with both the experimental observations [1] and previous results from submarine design formulas (SDF) [2]. In all nonlinear runs, the local collapse was initiated at the location of the minimum thickness, as demonstrated in Figures 3.9, 3.13 and 3.16. With further deformation, additional dimples (local buckling) occurred next to the initial buckling site as shown in Figure 3.10, 3.11, 3.14 and 3.17. This interframe collapse characteristic was also predicted by the coarsest finite element mesh as shown in Figures 3.6 and 3.7. However, this mesh did not have sufficient resolution to represent the local deformed geometry accurately. In addition to the local buckling in the central bay, the finest mesh also predicted buckling in the end bay at later stage of the nonlinear solution. This end bay buckling was not observed in the other three solutions.

The external pressure versus maximum radial displacement curves obtained by different models are compared in Figure 3.18, where the "mode jumping" phenomenon was predicted by all meshes except the coarsest one. The peak pressures obtained by these meshes are summarized in Table 3.4 and are displayed in Figure 3.19 versus the numbers of nodes in these meshes. These results indicated that the peak pressure predicted by Mesh R3 and Mesh R4 were in close agreement, indicating convergence of the nonlinear finite element solution. Based on this convergence study, Mesh R3 was found to be adequate for capturing nonlinear behaviour of the short cylinder and had been utilized to generate results to be discussed in the following sections. In the meantime, we also noticed that the peak pressures obtained in this study converged to a value lower than the measured peak pressure in the experiments. This discrepancy is likely to be caused by the uncertainty in the nonlinear material properties.

3.1.2   *Effect of Material Model*

Following the determination of the mesh suitable for nonlinear analysis of the short cylinder, the effect of the material model on the predicted nonlinear solution was investigated. Using mesh R3, nonlinear analyses were conducted using three different material models, including elastic-perfectly-plastic, bilinear and multi-linear stress-strain properties. The pressure versus maximum radial displacement curves obtained from these analyses are compared in Figure 3.20 and the predicted peak pressures are compared with the experimental data in Table 3.4. These results indicate that solutions using all material properties are almost identical in the pre-buckling range. However, the bilinear material model resulted in the highest peak load and the highest post-collapse stiffness. The use of multi-linear stress-strain property led to an early onset of plastic flow and a lower limit pressure level. The elastic-perfectly-plastic model predicted a peak load close to that from the bilinear model, but a post-buckling response similar to that from the multi-linear material model. These trends were consistent with expectations.

3.2   SECOND SHORT CYLINDER (L300-No3)

3.2.1   *Effect of Material Model*

Based on the results of the convergence study presented in the previous section, mesh R3 was most suitable for nonlinear analysis of the non-corroded short cylinder. This mesh was now adopted for analyses of the short cylinder with a simulated corrosion patch, as shown in Figure 3.21. This model was first generated using the SubSAS program using proper geometric properties including the measured thickness variation and out-of-circularities. The square-shaped corrosion patch was then introduced in the finite element model through a special purpose program, which adjusted node positions, element thicknesses and applied nodal offsets to all elements inside the corroded area. The thickness contour of the final model is given in Figure 3.22, where the corrosion patch is clearly indicated.

The nonlinear solution indicated that during the loading process, the corroded area buckled first forming a local dimple in the central bay as shown in Figure 3.23. This deformation pattern formed kinks along the edges of the corroded area which caused an increase in local bending stiffness. This localized hardening effect, along with the stiffness contribution of the surrounding stiffeners, resulted in an increase in load carrying capacity above the pressure level at which the initial dimple occurred in the central bay. Following collapse (maximum load) resulted in additional localized buckling of the cylinder wall adjacent to the original dimple, as depicted in Figure 3.24. Figure 3.25, which shows the location of the corroded area on a plot of deformed shape, confirmed this explanation, as does Figure 3.26, which shows load versus displacement curves for a point at the centre of the first dimple.

The numerically predicted peak collapse loads using different material models are compared with the experimentally measured values in Table 3.5, and the pressure-displacement curves obtained by using different material models are compared in Figure 3.26, where Node 908 was located at the centre of the corrosion patch and moved along the negative Z-direction during the solution. In addition to the solutions obtained using the bilinear stress-strain properties with and without strain hardening, Figure 3.26 includes three curves for multi-linear stress-strain curves based on the material test data in circumferential and axial directions as well as and averaged material curve.

These results indicate that use of the axial test data would result in an overestimate of the collapse pressure. In addition, it is interesting to note that the solution using the average material property lies almost in the middle of the other two curves. All curves in Figure 3.26 reflect the identical nonlinear deformation process for the corroded short cylinder. With increase of pressure, the corroded area was buckled first. However, after this local buckling, the cylinder was able to take more loads before peak collapse occurred.

3.2.2   Strain Histories

Once the nonlinear analyses were completed, the special purpose program, StrainExtractor, was executed to extract pressure-strain histories at all 48 strain gauge locations specified in Reference [1] and summarized in Table 2.4 in the previous chapter of this report. These extracted strain histories were stored in text files and were used to compare numerical results with the measured strain history data provided by the Scientific Authority.

The measured strain history of the circumferential strain in the flange of Frame 2 at 0° is compared with the finite element solutions obtained using various material models in Figure 3.27. All curves in this figure are in good agreement and indicate a local buckling of the corroded area followed by an overall collapse of the whole cylinder. The measured and predicted histories of circumferential strain on the inside of the shell at the center of the corrosion patch are compared in Figure 3.28. Excellent agreement between all curves is observed in the pre-buckling range. Immediately following the local buckling in the corroded area, the strain gauge measurement showed a sudden change of direction in the pressure-strain curve. This phenomenon was captured in all numerical solutions presented in Figure 3.28.

In order to judge the overall quality of the finite element solutions, measured and predicted pressure-strain histories at all strain gauge locations were compared, as shown in Figures 3.29-3.33. The finite element solutions shown in these figures were obtained using the multi-linear stress-strain curve extracted from the material test data in the circumferential direction given in Figure 2.11. This rather thorough comparison between the experimental and numerical solutions at the strain level indicates that the finite element method is accurate and reliable in predicting both global and local nonlinear behaviour of corroded stiffened cylinders under hydrostatic pressure.

3.3   THIRD SHORT CYLINDER (L300-NO4)

3.3.1   Effect of Material Model

This was another experimental short cylinder model with a simulated square corrosion patch in its central bay. Although this cylinder was designed to have the identical nominal geometry as the previous corroded short cylinder (L300-No3), the actual geometry, including the shell thicknesses and out-of-circularities, were slightly different due to the nature of the manufacturing process. As a result, the finite element model for this cylinder was generated from scratch using SubSAS, but the general layout of mesh R3 was preserved as shown in Figure 3.34. Once again, the square-shaped corrosion patch was applied to the SubSAS-generated finite element model using a special FORTRAN program. The thickness contour of the cylinder wall in the final model is shown in Figure 3.35.

The predicted nonlinear behaviour of this corroded short cylinder was very similar to that of the previous cylinder model. The deformed configurations shown in Figures 3.36 and 3.37 indicate that during the deformation process, local buckling first occurred in the corroded area and then progressed to the adjacent area, causing peak collapse of the cylinder into an interframe failure mode. The predicted final collapse loads using different material models are compared with the experimental data in Table 3.5 and the pressure-displacement curves are shown in Figure 3.38. Similar to the results for other cylinders, the bilinear model with isotropic hardening resulted in the highest collapse load, where as the solution from the elastic-perfectly-plastic model agreed well with the result of bilinear material in the pre-buckling region, but was in close agreement with the multi-linear solution in the post-buckling range.

3.3.2   Strain Histories

Since no strain gauge measurements were performed on this cylinder, a direct comparison of the measured and predicted strain histories was impossible. The computed strain histories of the circumferential strain in the flange of Frame 2 at 0° using various material models are presented in Figure 3.39. These results are comparable to those shown in Figure 3.28. A comparison of these two figures revealed some differences between the nonlinear behaviour of the two corroded short cylinders. First of all, the second cylinder (L300-No4) was slightly stiffer than the first one, resulting in an increased collapse pressure. Second, for L300-No4, the pressure actually dropped following the local buckling of the corroded area. However, for L300-No3, the local buckling in the corroded area resulted in either a plateau or slight drop in the pressure-strain history.

3.4   FIRST LONG CYLINDER (L510-No1)

3.4.1   Convergence Study

Similar to the nonlinear analyses of the short cylinders presented above, a convergence study was also conducted to determine the suitable mesh for predicting nonlinear collapse behaviour of the long cylinders. Four meshes of the long cylinders with different levels of the mesh refinement were created using SubSAS. These meshes are displayed in Figures 3.40-3.43, respectively, and the meshing parameters are summarized in Table 3.3. The measured out-of-circularities were included in these models, but the measured thickness variation in the central bay was not included.

The nonlinear collapse analyses were performed using bilinear material properties with kinematic hardening. The Young's modulus, yield stress and hardening modulus were taken from the test data in the circumferential direction shown in Figure 2.11. All these meshes predicted localized buckling in the early stage of the post-buckling response. Although the predicted buckling sites were different from model to model as indicated in Figures 3.44 - 3.47, the pressure versus maximum radial displacement curves obtained from these finite element models were in very close agreement as shown in Figure 3.48. The peak pressure values predicted by all meshes are almost identical as indicated in Table 3.6. However, small differences exist in the post-buckling responses, where a slightly higher stiffness was observed for local buckling occurring in the end bay. This was likely due to the larger stiffness contributions of the thicker cylinder wall in the tapered region. These results indicate that for the long cylinders, if the measured thickness variation is not included, then the pre-buckling response is nearly axisymmetric. As a result, the location of the first local buckling was controlled by the location of the first yielding in the

cylinder, which was extremely sensitive to the local stress distributions in the cylinder. More discussion on this characteristic will be presented later.

Based on the results of the convergence study, mesh R3 as shown in Figure 3.42 was chosen for nonlinear analyses of the long cylinder model in the present study.

3.4.2   Effect of Material Model

In order to study the effect of the material model on the predicted nonlinear behaviour of the long cylinder, further analyses were conducted using three elastic-plastic material models, including elastic-perfectly-plastic, bilinear with kinematic hardening and multi-linear stress-strain properties. Finite element model R3 identified in the convergence study was utilized.

Similar to the observations made in the convergence study, the nonlinear solutions obtained using different material models also predicted that the long cylinder collapsed in local buckling mode, but the local buckling occurred at different locations as shown in Figures 3.49-3.51. The predicted pressure versus radial displacement curves are in very good agreement as in Figure 3.52, indicating that the location of the initial local buckling was sensitive to the small differences in the stress field from model to model, which could be caused by factors like mesh layout and material model. The predicted peak pressure is also quite sensitive to the material properties, as suggested in Table 3.6.

To verify the accuracy of the finite element solutions, measured and predicted circumferential variations of the circumferential stress in the flange of Frame 4 at eight different load levels ranging from 1.0 MPa to 8.0 MPa were compared, as shown in Figure 3.53, based on the finite element solution obtained using the bilinear model with kinematic hardening. The experimental and numerical results are in close agreement, both showing a harmonic mode 3 component on top of a large axisymmetric strain field. This mode 3 component was consistent with the harmonic mode for overall buckling predicted by the Submarine Design Formula (SDF) [2]. Careful examinations of the destroyed specimens following well controlled pressure testing procedure indicated that the final failure mode was n=3, with a single buckling lobe dominating the post-collapse behaviour. This final failure mode observed in the experiments could be the consequence of progression of the initially localized buckling.

3.4.3   Effect of Boundary Condition

Nonlinear analyses were performed to investigate the influence of the boundary conditions on the predicted failure mode of the long cylinder. As mentioned in Section 2.6.3 in the previous chapter, the default boundary condition in the present study was the clamped boundary condition shown in Figure 2.19. In order to model the interaction between the end sections of the cylinder with the endcaps, two pinned boundary conditions were also created as depicted in Figures 2.20 and 2.21. These pinned boundary conditions were more flexible than the clamped boundary conditions and none of these boundary conditions enforced the condition of planar cross section at the loaded end. To enforce this requirement, an additional boundary condition was formulated using the rigid links as shown in Figure 2.22. The bilinear material with kinematic hardening was considered in all 4 analyses.

The final deformed shapes of the long cylinder predicted using different boundary conditions are presented in Figures 3.54-3.57. All of them showed local buckling, but at different locations. The pressure versus maximum radial displacement curves for different boundary conditions are

compared in Figure 3.58, where the peak pressure values obtained from all four runs are almost identical (as shown in Table 3.6), but the post-buckling stiffness for local failure in the end bay is slightly higher than that for local buckling in the central bay. These results suggested that the predicted peak pressure is not sensitive to the boundary conditions, but the location of the local buckling is largely influenced by the small differences in the stress field, which could be introduced by the definition of boundary conditions.

In order to further assess the influence of boundary conditions on the nonlinear solutions, measured strain histories at four gauge locations with the finite element predictions obtained using different boundary conditions were compared. These strain components included axial strain on the outside surface of the cylinder wall at the centre bay (Figure 3.59), circumferential strain on the outside surface of the cylinder wall at the central bay (Figure 3.60), axial strain on the outside surface of the cylinder wall at the end bay (Figure 3.61) and axial strain on the inside wall of the cylinder wall at the central bay (Figure 3.62). These figures indicated that the experimental and numerical results are in reasonable agreement, and the numerical results from different boundary conditions are almost identical until the local buckling starts to appear.

3.4.4   Effect of Thickness Variation

As mentioned earlier, the finite element models used for nonlinear analyses of the long cylinder in the preceding sections did not include the measured thickness variation in the circumferential direction. The influence of the thickness variation on predicted nonlinear behaviour is described in the present section.

Since thickness measurements were available for only the middle section of the cylinder, the measured circumferential variation of the thickness was applied to the centre bay uniformly between the adjacent stiffeners and an average thickness was used elsewhere, as shown in Figure 3.63. Three nonlinear analyses were performed using different material models, including elastic-perfectly-plastic, bilinear and multi-linear based on the test data in the circumferential direction, but only the clamped boundary conditions were considered. In this case, the failure mode of the cylinder was dominated by the cylinder thickness, such that all solutions indicated initial local buckling occurring in central bay at the location of minimum shell thickness, as shown in Figure 3.64.

In order to verify the overall accuracy of the finite element solution, measured strain histories at all strain gauge locations were compared with the predictions using the multi-linear material model, as shown in Figures 3.65-3.68. There is very good agreement between these solutions. For an even closer comparison, the measured strain histories at four strain gauges were plotted against the predictions using different material models in Figures 3.69-3.72. These figures indicate that although the solutions using different material models were almost identical in the pre-buckling range, they became significantly different as soon as plastic deformations occurred. Among them, the solution based on the multi-linear stress-strain curve provided best agreement with the experimental data.

Figures 3.65-3.68 show that the finite element method consistently under-estimated the pre-buckling stiffness, resulting in overestimated strains in the pre-buckling region. It is suggested that this was a consequence of using material test data in the circumferential direction in an isotropic plasticity model in the nonlinear analyses. In order to study the effect of the elastic modulus on the predicted strain histories, one additional run was performed using bilinear material model, where

the Young's modulus was increased to 75,000 MPa consistent with the experimental data in the axial direction. In this case, the increased Young's modulus was applied in all directions. Other material parameters, such as the yield stress and hardening modulus, were remained unchanged. The predicted strain histories are shown in Figures 3.69-3.72 under legend "Bilinear-Axial". As expected, an improved agreement between the experimental and numerical results was obtained in the pre-buckling range.

The pressure-maximum radial displacement curves predicted by using different material models with and without thickness variation are compared in Figure 3.73. The peak pressure values obtained using different material models are summarized in Table 3.6. These solutions indicate that inclusion of the thickness variation only leads to a very small reduction on predicted peak load levels and the increase of Young's modulus does not cause noticeable changes in the pressure-displacement characteristics of the cylinder.

3.4.5   Effect of Self Weight

One of the requirements of the present contract was to investigate the significance of self-weight on the nonlinear behaviour of the test cylinder. This numerical investigation was performed using the long cylinder L510-No1. In the present finite element analyses, the influence of the self-weight was represented by an additional load case, which included the gravitational forces of the stainless steel endcap, the aluminium cylinder and the buoyancy force generated by the mineral oil pressure testing fluid. This load case contained a translational acceleration in the axial direction and a group of concentrated forces acting on the end section, as shown in Figure 3.74. The deformed configuration and axial stress contour due to the self-weight are presented in Figures 3.75 and 3.76, respectively. It should be noted that because the magnitude of the displacements generated by the self-weight was very small, a huge displacement amplification factor had been utilized for purposes of visualization. The finite element analysis indicate that the maximum tensile axial stress of 0.065 MPa occurred at the junction between the thinner cylinder and the tapered section near the left end in Figure 3.76. This agreed with the result from a simple hand calculation.

The VAST code permits multiple load cases to be considered in nonlinear analyses. In this case, a group of load parameters were utilized to scale each of the reference load vectors independently. The analyst was only allowed to activate one load case at a time, but the active load case could be changed by terminating and restarting a nonlinear analysis. In the present analysis, the load case describing the self-weight was fully applied to the cylinder model in the first load step and from the second step on, the nonlinear run was started with the load case describing the hydrostatic pressure. The final deformed configuration obtained with the effect of self-weight is displayed in Figure 3.77. The figure shows local buckling at the end bay close to the free end. This was in agreement with expectations. The self weight caused an initial axial tensile stress that acted to counter the compressive stresses caused by the applied external pressure. Since the initial tensile stress was lowest at the end bay close to the free end, first yield, and hence buckling, was expected to occur there. The pressure versus maximum radial displacement curves obtained with and without the self-weight are compared in Figure 3.78 and peak pressures predicted for both cases are compared with the experimental data in Table 3.6. These results show that the self-weight had no influence on the predicted collapse pressure. The difference in the post-buckling stiffness in these solutions was due to the location of the local buckling.

3.4.6   Effect of Material Overlap at Plate Junction

All the finite element models considered above were constructed using the mid-surface geometry. In these models, small material overlaps occurred along the intersections of structural members, such as at the web-cylinder and web-flange junctions where elements meet at right angles. One requirement of the present contract was to assess the significance of this material overlap on the nonlinear solutions.

In order to fulfill this requirement, a special finite element mesh of the long cylinder was generated by modifying an existing model created originally by SubSAS. These modifications included reducing the web height by subtracting half thicknesses of the cylinder and flange, adding new nodes along the upper and lower edges of web, and applying rigid links to enforce displacement compatibility conditions on all six degrees-of-freedom along the junctions. This was achieved through a specially developed FORTRAN program. The new finite element model without material overlaps is displayed in Figure 3.79 and its local details are shown in Figure 3.80. The measured thickness variation was not included in this model and the bilinear material property was utilized to describe plastic deformation.

The deformed configuration predicted by using this new finite element model is shown in Figures 3.81 and 3.82, where two local buckling locations were observed at the end bay. The pressure versus maximum radial displacement curves obtained using finite element models with and without material overlap are compared in Figure 3.83 and the peak pressure values obtained for both cases are given in Table 3.6. Very close agreement between them is obtained, indicating that the small material overlap in finite element models did not significantly affect the predicted nonlinear behaviour.

3.5   SECOND LONG CYLINDER (L510-NO2)

3.5.1   Effect of Material Model

In order to include the simulated flange corrosions in nonlinear finite element analyses, the nodes in the corroded area were adjusted axially outside SubSAS using a specially developed FORTRAN code. The finite element model of the corroded cylinder and the local details around the reduced flange are shown in Figures 3.84 and 3.85, respectively. Clamped boundary conditions were applied.

Nonlinear solutions were obtained for three material models, including elastic-perfectly-plastic, bilinear and multi-linear. The predicted final deformed configuration and pressure-maximum radial displacement curves are present in Figures 3.86, 3.87 and 3.88, respectively. The solutions using all material models predicted local buckling at the central bay close to the simulated corrosion. This was because both the weakened flange and thinnest cylinder wall occurred at the same circumferential location. The detailed plot of the deformed shape in the buckled area indicated that the stiffener deformed into a "V" shape, which was also consistent with the observations made from the experiment. The predicted peak pressure values summarized in Table 3.7 and pressure-displacement curves in Figure 3.88 clearly demonstrate that, in addition to the effect that the material model has on load carrying capacity, the flange corrosion also significantly reduced the load carrying capacity of the long cylinder.

3.6   PENETRATION CYLINDER

3.6.1   *Effect of Out-of-Circularities*

The finite element model for nonlinear analysis of the experimental cylinder with penetrations is shown in Figures 3.89 and 3.90. This model was initially generated for linear analysis in Phase I of the contract [2]. In the current phase, this linear finite element model was modified to include nonlinear material property based on a bilinear elastic-plastic model with kinematic hardening. Clamped boundary conditions were applied in all analyses of the penetration cylinder.

Because this finite element model was originally generated for linear analyses, the measured out-of-circularities were not included. We noticed that for this particular cylinder model the penetrations introduce more significant geometric imperfections than the out-of-circularities. Hence, the nonlinear behaviour of this cylinder should be dominated by the penetrations instead of the out-of-circularities. In order to prove this hypothesis, we first performed a nonlinear analysis using this geometrically "perfect" model (that is, a penetration cylinder model with no out-of-circularities). This nonlinear analysis predicted that the cylinder would collapse into an overall buckling mode of n=3 (where n is the harmonic mode number). The predicted final deformed configuration of the cylinder is shown in Figures 3.91-3.93 which show 3D views from the top and bottom of the cylinder and an end view. Table 3.8 shows a comparison between computed peak pressures and the experimentally measured peak pressure. The row marked "no OOC" shows the comparison between the computed pressure for the "perfect" penetration model and the measured pressure. Very close agreement is observed.

In order to further verify the overall accuracy of the finite element results, comparisons between measured and predicted strain histories at various strain gauge locations were made. First, we compared calculated and measured profiles of circumferential strains along the circumference on the top of the center stiffener #6 under various external pressures, as shown in Figure 3.94. The finite element analysis resulted in strain distributions which are in good agreement with the measured values, but the magnitude of the strain is slightly underestimated. Secondly, the predicted and measured strain histories for the entire loading process were compared at selected strain gauge locations, including circumferential strains at five locations on top of the central stiffener #6 (in Figure 3.95) and vertical and horizontal strains on the inside wall of Penetration A (in Figure 3.96). The strain gauge locations on the penetration model are shown in Figure 3.97. Figure 3.95 shows that the strain histories at 0°, 120° and 240° are similar. Each show an increase of compressive strain in the pre-buckling range due to hydrostatic pressure followed by a decrease of compression close to the collapse load at which point these lines start to deform outwards away from the centerline of the cylinder. Based on the same analysis, strain histories at 180° and 300° show that the compressive strain continuously increases up to and beyond the collapse load. These strain variations clearly indicate a deformation pattern of n=3. It is also interesting to note that in the nonlinear finite element solutions, the curves corresponding to 120° and 240° are almost identical, but the measured curves for these angles are different. This is because that the measured out-of-circularities were not included in this finite element model. The predicted and measured strain histories on the inside wall of Penetration A are also in reasonably good agreement. For most of the strain components, the finite element solutions are lower than the measured values. This might be associated with the uncertainty in the material properties.

To quantify the influence of the out-of-circularities (OOC) on the nonlinear behaviour of the penetration cylinder model, measured OOC had to be introduced in the finite element model. Because the current version of SubSAS cannot handle out-of-circularities in models involving penetrations, a specialized FORTRAN program was again developed for this purpose. This program reads in an existing geometrically "perfect" finite element model and introduces the measured OOC by adjusting the nodal coordinates of all nodes on the cylinder wall and the stiffeners. For a given point in the finite element model, the OOC is calculated by using a Fourier series expression along the circumference and a B-spline approximation in the axial direction, similar to the algorithm implemented in SubSAS. Nodes on the penetrations are not modified.

Measured OOCs were provided by the Scientific Authority as radius values taken at 18 equally spaced circumferential locations at all stiffeners and the end rings. Circumferential angles were measured from the centerline of Penetration A [1]. However, the positive direction for the angle measurements was not recorded. As a result, two possibilities exist. One is to measure the angle clockwise from the positive Y-direction to the negative Z-direction (Angle Definition I) as shown in Figure 3.97, and the other possibility is to measure angle counter clockwise from the positive Y-direction to the positive Z-direction (Angle Definition II). Both definitions were considered in the present work.

The final deformed configuration of the cylinder obtained by including a full amount of measured OOC based on angle definition I (AD I) is presented in Figures 3.98-3.100 from different view angles. The deformed shapes indicate that the cylinder still collapsed into a mode of n=3. However, the deformation pattern is no longer symmetric about the vertical center plane as shown in Figure 3.93. The predicted circumferential strain profiles at the center stiffener are compared with experimental results in Figure 3.101, and the computed strain histories on top of the center stiffener #6 and inside wall of Penetration A are compared with the measurements in Figures 3.102 and 3.103, respectively. By comparing Figures 3.95 and 3.102, we realized that the inclusion of the measured OOC based on the first angle definition resulted in an improved agreement between the predicted and measured strain histories for 0° and also made the curves for 120° and 240° to move in the desired direction. The experimental data indicated that the strain at 120° is less than the strain at 0°, whereas the strain at 240° is greater than the strain at 0°. This trend is captured in the finite element solution after the measured OOC is included. However, the differences between the numerical solutions obtained with and without the measured OOC are very small in general. This observation confirmed our earlier hypothesis that the nonlinear response of this cylinder is dominated by the penetrations rather than the small geometric imperfections.

The finite element results obtained by using the measured OOC based on angle definition II (AD II) are presented in Figures 3.104-3.107. In this case, the finite element results still indicated that the cylinder failed in a mode of n=3. Furthermore, it is interesting to note that if the deformed configuration shown in Figure 3.105 is flipped 180° about the center vertical axis, it would become almost identical to the corresponding figure for the case of measured OOC based on angle definition I in Figures 3.100. This relationship also exists between Figures 3.101 and 3.106, which show the profiles of circumferential strain in both cases. Examining Figure 3.107, it is noticed that with the inclusion of the measured OOC based on angle definition II, an improved agreement was obtained for strain history at 0°, however, the curves corresponding to 120° and 240° moved to a direction inconsistent with the experimental results. These results suggested that angle definition I is consistent with the OOC measurement.

In order to investigate the effect of the magnitude of the OOC on the nonlinear results, analyses were performed for two additional cases, in which 200% and 500% of the measured OOC were superimposed onto the finite element model based on angle definition I. The results obtained with 200% OOC are displayed in Figures 3.108-119. These results still show that the cylinder fails under an overall collapse mode, but the mode number is no longer strictly n=3. If the magnitude of OOC is further increased to 500% of the measured value, the cylinder is found to collapse with a localized buckling mode as shown in Figures 3.114-116. The strain distribution at stiffener #6 is totally changed as indicated in Figures 3.117-3.118 and there is no correlation between the finite element solution and the experimental results that were taken for much small OOC. The predicted strain histories at points on the inside wall of Penetration A are not significantly altered. This is because no geometric imperfection was introduced in the finite element model at the penetrations.

The peak pressures predicted for different amounts of out-of-circularities are summarized in Table 3.8 and the pressure-radial displacement curves are given in Figure 3.120. These results indicated that the both peak pressure and the pre-buckling stiffness of the cylinder increases monotonically with the increase of the magnitude of OOC. The trend is also consistent with our expectation.

3.6.2   *Superposition of Linear Buckling Mode*

For highly nonlinear problems, such as prediction of plastic collapse of stiffened cylinders as considered in the present work, numerical stability of the finite element solution can be improved by introducing a small amount of a selected linear buckling mode on to the original undeformed finite element model. This solution technique had been incorporated into the VAST program and successfully utilized in the calculation of load-shortening behaviour of stiffened panel structures of various configurations.

To use this analysis option, a linear buckling (eigenvalue) analysis must be performed using VAST to obtain the desired buckling mode shape before the nonlinear run takes place. When setting up the VAST USE file, which contains the various analysis parameters, for nonlinear analysis, the user can specify a mode number and magnitude for the desired buckling mode shape and the VAST program will automatically retrieve the appropriate buckling mode, scale it based on the user-defined magnitude and superimpose it to the initial finite element geometry. However, in some situations, selection of proper magnitude for the desired buckling mode shape for inclusion into the finite element mode may not be a simple task. If the magnitude is too small, the nonlinear solution cannot be stabilized effectively. If it is too large, the predicted nonlinear behaviour can be significantly changed. In this section, we present a set of interesting numerical results to demonstrate the influence of the magnitude of the superimposed buckling mode on the predicted failure mode of the cylinder.

The linear buckling mode used for the present study is shown in Figure 3.121 and 3.122. This was the first mode from a linearized eigenvalue analysis and corresponded to a critical pressure of 13.39 MPa. Comparing the end view of the linear buckling mode shape showing in Figure 3.122 and the final deformation shape from the nonlinear analysis in Figure 3.94, it was realized that both corresponded to harmonic mode n=3, but were different by 30° in orientation. Actually, the second mode from the linear buckling analysis was identical to Figure 3.94 with a slightly higher critical pressure value. Four nonlinear analyses were conducted using different magnitudes of buckling mode shape defined in terms of the maximum deflection values of 0.002mm, 0.01mm, 0.05mm and 0.2mm, respectively. These corresponded to 0.074%, 0.37%, 1.85% and 7.4% of the nominal thickness of the cylinder wall. The final deformed configurations obtained from these

nonlinear runs are displayed in Figures 3.123-3.126 and the corresponding peak pressure values are given in Table 3.8. These results indicated that with the increase of the magnitude of the superimposed buckling mode, the predicted final failure mode became closer and closer to the superimposed buckling mode shape.

3.7   COMPARISON WITH SDF PREDICTIONS

A very comprehensive study of the six experimental cylinders was performed in Phase I of the present contract using the Submarine Design Formulas (SDF) [2]. In these calculations, external pressures corresponding to various limit states, such as shell and stiffener yielding, interframe buckling and overall collapse, were obtained using three independent submarine design and analysis programs, named PRHDEF [4], PD004B [5] and K79 [6] developed by DRDC Atlantic, the Ministry of Defence (MOD) of the UK and DRDC Atlantic, respectively. In the present phase of work, the interframe and overall collapse pressures predicted by the SDF are compared with the limit pressures measured experimentally and predicted numerically by the 3D nonlinear finite element analyses.

The SDF parameters considered in this comparison are summarized in Table 3.9. Most of these parameters included the effect of plastic deformations and the material test data in the axial direction was utilized to determine the nonlinear material properties. The interframe and overall collapse pressures predicted by SDF are compared with the experimental and numerical results in Tables 3.10, 3.11 and 3.12, for short, long and penetration cylinders, respectively. These direct comparisons indicated that among all the SDF parameters, Pco, the overall elasto-plastic collapse pressure predicted by the numerical method developed by Kendrick [6] provided a close agreement with the experimental data for the cylinders without corrosion. However, for corroded models, because the corrosions were assumed to be uniform along the circumference, the SDF resulted in a significant underestimation of the loading carrying capability of the cylinders. For cylinder with penetrations, the SDF results were also considerably lower than the measured and predicted critical pressure levels, because the stiffening effect of the penetration could not be taken into account by the simple Submarine Design Formulas.

Another difference between the SDF results and the 3D finite element solutions is that the former always predict a circumferential wave number of the failure mode, but the later predict localized buckling at the early stage of the post-collapse response, forming a local dimple in the cylinder, and the location of the first buckling is highly sensitive to small variations in the stress field.

Table 3.1: Summary of Experimental Cylinders Analyzed in the Present Work

Model Designation	Description
L300-No2	Short cylinder with no simulated corrosion.
L300-No3	Short cylinder with simulated corrosion on cylinder wall.
L300-No4	Short cylinder with simulated corrosion on cylinder wall.
L510-No1	Long cylinder with no simulated corrosion.
L510-No2	Long cylinder with no simulated flange corrosion.
Penetration model	Long cylinder with two penetration and reinforcements.

Table 3.2: Convergence Study Model Summary for Short Cylinders

		Mesh Refinement			
		L300-No2 (R1)	L300-No2 (R2)	L300-No2 (R3)	L300-No2 (R4)
nodes	total	4,680	13,968	17,568	55,584
elements	total	4,608	13,824	18,432	55,296
	circumference	72	144	144/288	288
	between stiffeners	4	8	8/16	16
	web	4	4	4	8
	flange	4	4	4	8

Table 3.3: Convergence Study Model Summary for Long Cylinders

		Mesh Refinement			
		L510-No1 (R1)	L510-No1 (R2)	L510-No1 (R3)	L510-No1 (R4)
nodes	total	8,208	14,248	19,456	23,760
elements	total	8,280	14,144	19,432	23,616
	circumference	72	104	128	144
	between stiffeners	4	6	7	8
	web	4	4	4	4
	flange	4	4	4	4

Table 3.4: Comparison of Measured and Predicted Collapse Pressures for Non-Corroded Short Cylinder L300-No2.

	Collapse pressure (MPa)	Difference from Exp (%)
Convergence Study: Clamped BC, Bilinear Material, Kinematic Hardening		
Experiment	7.868	
Mesh R1 (4680 nodes)	7.604	-3.355
Mesh R2 (13968 nodes)	7.310	-7.092
Mesh R3 (17568 nodes)	7.244	-7.931
Mesh R4 (55584 nodes)	7.223	-8.198
Effect of Material Model: Clamped BC, Mesh R3		
Experiment	7.868	
Perfectly plastic	7.389	-6.088
Bilinear, isotropic hardening	7.484	-4.881
Multi-linear (circum.)	7.340	-6.711

Table 3.5: Comparison of Measured and Predicted Collapse Pressures for the Corroded Short Cylinder Models L300-No3 and L300-No4.

	Collapse pressure (MPa)	Difference from Exp (%)
L300-No3, Mesh R3		
Experiment	6.773	
Perfectly plastic	6.352	-6.216
Bilinear, isotropic hardening	6.752	-0.310
Multi-linear (circum.)	6.405	-5.433
Multi-linear (axial)	7.145	5.492
Multi-linear (average)	6.760	-0.192
L300-No4, Mesh R3		
Experiment	6.940	
VAST, perfectly plastic	6.772	-2.421
VAST, isotropic hardening	7.251	4.481
VAST, multi-linear (circum.)	6.795	-2.089

Table 3.6: Comparison of Measured and Predicted Collapse Pressures for Non-corroded Long Cylinder L510-No1.

	Collapse pressure (MPa)	Difference from Exp (%)
Convergence Study: Clamped BC, Kinematic Hardening		
Experiment	9.049	
Mesh R1 (8280 nodes)	9.790	8.189
Mesh R2 (14248 nodes)	9.704	7.238
Mesh R3 (19456 nodes)	9.687	7.051
Mesh R4 (23760 nodes)	9.662	6.774
Effect of Material Model: Mesh R3, Clamped BC		
Experiment	9.049	
Perfectly plastic	9.471	4.663
Kinematic hardening	9.687	7.051
Multi-linear (circum.)	9.560	5.647
Effect of Boundary Condition: Mesh R3, Kinematic Hardening		
Experiment	9.049	
Clamped (BC I)	9.687	7.051
Pinned 1 (BC II)	9.676	6.929
Pinned 2 (BC III)	9.664	6.796
Rigid Link (BC IV)	9.685	7.028
Effect of Thickness Variation: Mesh R3, Clamped BC		
Experiment	9.049	
Perfectly plastic	9.404	3.923
Kinematic hardening	9.536	5.382
Multi-linear (circum.)	9.451	4.442
Effect of Self-Weight: Mesh R3, Clamped BC, Kinematic Hardening		
Experiment	9.049	
No self-weight	9.687	7.051
With self-weight	9.682	6.995
Effect of Material Overlap: Mesh R3, Clamped BC, Kinematic Hardening		
Experiment	9.049	
With overlap	9.687	7.051
No overlap	9.624	6.354

Table 3.7: Comparison of Measured and Predicted Collapse Pressures for Flange Corroded Long Cylinder L510-No2.

	Collapse pressure (MPa)	Difference from Exp (%)
Effect of Material Model: Mesh R3, Clamped BC		
Experiment	8.594	
Perfectly plastic	9.114	6.051
Kinematic hardening	9.192	6.958
Multi-linear (circum.)	8.916	3.747

Table 3.8: Comparison of Measured and Predicted Collapse Pressures for the Penetration Cylinder Model.

	Collapse pressure (MPa)	Difference from Exp (%)
Effect of Measured Out-of-Circularities: Kinematic Hardening		
Experiment	8.998	
No OOC	8.961	-0.411
100% measured OOC (AD I)	8.948	-0.556
100% measured OOC (AD II)	8.947	-0.567
200% measured OOC	8.895	-1.145
500% measured OOC	8.560	-4.868
Effect of Superimposed Linear Buckling Mode: Perfectly-Plastic Model		
Experiment	8.998	
Max imperfection = 0.0 mm	8.961	-0.411
Max imperfection = 0.002 mm	8.948	-0.556
Max imperfection = 0.01 mm	8.886	-1.245
Max imperfection = 0.05 mm	8.596	-4.468
Max imperfection = 0.2 mm	7.997	-11.125

Table 3.9: Collapse Pressures from Submarine Design Formula (SDF) Used to Compare with Experimental Results and 3D Finite Element Predictions.

SDF Parameter	Definition
Interframe Collapse	
Ppy	External pressure causing interframe collapse of a ring-stiffened cylinder, precipitated by yielding of the shell plating
Pci (Lower)	Interframe collapse pressure as determined from the British Standard Specification (BS) 5500 lower bound empirical curve [4]
Pci (Mean)	Interframe collapse pressure as determined from the Sea System Publication (SSP) 74 mean empirical curve [5,6]
Overall Collapse	
Py(n)	External pressure causing overall collapse of a ring-stiffened cylinder, precipitated by frame yielding
PP	External pressure causing overall collapse of a ring-stiffened cylinder, precipitated by shell yielding
Pco	Overall elasto-plastic collapse pressure as predicted by the numerical method developed by Kendrick

Table 3.10: Comparison of Collapse Pressures (MPa) Predicted by SDF and Nonlinear 3D Finite Element with the Experimental Results for Short Cylinders

	Submarine Design Formula			Nonlinear 3D FE	Experiment
	PRHDEF	**PD004B**	**K79**		
Model: L300-No2					
Ppy	7.054	7.017	6.994	7.340	7.868
Pci (lower)	5.618				
Pci (mean)		6.675	6.646		
Py(n)	11.000 (n=4)	8.879 (n=20)	10.666 (n=5)		
PP	7.487	7.528	7.523		
Pco			7.754 (n=2)		
Model: L300-No3					
Ppy	5.045	5.034	4.849	6.404	6.773
Pci (lower)	3.310				
Pci (mean)		4.265	4.257		
Py(n)	10.200 (n=4)	13.307 (n=20)	9.874 (n=4)		
PP	5.705	5.753	5.774		
Pco			6.071 (n=5)		

Table 3.11: Comparison of Collapse Pressures (MPA) Predicted by SDF and Nonlinear 3D Finite Element with the Experimental Results for Long Cylinders

	Submarine Design Formula			Nonlinear 3D FE	Experiment
	PRHDEF	**PD004B**	**K79**		
Model: L510-No1					
Ppy	8.522	8.491	8.467	9.451	9.049
Pci (lower)	7.290				
Pci (mean)		8.543	8.503		
Py(n)	7.300 (n=4)	11.030 (n=3)	8.381 (n=3)		
PP	8.471	8.450	8.303		
Pco			9.159 (n=3)		
Model: L510-No2					
Ppy	8.215	8.192	8.168	8.916	8.594
Pci (lower)	6.946				
Pci (mean)		8.151	8.113		
Py(n)	5.004 (n=3)	8.852 (n=3)	6.369 (n=3)		
PP	7.890	7.842	7.535		
Pco			7.737 (n=3)		

Table 3.12: Comparison of Collapse Pressures (MPa) Predicted by SDF and Nonlinear 3D Finite Element with the Experimental Results for Penetration Cylinder

	Submarine Design Formula			Nonlinear 3D FE	Experiment
	PRHDEF	**PD004B**	**K79**		
Model: Penetration					
Ppy	7.371	7.138	7.072	8.961	8.998
Pci (lower)	6.562				
Pci (mean)		7.496	7.409		
Py(n)	5.155 (n=3)	8.647 (n=3)	5.809 (n=3)		
PP	5.812	5.800	5.657		
Pco			7.059 (n=3)		
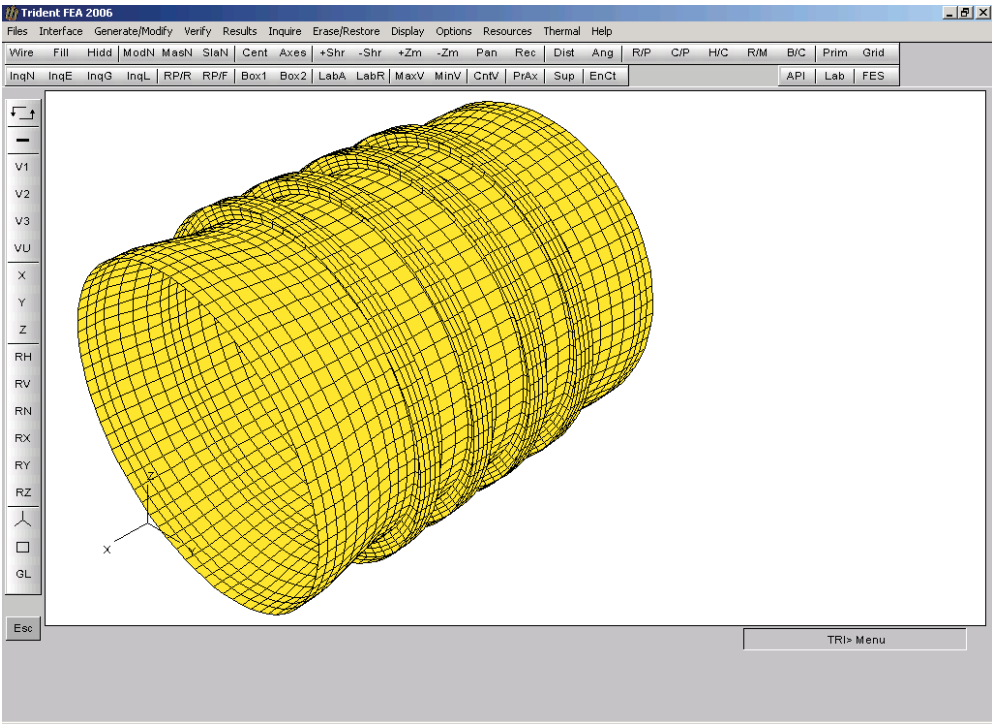
Figure 3.1: Mesh Refinement 1 (R1) for Short Cylinder L300-No2.
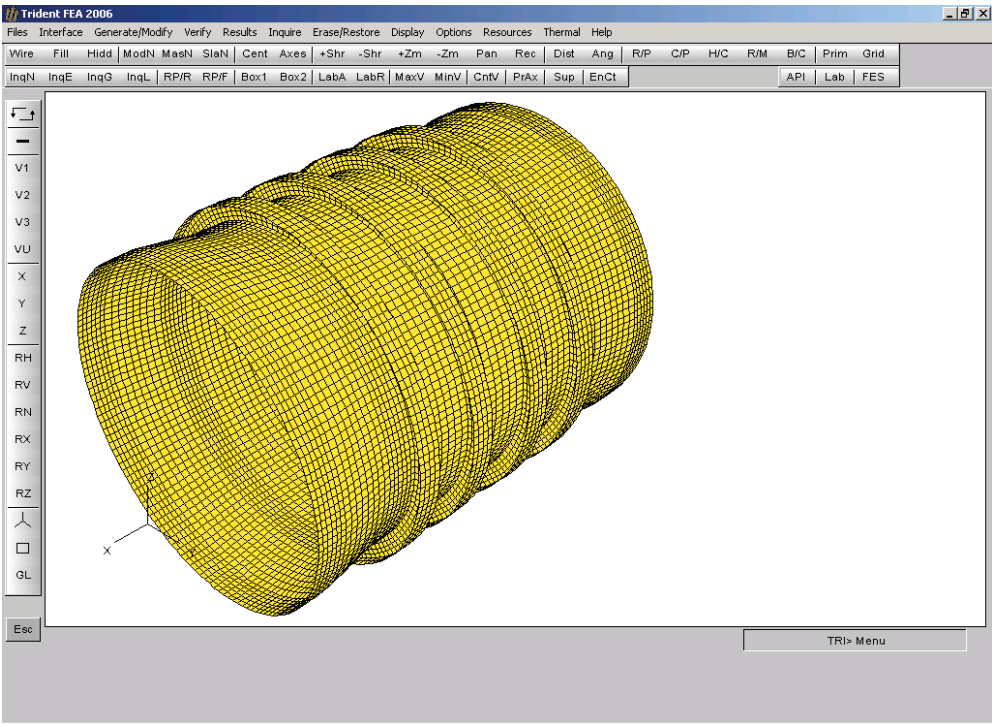
Figure 3.2: Mesh Refinement 2 (R2) for Short Cylinder L300-No2.
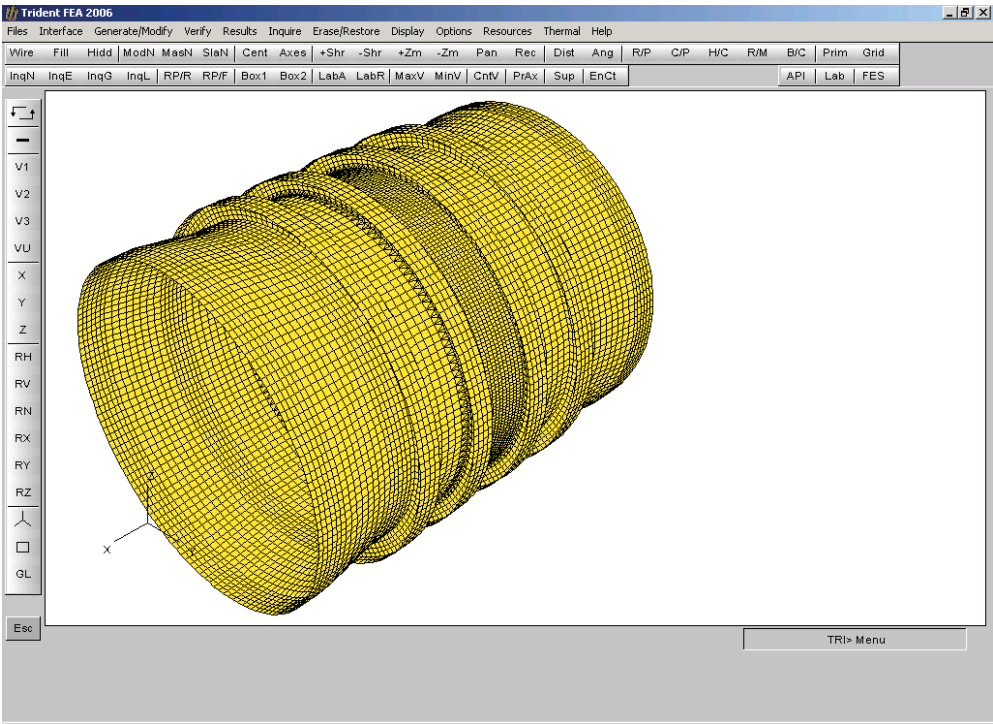
Figure 3.3: Mesh Refinement 3 (R3) for Short Cylinder L300-No2.
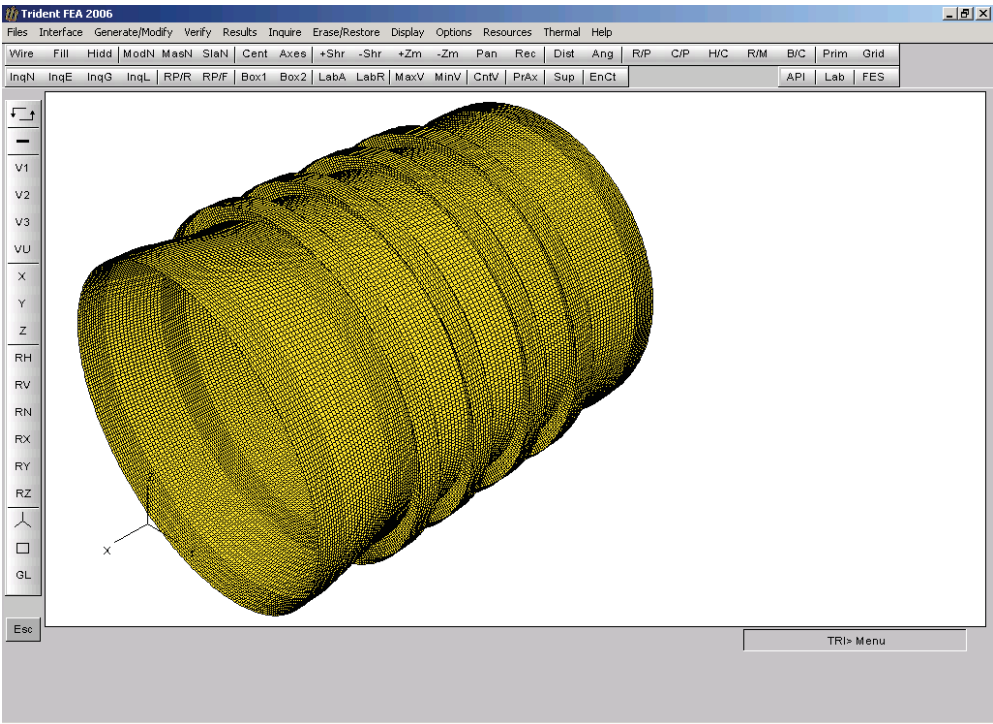
Figure 3.4: Mesh Refinement 4 (R4) for Short Cylinder L300-No2.
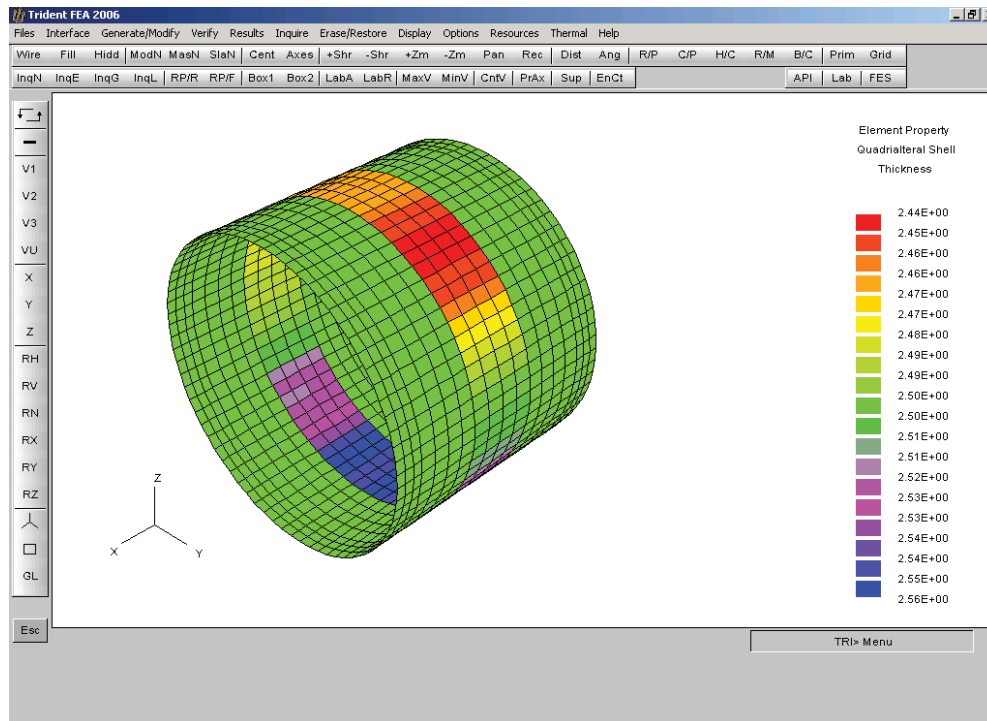
Figure 3.5: Thickness Variation along the Circumference in Central Bay.
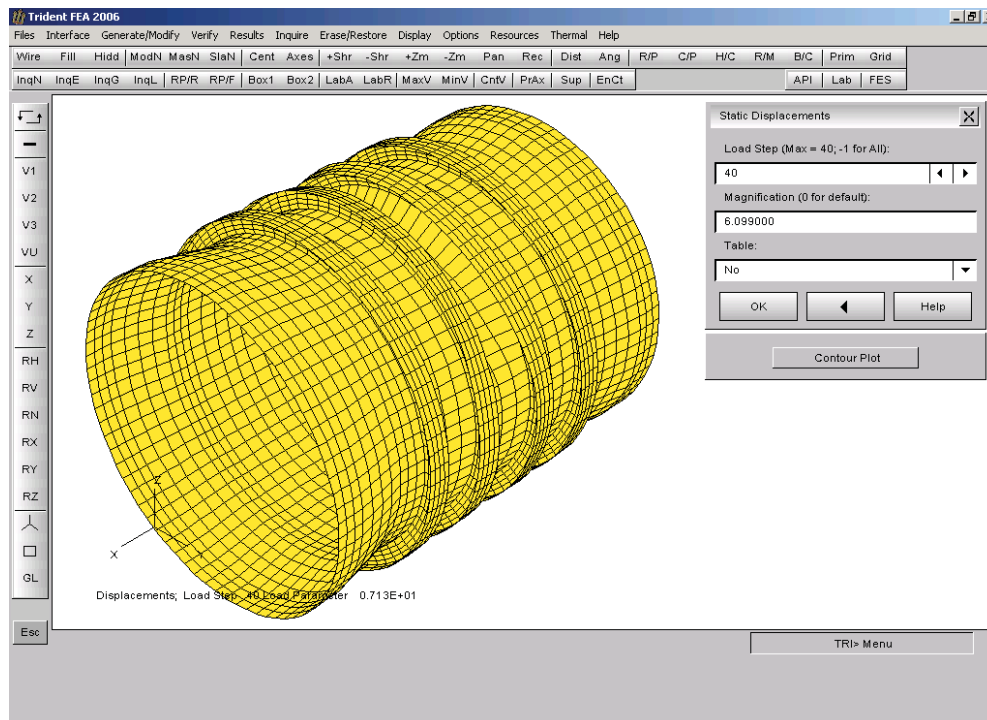
Figure 3.6: Final Deformed Shape of Cylinder L300-No2 Predicted by Mesh R1 (3D View).
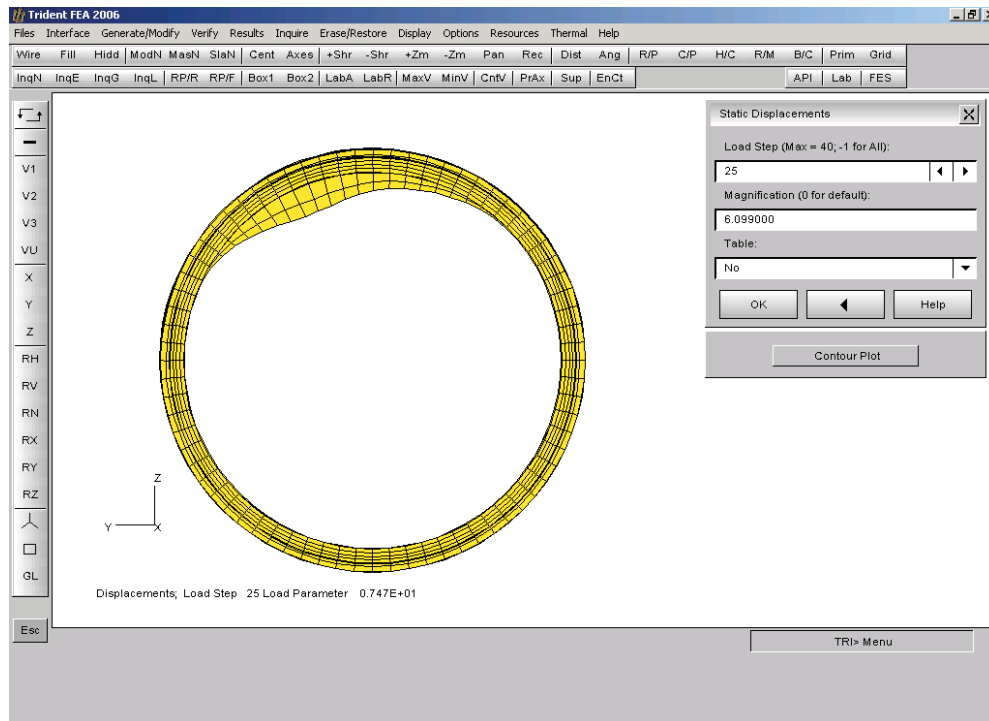
Figure 3.7: Intermediate Deformed Shape (at Load Step 25) of Cylinder L300-No2 Predicted by Mesh R1 (End View).
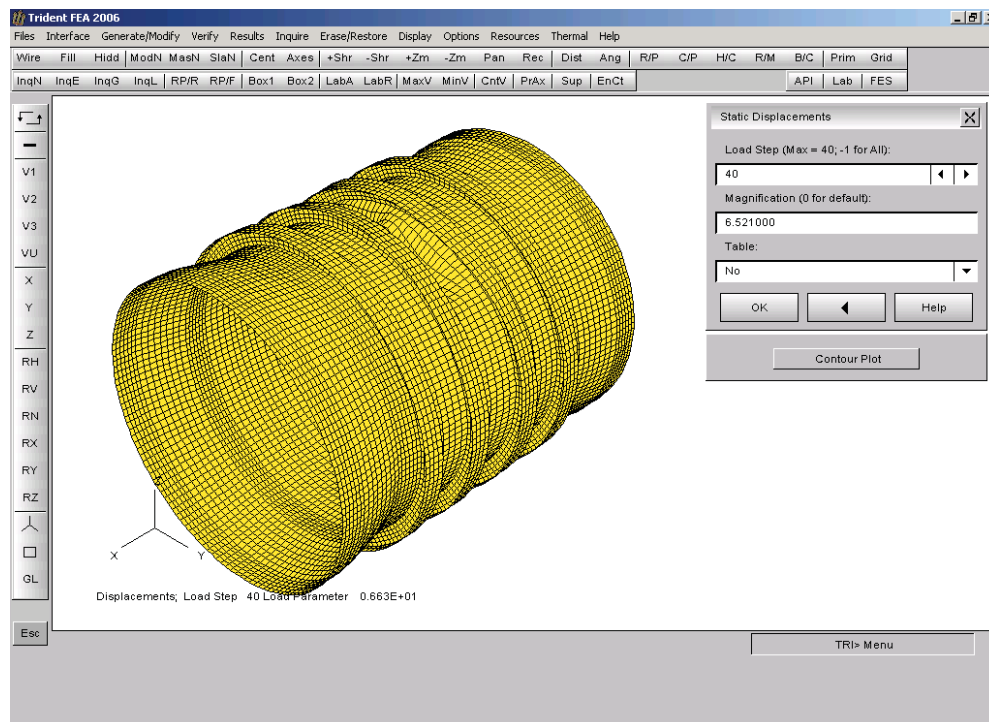
Figure 3.8: Final Deformed Shape of Cylinder L300-No2 Predicted by Mesh R2 (3D View).
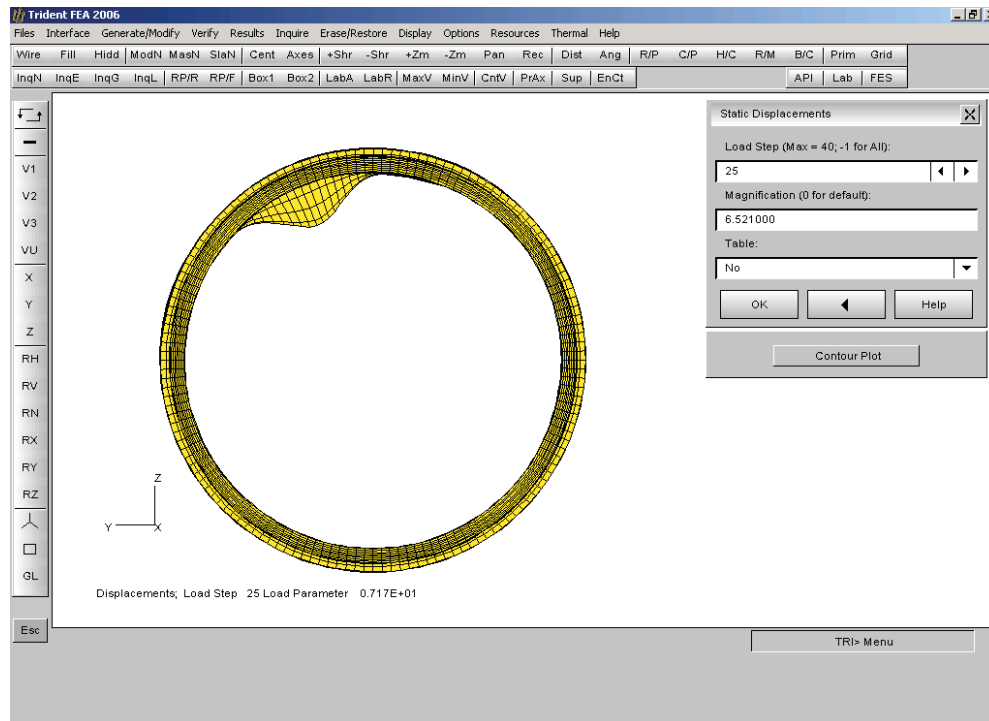
Figure 3.9: Intermediate Deformed Shape (at Load Step 20) of Cylinder L300-No2 Predicted by Mesh R2 (End View).
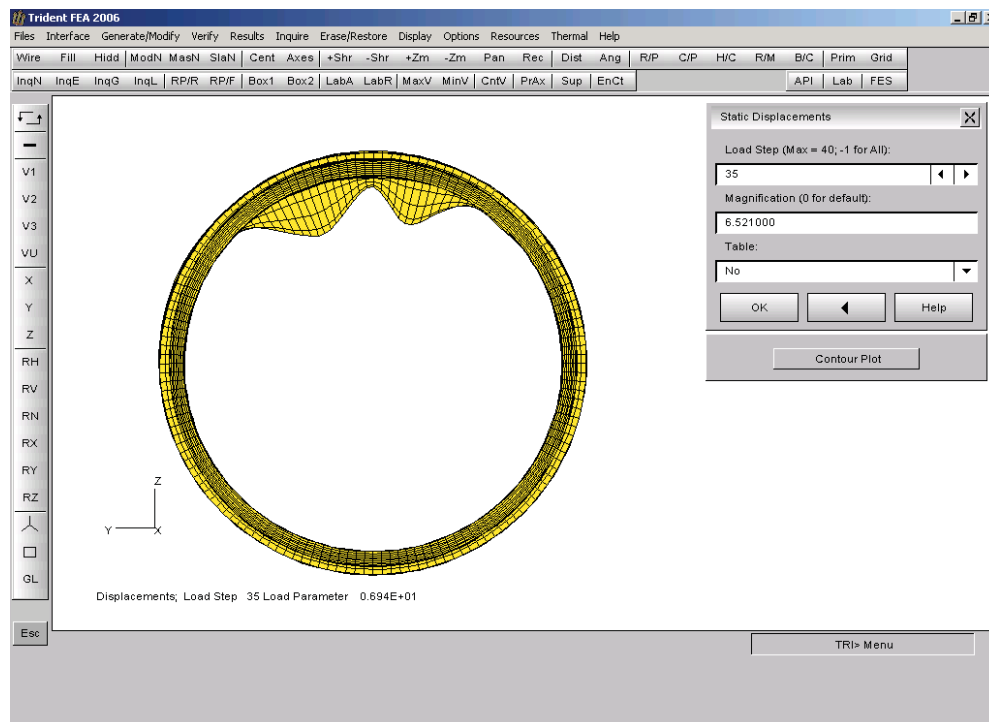
Figure 3.10: Intermediate Deformed Shape (at Load Step 35) of Cylinder L300-No2 Predicted by Mesh R2 (End View).
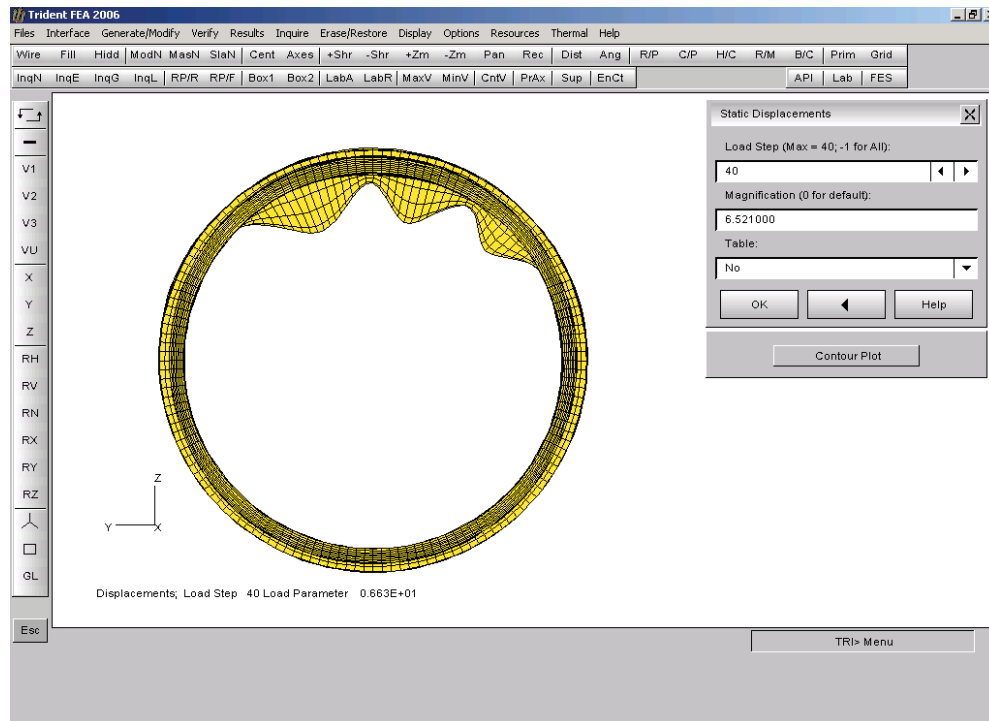
Figure 3.11: Final Deformed Shape (at Load Step 40) of Cylinder L300-No2 Predicted by Mesh R2 (End View).
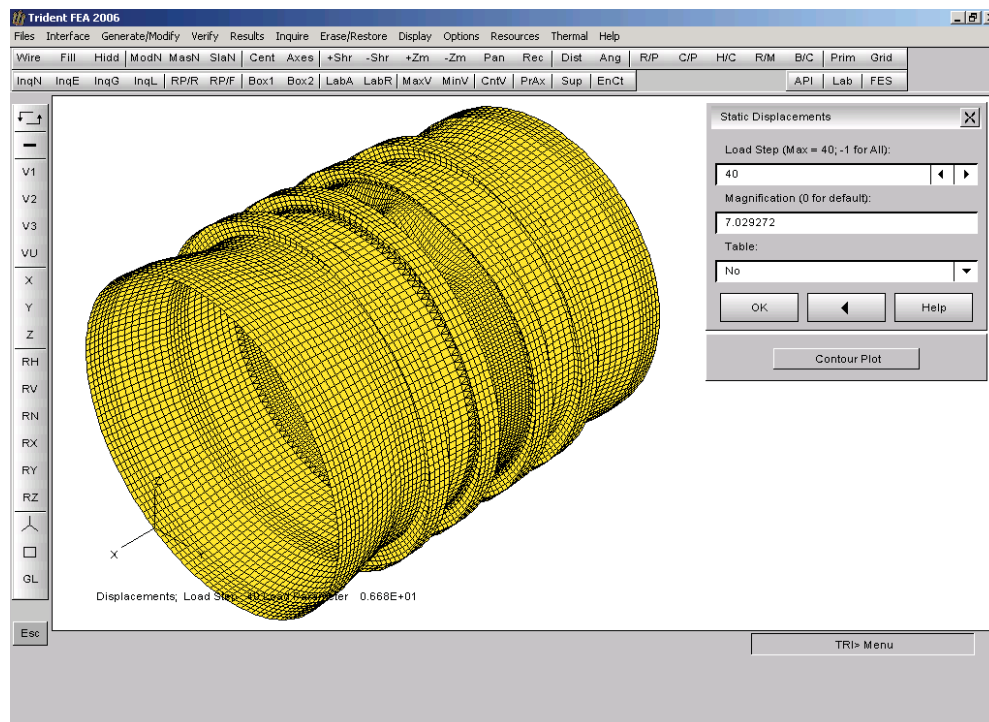
Figure 3.12: Final Deformed Shape of Cylinder L300-No2 Predicted by Mesh R3 (3D View).
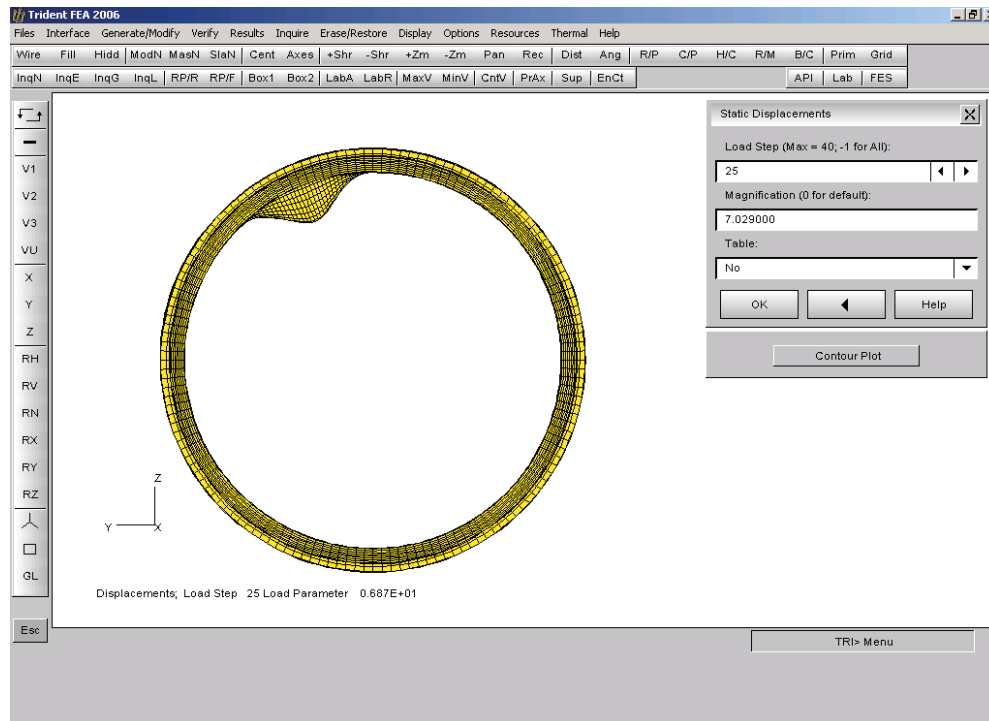
Figure 3.13: Intermediate Deformed Shape (at Load Step 25) of Cylinder L300-No2 Predicted by Mesh R3 (End View).
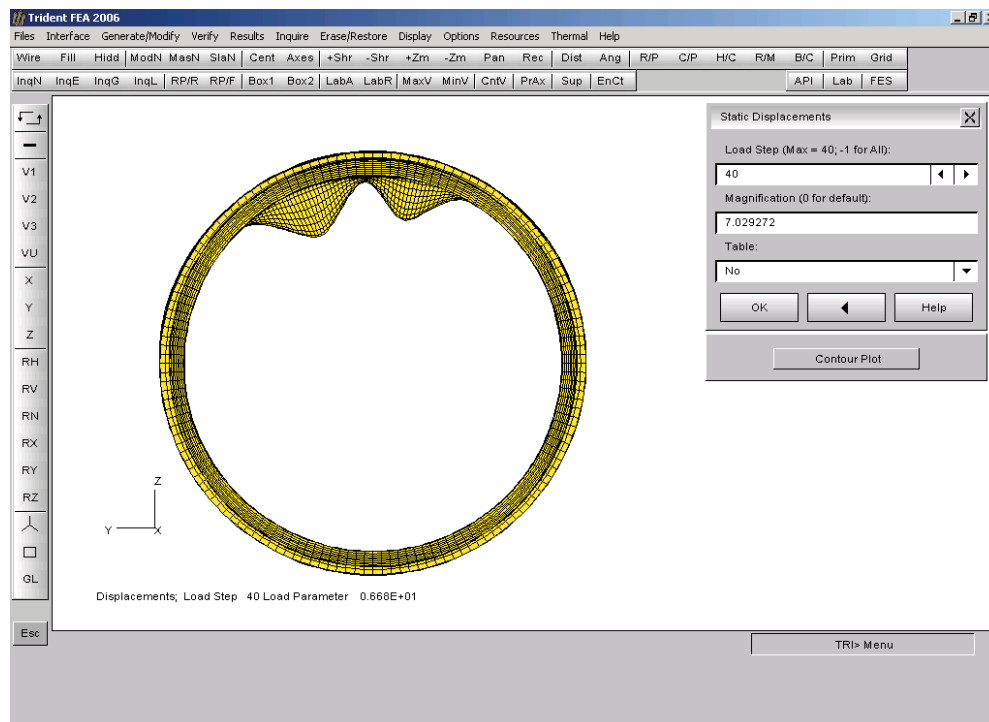
Figure 3.14: Final Deformed Shape (at Load Step 40) of Cylinder L300-No2 Predicted by Mesh R3 (End View).
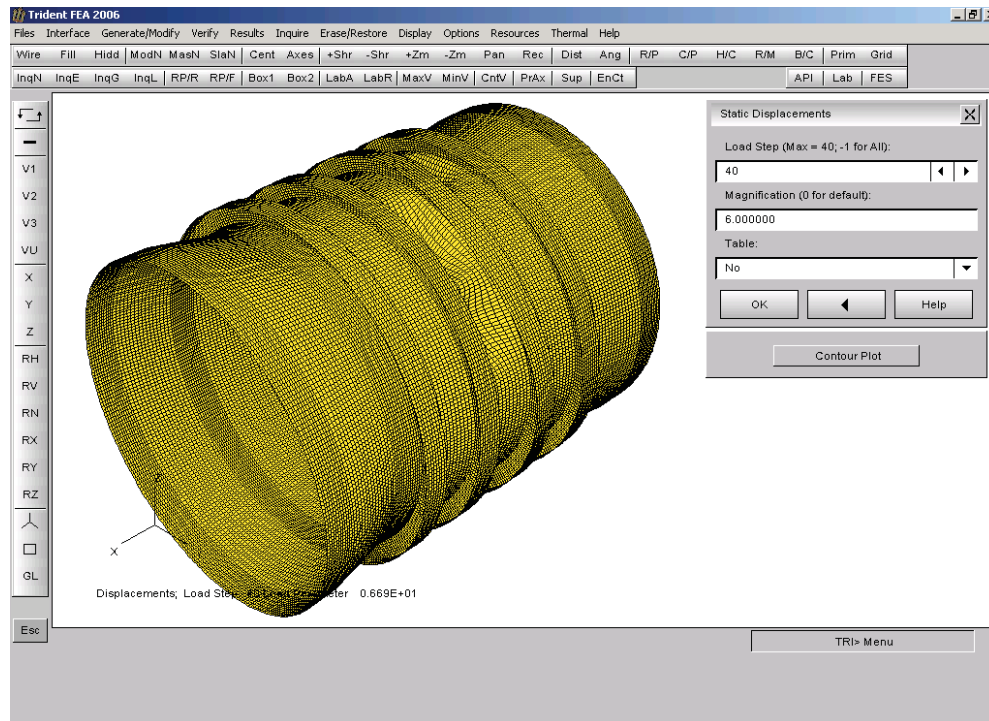
Figure 3.15: Final Deformed Shape of Cylinder L300-No2 Predicted by Mesh R4 (3D View).
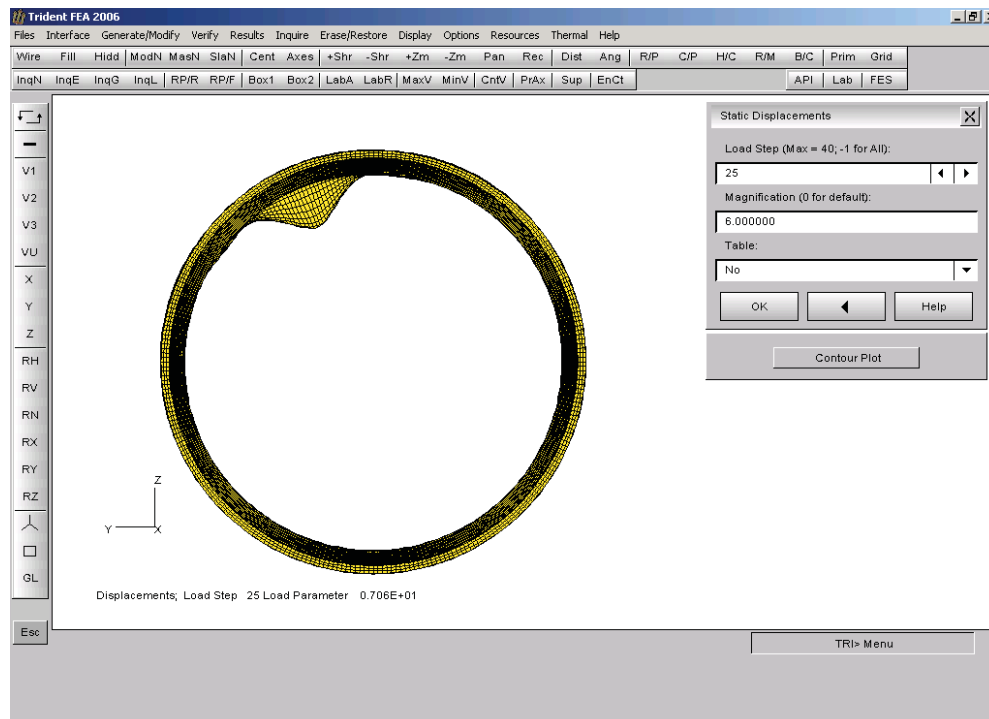
Figure 3.16: Intermediate Deformed Shape (at Load Step 25) of Cylinder L300-No2 Predicted by Mesh R4 (End View).
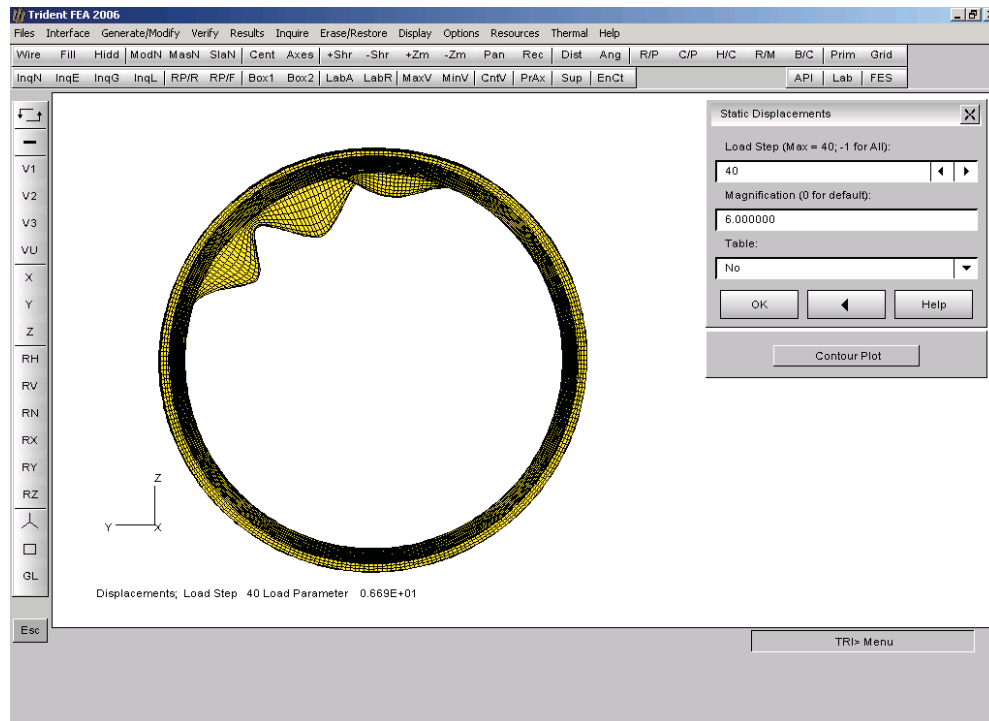
Figure 3.17: Final Deformed Shape (at Load Step 40) of Cylinder L300-No2 Predicted by Mesh R4 (End View).
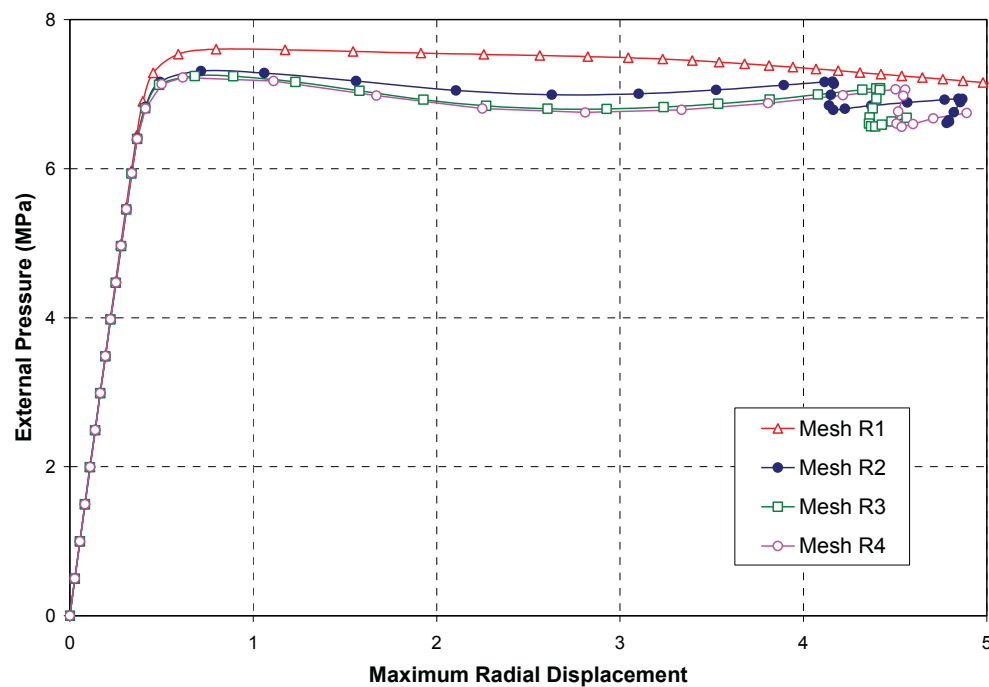
Figure 3.18: Comparison of Pressure-Maximum Radial Displacement Curves for Short Cylinder L300-No2 Obtained Using Different Meshes.
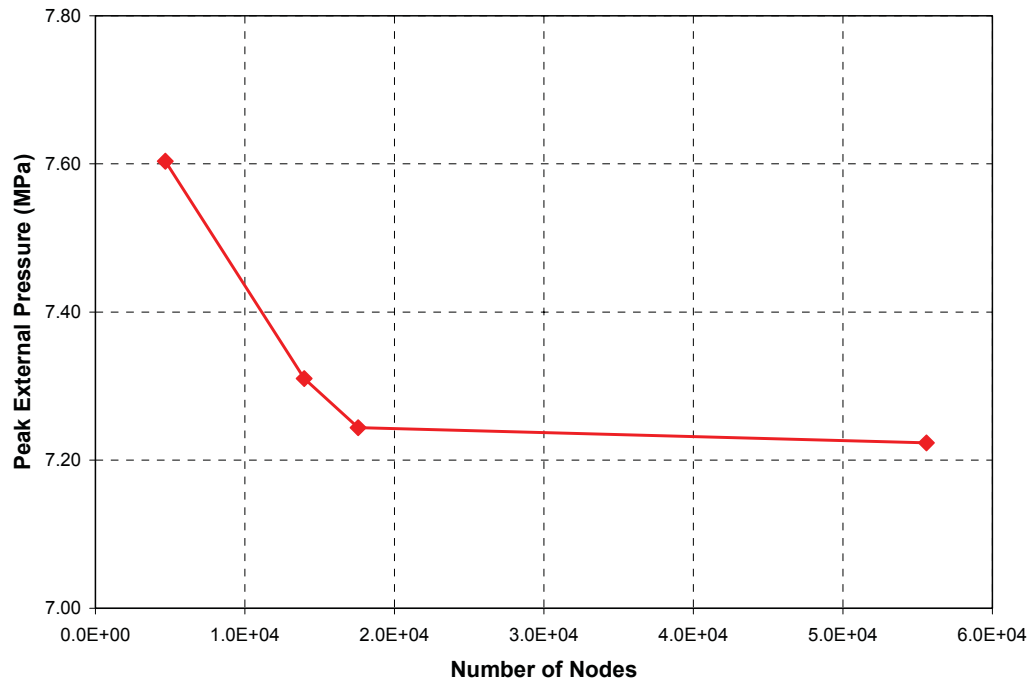
Figure 3.19: Comparison of Pressure-Displacement Curves for Short Cylinder L300-No2 Obtained by Using Different Nonlinear Material Models.
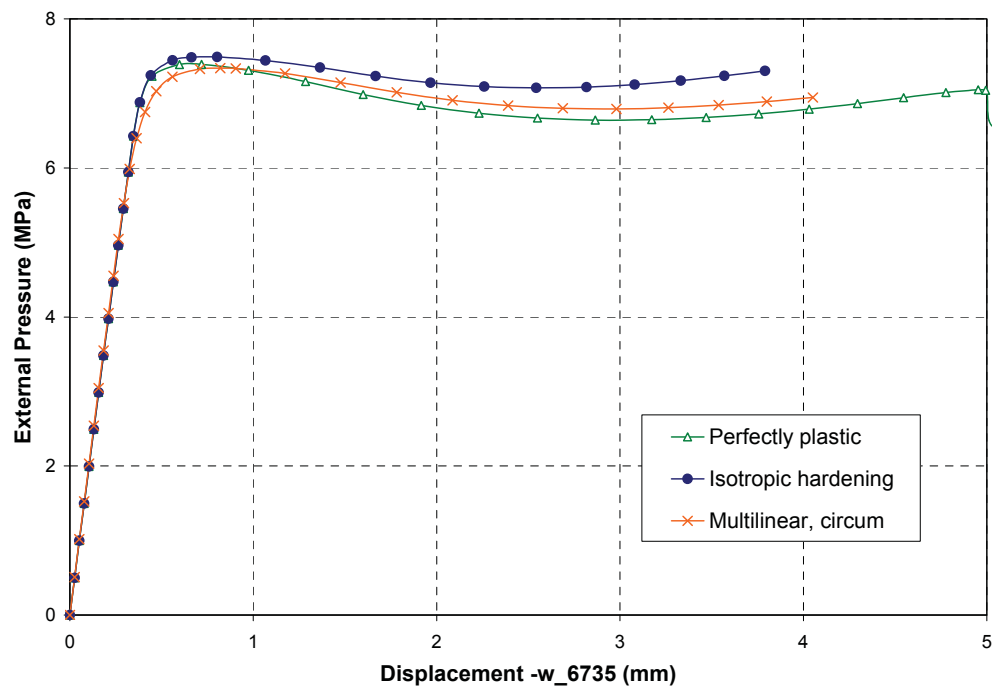
Figure 3.20: Comparison of Pressure-Displacement Curves for Short Cylinder L300-No2 Obtained by Using Different Nonlinear Material Models.
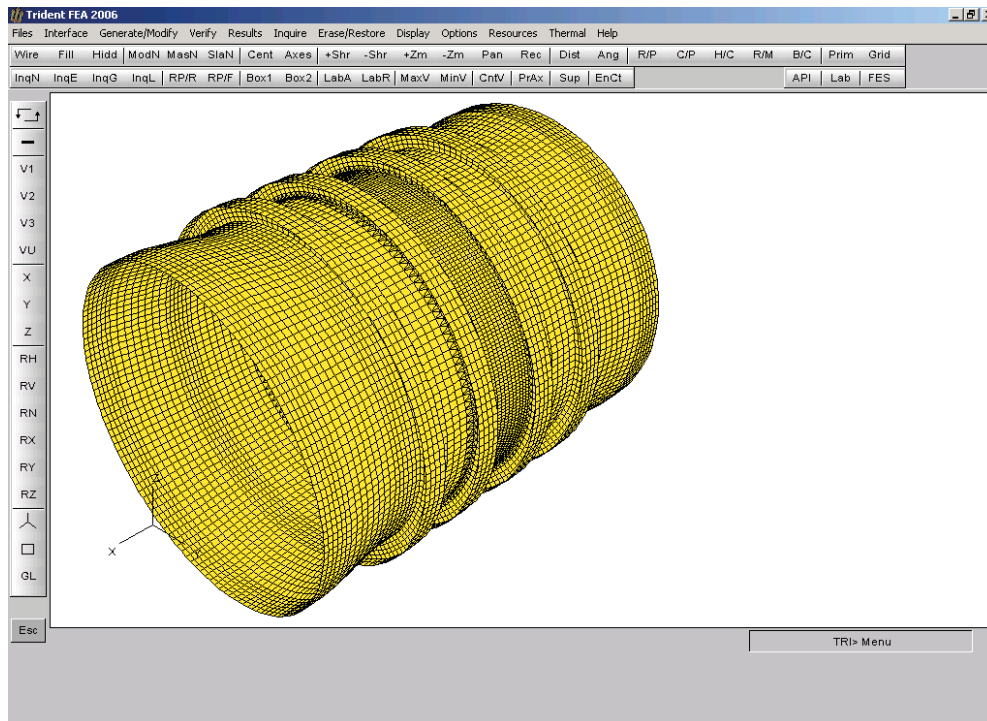
Figure 3.21: Finite Element Model for Corroded Short Cylinder L300-No3.
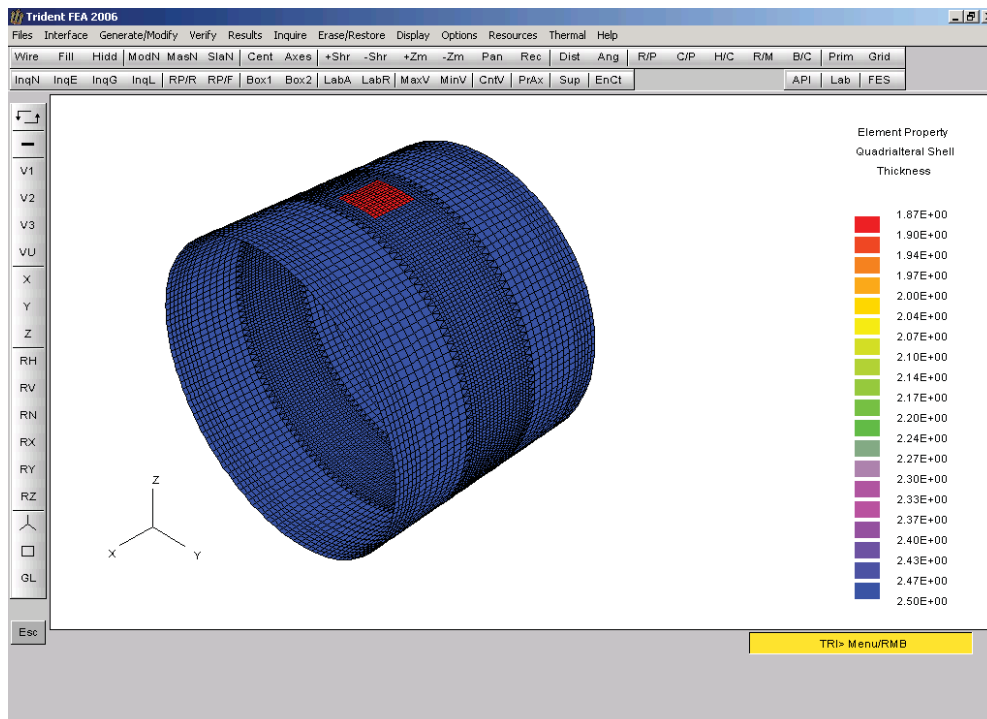
Figure 3.22: Thickness Contour Indicating the Simulated Corrosion Patch.
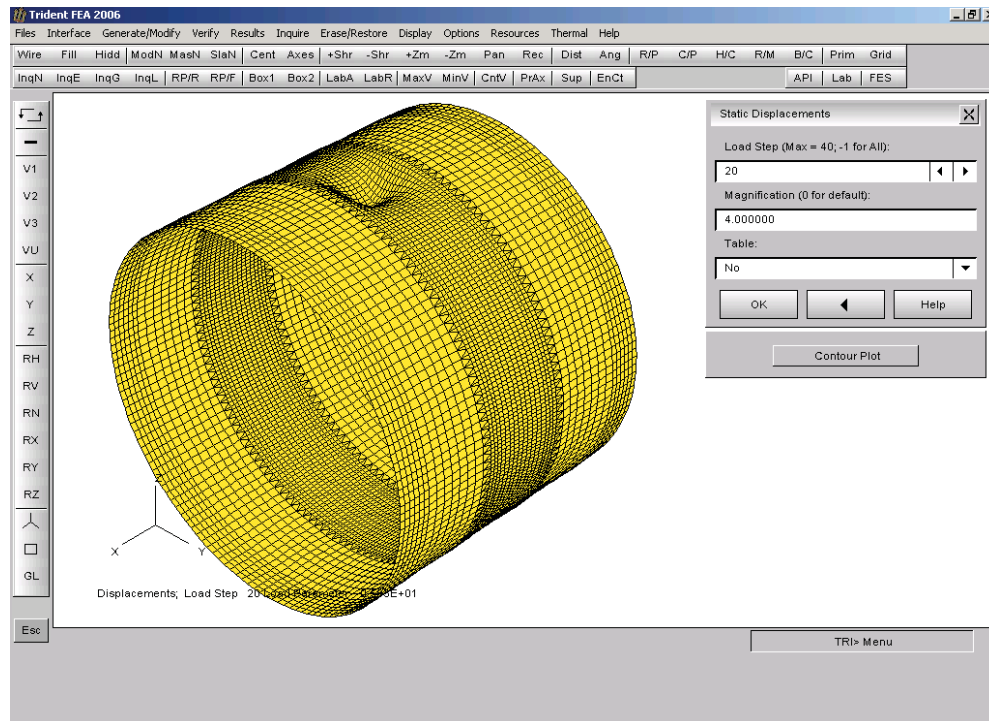
Figure 3.23: Intermediate Deformed Shape (at Load Step 20) Showing Buckling in the Corroded Area.
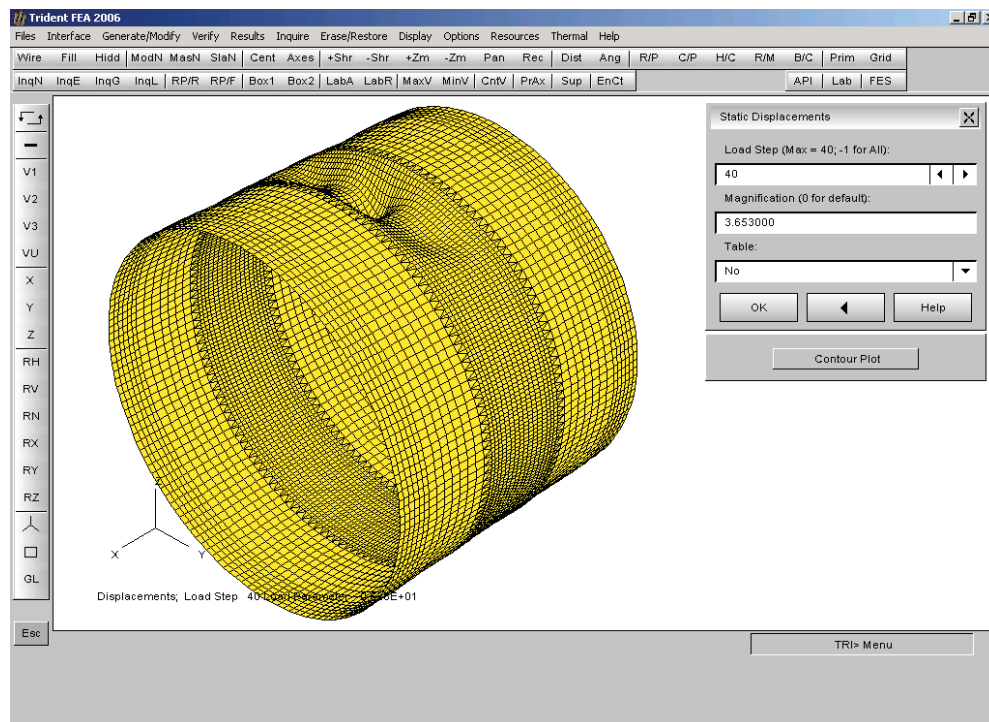
Figure 3.24: Final Deformed Shape (at Load Step 40) Showing Progressive Buckling Adjacent to the Corrosion Patch.
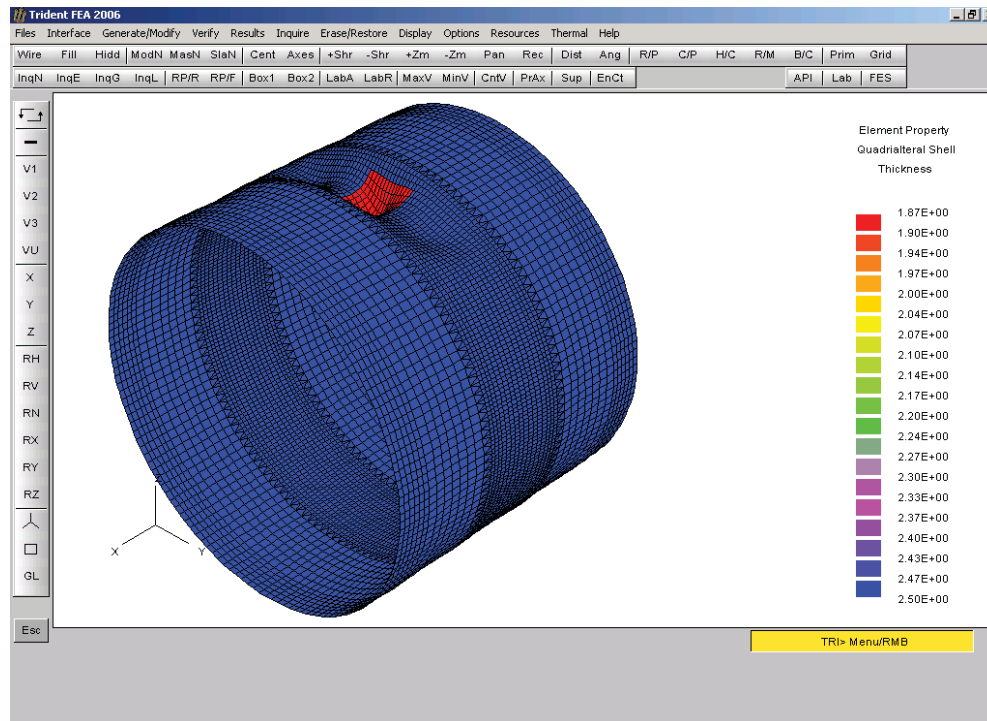
Figure 3.25: Thickness Contour Shown on Top of Final Deformed Shape.
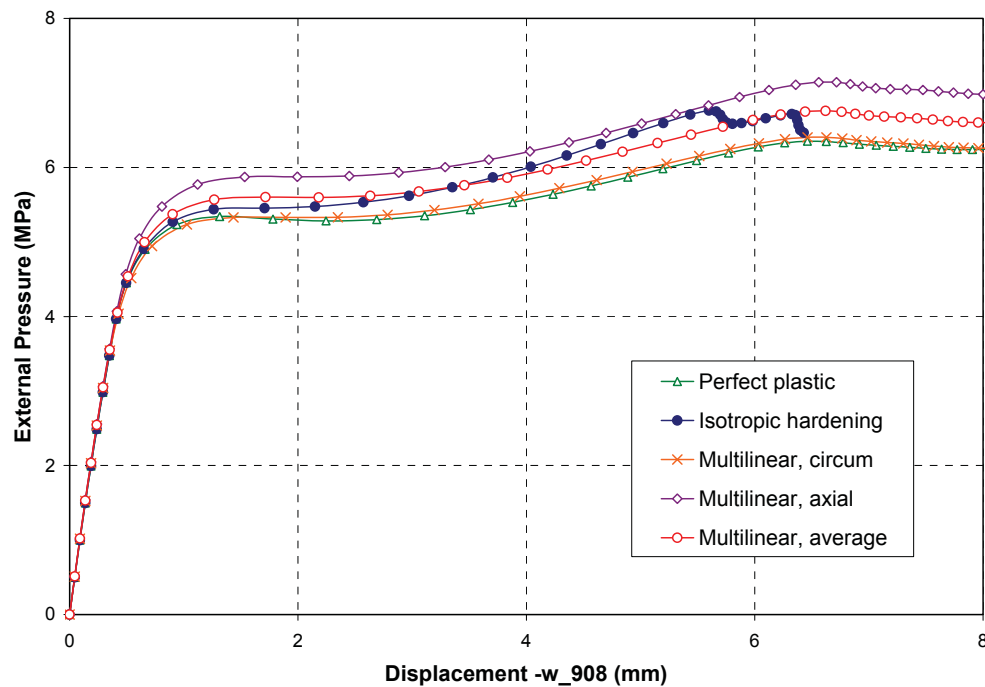
Figure 3.26: Comparison of Pressure-Displacement Curves for Short Cylinder L300-No3 Predicted Using Different Material Models.
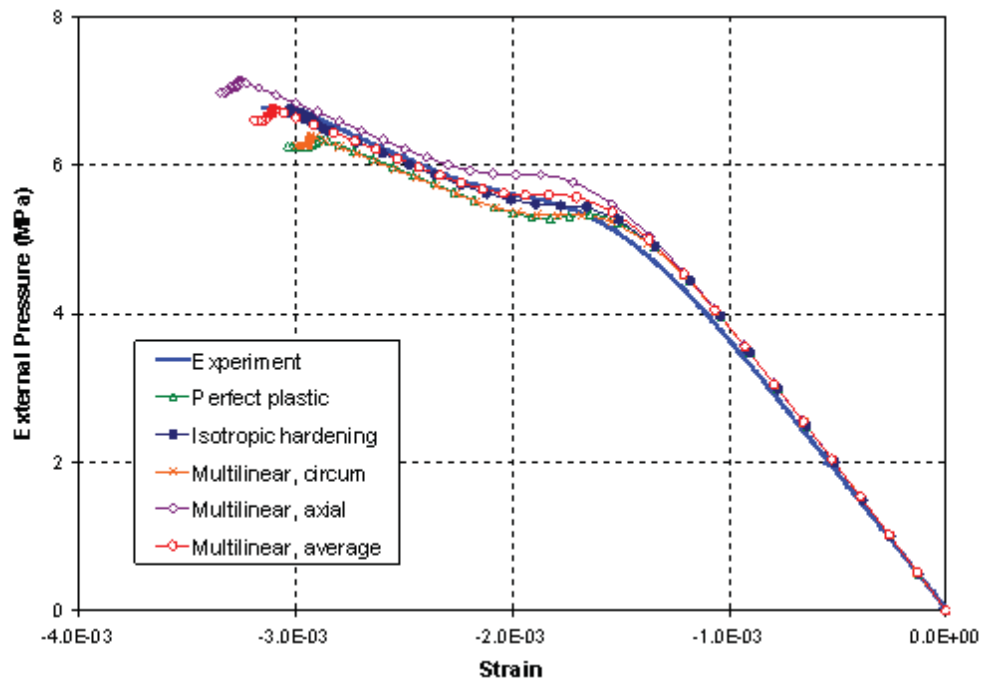
Figure 3.27: Comparison of Measured and Predicted Histories of Circumferential Strain in Flange of Frame #2 at 0°.
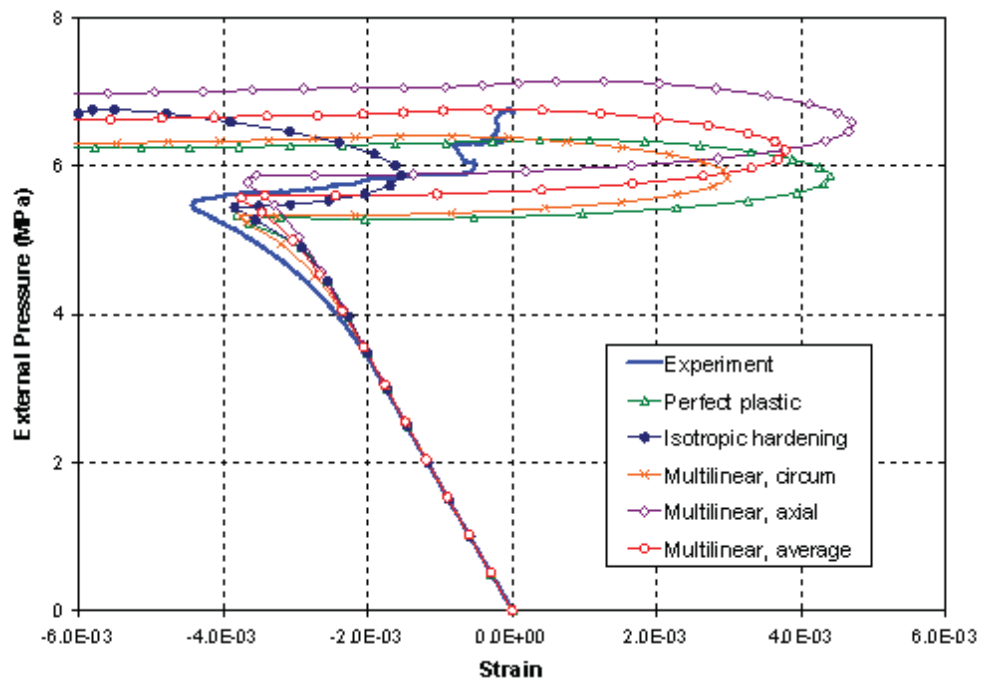
Figure 3.28: Comparison of Measured and Predicted Histories of Circumferential Strain on Inside of Shell at Center Bay at 0°.
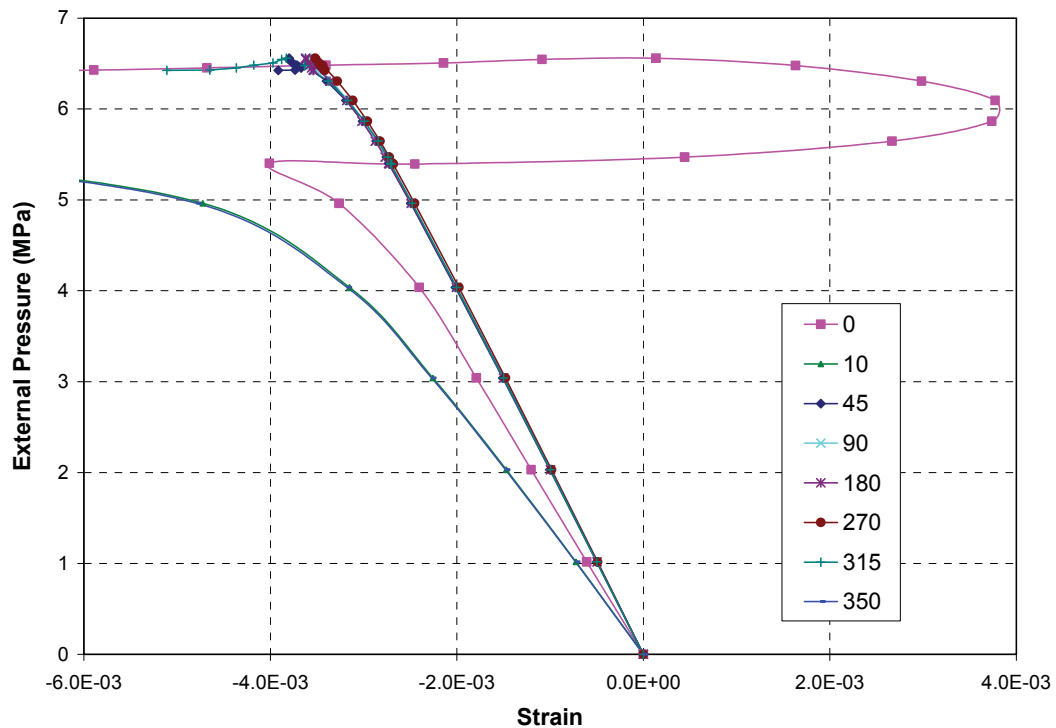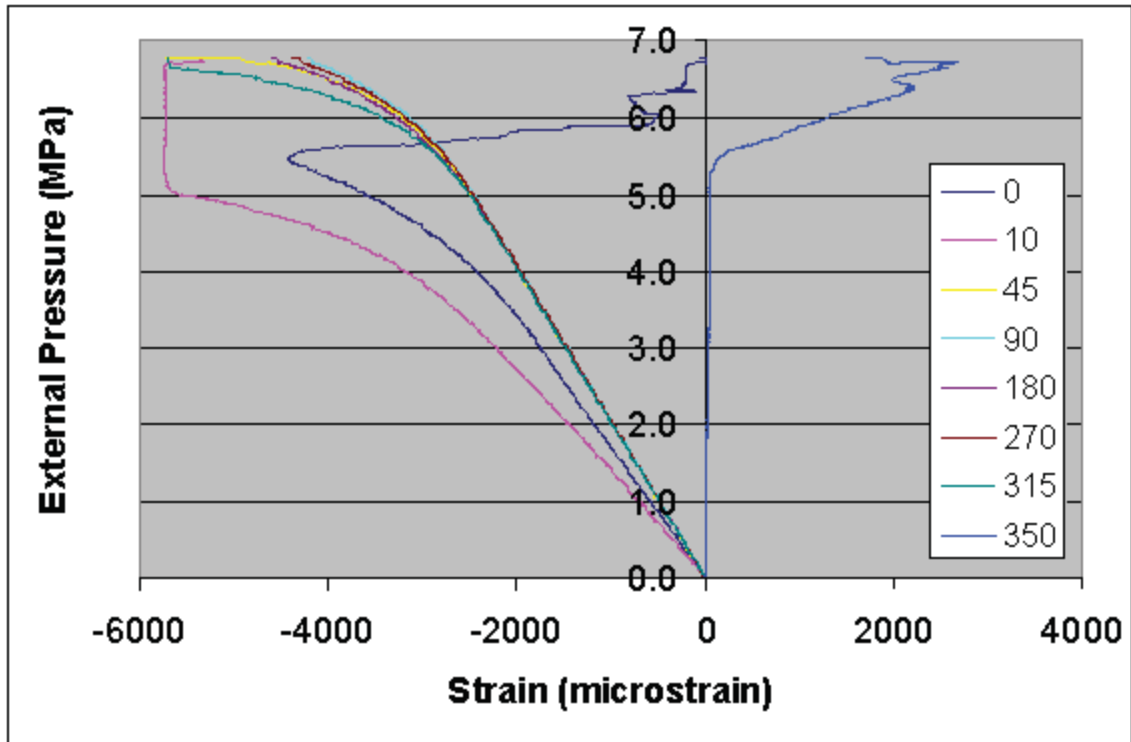
Figure 3.29: Comparison of Measured (top) and Predicted (bottom) Histories of Circumferential Strain on Inside of Shell at Central Bay.
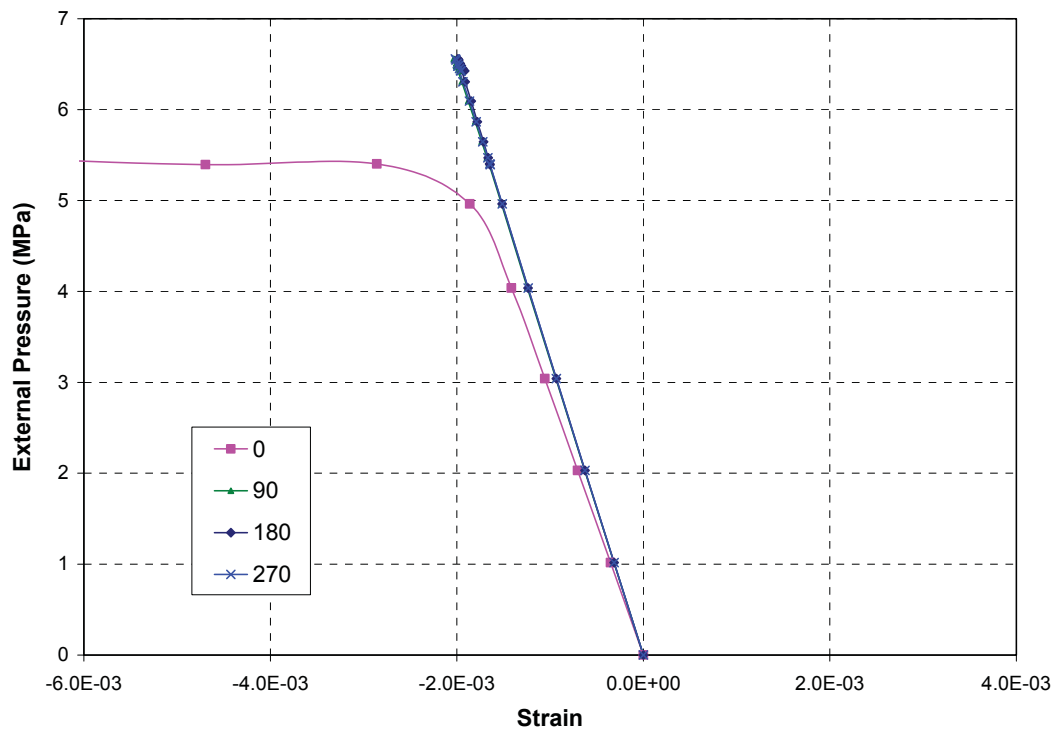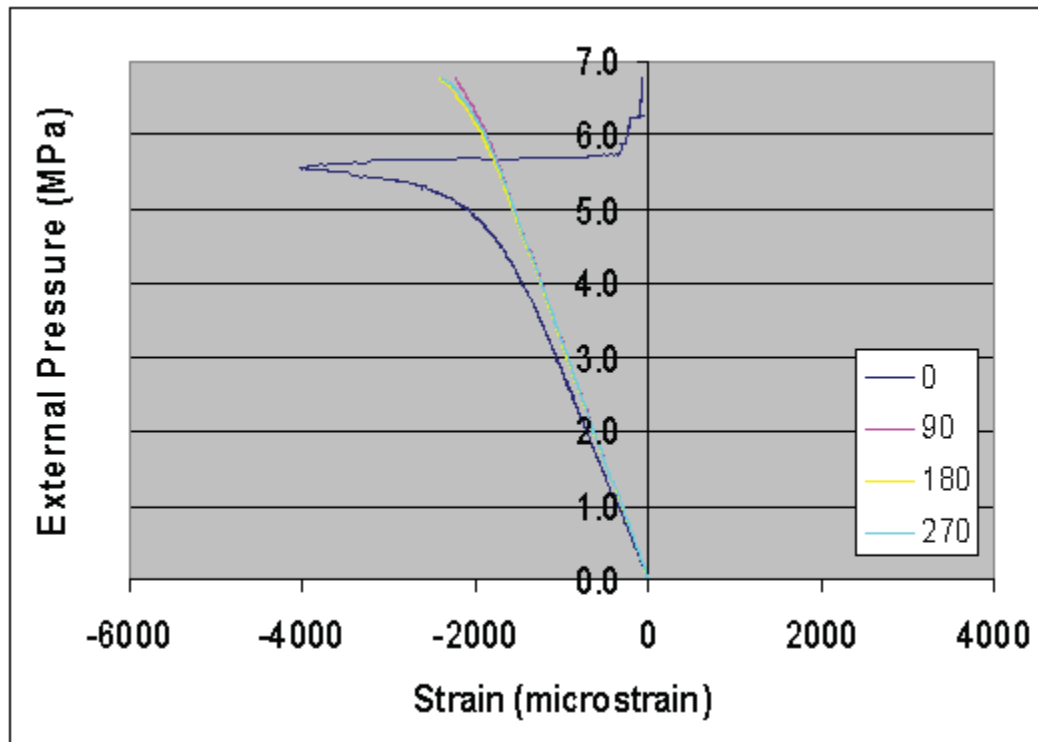
Figure 3.30: Comparison of Measured (top) and Predicted (bottom) Histories of Circumferential Strain on Outside of Shell at Central Bay.
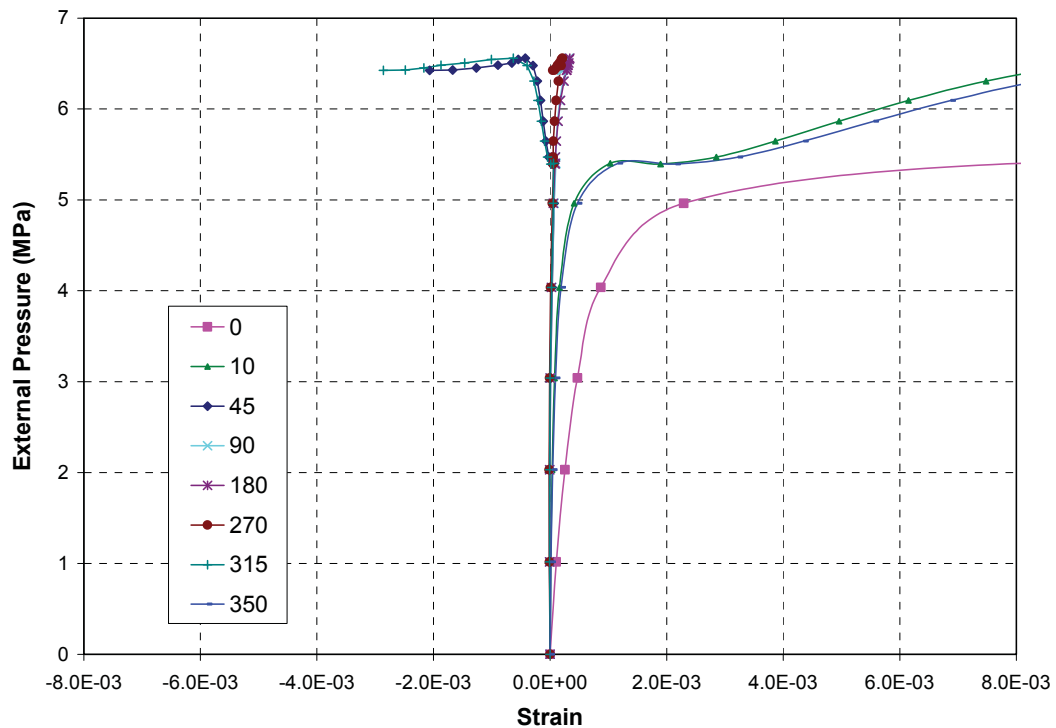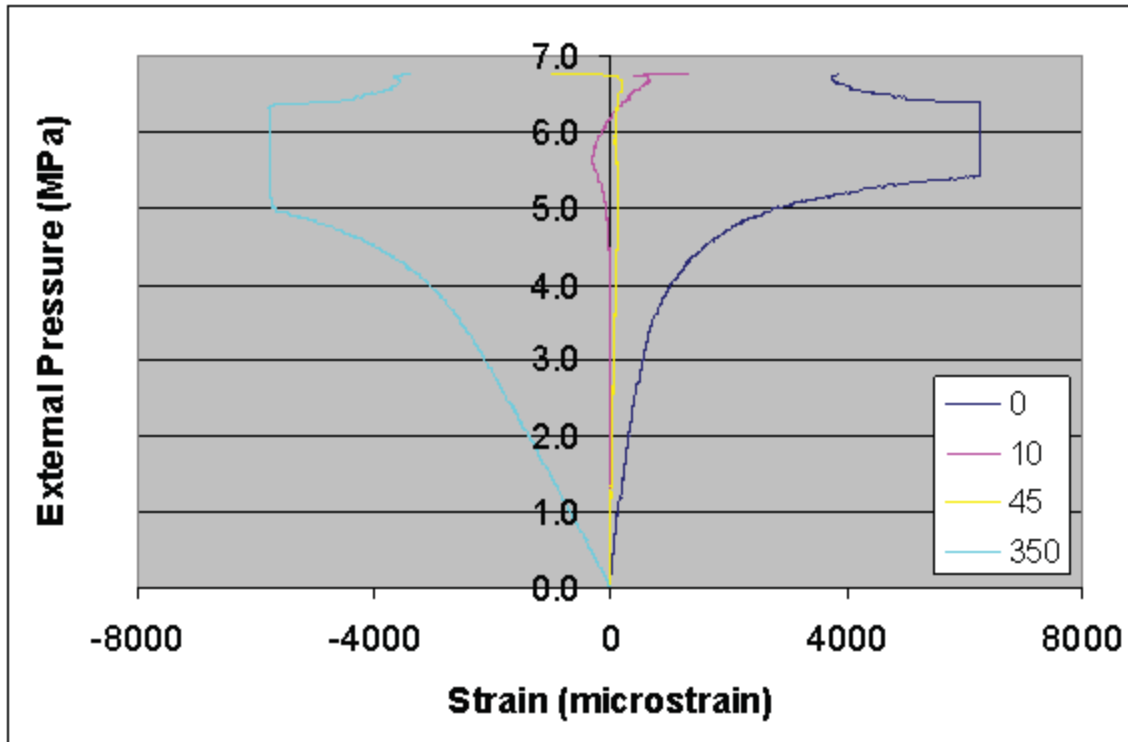
Figure 3.31: Comparison of Measured (top) and Predicted (bottom) Histories of Axial Strain on Inside of Shell at Central Bay.
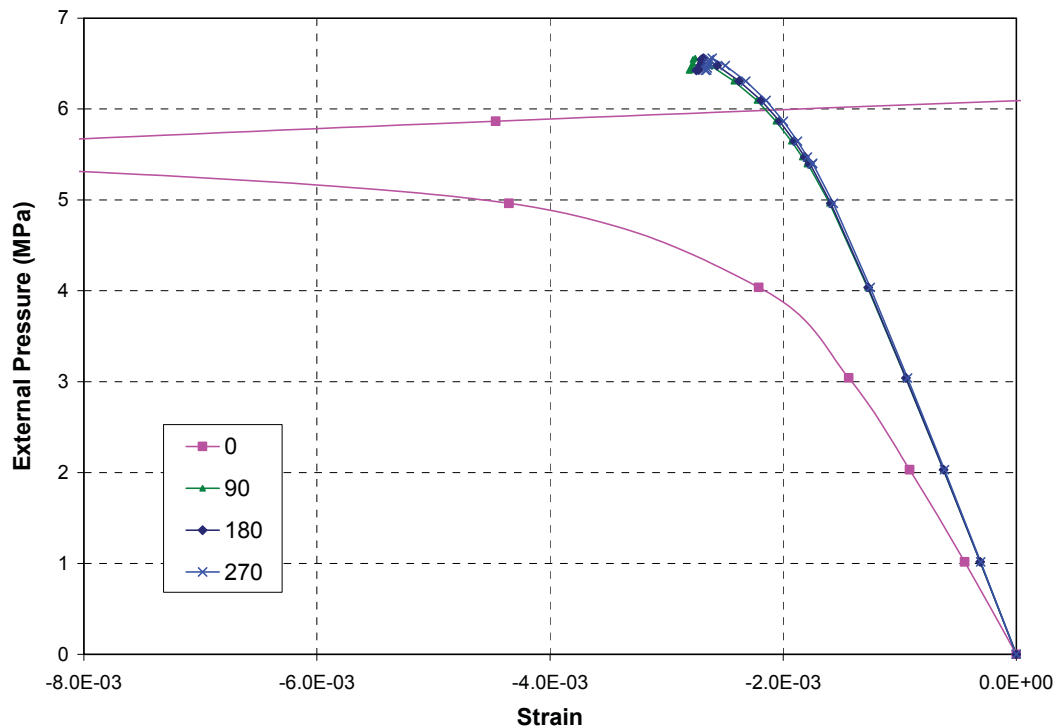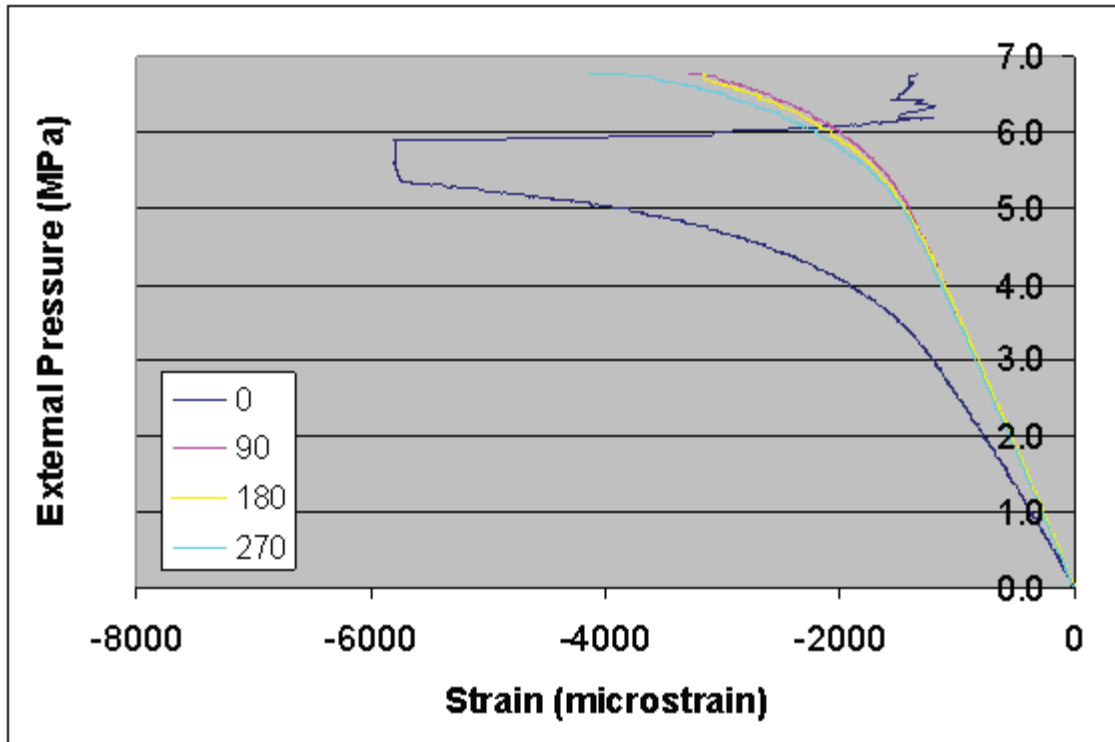
Figure 3.32: Comparison of Measured (top) and Predicted (bottom) Histories of Axial Strain on Outside of Shell at Central Bay.
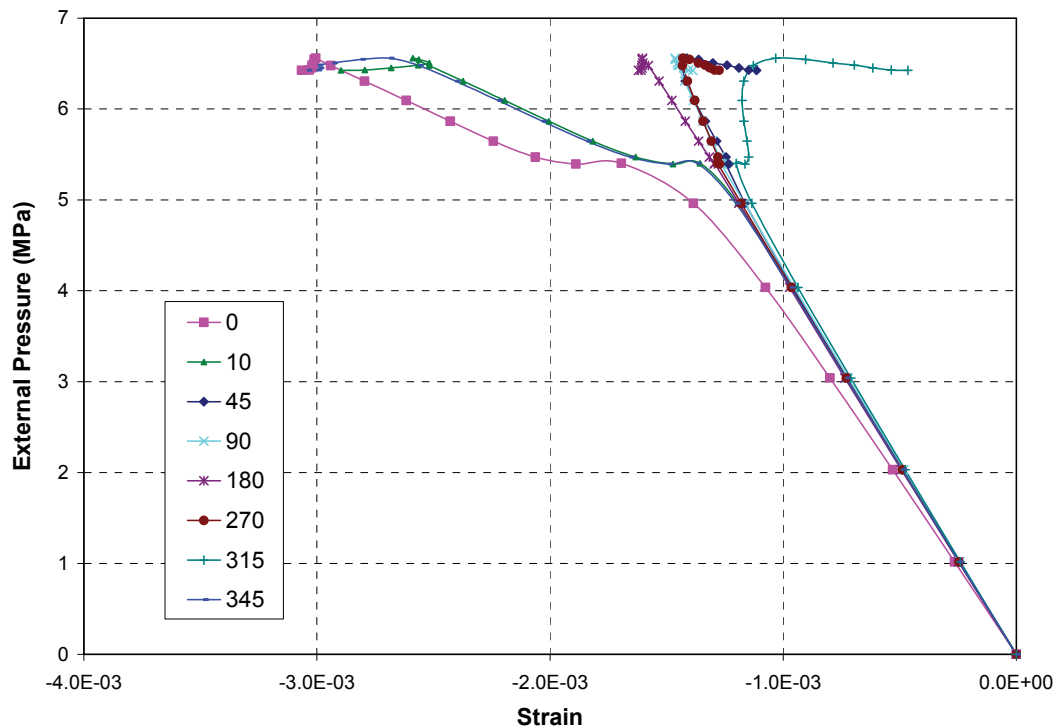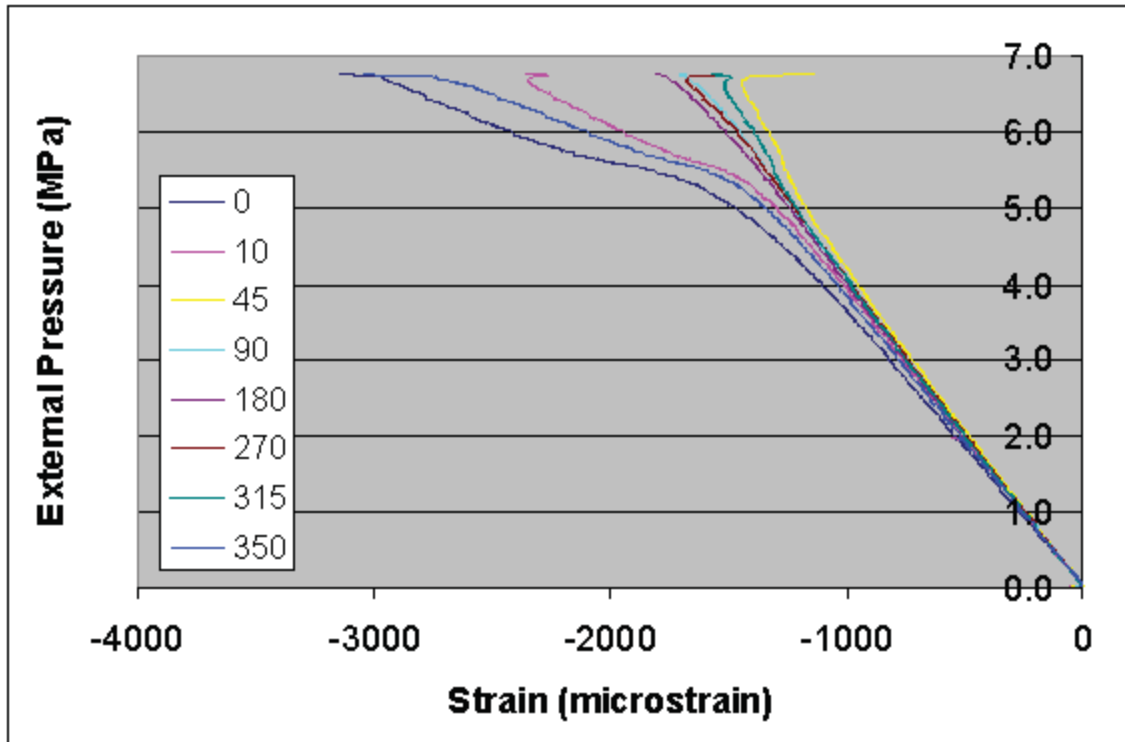
Figure 3.33: Comparison of Measured (top) and Predicted (bottom) Histories of Circumferential Strain on Flange of Frame #2.
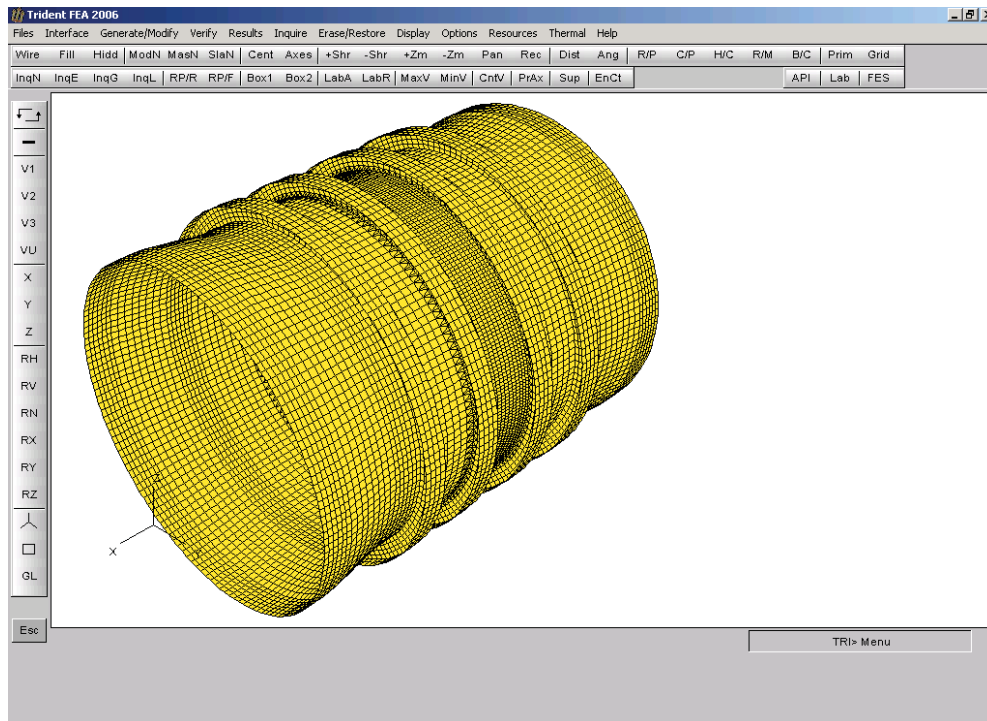
Figure 3.34: Finite Element Model for Corroded Short Cylinder L300-No4.
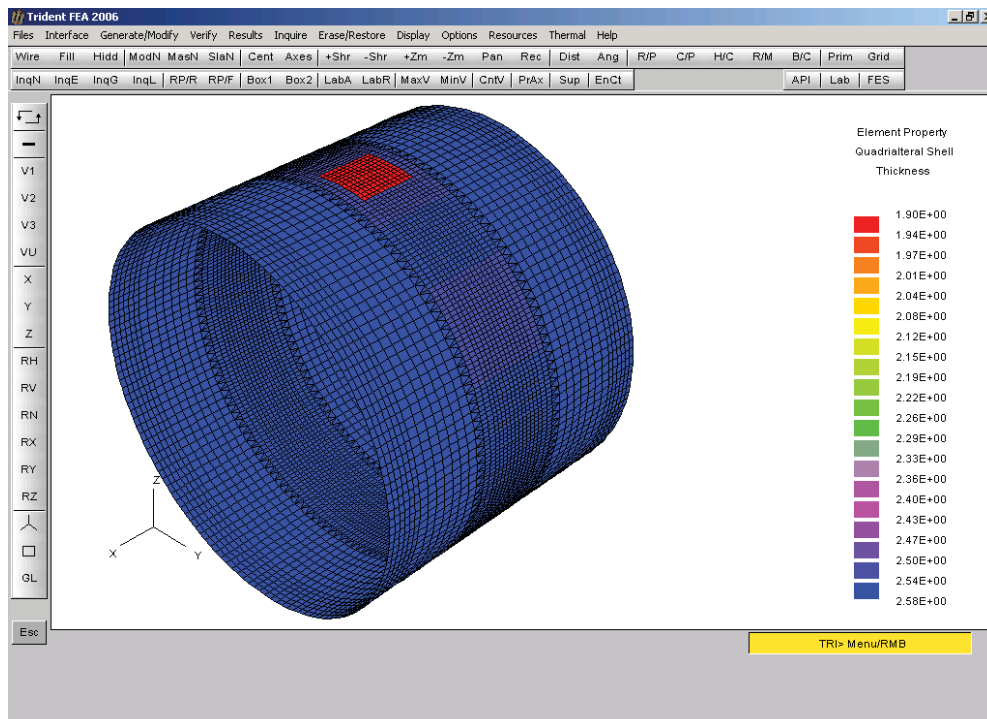
Figure 3.35: Thickness Contour Indicating the Simulated Corrosion Patch.
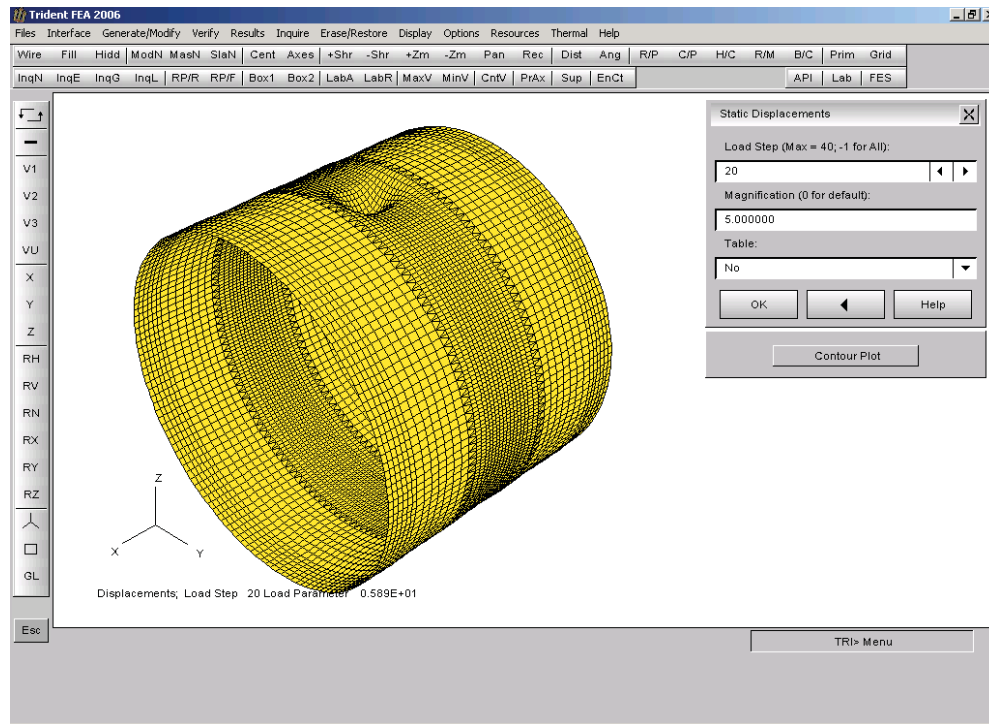
Figure 3.36: Intermediate Deformed Shape (at Load Step 20) Showing Buckling of the Corroded Area.
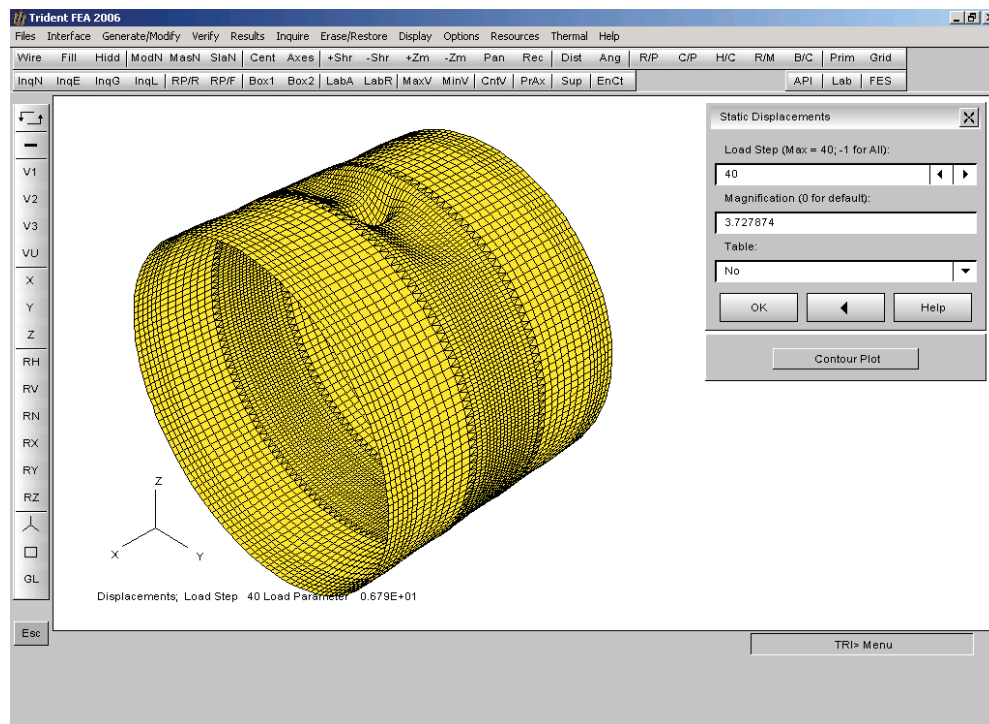
Figure 3.37: Final Deformed Shape (at Load Step 40) Showing Progressive Buckling Adjacent to the Corroded Patch.
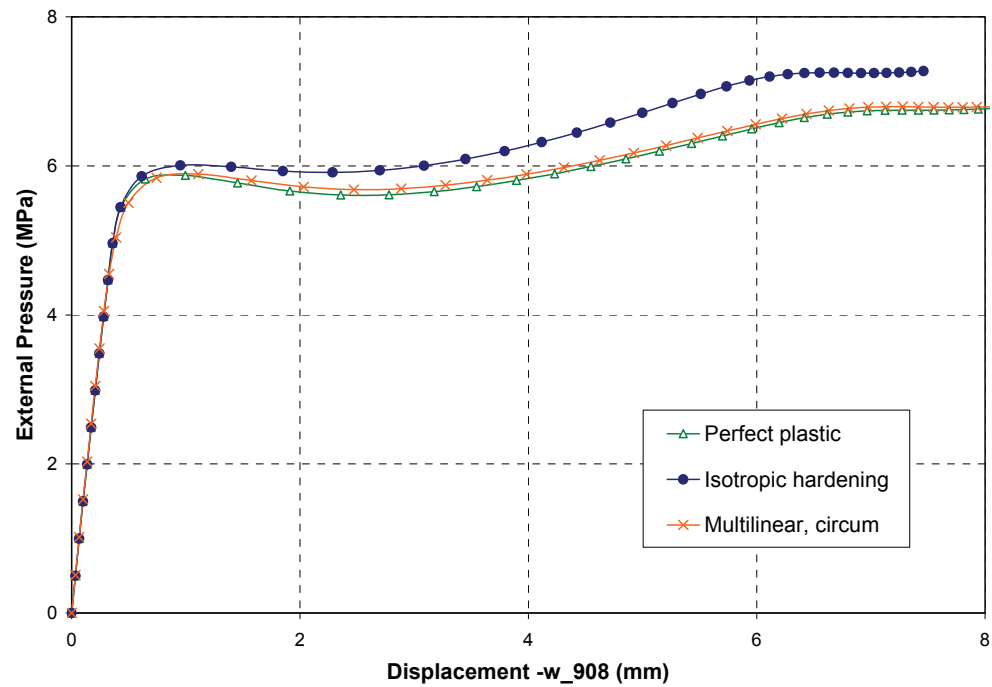
Figure 3.38: Comparison of Pressure-Displacement Curves for Short Cylinder L300-No4 Predicted Using Different Material Models.
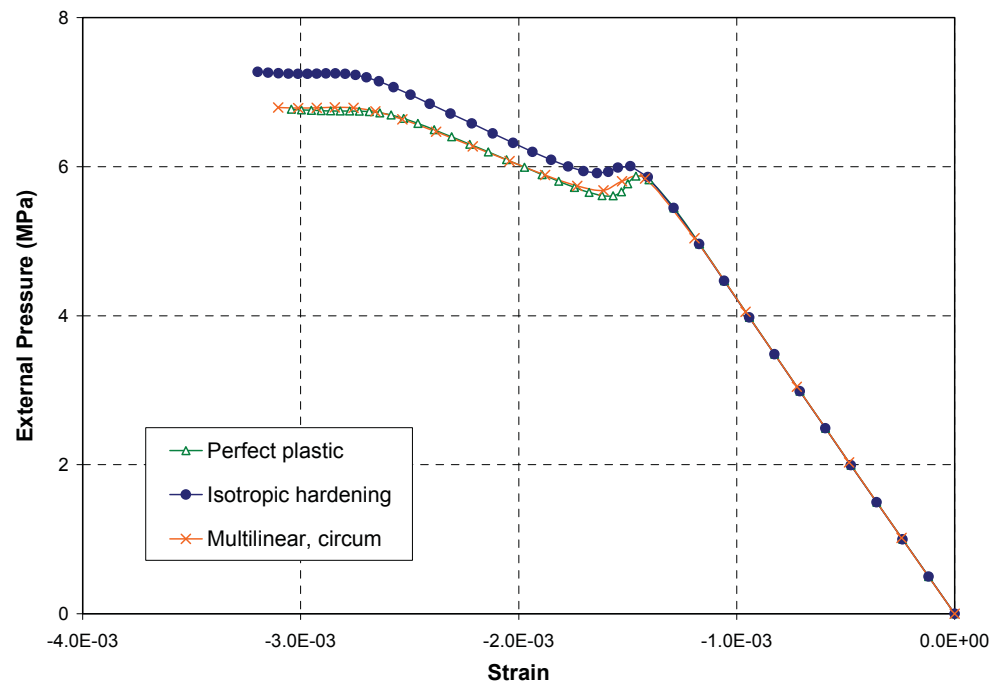
Figure 3.39: Comparison of Predicted Histories of Circumferential Strain in Flange of Frame #2 at 0°.
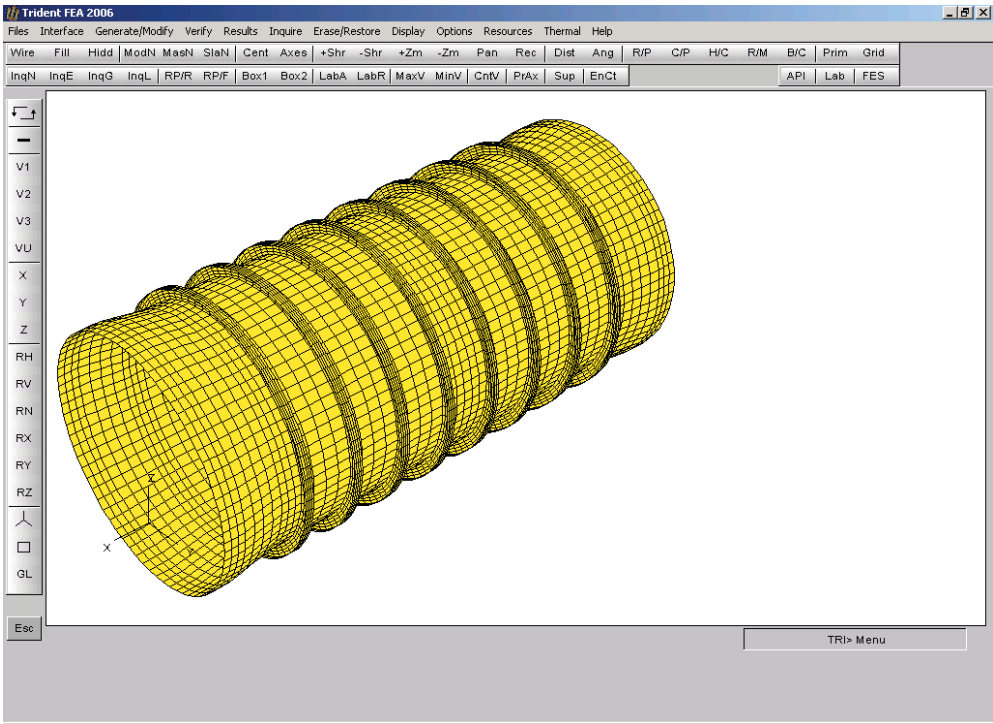
Figure 3.40: Mesh Refinement 1 (R1) for Long Cylinder L510-No1.
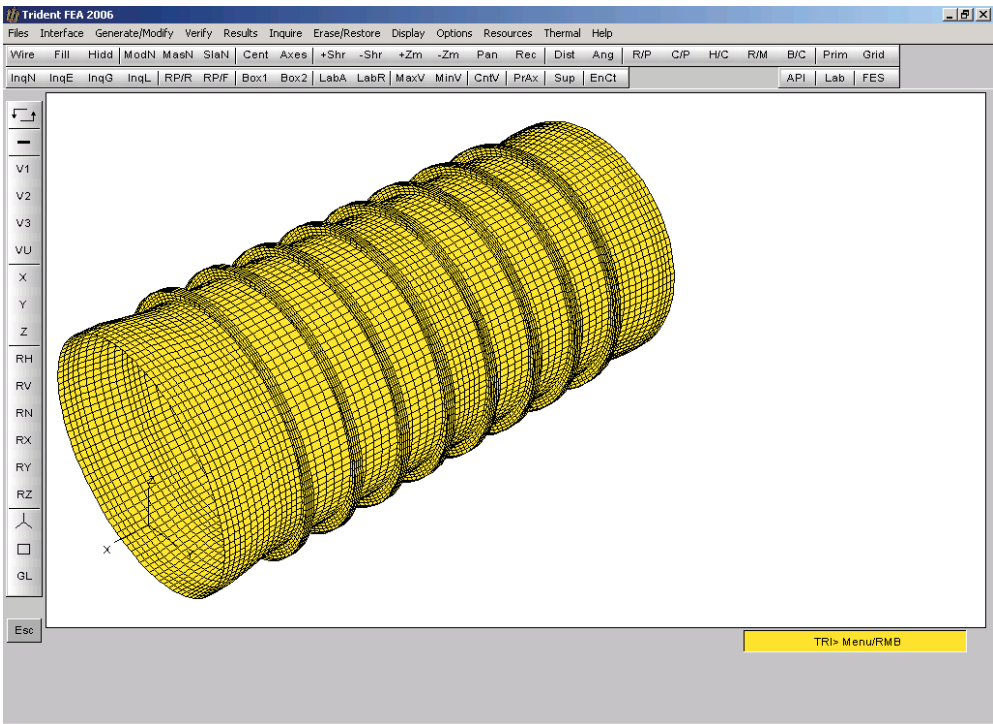
Figure 3.41: Mesh Refinement 2 (R2) for Long Cylinder L510-No1.

Figure 3.42: Mesh Refinement 3 (R3) for Long Cylinder L510-No1.

Figure 3.43: Mesh Refinement 4 (R4) for Long Cylinder L510-No1.
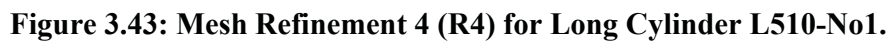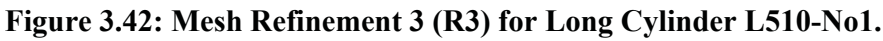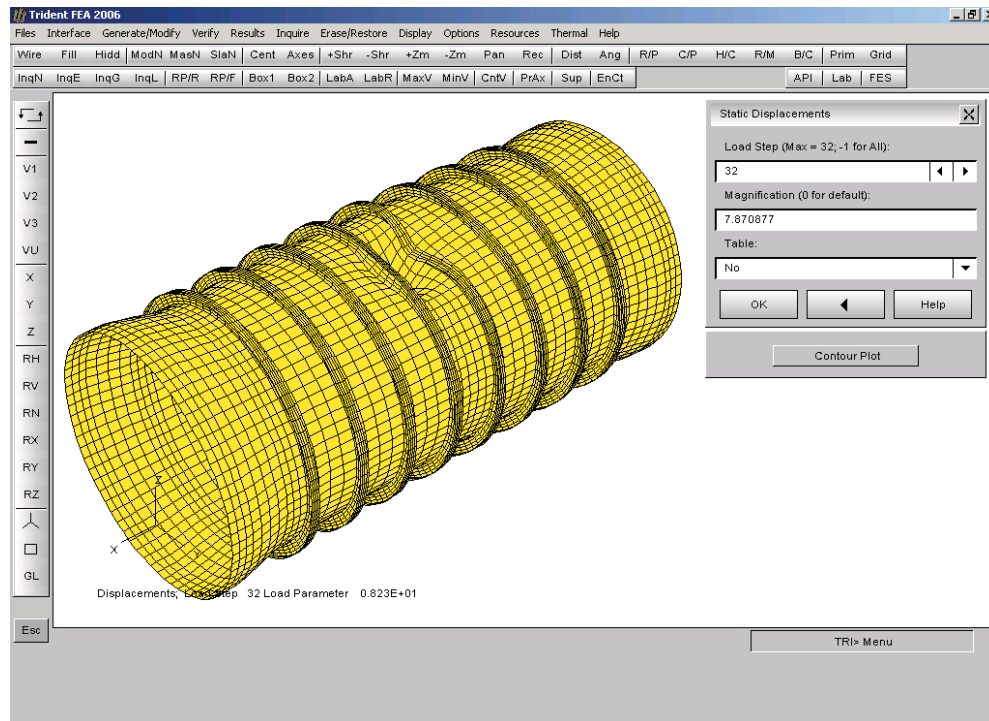
Figure 3.44: Final Deformed Shape Predicted by Mesh R1 Showing Local Buckling First Occurred at Central Bay.
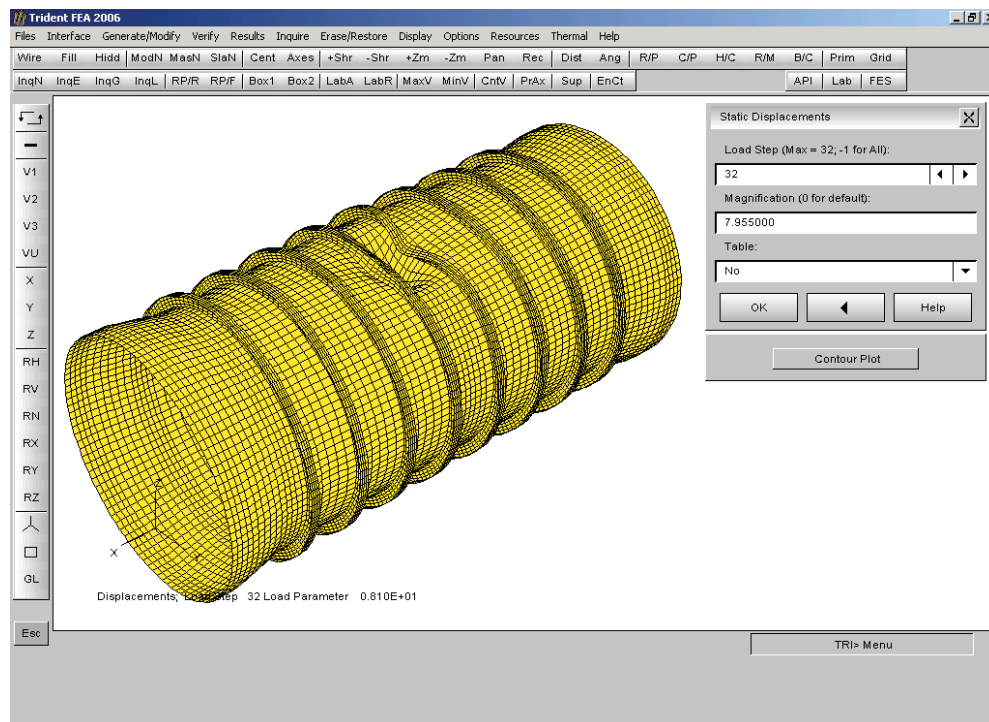
Figure 3.45: Final Deformed Shape Predicted by Mesh R2 Showing Local Buckling First Occurred at Central Bay.
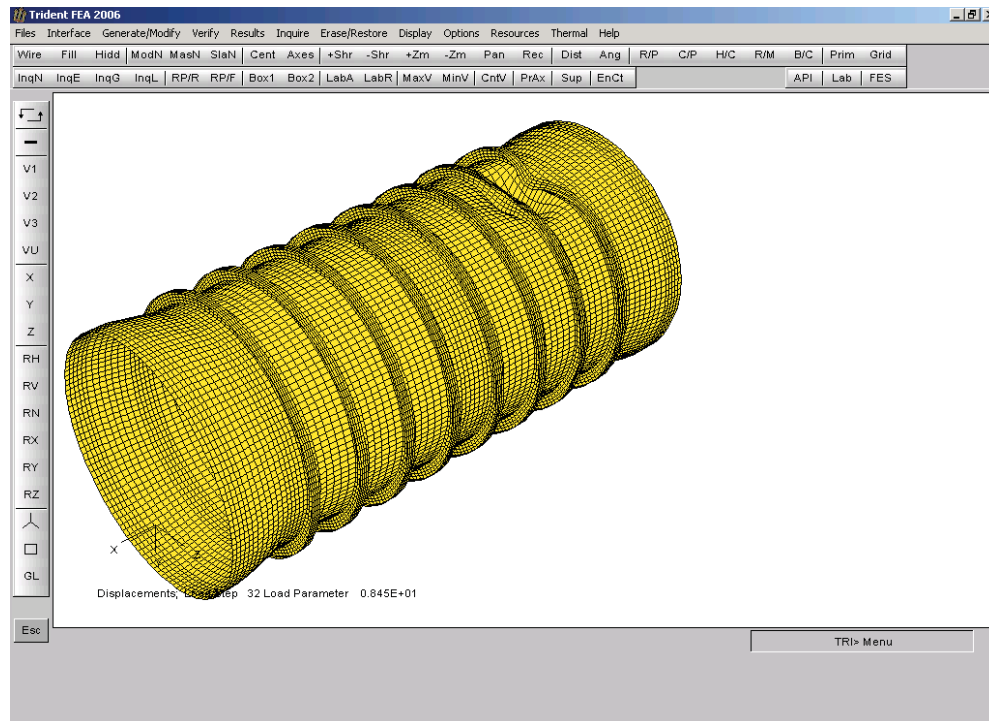
Figure 3.46: Final Deformed Shape Predicted by Mesh R3 Showing Local Buckling First Occurred at End Bay.
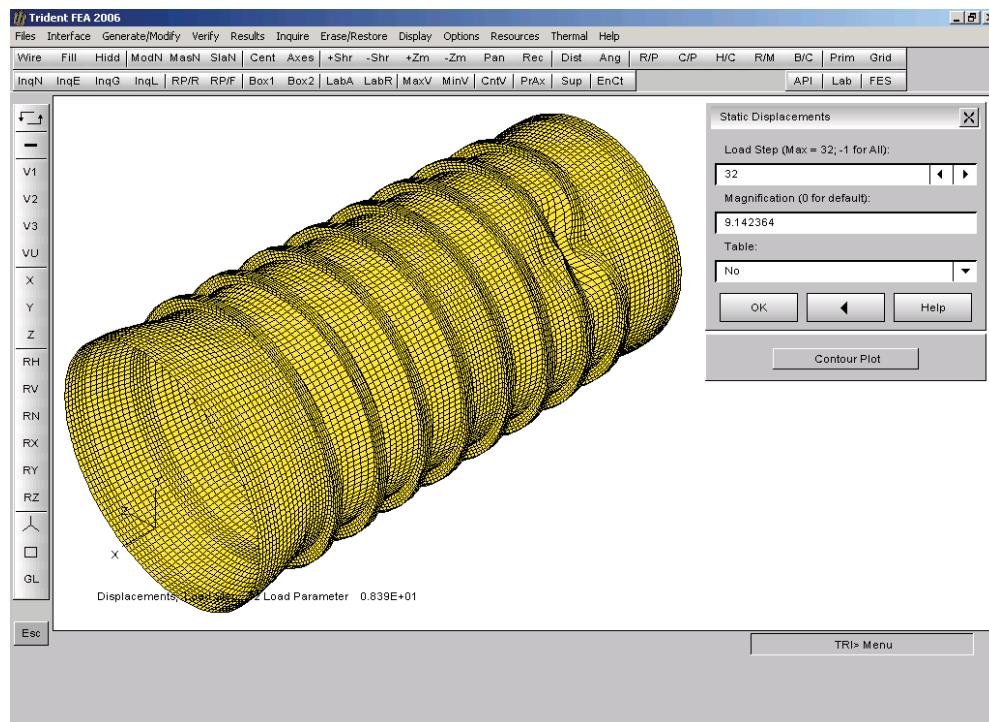
Figure 3.47: Final Deformed Shape Predicted by Mesh R4 Showing Local Buckling First Occurred at End Bay.
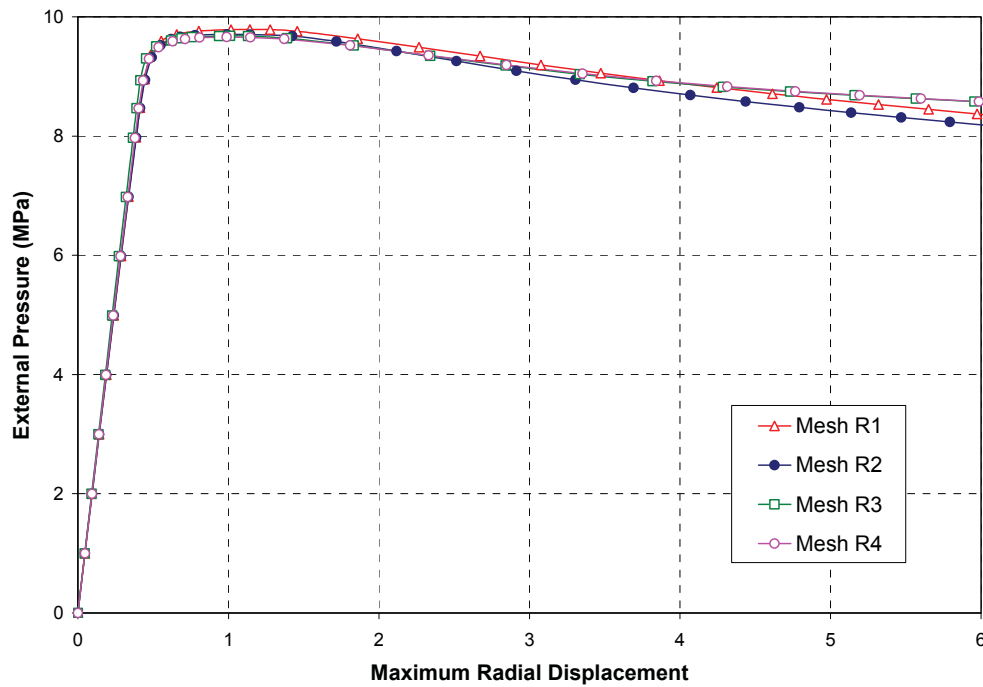
Figure 3.48: Comparison of Pressure-Maximum Radial Displacement Curves for Long Cylinder L510-No1 Predicted by Difference Meshes.
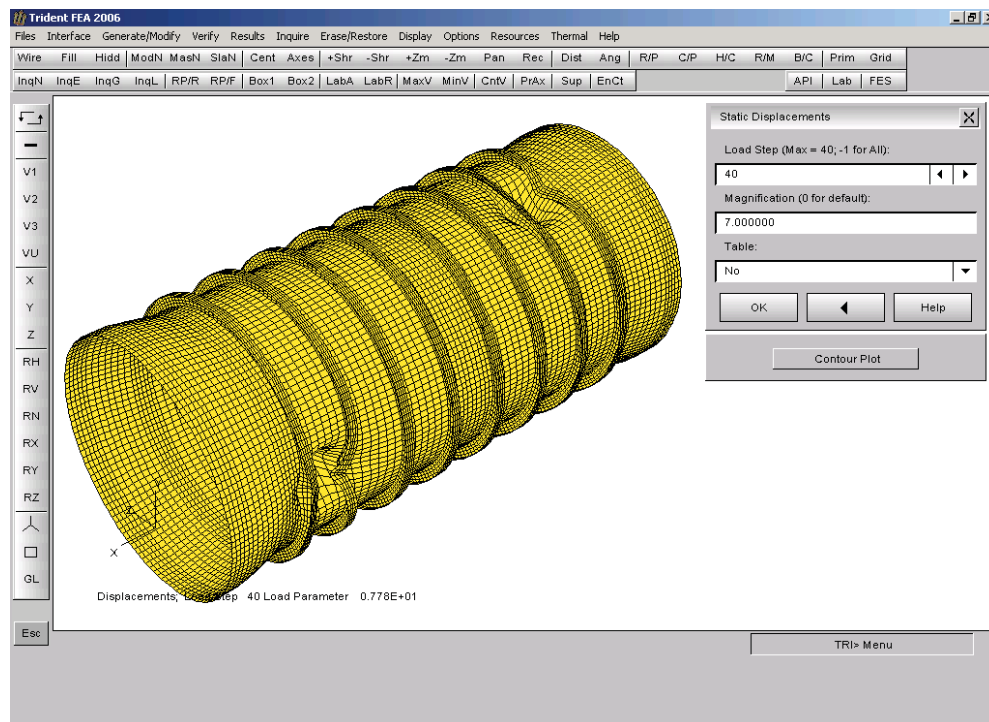
Figure 3.49: Final Deformed Shape Predicted by Mesh R3 Using Elastic-Perfectly-Plastic Material Property.
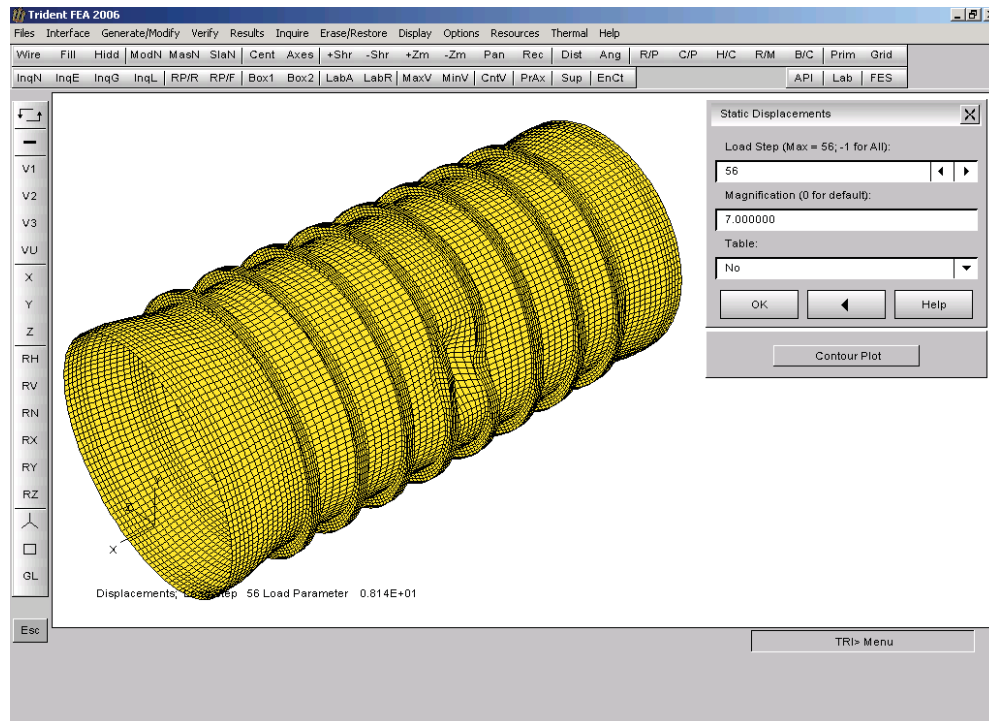
Figure 3.50: Final Deformed Shape Predicted by Mesh R3 Using Bilinear Material Property with Kinematic Hardening.
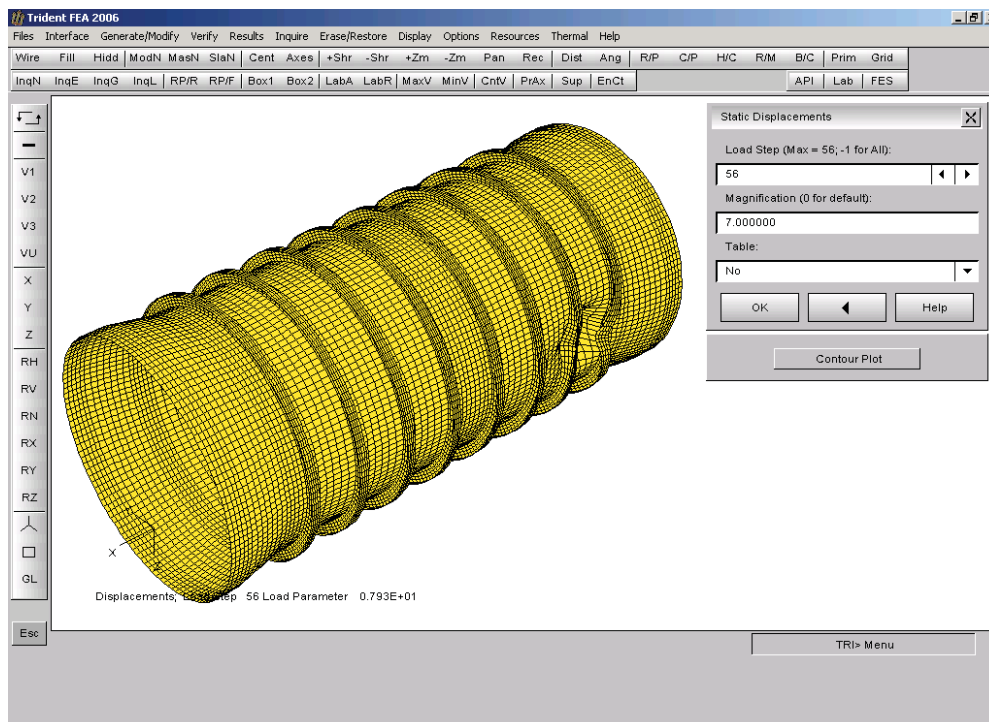
Figure 3.51: Final Deformed Shape Predicted by Mesh R3 Using Multi-Linear Stress-Strain Property.
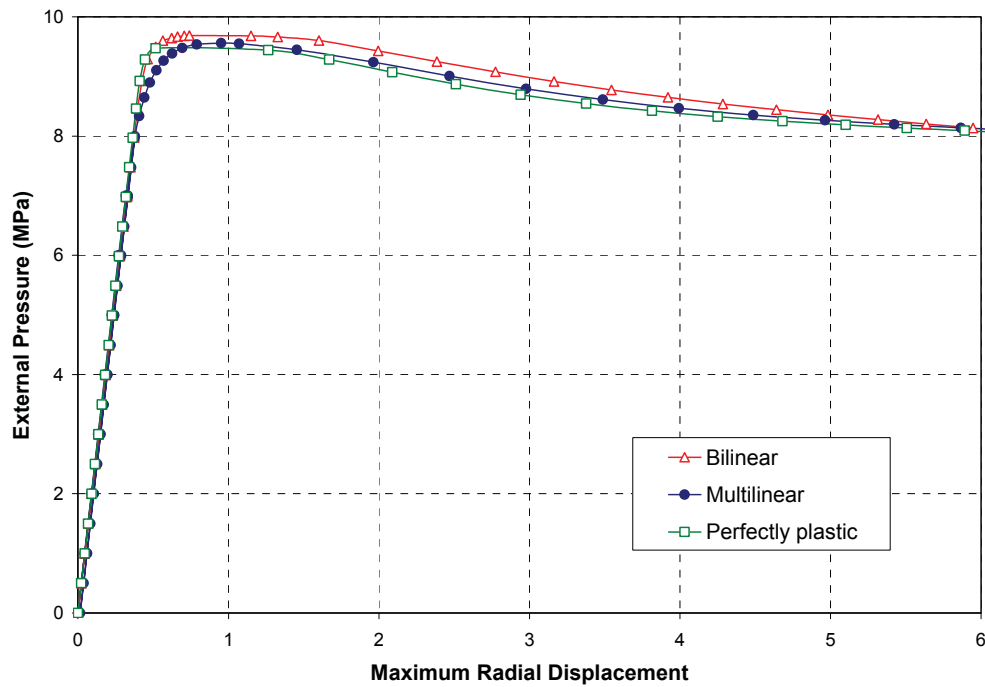
Figure 3.52: Comparison of Pressure-Maximum Radial Displacement Curves for Long Cylinder L510-No1 Predicted by Mesh R3 Using Different Material Models.
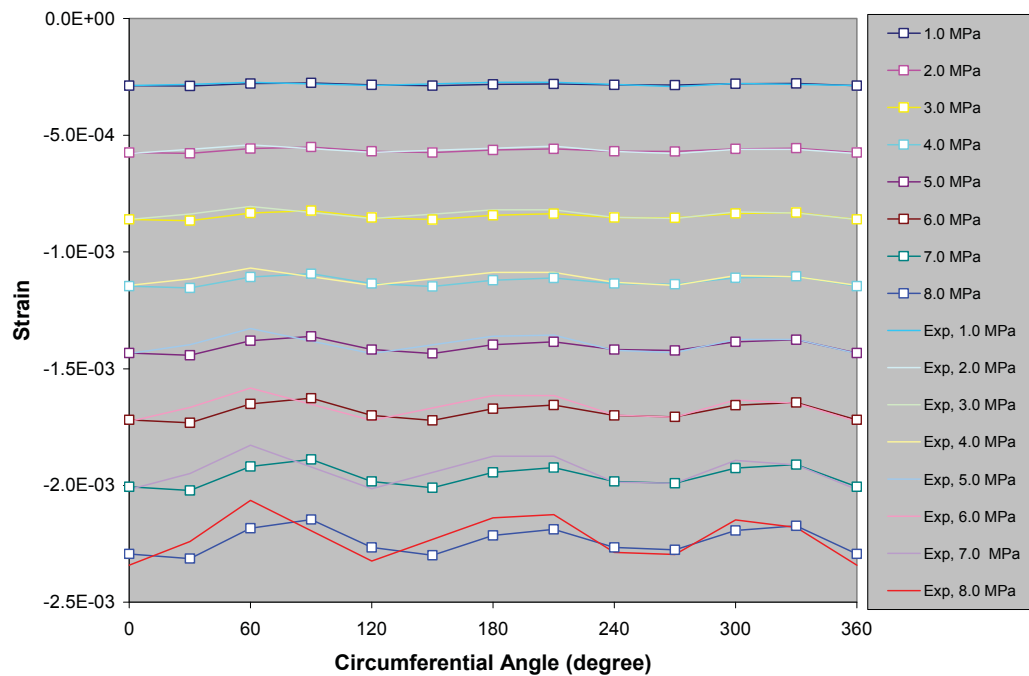
Figure 3.53: Comparison of Predicted (with Symbols) and Measured Circumferential Profiles of the Circumferential Strain in Flange of Frame #4.
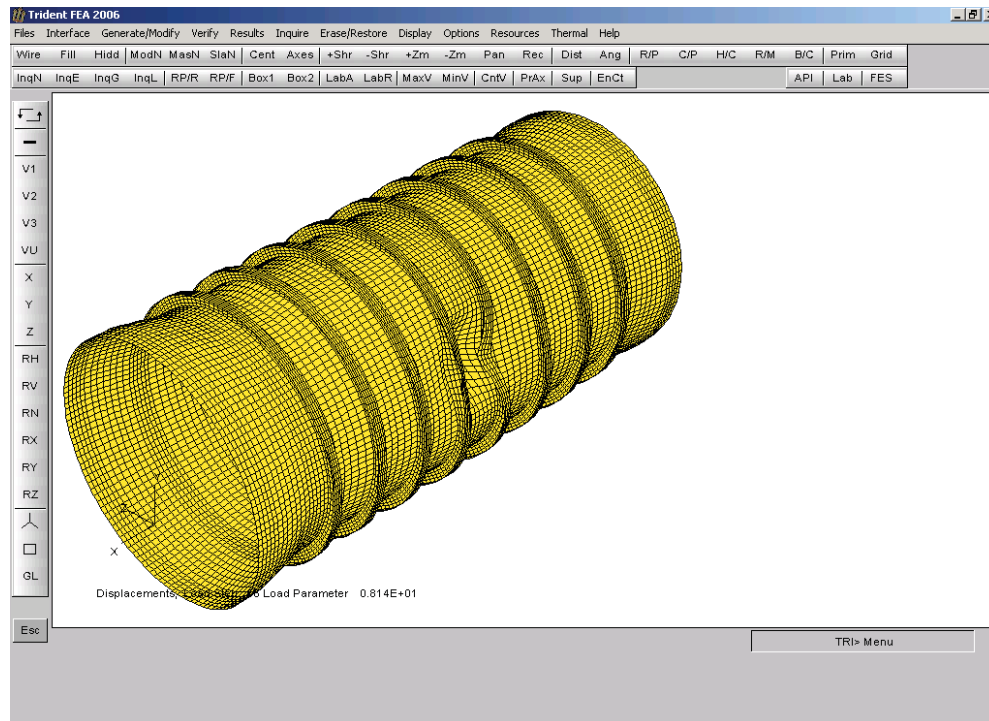
Figure 3.54: Final Deformed Shape of Cylinder L510-No1 Predicted Using Mesh R3, Bilinear Material Model and Clamped Boundary Condition (BC I).
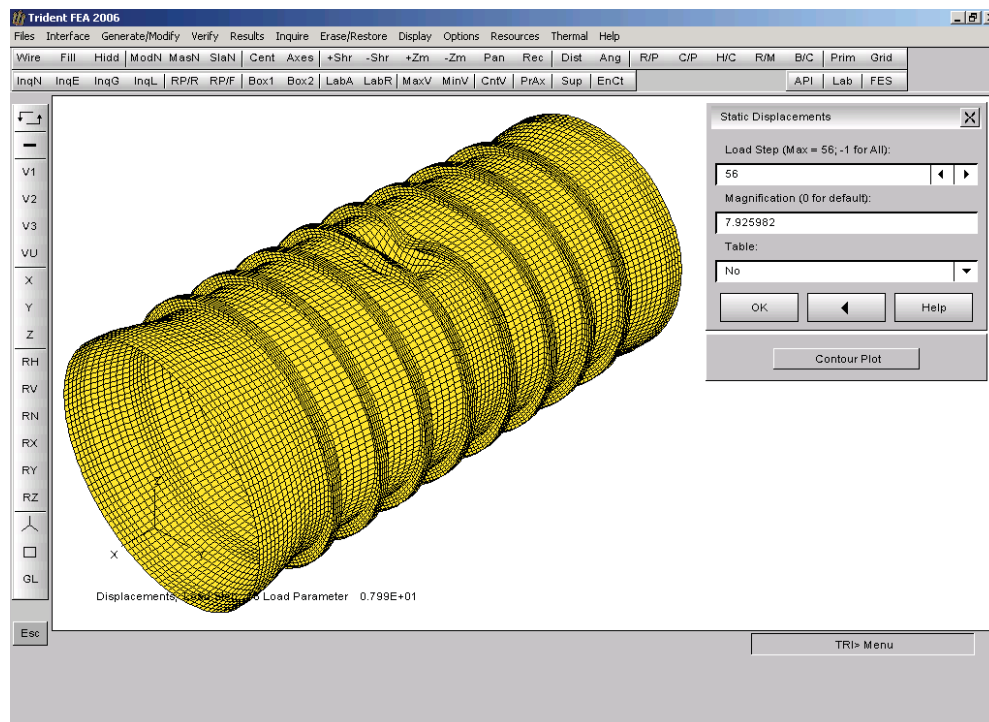
Figure 3.55: Final Deformed Shape of Cylinder L510-No1 Predicted Using Mesh R3, Bilinear Material Model and Pinned Boundary Condition (BC II).
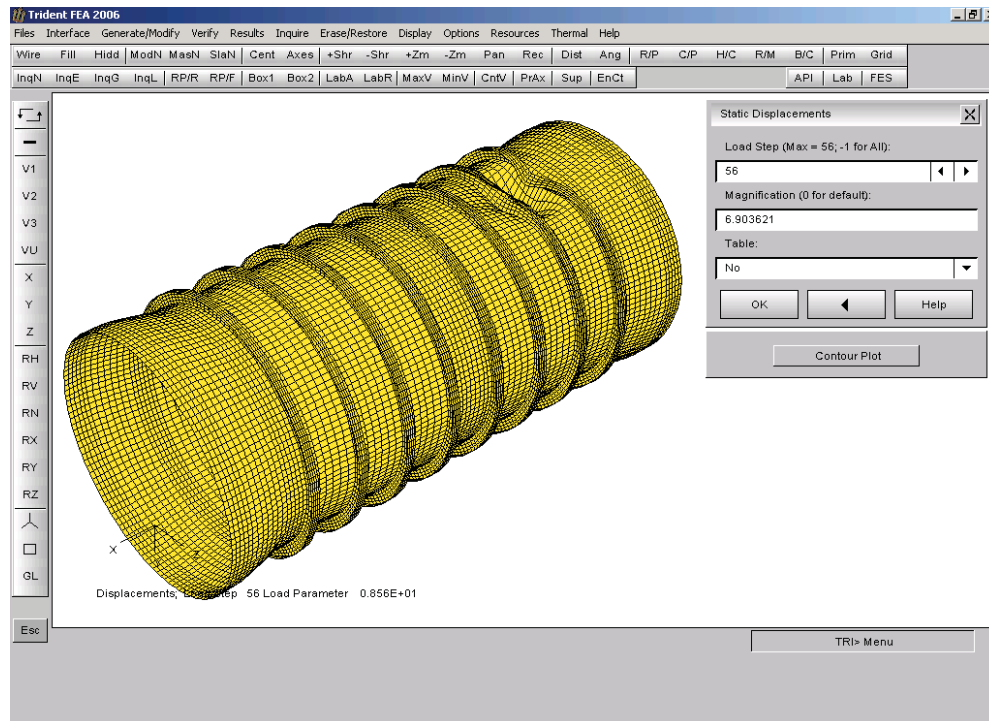
Figure 3.56: Final Deformed Shape of Cylinder L510-No1 Predicted Using Mesh R3, Bilinear Material Model and Double Pinned Boundary Condition (BC III).
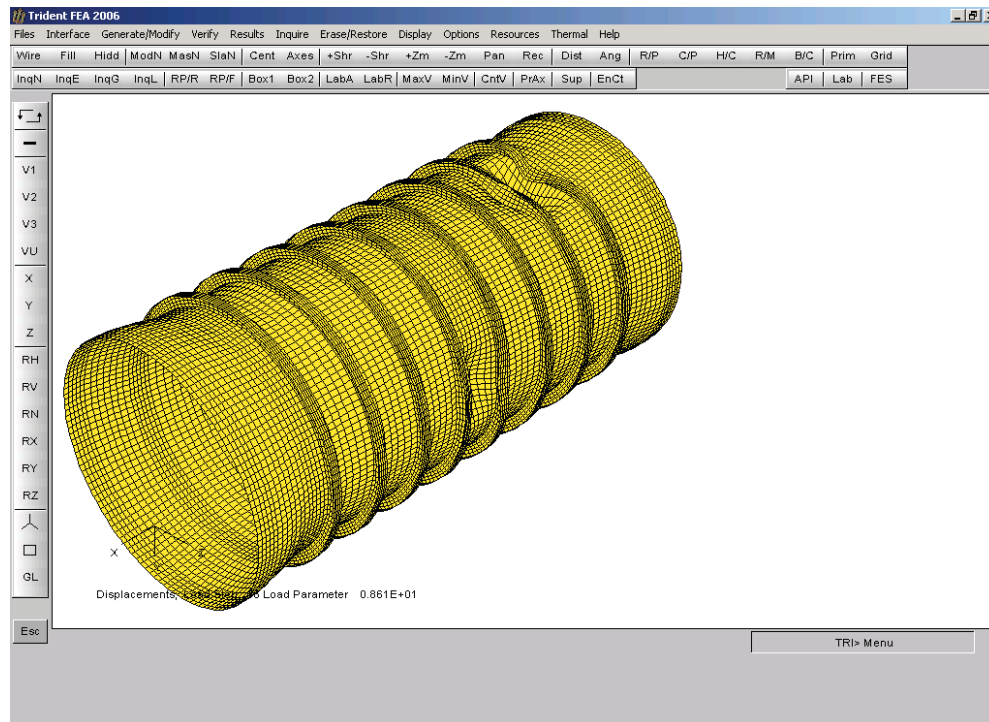
Figure 3.57: Final Deformed Shape of Cylinder L510-No1 Predicted Using Mesh R3, Bilinear Material Model and Rigid Link Boundary Condition (BC IV).
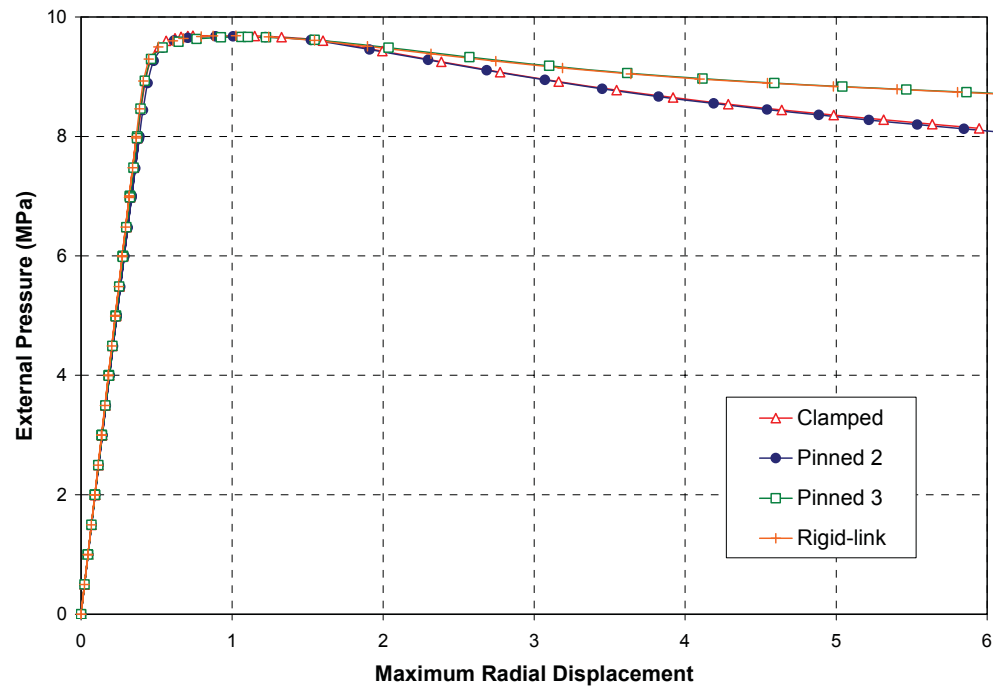
Figure 3.58: Comparison of Pressure-Maximum Radial Displacement Curves Predicted Using Different Boundary Conditions.
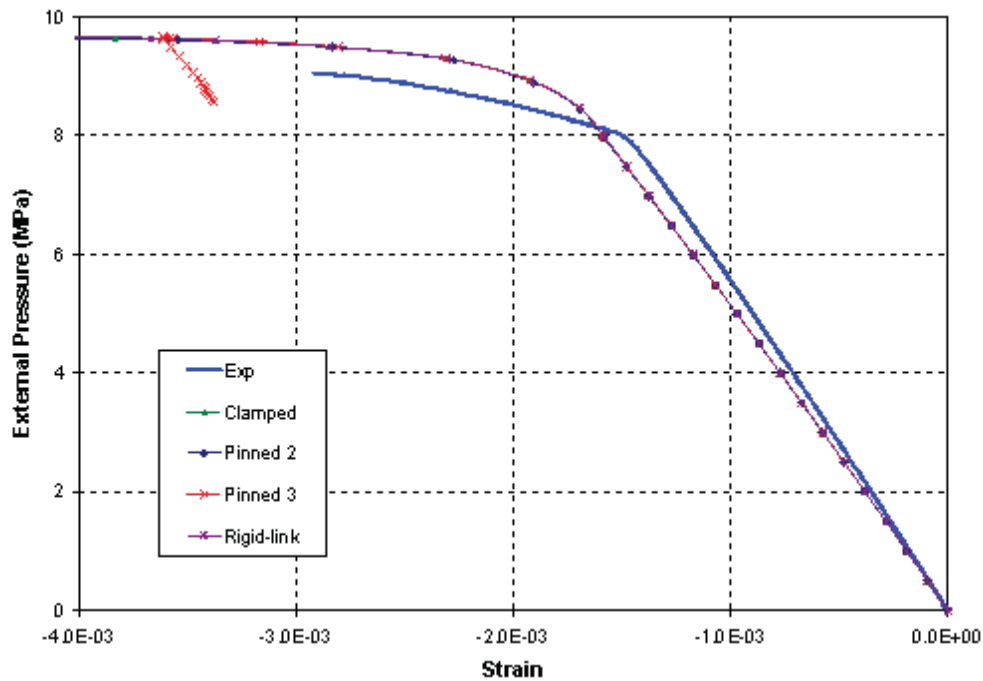
Figure 3.59: Comparison of Measured History of Axial Strain on Outside of Shell at Central Bay at 0° with Predictions Using Various BCs.
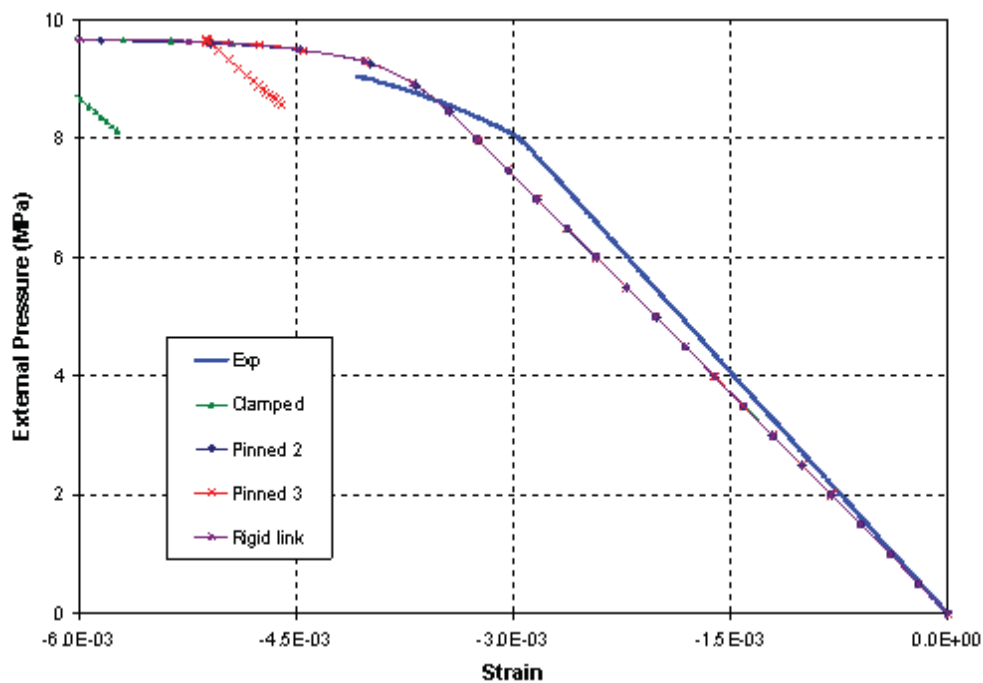
Figure 3.60: Comparison of Measured History of Circumferential Strain on Outside of Shell at Central Bay at 0° with Predictions Using Various BCs.
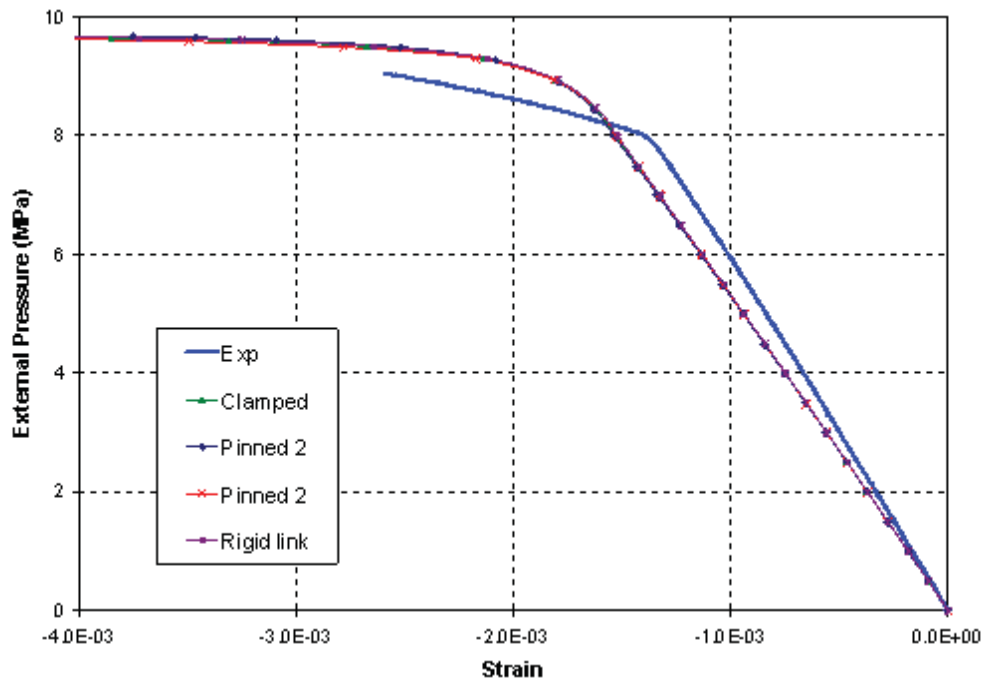
Figure 3.61: Comparison of Measured History of Axial Strain on Outside of Shell at End Bay (Fr#1-Fr#2) at 0° with Predictions Using Various BCs.
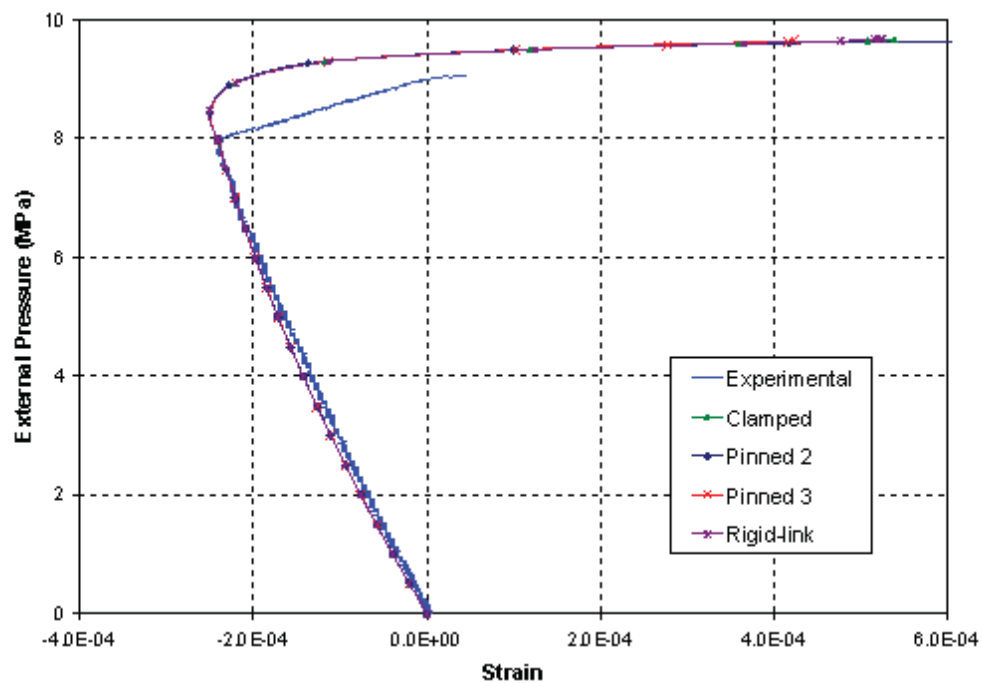
Figure 3.62: Comparison of Measured History of Axial Strain on Inside of Shell at Central Bay at 60° with Predictions Using Various BCs.
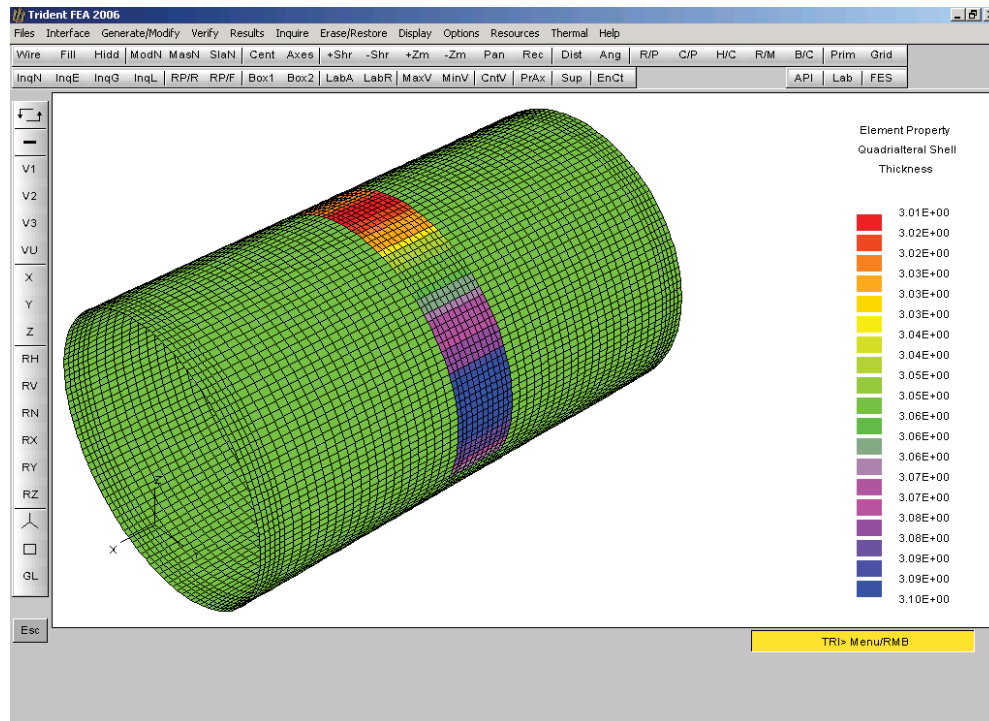
Figure 3.63: Thickness Variations along the Circumference at Central Bay.
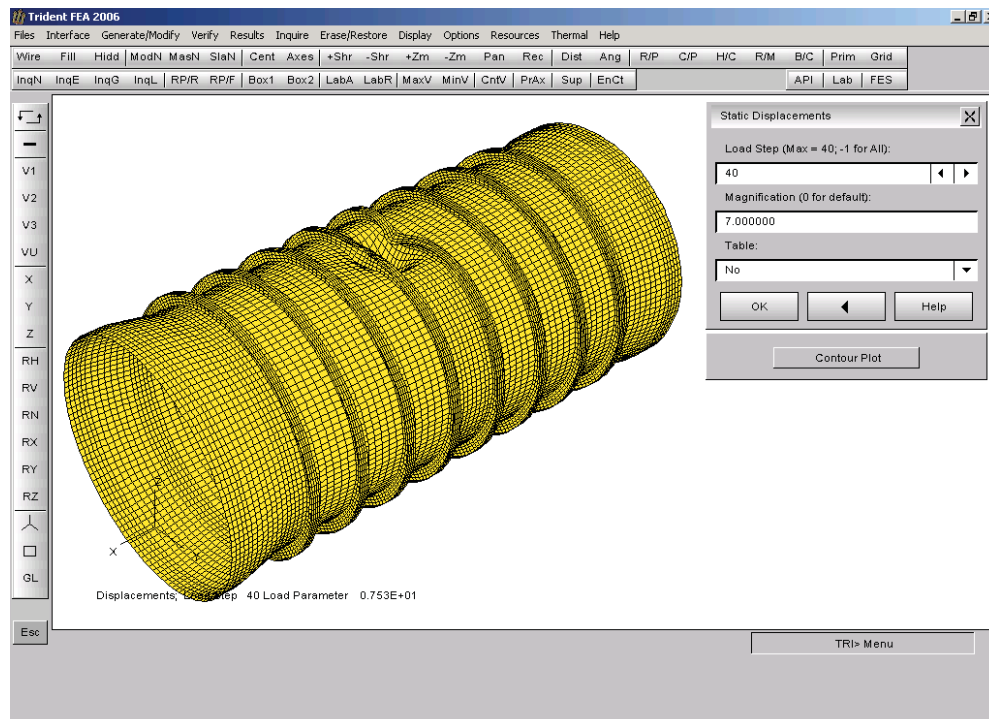
Figure 3.64: Final Deformed Shape Predicted by Finite Element Models with Measured Thickness Variations.
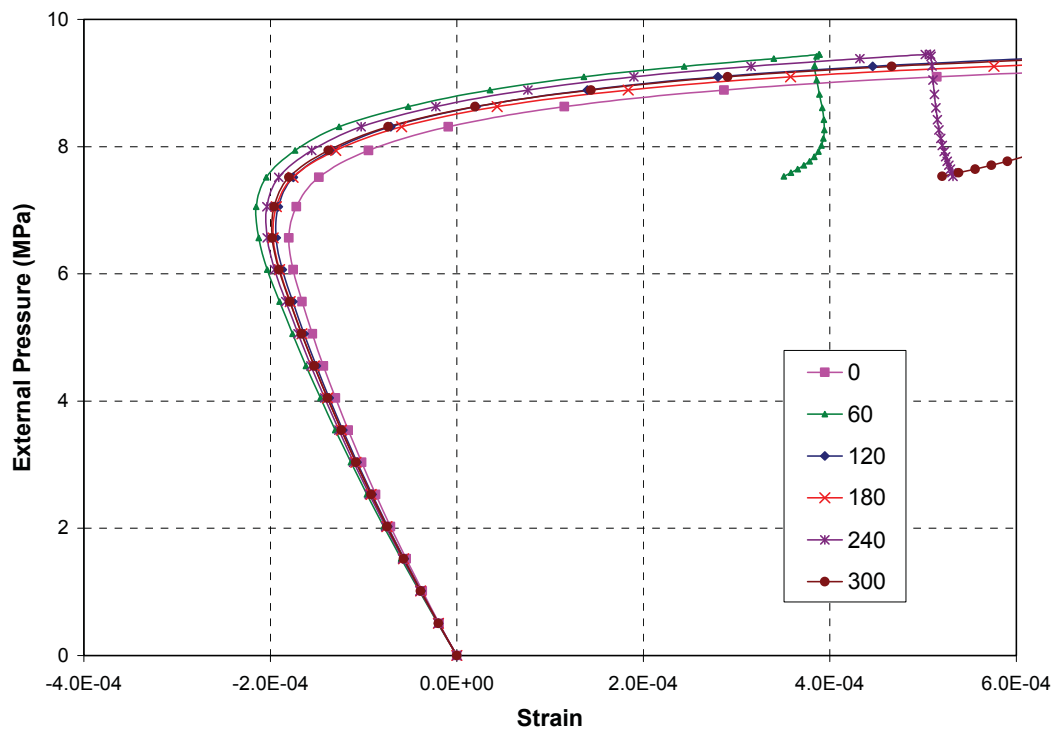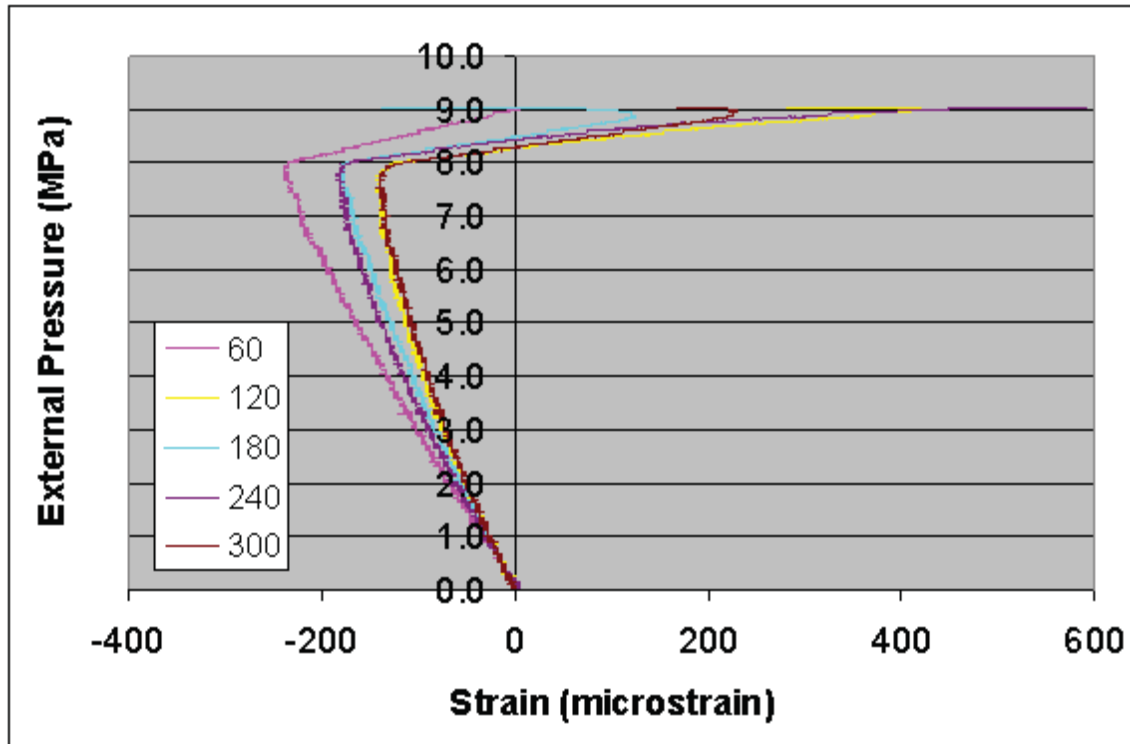
Figure 3.65: Comparison of Measured (top) and Predicted (bottom) Histories of Axial Strain on Inside of Shell at Central Bay.
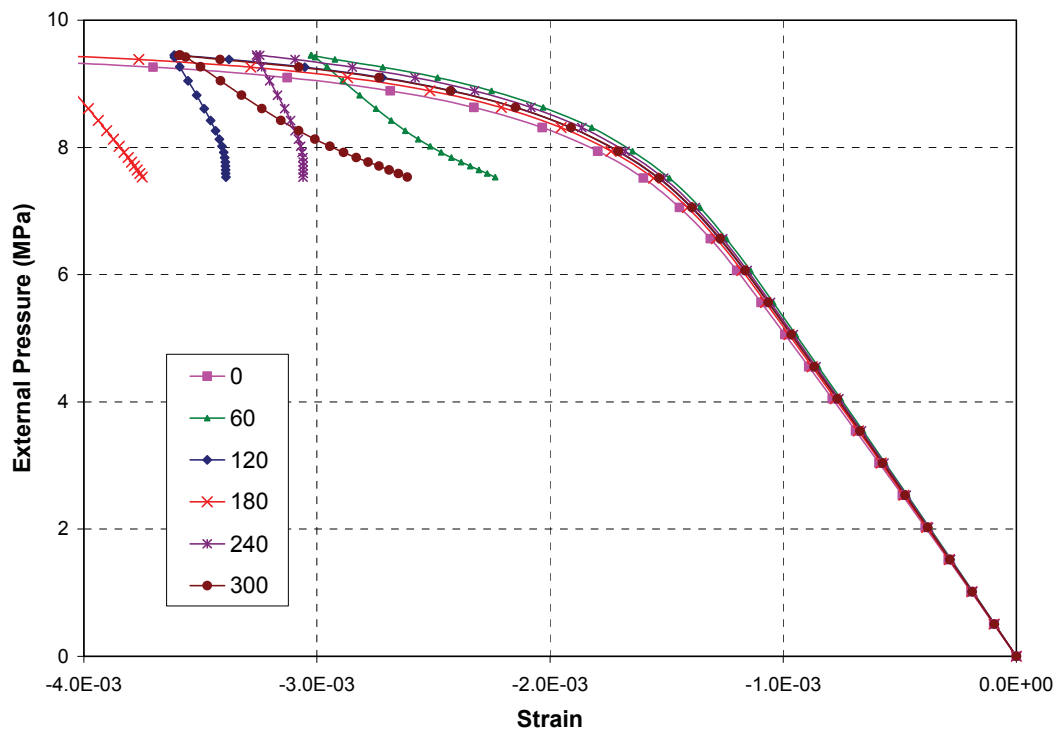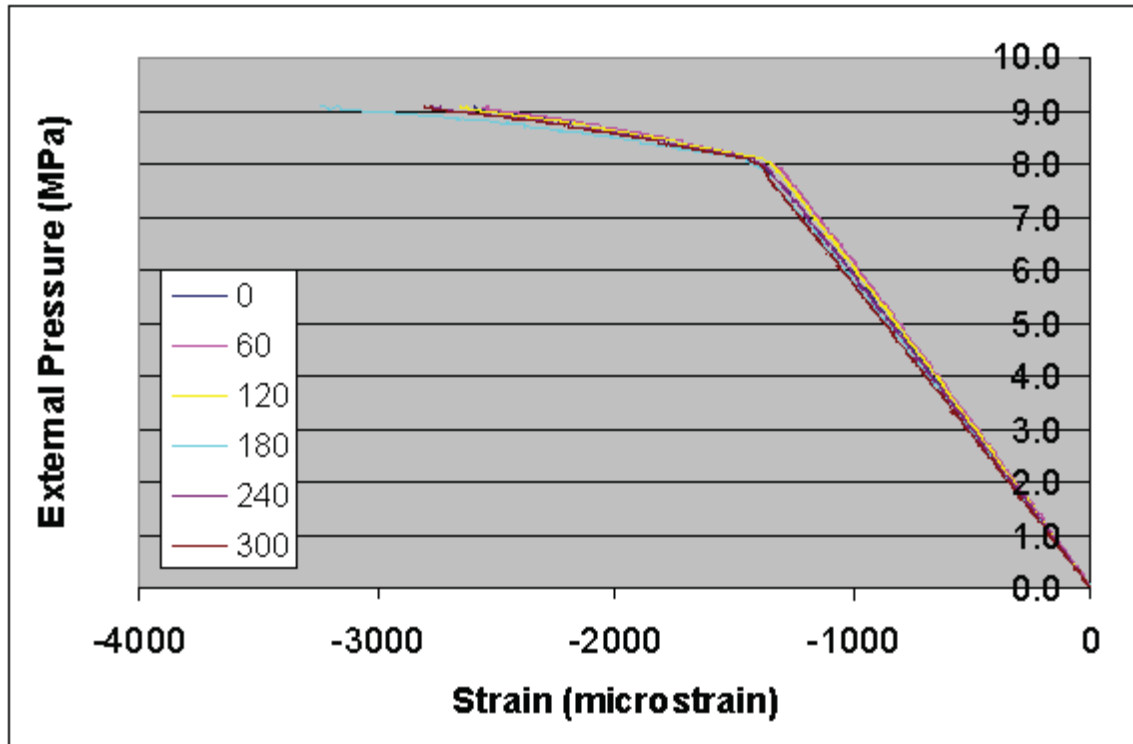
Figure 3.66: Comparison of Measured (top) and Predicted (bottom) Histories of Axial Strain on Outside of Shell at Central Bay.
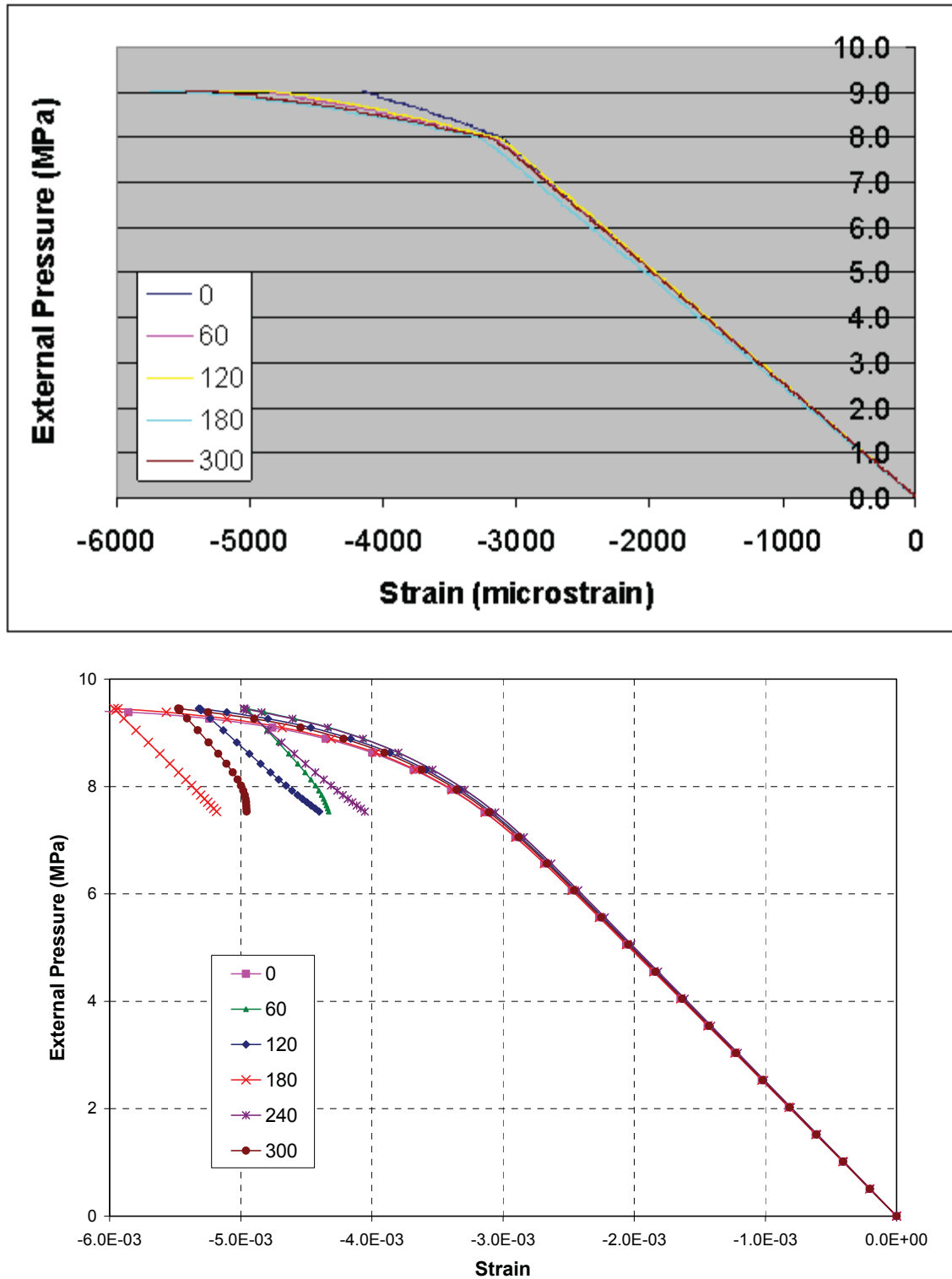
Figure 3.67: Comparison of Measured (top) and Predicted (bottom) Histories of Circumferential Strain on Inside of Shell at Central Bay.
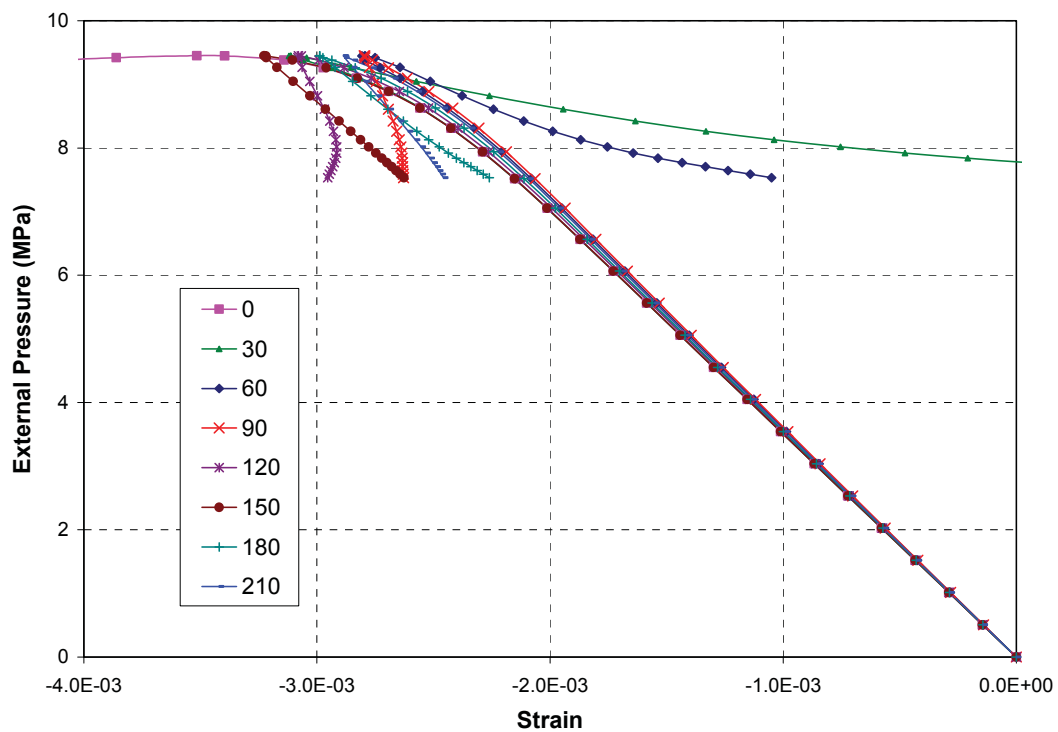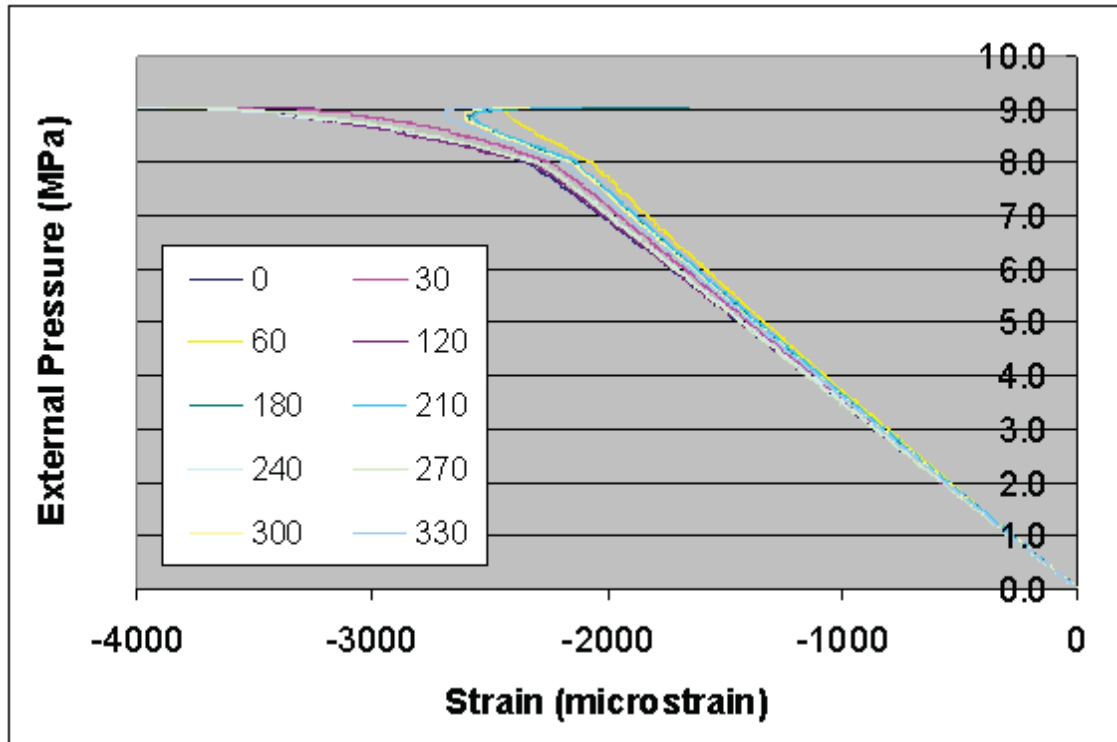
Figure 3.68: Comparison of Measured (top) and Predicted (bottom) Histories of Circumferential Strain in Flange of Frame #4.
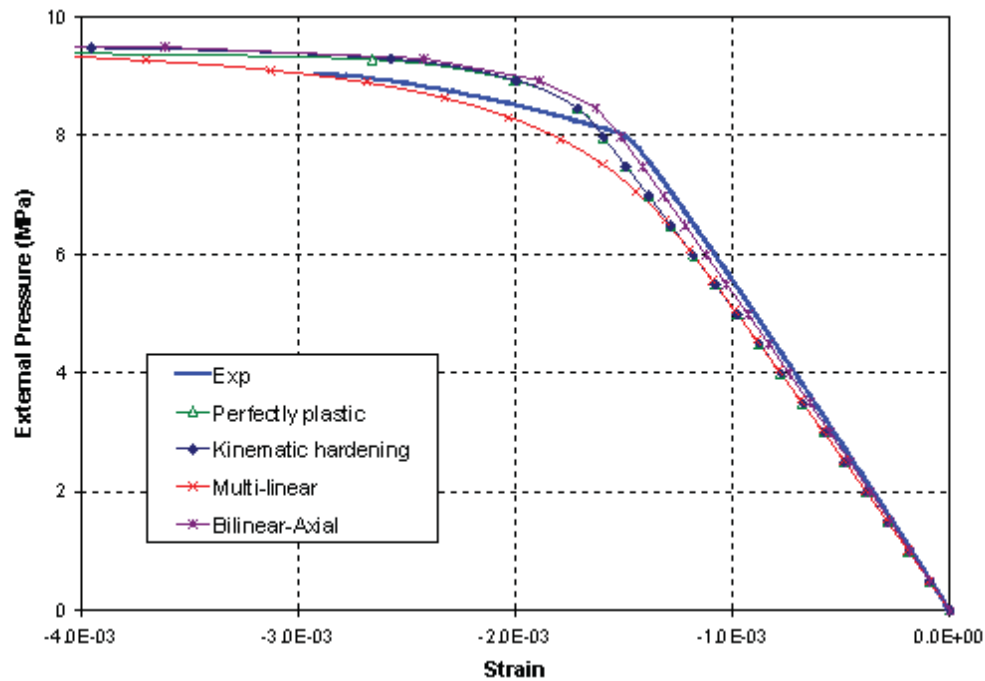
Figure 3.69: Comparison of Measured Axial Strain History on Outside of Shell at Central Bay at 0° and Predictions Using Different Material Models.

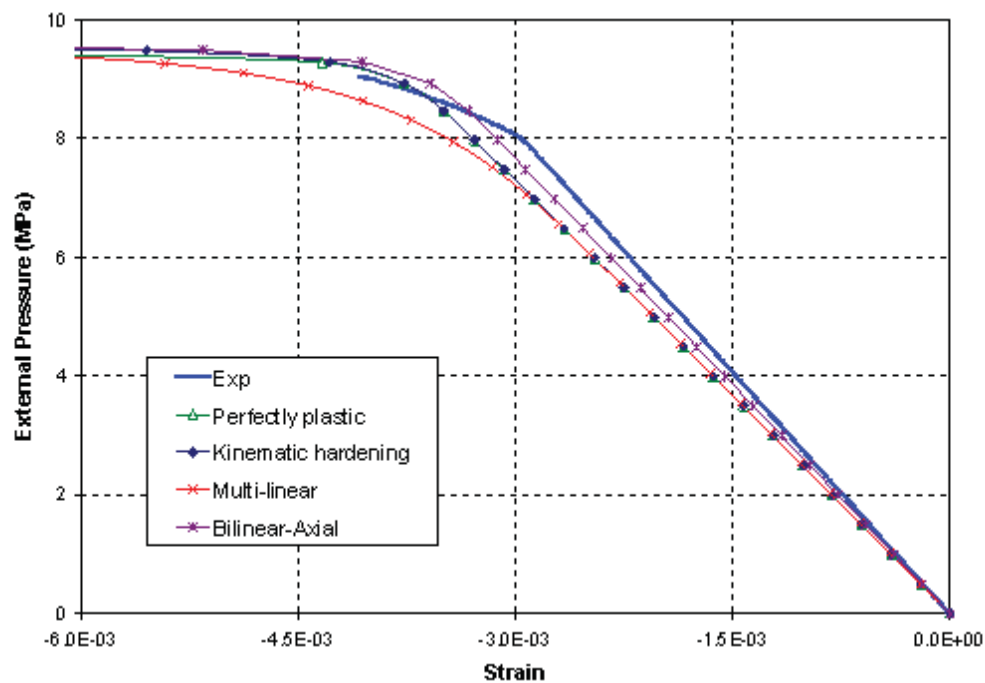**Figure 3.70: Comparison of Measured Circumferential Strain History on Outside of Shell at Central Bay at 0° and Predictions Using Different Material Models.**
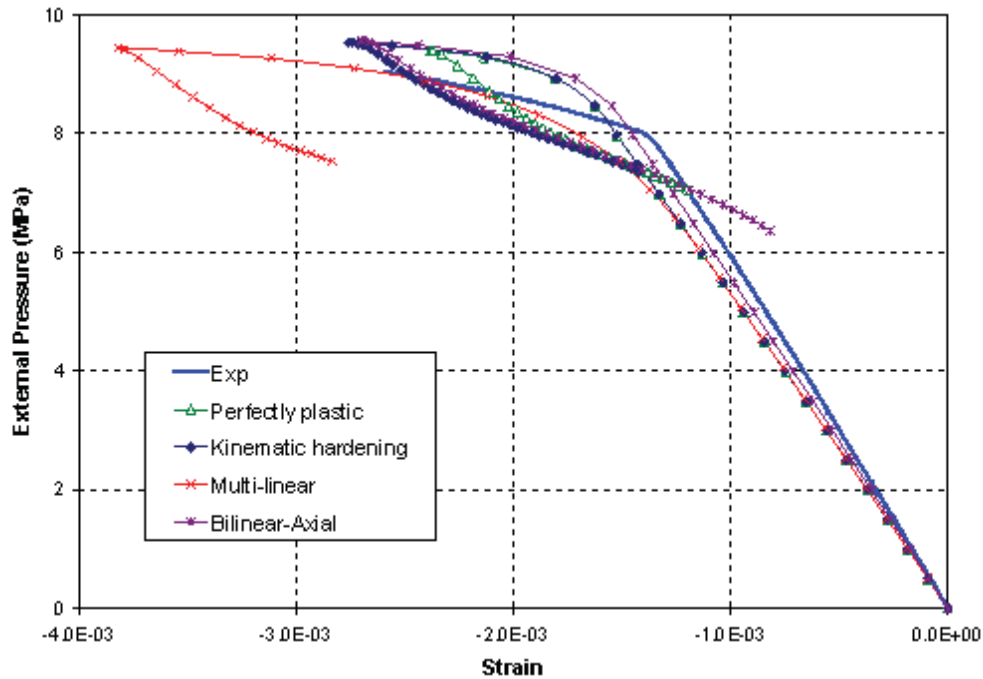
Figure 3.71: Comparison of Measured Axial Strain History on Outside of Shell at End Bay (Fr#1-Fr#2) at 0° and Predictions Using Different Material Models.
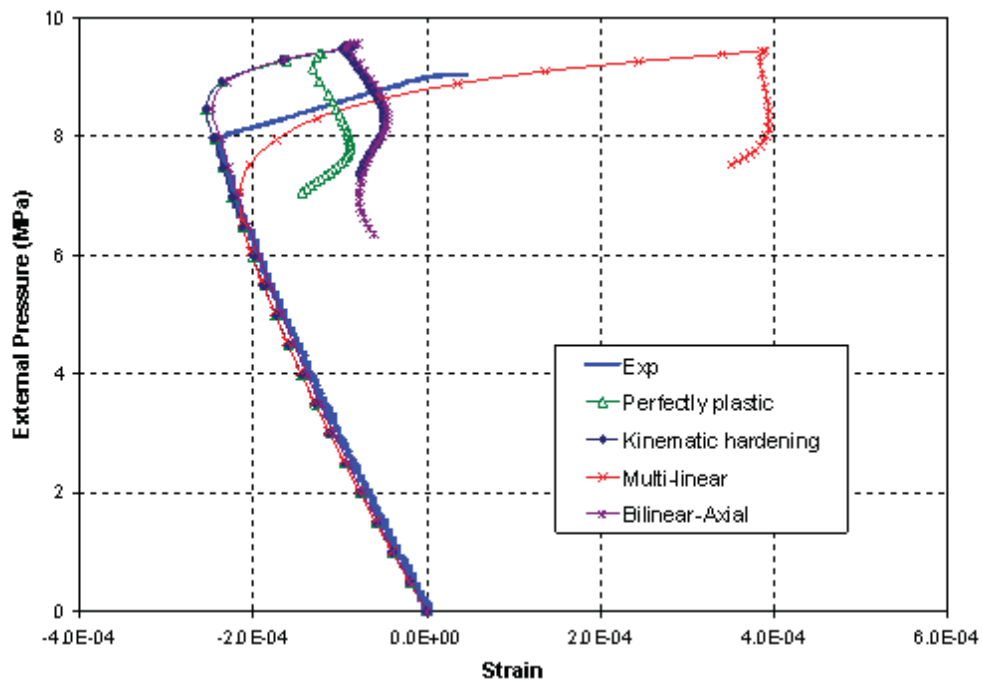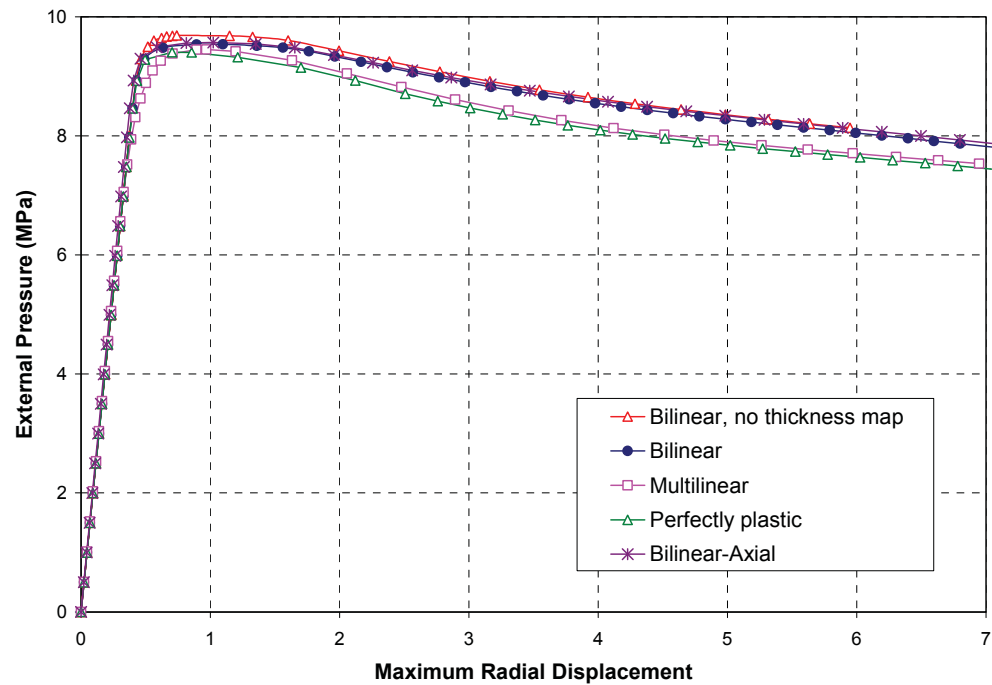

Figure 3.72: Comparison of Measured Axial Strain History on Inside of Shell at Central Bay at 60° and Predictions Using Different Material Models.

Figure 3.73: Comparison of Pressure-Maximum Radial Displacement Curves Predicted by Models with Thickness Variation Using Different Material Models.
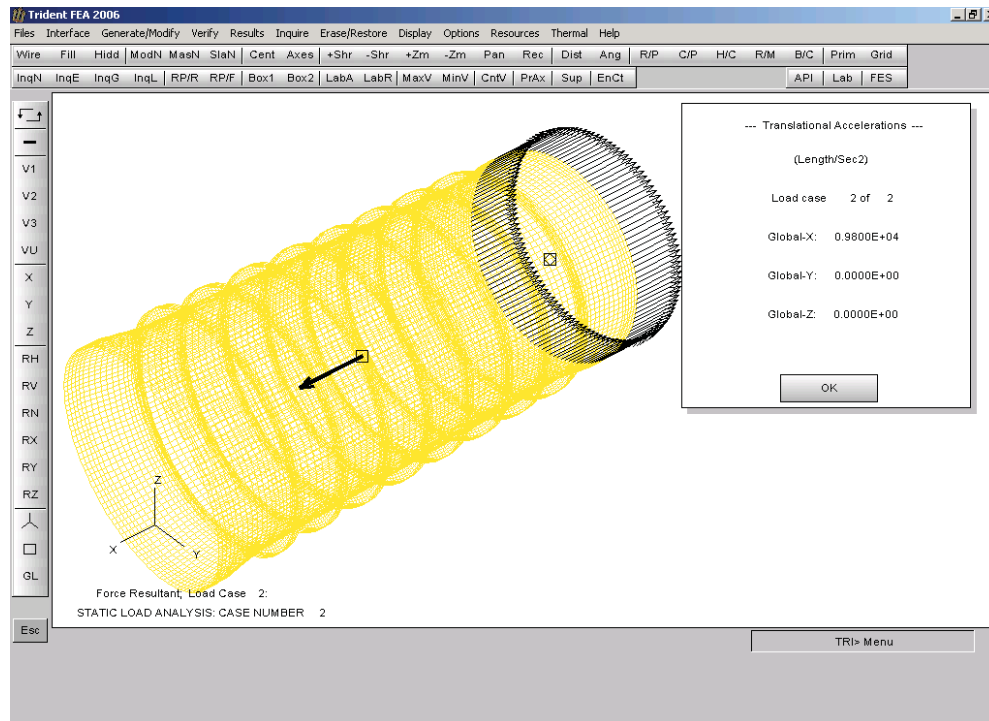
Figure 3.74: Load Case Representing Self-Weight of Cylinder and Endcap Submerged in Oil.
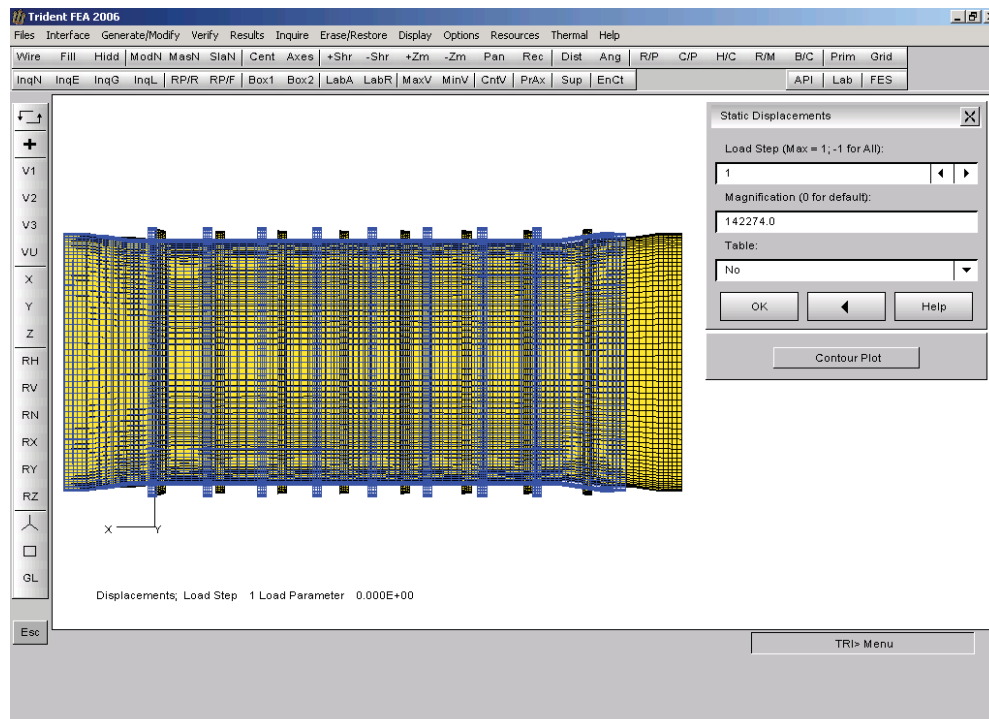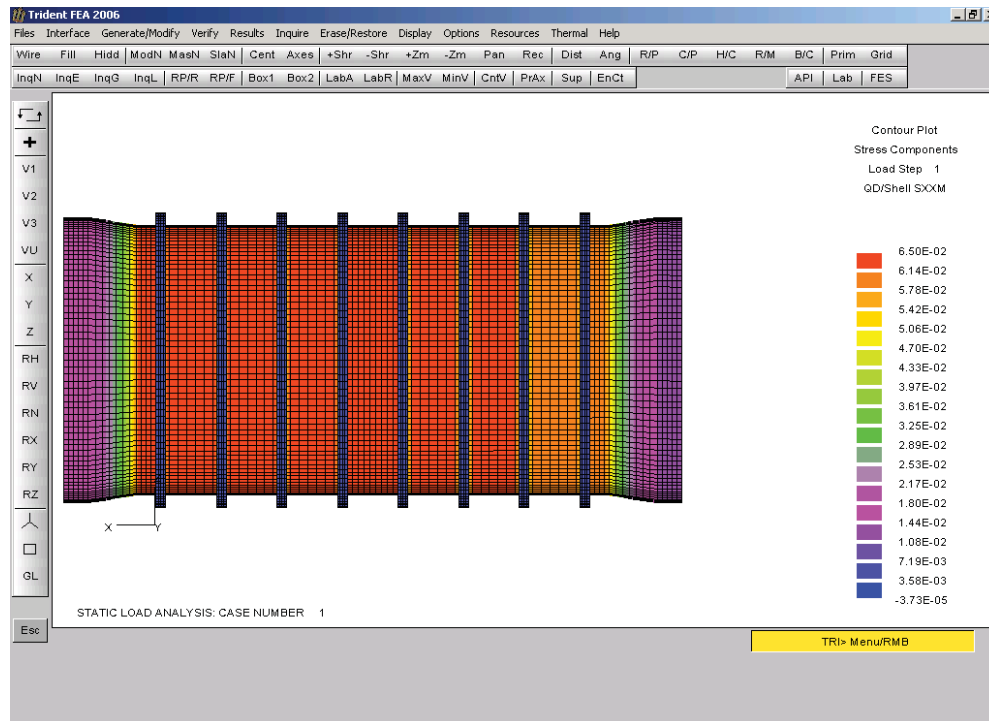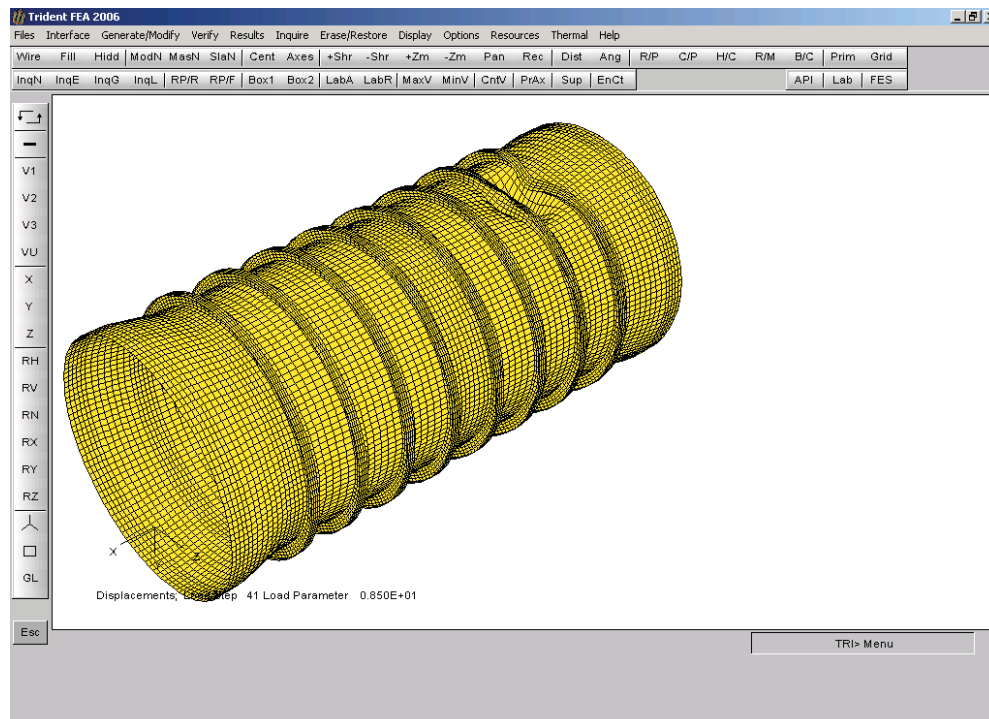

Figure 3.75: Deformation of Cylinder Caused by Self-Weight.

Figure 3.76: Axial Stress in Cylinder Caused by Self-Weight.

Figure 3.77: Final Deformed Shape of Cylinder Predicted with Influence of Self-Weight.

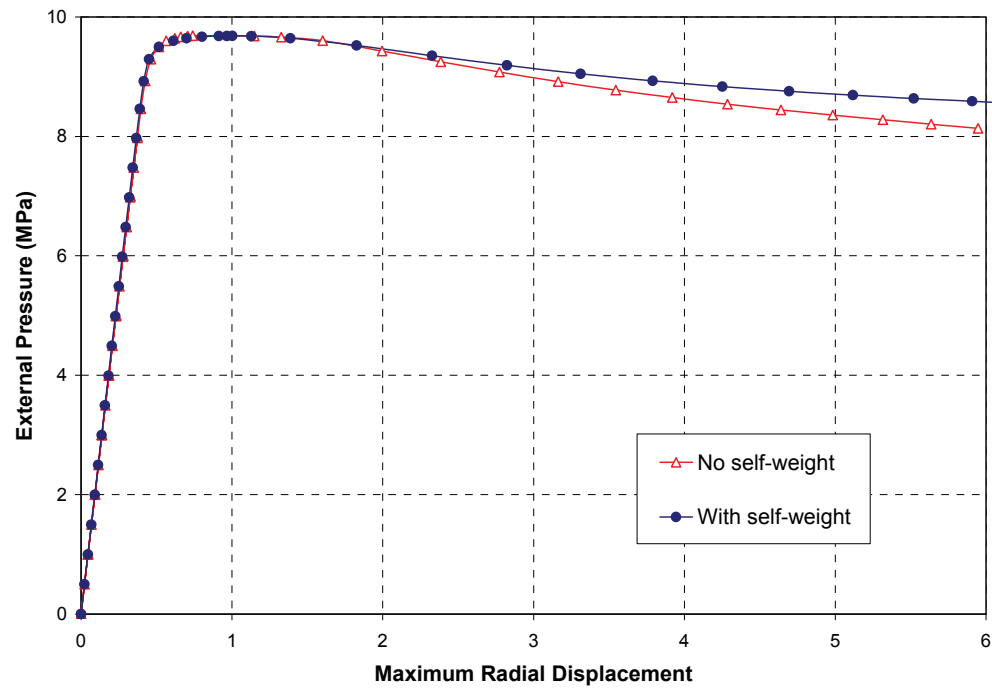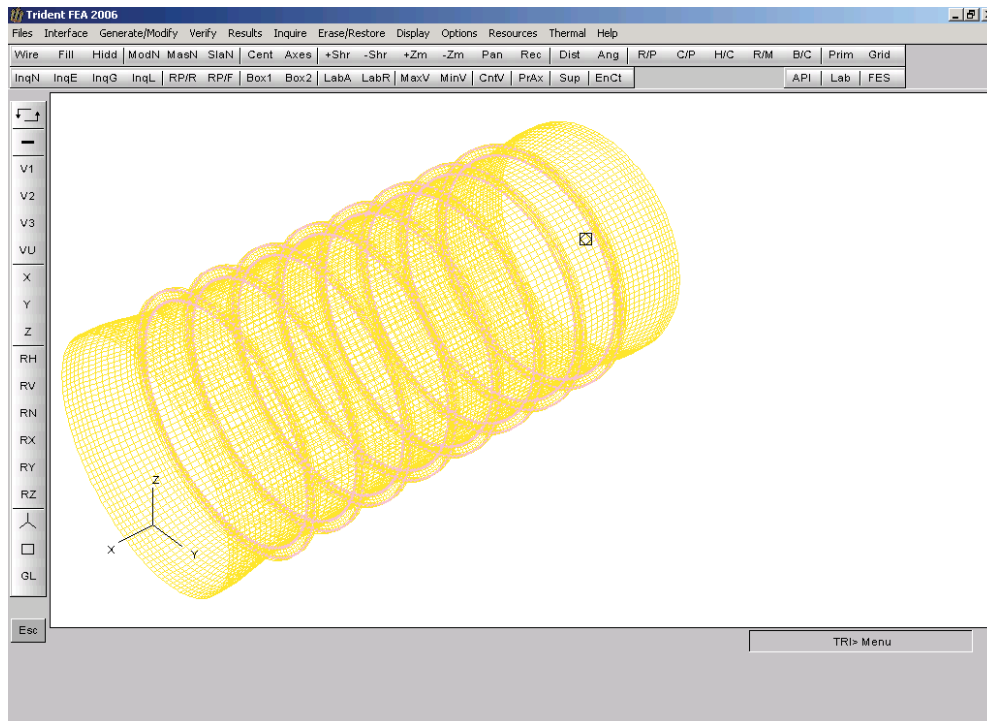**Figure 3.78: Comparison of Predicted Pressure-Maximum Radial Displacement Curves with and without Influence of the Self-Weight.**

Figure 3.79: Finite Element Model for the Long Cylinder without Material Overlap at the Web-Cylinder Wall and Web-Flange Intersections.
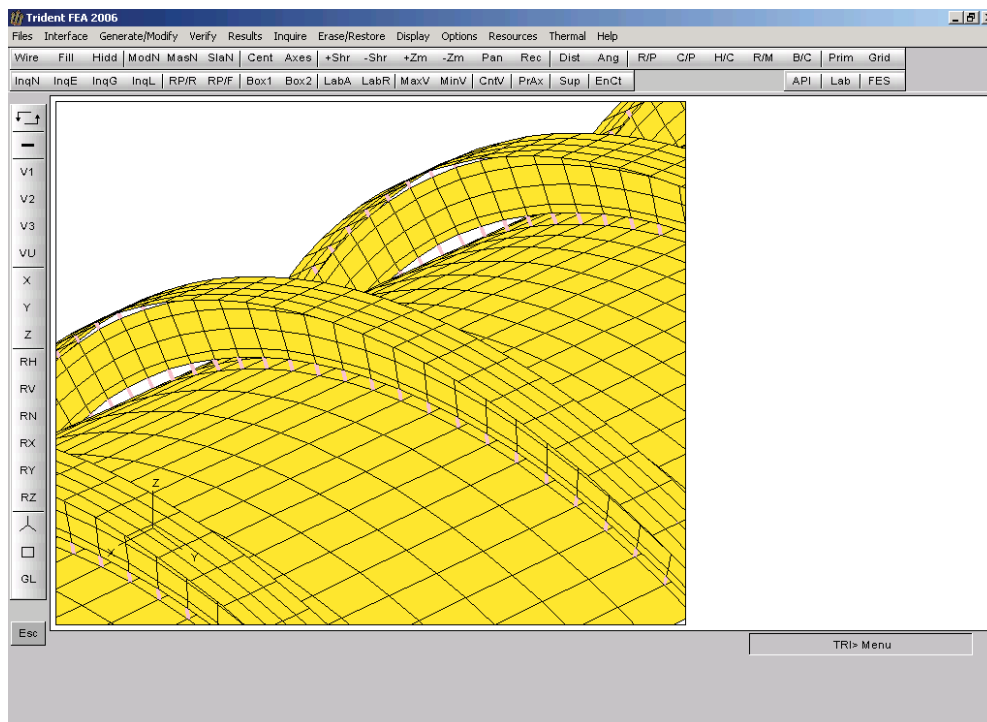
Figure 3.80: Details of the Finite Element Model without Material Overlap at the Web-Cylinder Wall and Web-Flange Intersections.
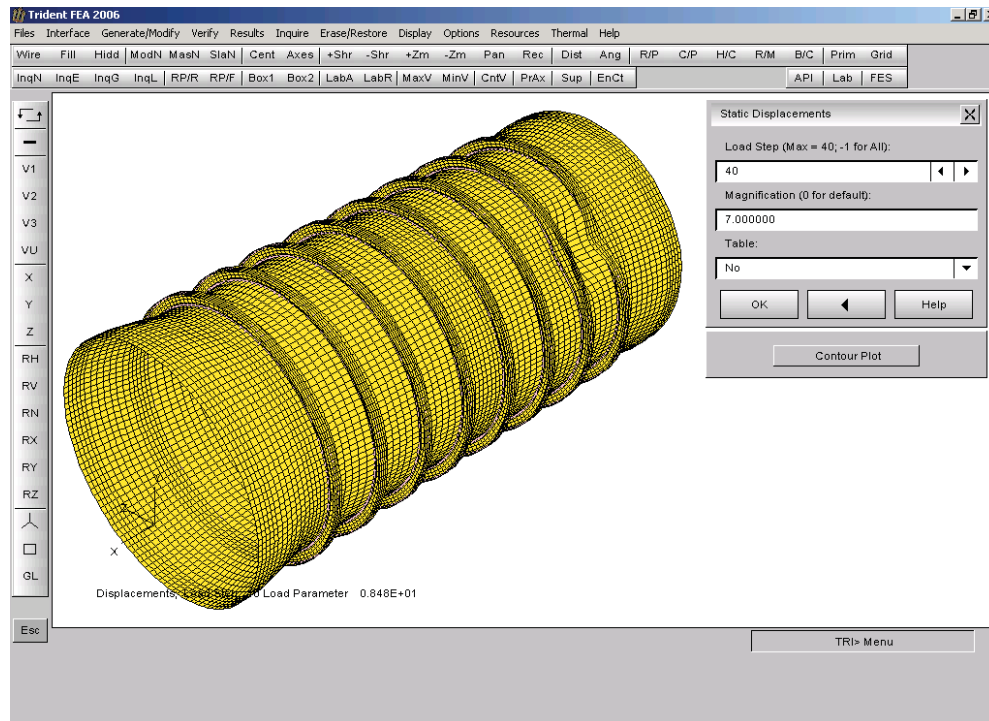
Figure 3.81: Final Deformed Shape Predicted Using the Model without Material Overlap at Shell Intersections (3D View).
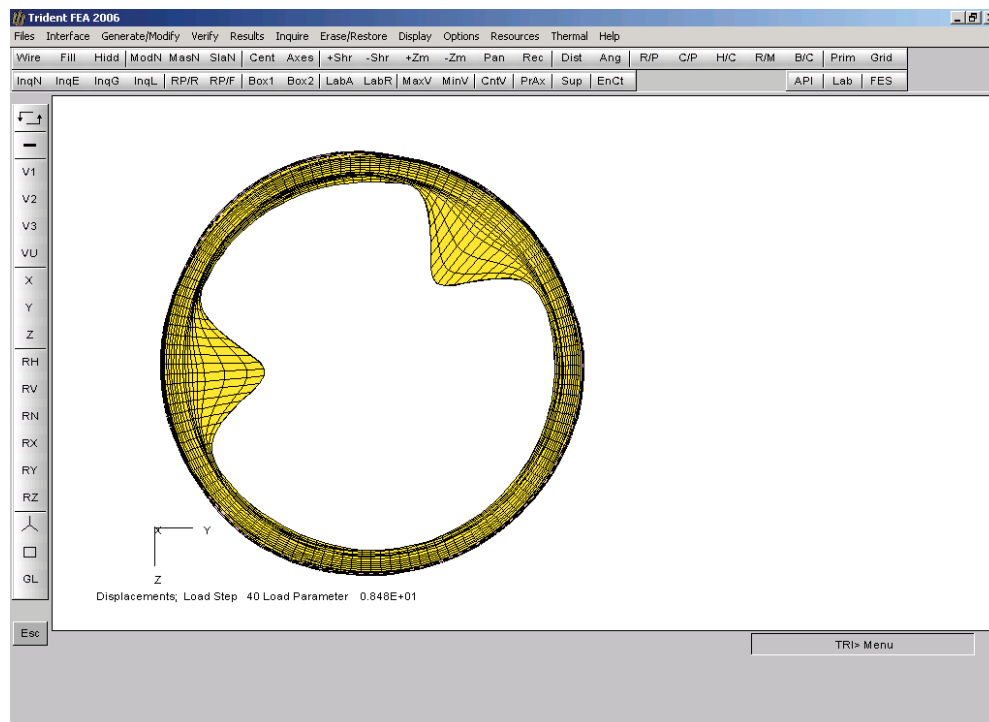
Figure 3.82: Final Deformed Shape Predicted Using the Model without Material Overlap at Shell Intersections (End View).
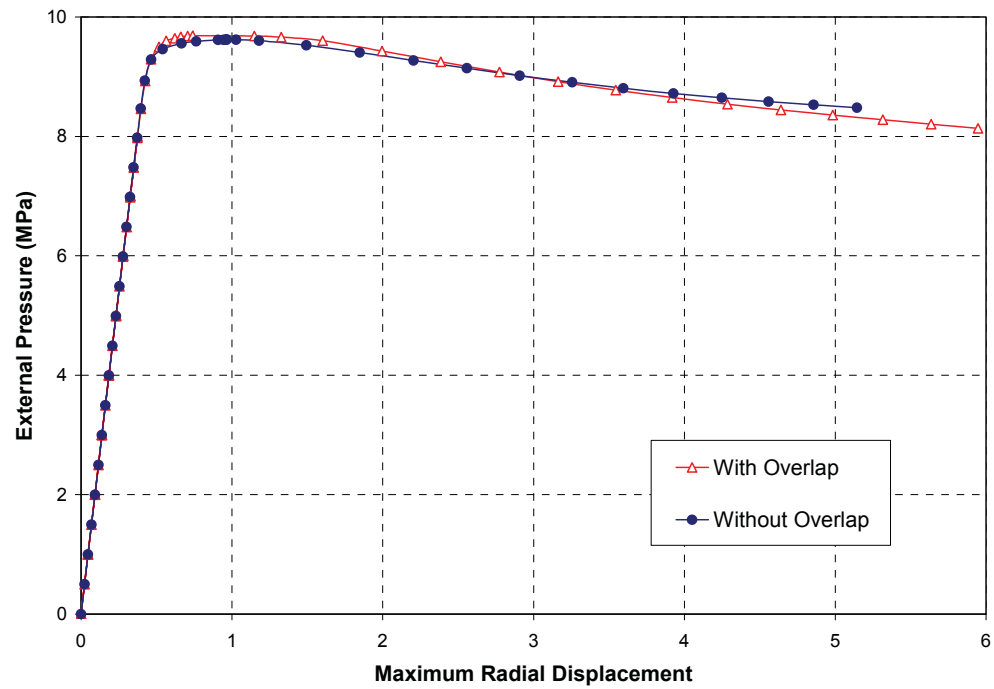
Figure 3.83: Comparison of Pressure-Maximum Radial Displacement Curves Predicted Using Models with and without Material Overlap.
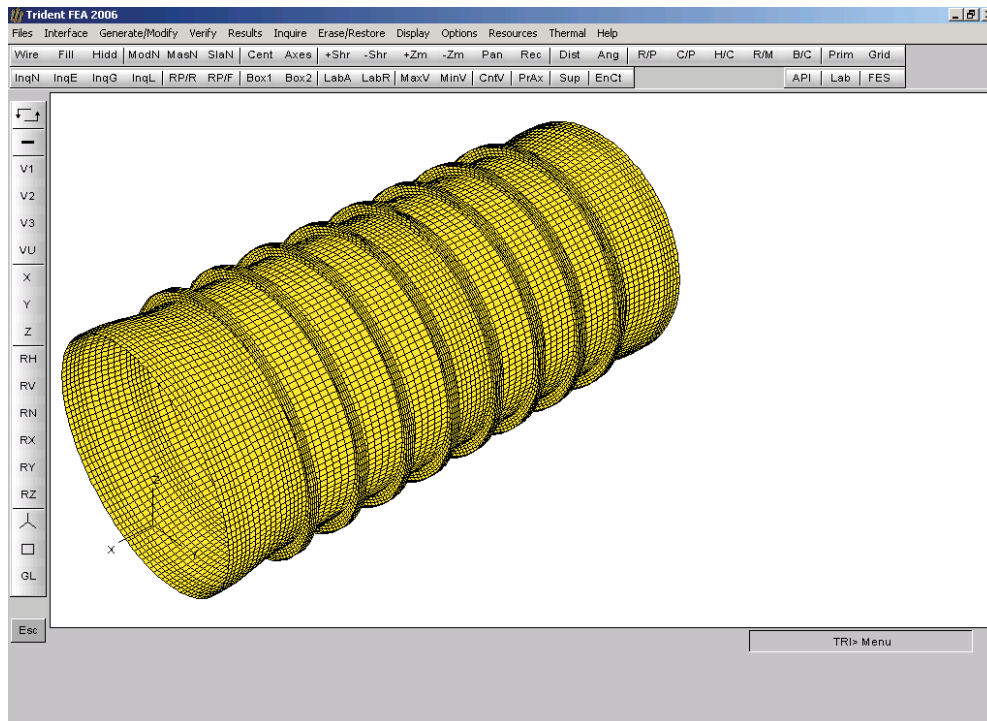
Figure 3.84: Finite Element Model of Long Cylinder with Simulated Flange Corrosions L510-No2.
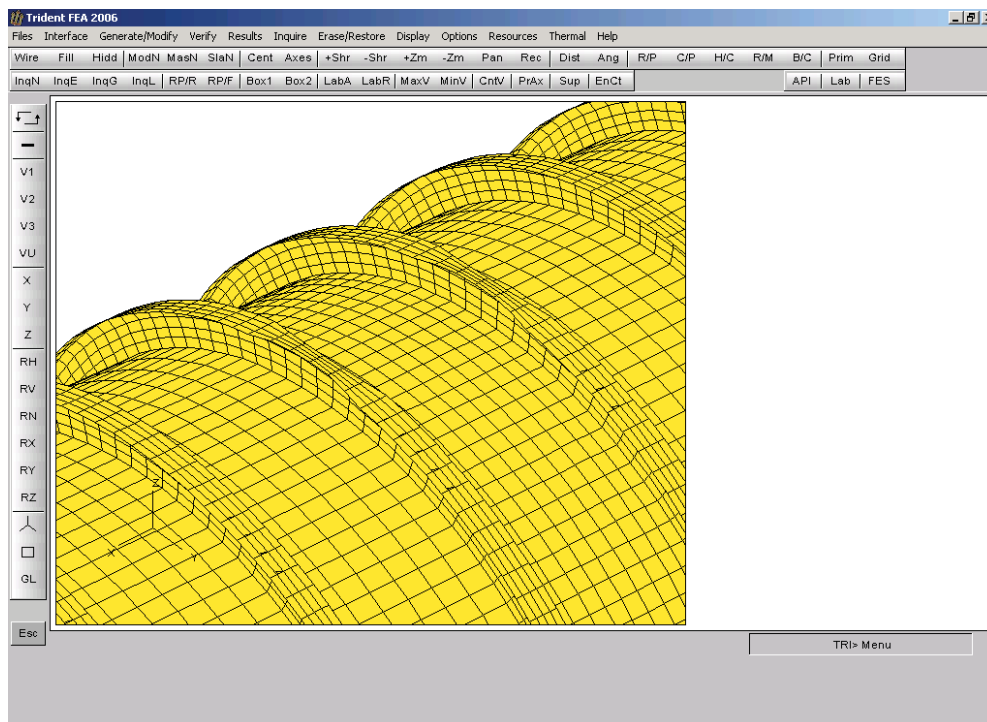
Figure 3.85: Details of Finite Element Model of Long Cylinder with Simulated Flange Corrosions.
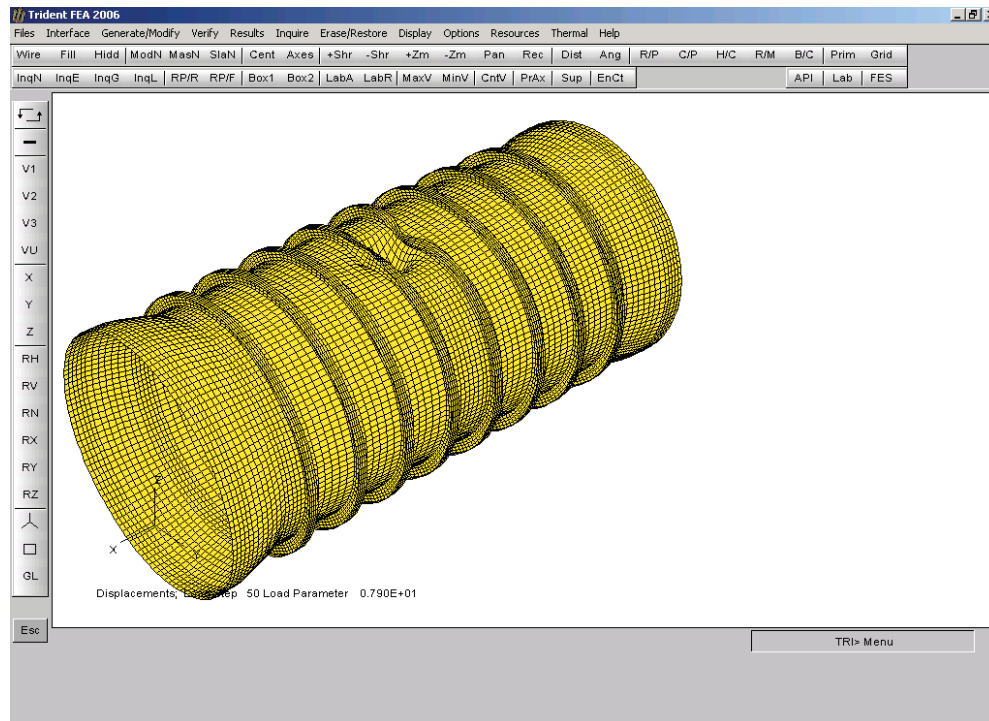
Figure 3.86: Final Deformed Shape of Long Cylinder with Simulated Flange Corrosions.
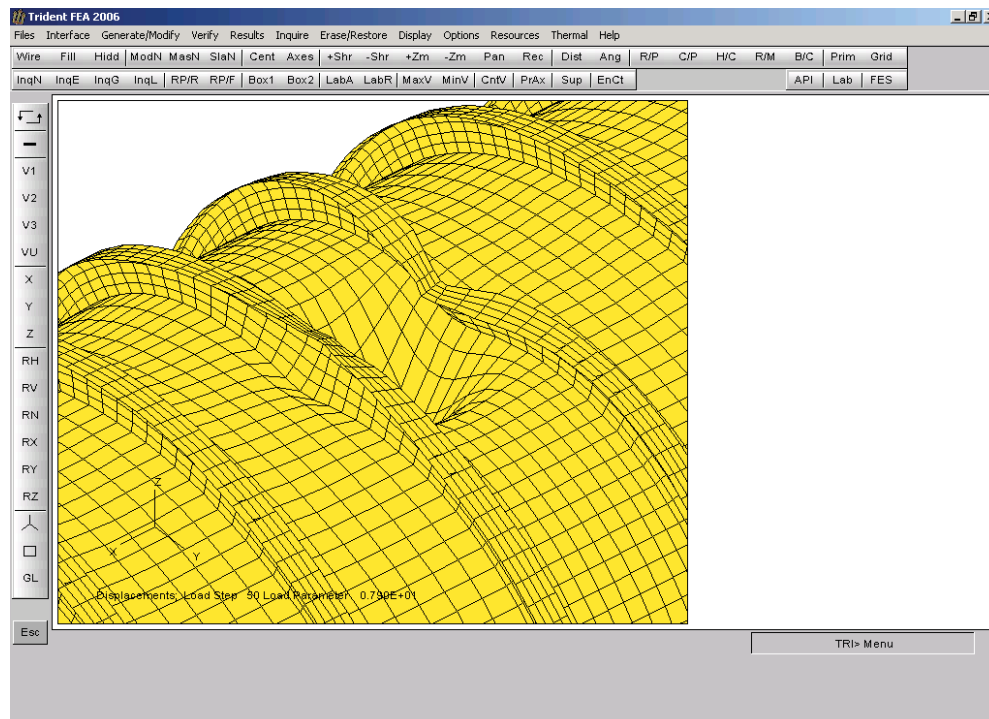
Figure 3.87: Details of Final Deformed Shape of Long Cylinder with Simulated Flange Corrosions.
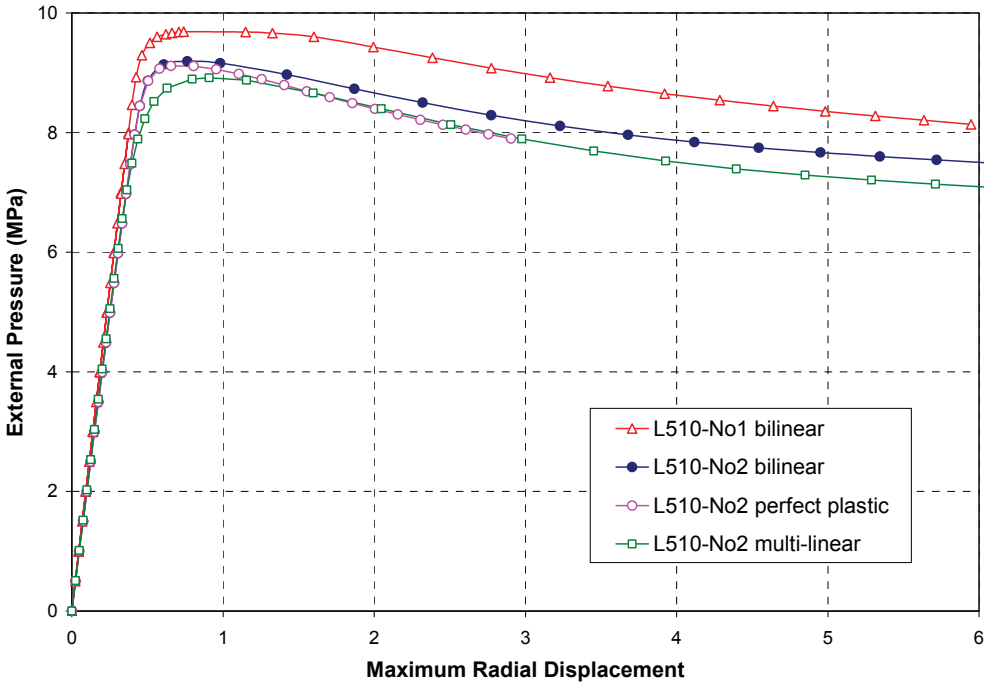
Figure 3.88: Comparison of Pressure-Radial Displacement Curves for Cylinder with Simulated Flange Corrosions Predicted Using Different Material Models.
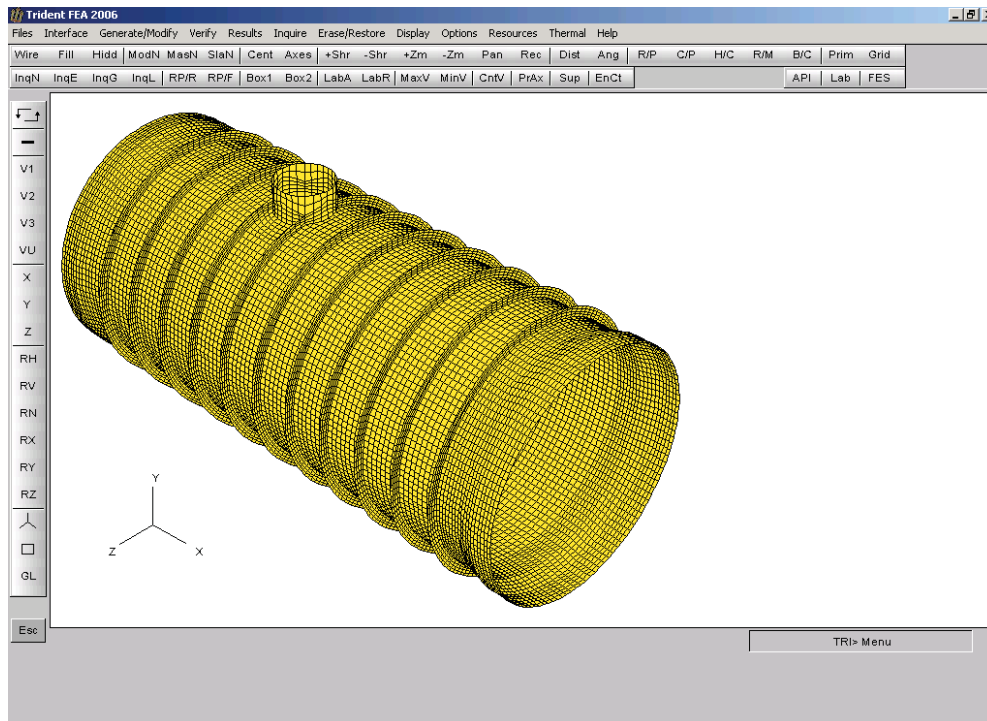
Figure 3.89: Finite Element Model of Cylinder with Penetrations (Top View).
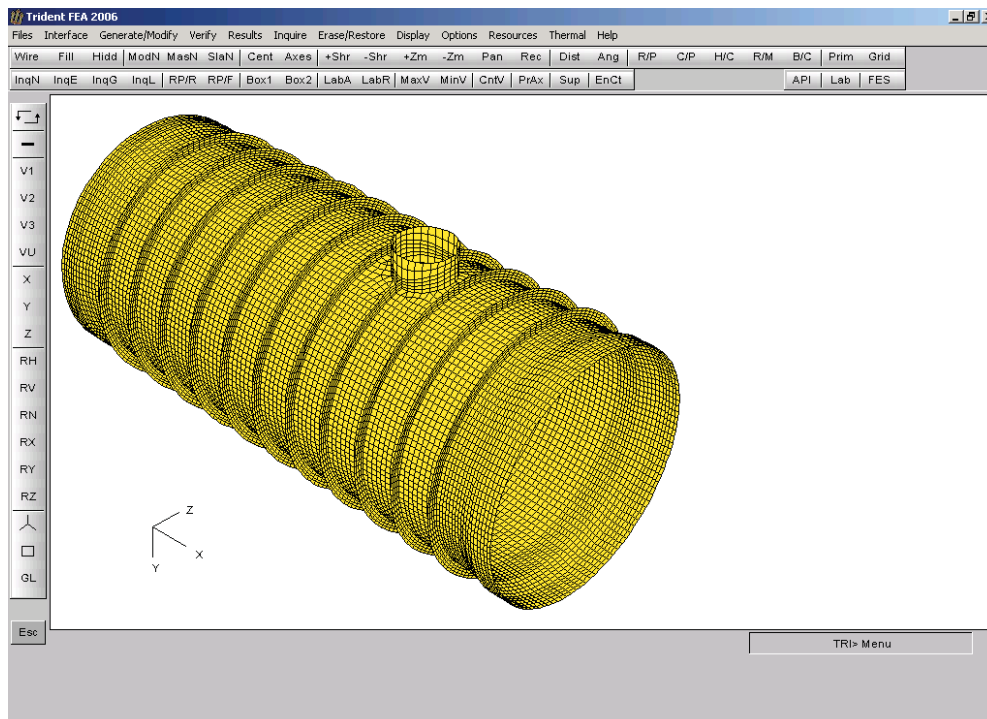
Figure 3.90: Finite Element Model of Cylinder with Penetrations (Bottom View).
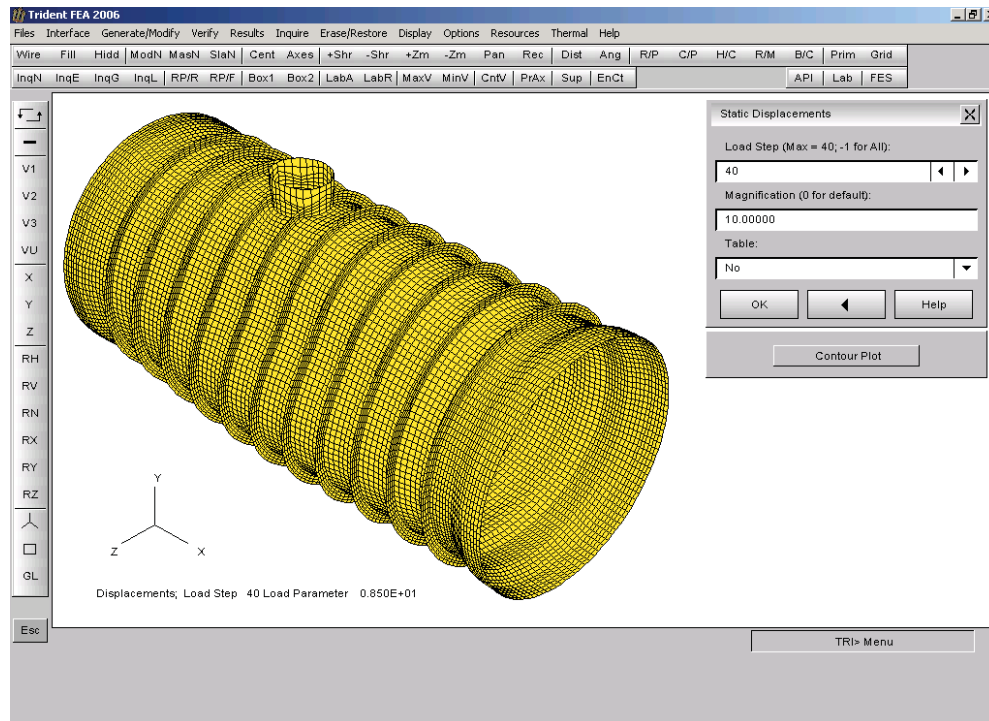
Figure 3.91: Final Deformed Shape of Penetration Cylinder without Measured Out-Of-Circularities (Top View).
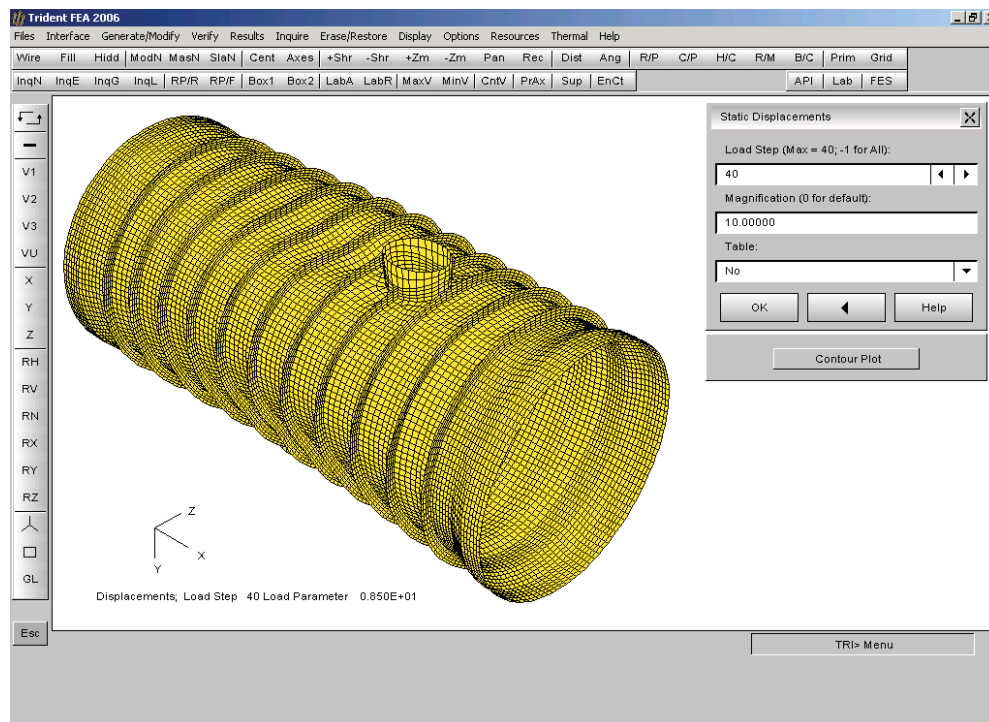
Figure 3.92: Final Deformed Shape of Penetration Cylinder without Measured Out-Of-Circularities (Bottom View).
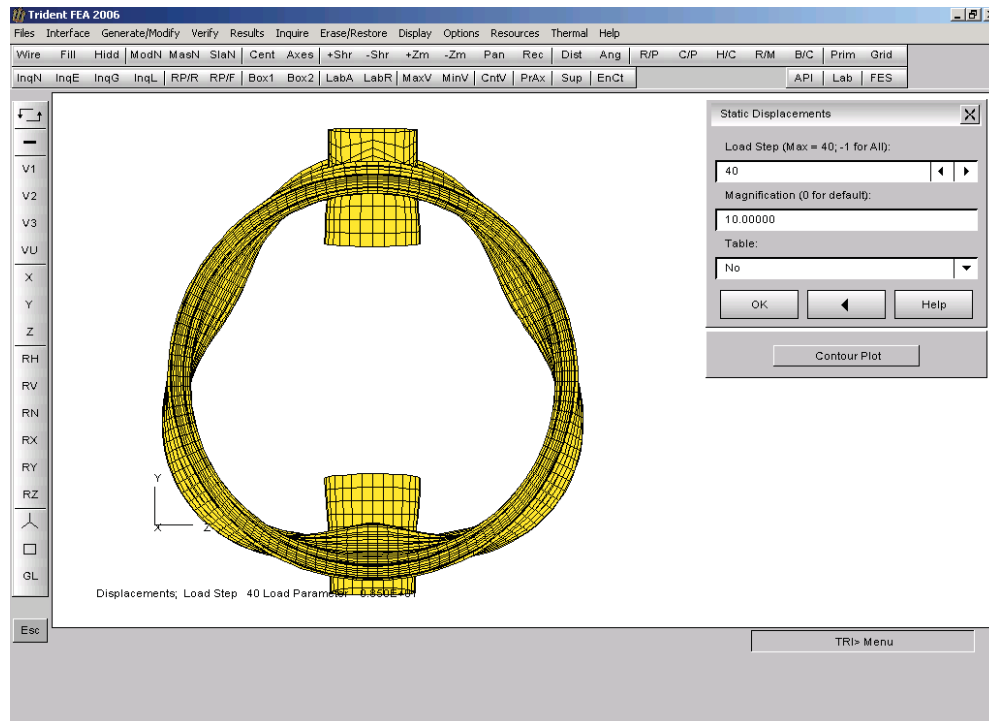
Figure 3.93: Final Deformed Shape of Penetration Cylinder without Measured Out-Of-Circularities (End View).
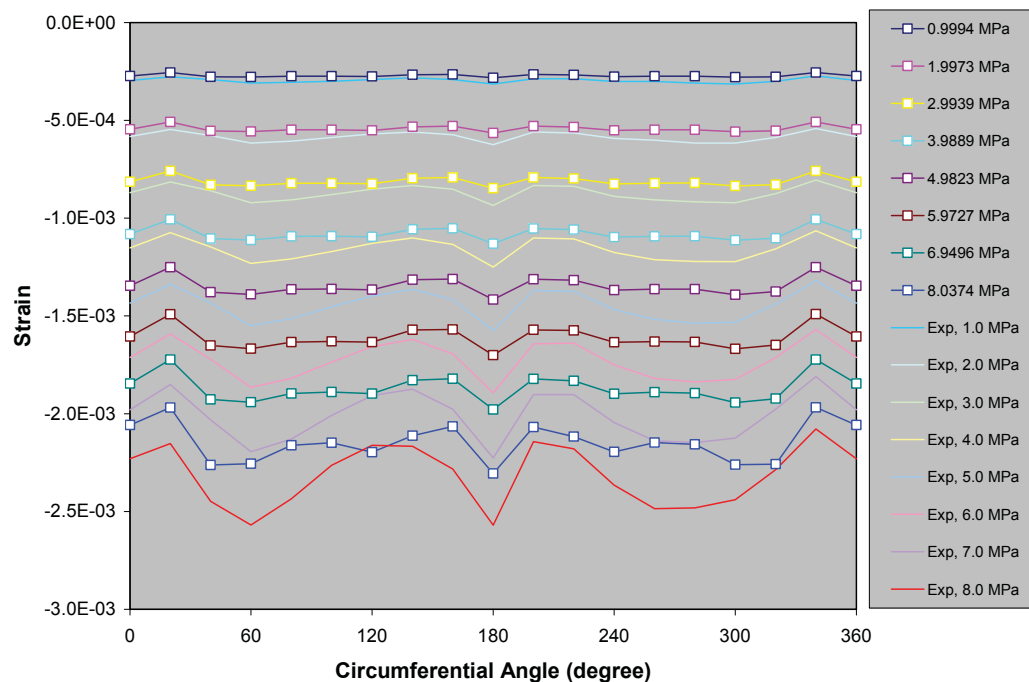
Figure 3.94: Comparison of Predicted (with Symbols) and Measured Profiles of the Circumferential Strain on Central Stiffener #6 without Measured OOC.

Figure 3.95: Comparison of Predicted (with Symbols) and Measured Histories of Circum-ferential Strains on Outside of Stiffener #6 without Measured OOC.

Figure 3.96: Comparison of Predicted (with Symbols) and Measured Histories of Strains on Inside Wall of Penetration A without Measured OOC.

Figure 3.97: Strain Gauge Locations on the Experimental Cylinder Model with Penetrations (Reproduced from Reference [1]).

Figure 3.98: Final Deformed Shape of Penetration Cylinder with 100% Measured Out-Of-Circularities Based on Angle Definition I (Top View).

Figure 3.99: Final Deformed Shape of Penetration Cylinder with 100% Measured Out-Of-Circularities Based on Angle Definition I (Bottom View).

Figure 3.100: Final Deformed Shape of Penetration Cylinder with 100% Measured Out-Of-Circularities Based on Angle Definition I (End View).

Figure 3.101: Comparison of Predicted (with Symbols) and Measured Profiles of the Circumferential Strain on Central Stiffener #6 with 100% Measured Out-Of-Circularities Based on Angle Definition I.

Figure 3.102: Comparison of Predicted (with Symbols) and Measured Histories of Circumferential Strains on Outside of Stiffener #6 with 100% Measured Out-Of-Circularities Based on Angle Definition I.

Figure 3.103: Comparison of Predicted (with Symbols) and Measured Histories of Strains on Inside Wall of Penetration A with 100% Measured Out-Of-Circularities Based on Angle Definition I.
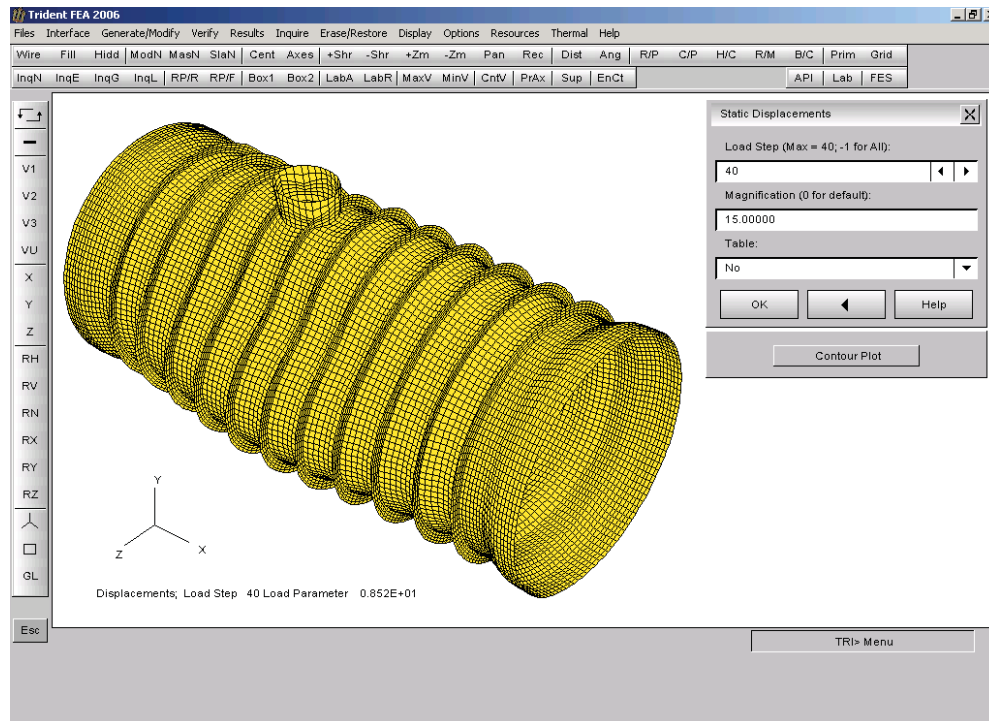
Figure 3.104: Final Deformed Shape of Penetration Cylinder with 100% Measured Out-Of-Circularities Based on Angle Definition II (Top View).
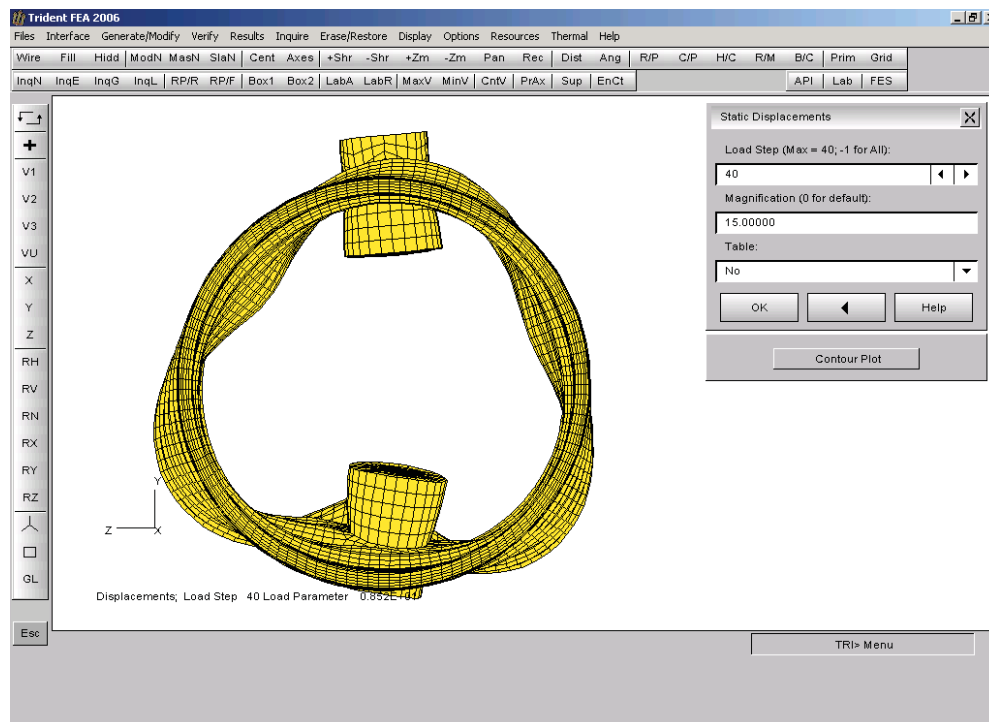
Figure 3.105: Final Deformed Shape of Penetration Cylinder with 100% Measured Out-Of-Circularities Based on Angle Definition II (End View).
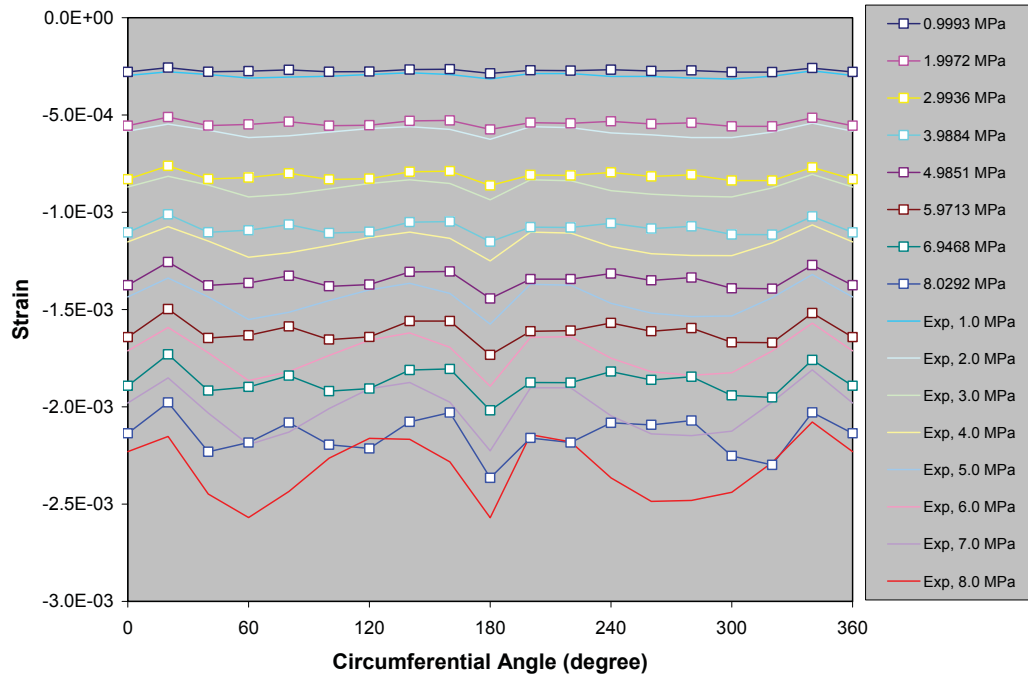
Figure 3.106: Comparison of Predicted (with Symbols) and Measured Profiles of the Circumferential Strain on Central Stiffener #6 with 100% Measured Out-Of-Circularities Based on Angle Definition II.
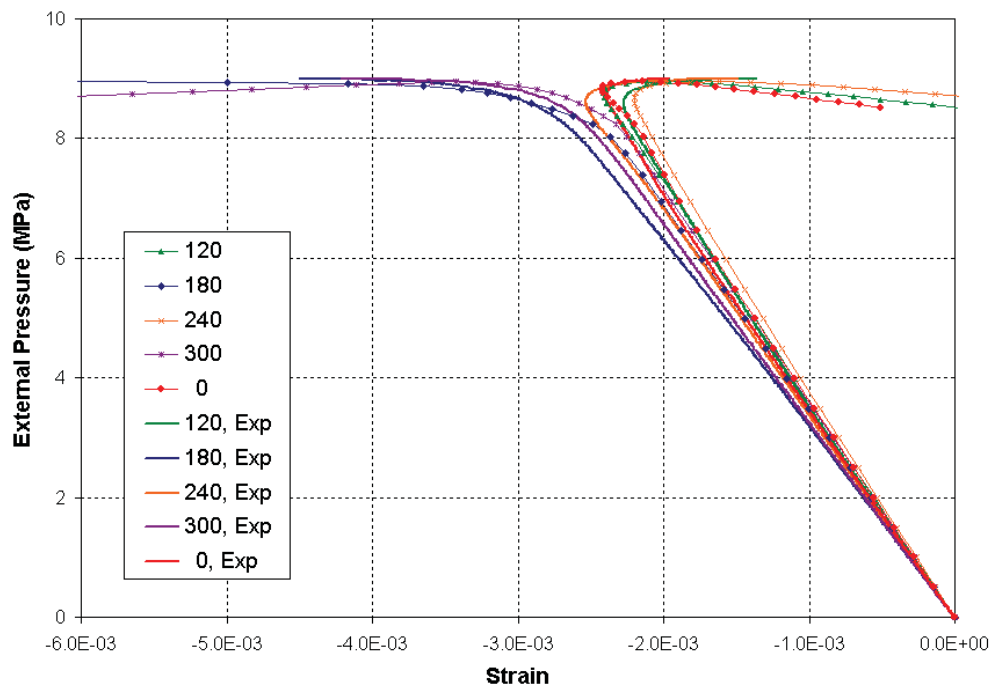
Figure 3.107: Comparison of Predicted (with Symbols) and Measured Histories of Circumferential Strains on Outside of Stiffener #6 with 100% Measured Out-Of-Circularities Based on Angle Definition II.
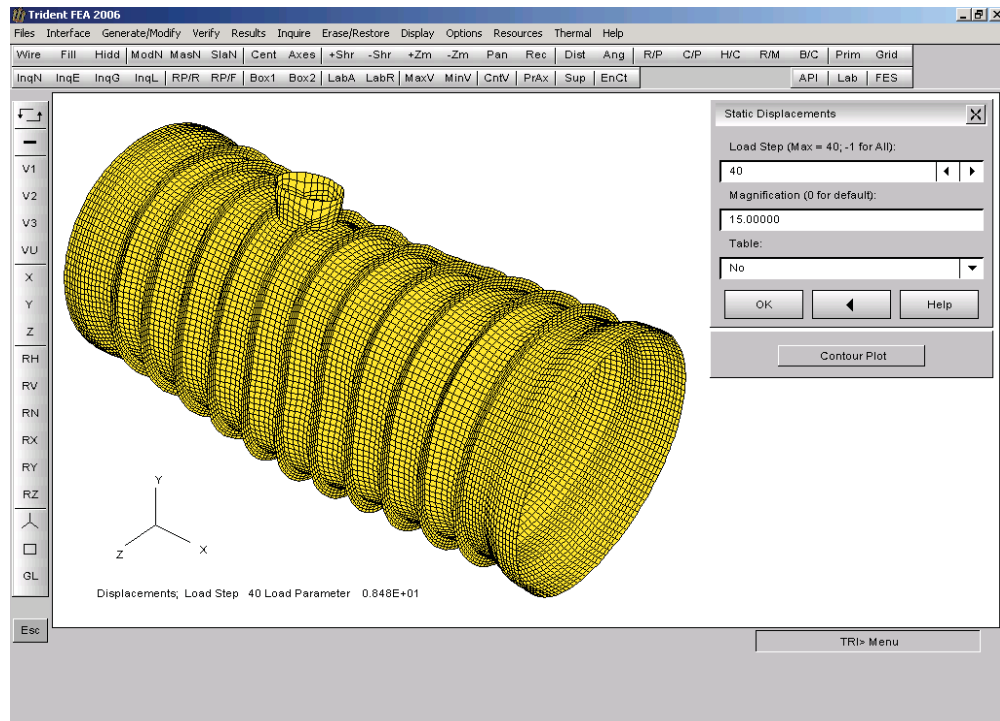
Figure 3.108: Final Deformed Shape of Penetration Cylinder with 200% Measured Out-Of-Circularities (Top View).
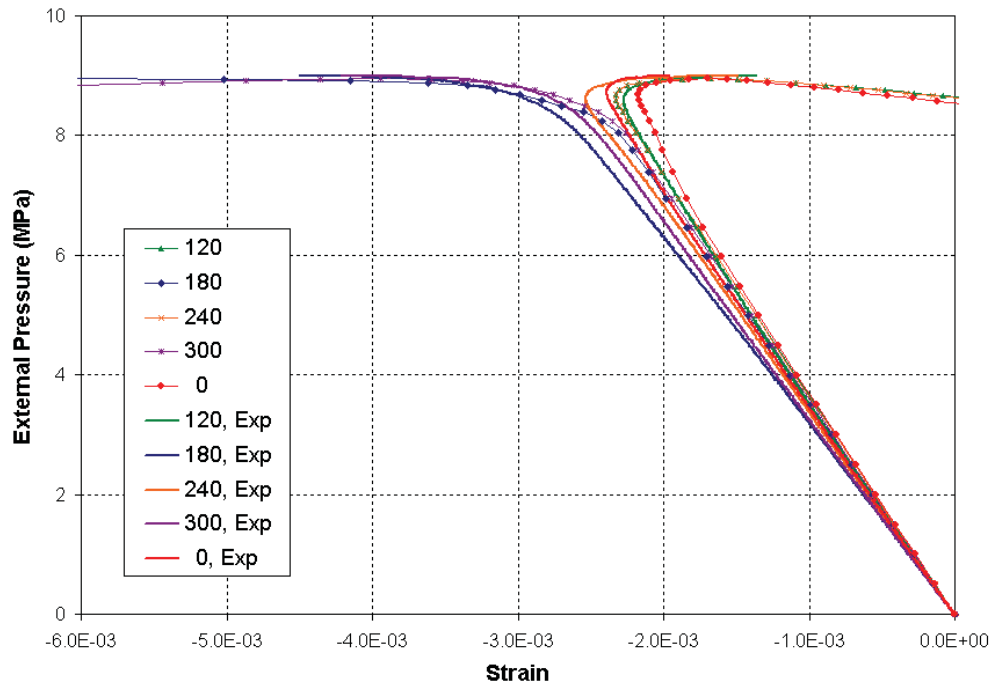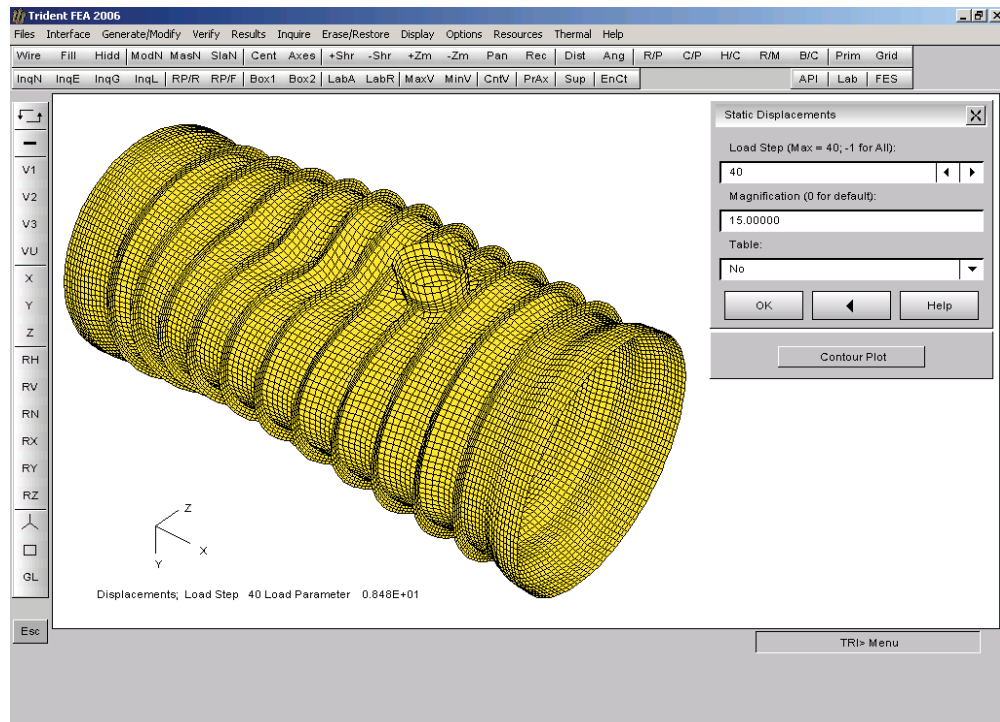

Figure 3.109: Final Deformed Shape of Penetration Cylinder with 200% Measured Out-Of-Circularities (Bottom View).
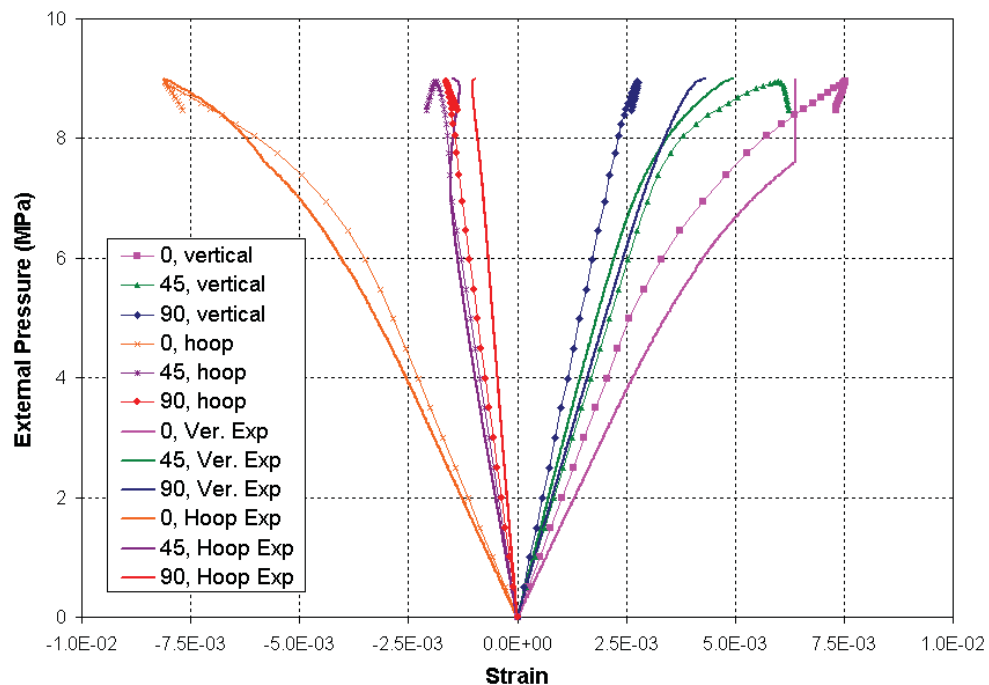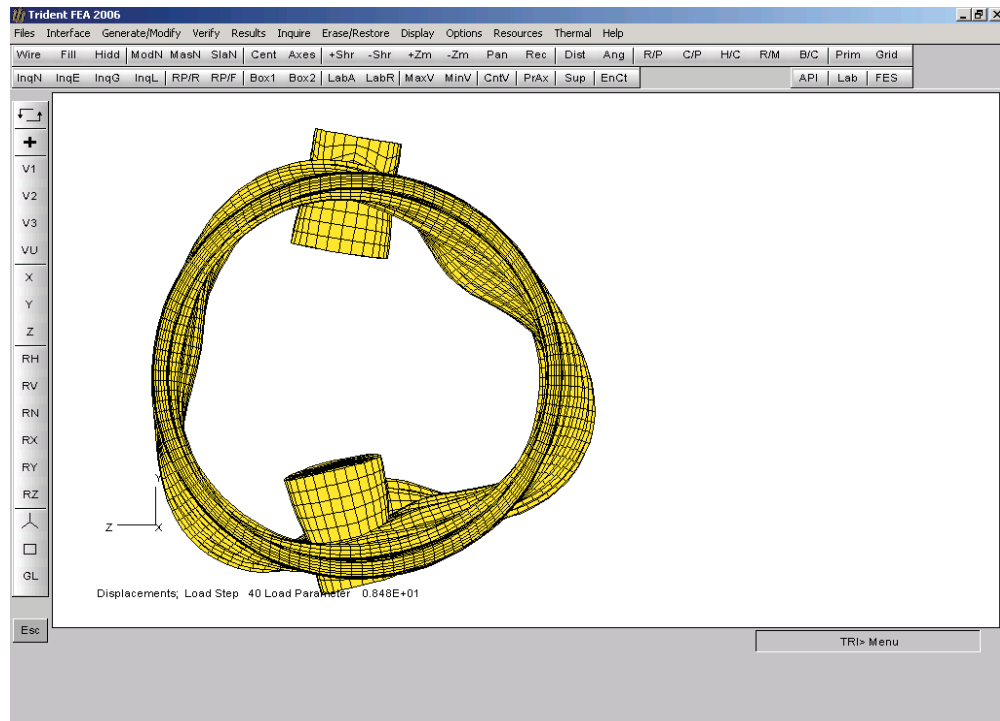
Figure 3.110: Final Deformed Shape of Penetration Cylinder with 200% Measured Out-Of-Circularities (End View).
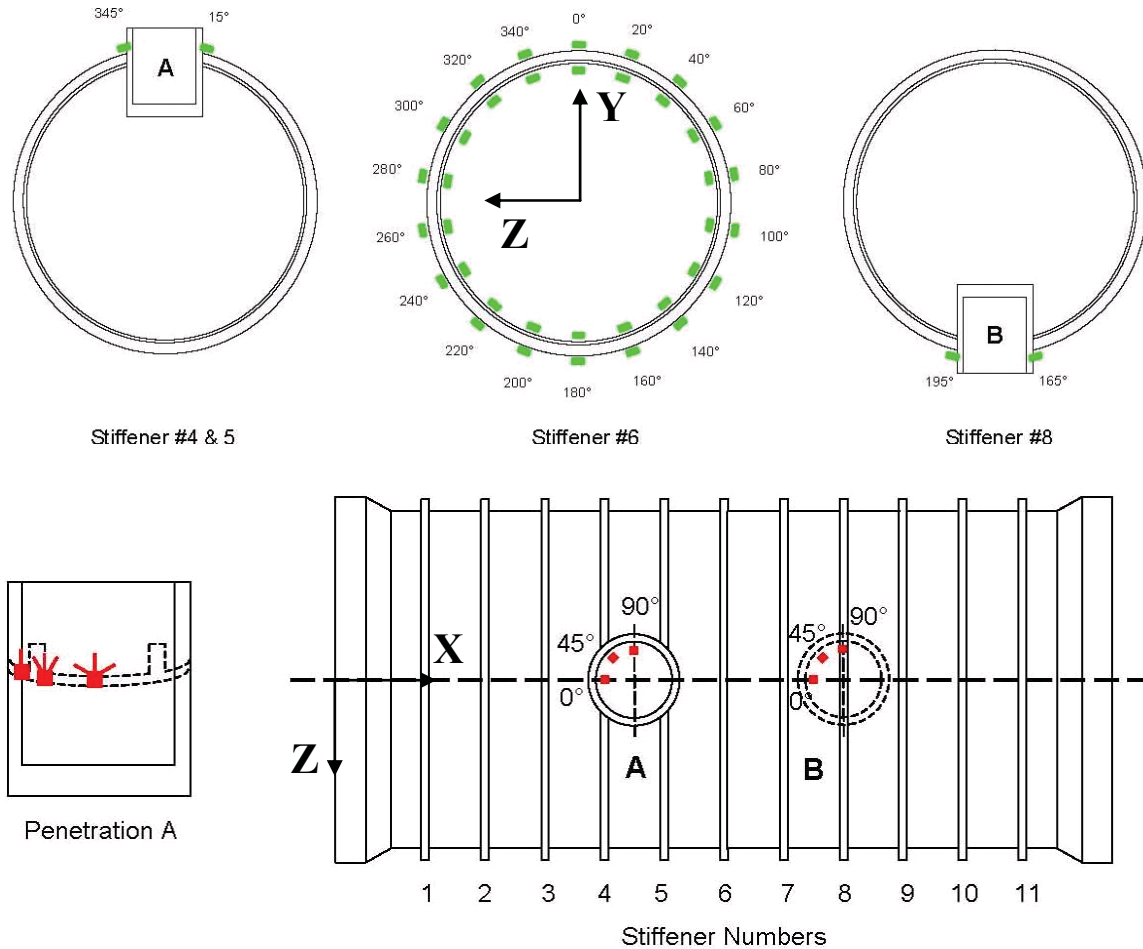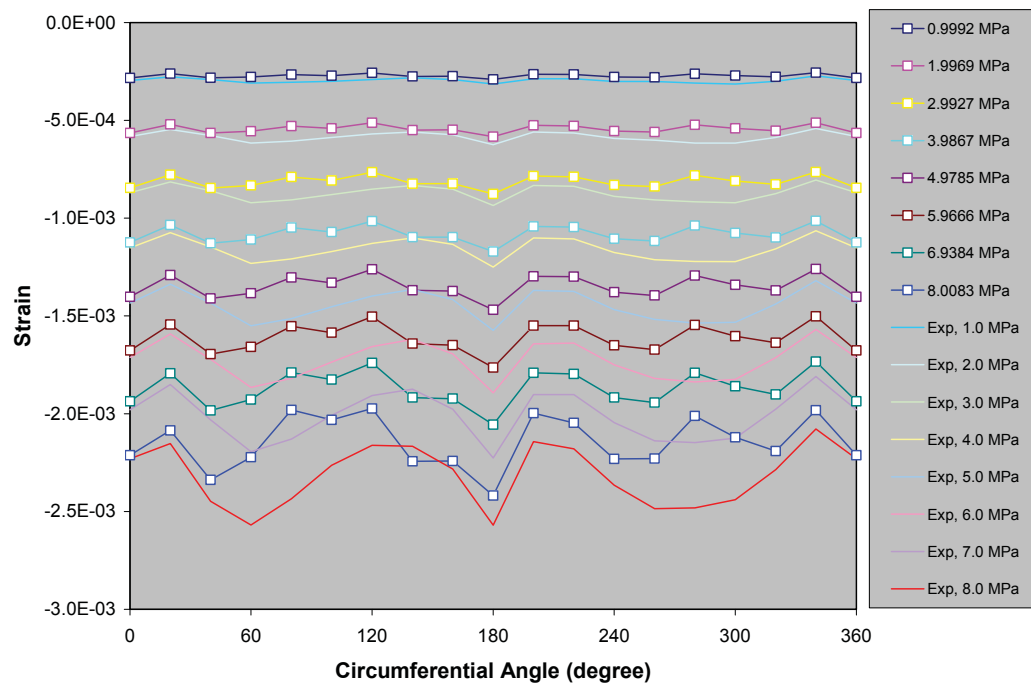

Figure 3.111: Comparison of Predicted (with Symbols) and Measured Profiles of the Circumferential Strain on Central Stiffener #6 with 200% Measured Out-Of-Circularities.
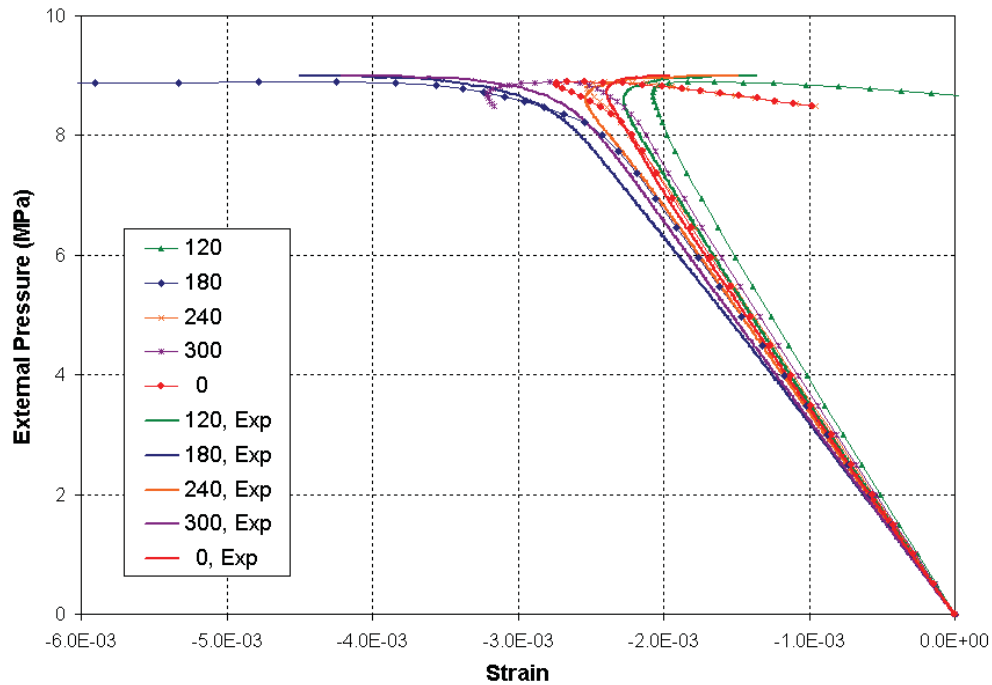
Figure 3.112: Comparison of Predicted (with Symbols) and Measured Histories of Circumferential Strains on Outside of Stiffener #6 with 200% Measured Out-Of-Circularities.
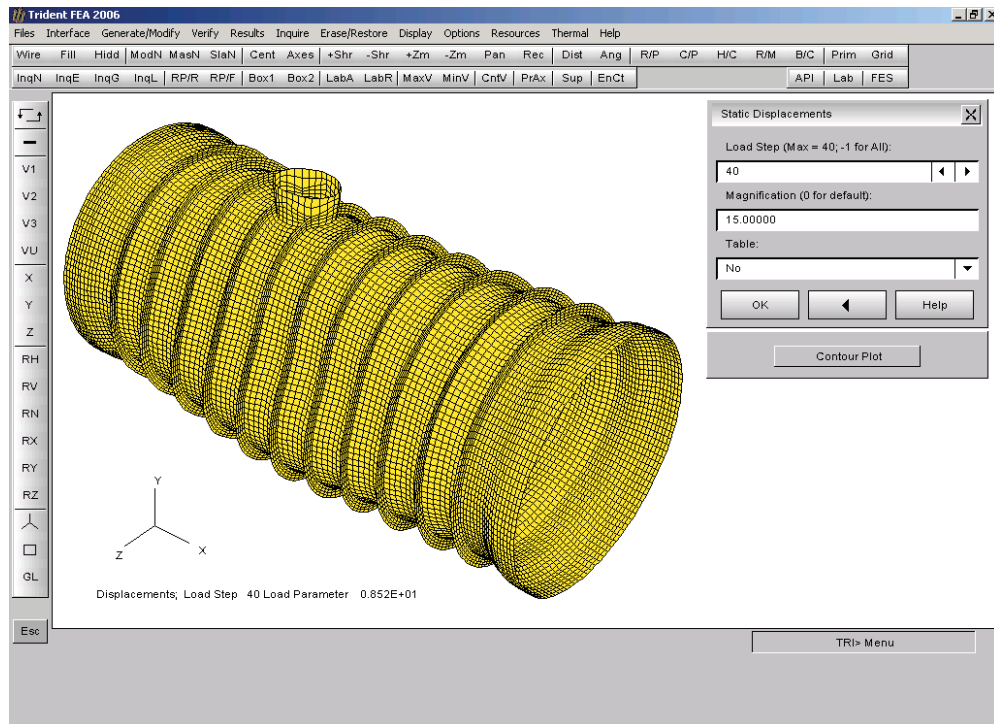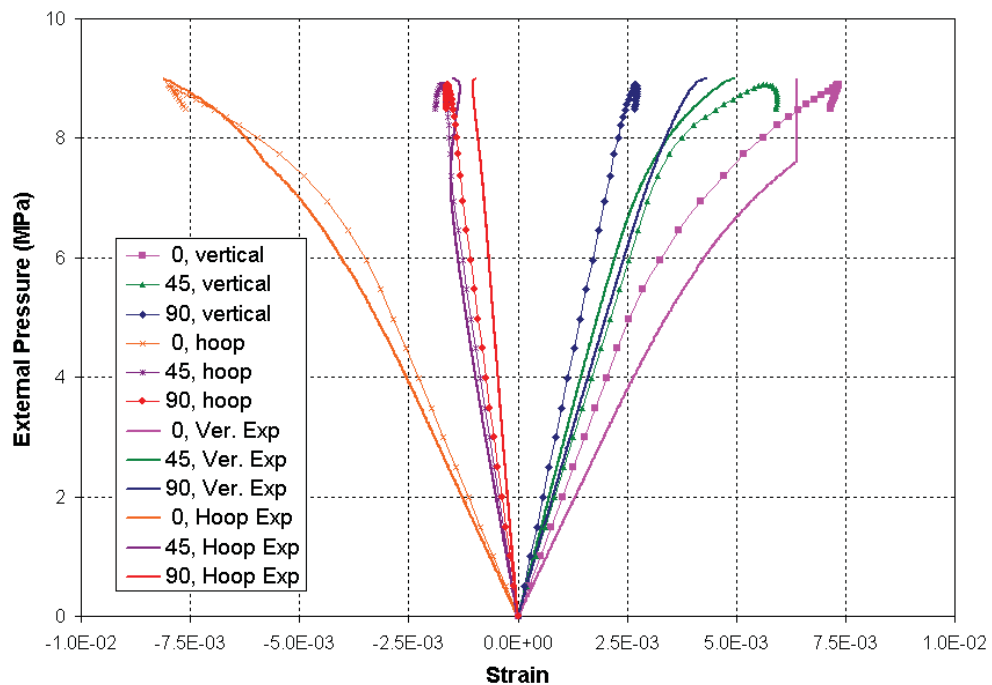

Figure 3.113: Comparison of Predicted (with Symbols) and Measured Histories of Strains on Inside Wall of Penetration A with 200% Measured Out-Of-Circularities.
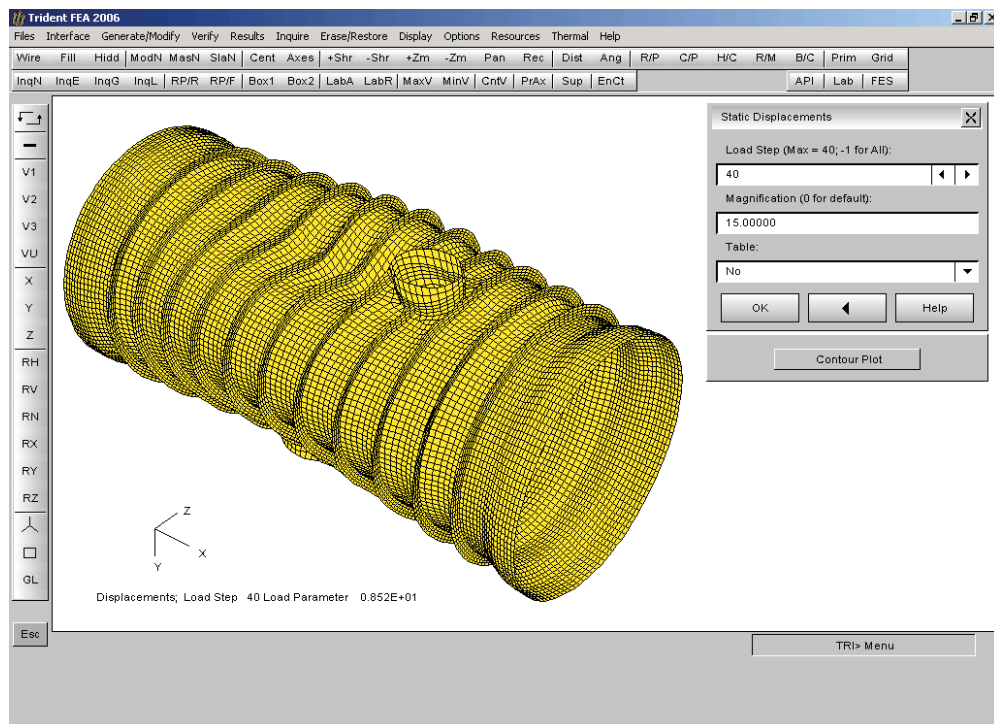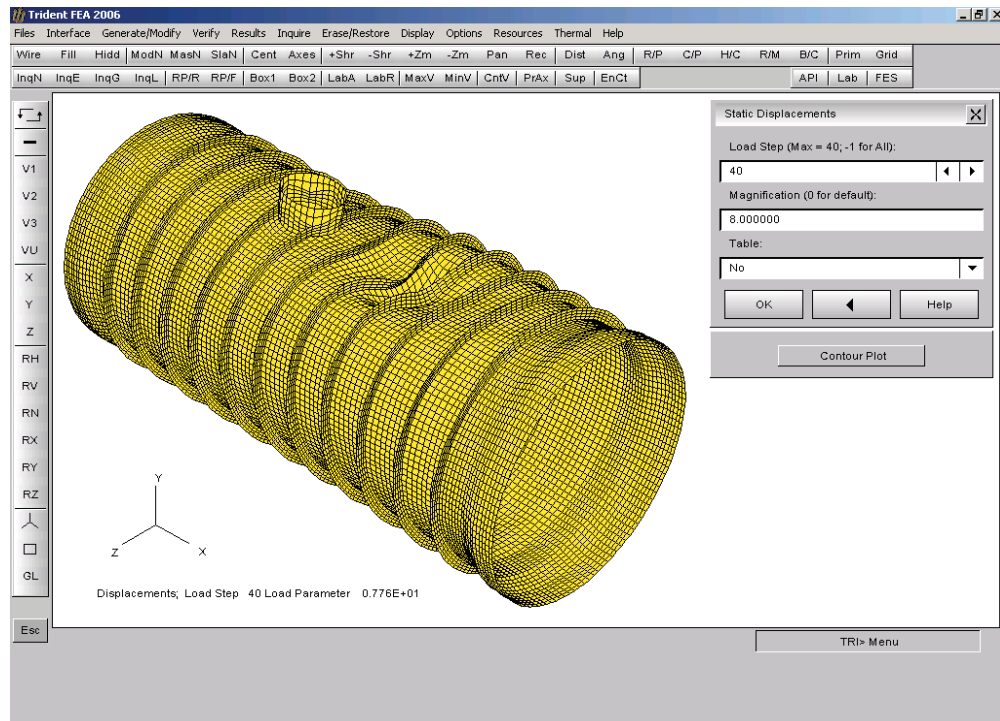
Figure 3.114: Final Deformed Shape of Penetration Cylinder with 500% Measured Out-Of-Circularities (Top View).
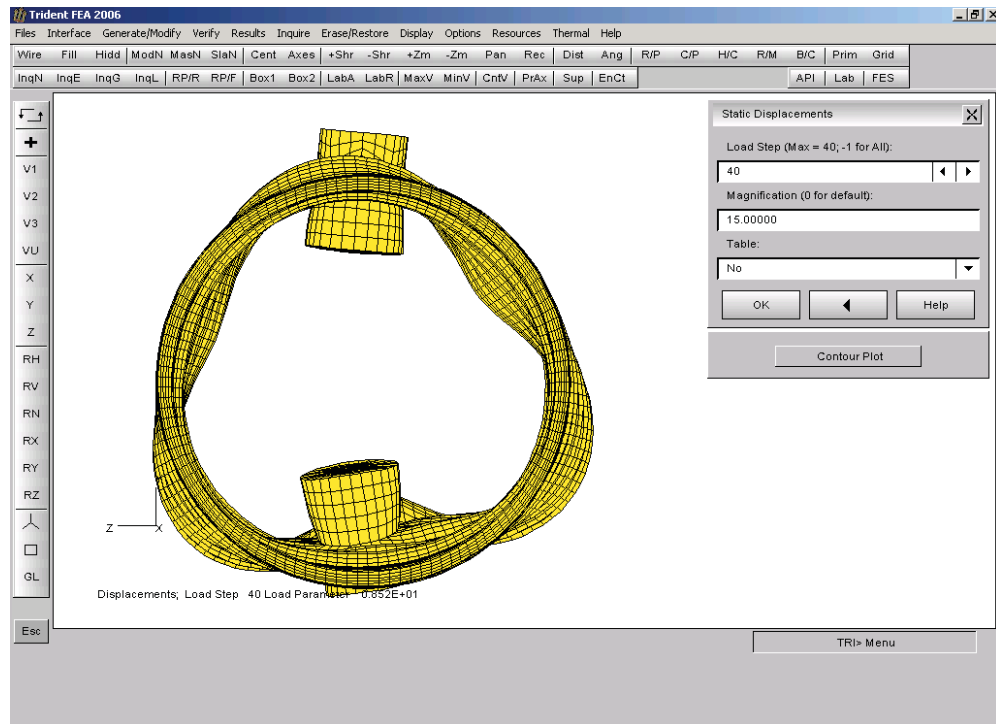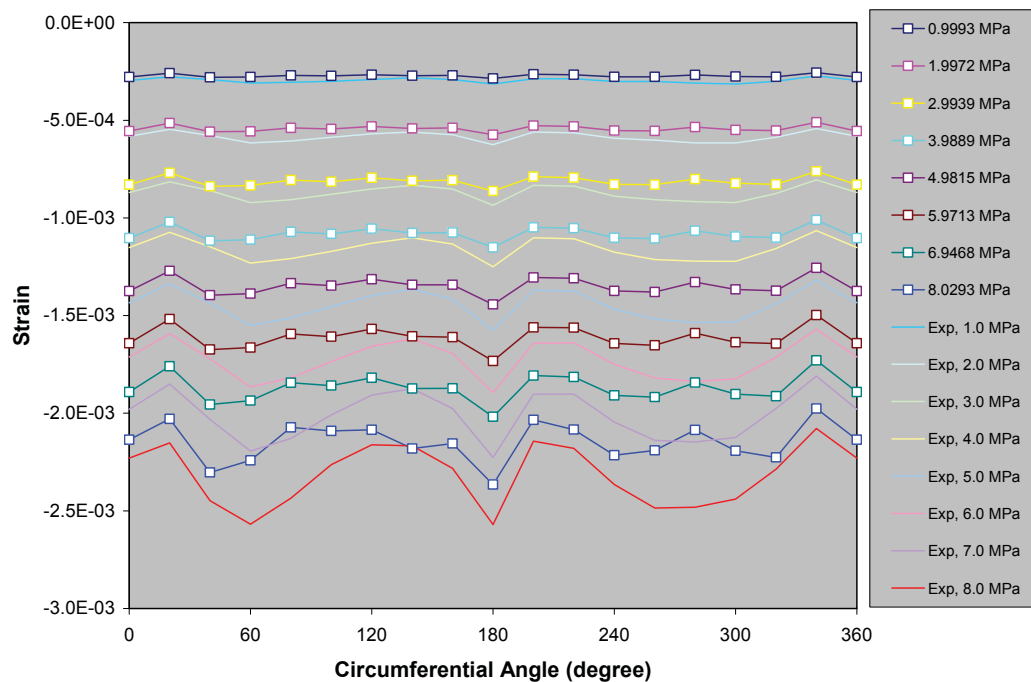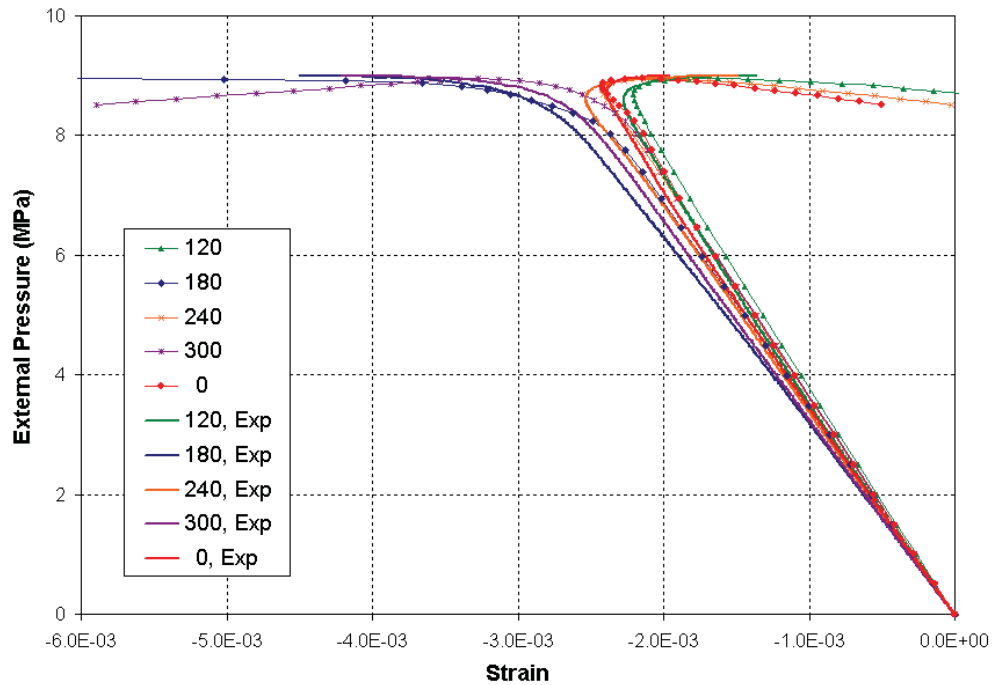

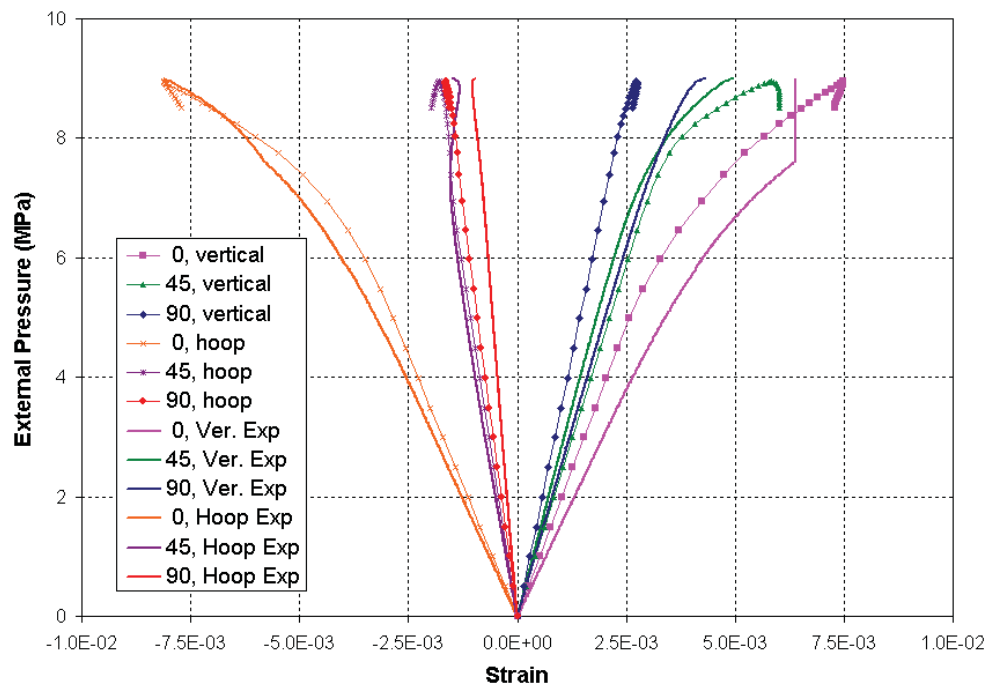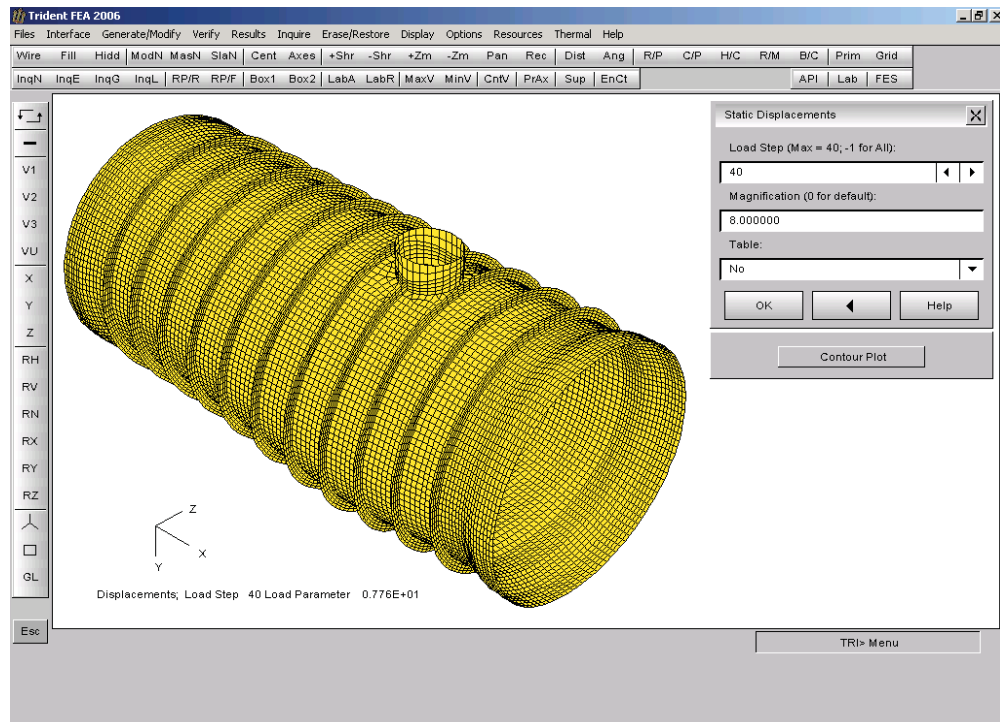**Figure 3.115: Final Deformed Shape of Penetration Cylinder with 500% Measured Out-Of-Circularities (Bottom View).**
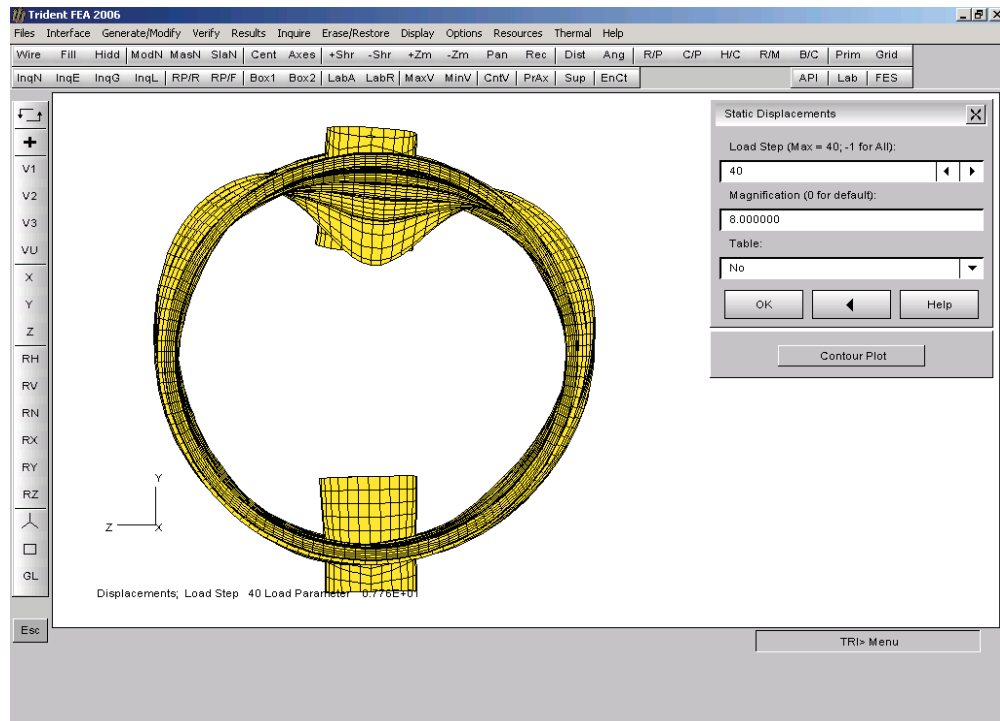
Figure 3.116: Final Deformed Shape of Penetration Cylinder with 500% Measured Out-Of-Circularities (End View).
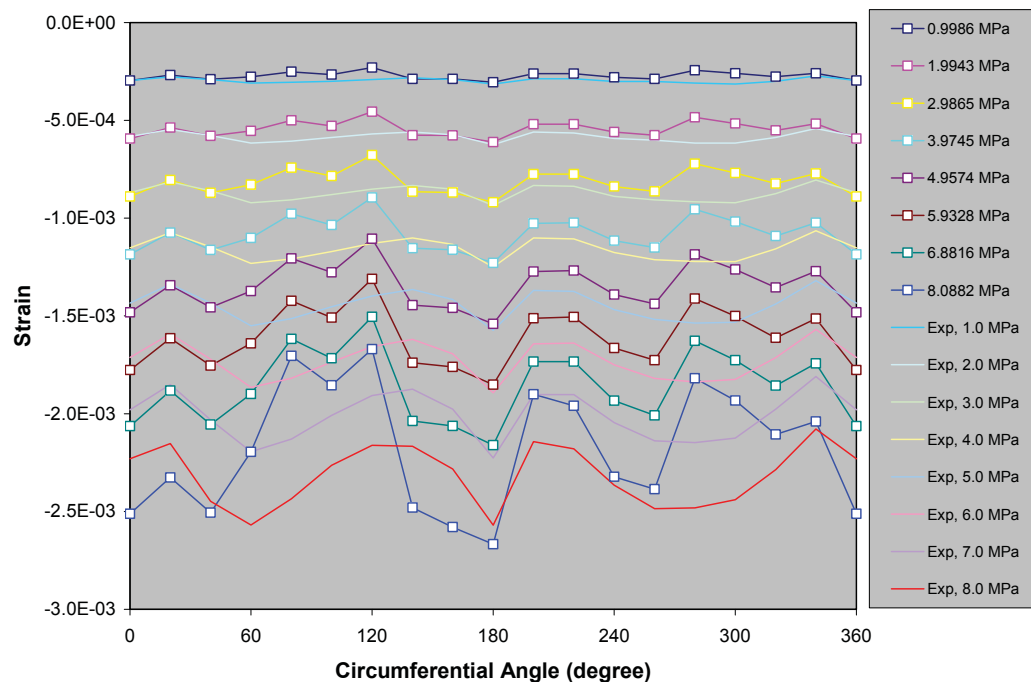
Figure 3.117: Comparison of Predicted (with Symbols) and Measured Profiles of the Circumferential Strain on Central Stiffener #6 with 500% Measured Out-Of-Circularities.
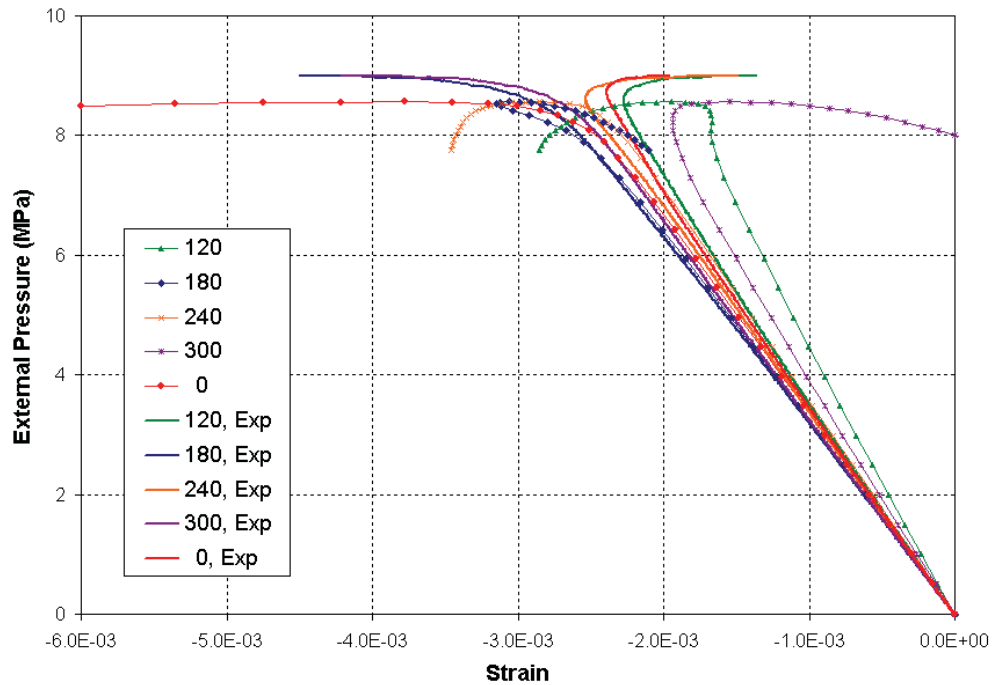
Figure 3.118: Comparison of Predicted (with Symbols) and Measured Histories of Circumferential Strains on Outside of Stiffener #6 with 500% Measured Out-Of-Circularities.
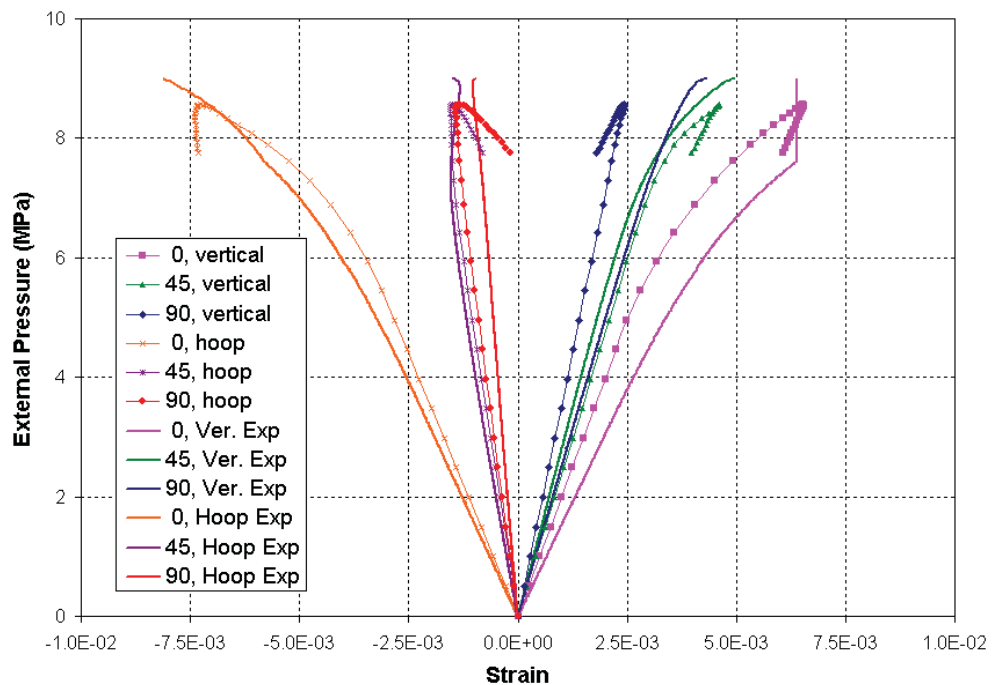
Figure 3.119: Comparison of Predicted (with Symbols) and Measured Histories of Strains on Inside Wall of Penetration A with 500% Measured Out-Of-Circularities
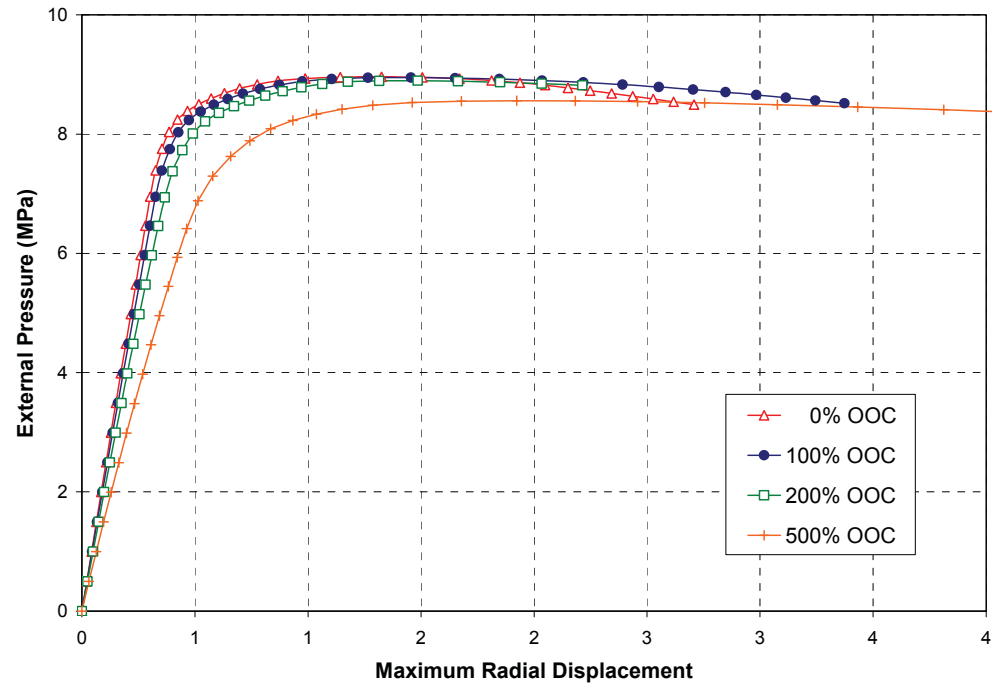
Figure 3.120: Comparison of Predicted Pressure-Radial Displacement Curves of the Penetration Cylinder with Different Amplitudes of Out-Of-Circularities.
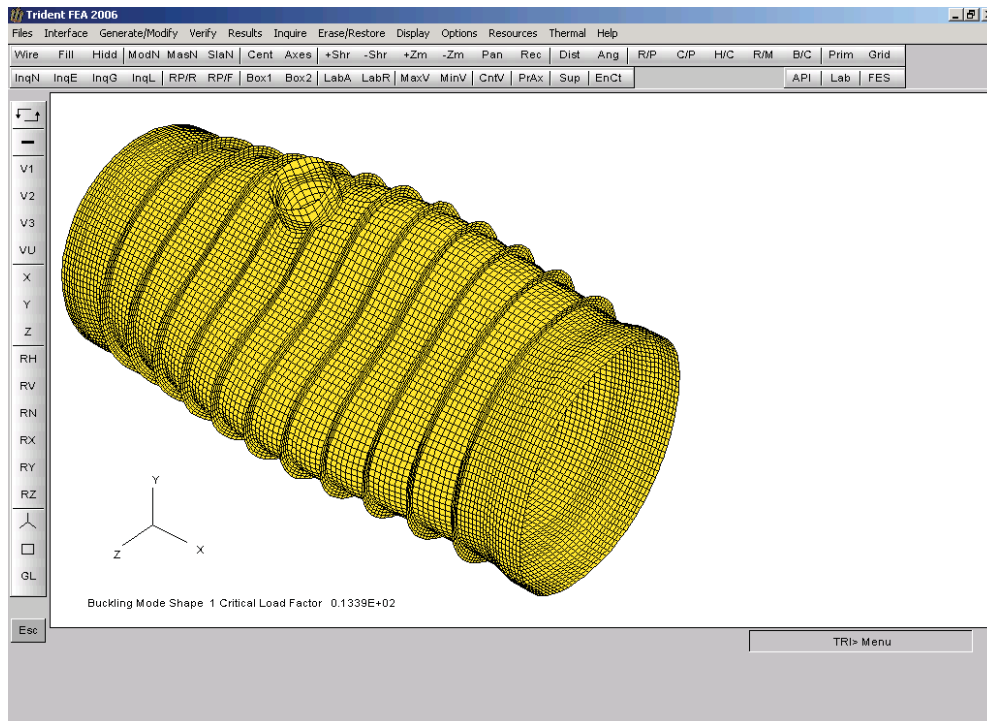
Figure 3.121: First Linear Buckling Mode Shape of Penetration Cylinder (3D View).
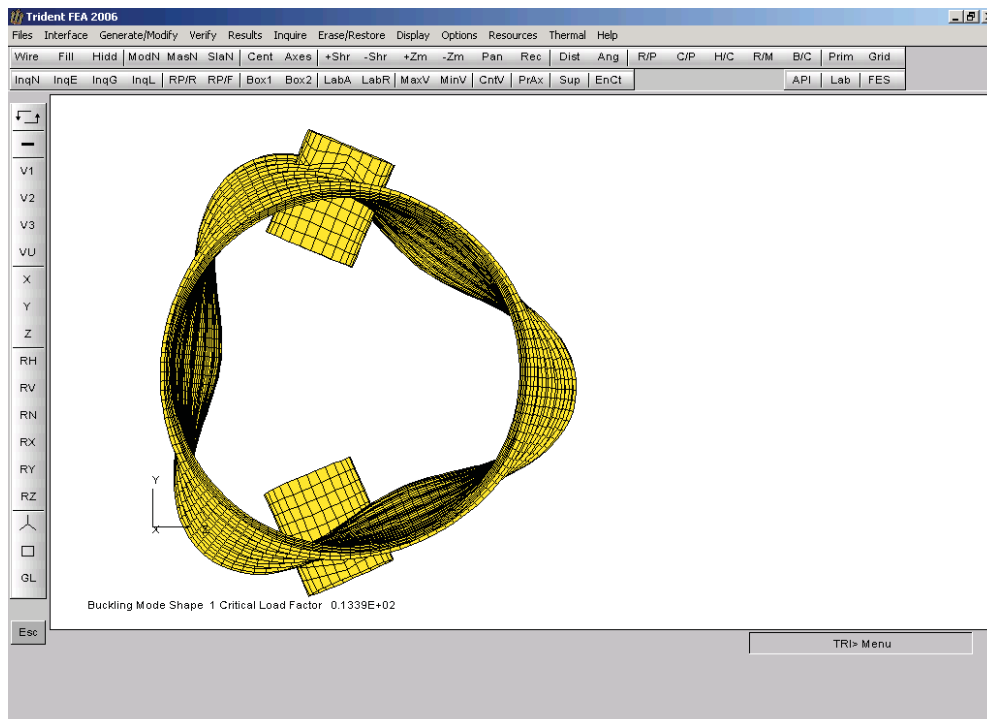
Figure 3.122: First Linear Buckling Mode Shape of Penetration Cylinder (End View).

Displacements; Load Step 40 Load Parameter 0.848E+01
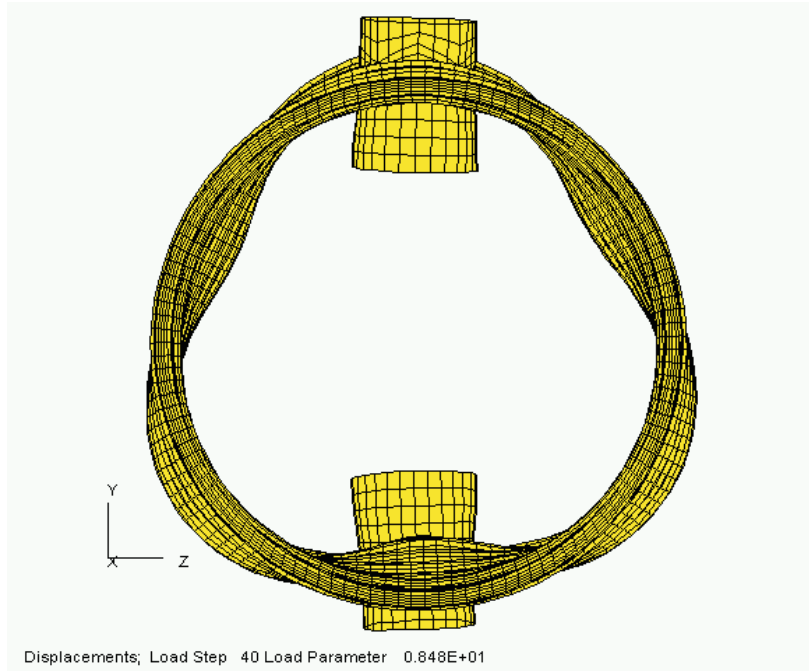
Figure 3.123: Final Deformed Shape Obtained by Superimposing the First Linear Buckling Mode (Maximum Deflection=0.002mm).

Displacements; Load Step 40 Load Parameter 0.838E+01
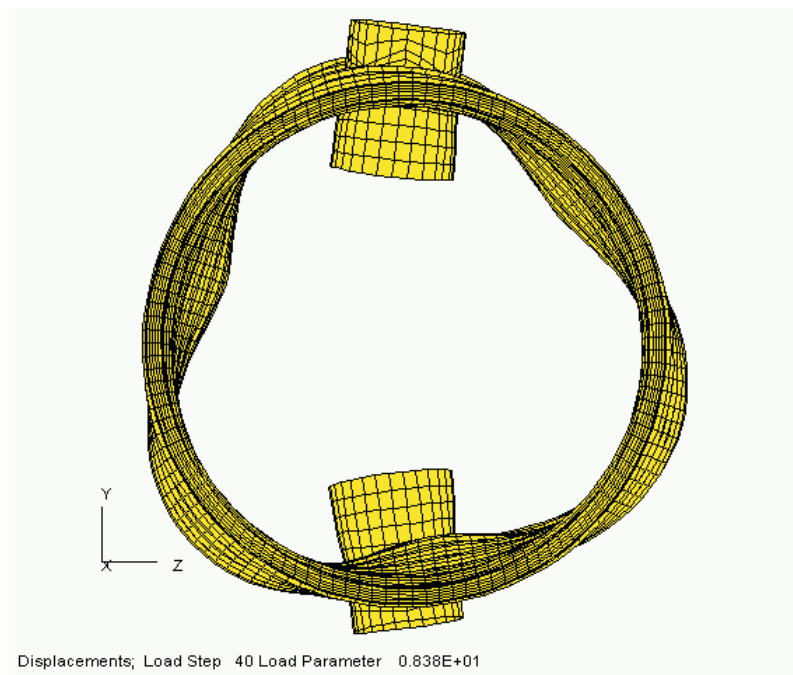
Figure 3.124: Final Deformed Shape Obtained by Superimposing the First Linear Buckling Mode (Maximum Deflection =0.01mm).

Displacements; Load Step 40 Load Parameter 0.805E+01
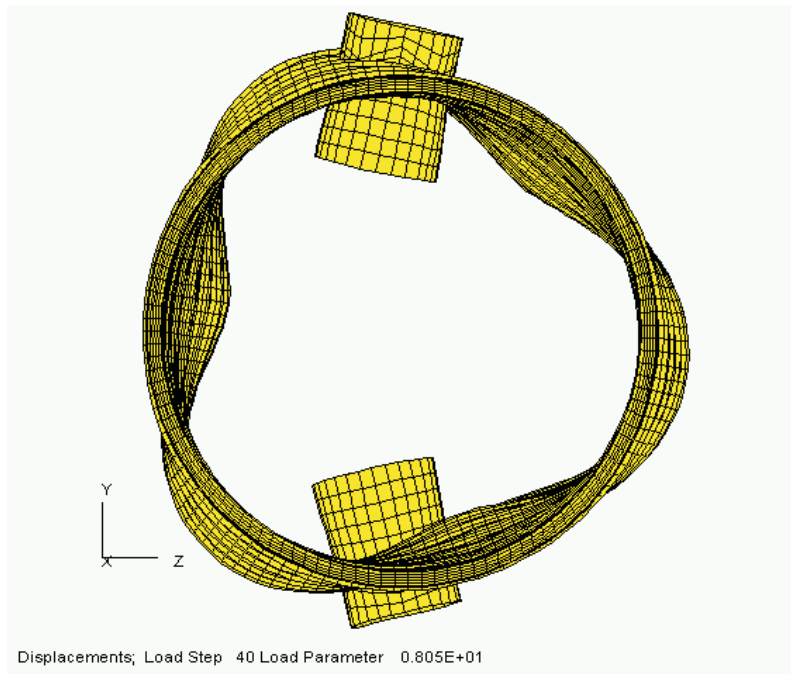
Figure 3.125: Final Deformed Shape Obtained by Superimposing the First Linear Buckling Mode (Maximum Deflection =0.05mm).

Displacements; Load Step 40 Load Parameter 0.753E+01
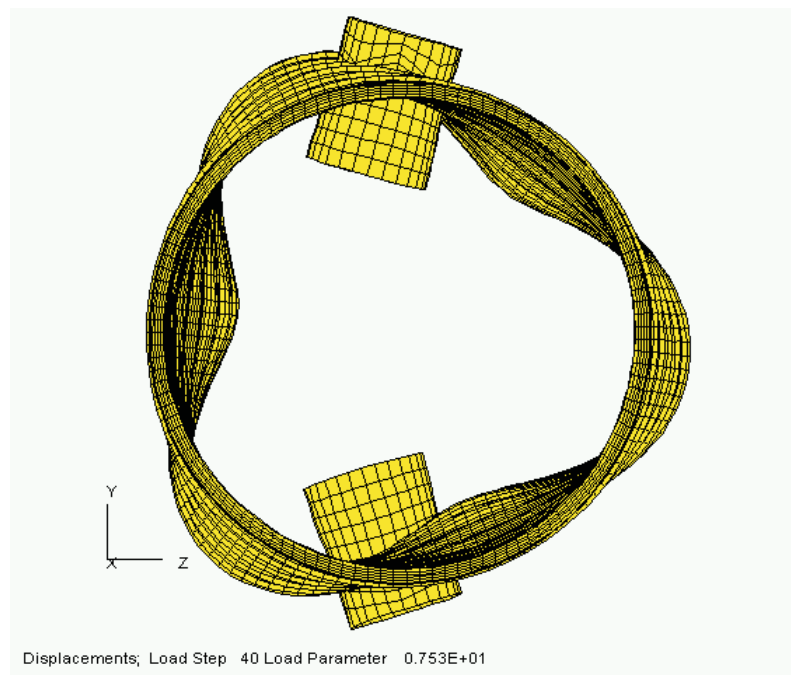
Figure 3.126: Final Deformed Shape Obtained by Superimposing the First Linear Buckling Mode (Maximum Deflection =0.2mm).

4.0 CONCLUSIONS AND RECOMMENDATIONS

In this report, we have presented work performed under Phase 2 of a three-phase contract entitled "Submarine Structure Modeling and Analysis for Life-Cycle Management". The objective of this phase was to validate structural strength analysis and corrosion modeling procedures provided in the SubSAS code through comparison of the numerically predicted and experimentally measured nonlinear collapse behaviour of six cylindrical specimens. This objective has been successfully achieved.

The finite element models used in the present work were all generated using the SubSAS program. These models were based on the 4-noded quadrilateral shell element and included the measured shell thickness variations and out-of-circularities. The tapered sections and corrosion patches were modelled outside SubSAS using specially developed FORTRAN programs. The finite element model for the cylinder with penetrations was partially generated using SubSAS, but completed by using Trident FEA.

The nonlinear calculations in this work were performed using the VAST finite element program, which was the solver engine incorporated into the SubSAS program. In these nonlinear analyses, convergence studies were first conducted to determine the adequate meshes for capturing nonlinear collapse behaviour of cylinders of different geometric configurations. To investigate the effect of material properties, nonlinear solutions were obtained for each cylinder specimen using three different material models, including elastic-perfectly-plastic, bilinear model with isotropic and kinematic strain hardening, and multi-linear stress-strain properties. The material test data in the circumferential direction were utilized in most of the nonlinear analyses, but the axial test data were considered for the long cylinder model. Other factors affecting the nonlinear responses of the stiffened cylinders, such as boundary conditions, self-weight and meshing details at shell-shell junctions, were also investigated. In order to assess overall accuracy of the finite element solutions, direct comparison of measured and computed strain-pressure histories were performed at all strain gauge locations. The experimentally measured and numerically predicted critical pressures were compared with predictions from the submarine design formulas (SDF). This comparison indicated that for non-corroded cylinders, the SDF results were reasonably accurate. However, for corroded cylinders and the cylinder with penetrations, the use of submarine design formulas would result in significant underestimation of the load carrying capacities.

The numerical results presented in this report demonstrate that the VAST finite element program is capable of predicting nonlinear collapse behaviour of non-corroded and corroded stiffened cylindrical shells accurately. Among the factors considered, the pattern of thickness variations in the cylinder wall, including localized corrosions, played a dominant role in controlling failure modes of the test stiffened cylinders whereas the material property had the most significant influence on the computed pressure-displacement response. Geometric imperfections also have a significant influence on the collapse behaviour of the cylinder, especially when the pattern of the imperfection coincided with a buckling mode shape. Due to the anisotropic property of the 6082-T6 aluminium tubing shown by the TNO material tests [2], we highly recommend that an orthotropic plasticity model be implemented in the VAST and SubSAS programs, and utilized in future nonlinear finite element analyses of experimental cylinders.

Among the elastic-plastic material models considered in the present analyses, the overlay model using multi-linear stress-strain curves resulted in the best agreement with the experimental results. However, this method is relatively more expensive than the bilinear models from the

computational point of view. The elastic-perfectly-plastic model and the bilinear stress-strain model with kinematic hardening are less expensive than the overlay model, and in most cases, produce acceptable numerical solutions. If the computation time is not a critical factor, the overlay model is still highly recommended. Compared with the experimental results, the bilinear elastic-plastic model with isotropic hardening was the worst model considered, and thus, should be avoided in practical engineering analyses.

Material properties for these test cylinders are orthotropic, likely due to the manufacturing process of the extruded aluminium tubing. In order to quantify the effect of the material anisotropy on the predicted collapse pressure and failure mode, nonlinear solutions were obtained for short cylinder L300-No3 using the circumferential, axial and average material properties. Based on the results presented in Table 3.5 and Figure 3.26, the material properties have a significant effect on the accuracy of the numerical solutions and an anisotropic plasticity model should be recommended. However, if an anisotropic is not available, an isotropic plasticity model should be used with the circumferential material properties, which should lead to acceptable numerical solutions. In case an anisotropic plasticity model is to be implemented in VAST for future nonlinear analyses, the Huber-Mises yield criterion generalized by Hill for anisotropic materials seems to be an attractive candidate as it has been utilized by a number of researchers in nonlinear analyses of plate and shell structures [7-9].

There is no need to include the endcaps explicitly in the finite element model. However, the end load acting on the endcaps and the constraints provided by the endcaps must be properly modelled. This can be achieved by applying the endcap loads to the shell end surfaces uniformly and constraining the rotational degrees-of-freedom at the shell ends. The translational degrees-of-freedom should be fully constrained at one end, but the other end should be allowed to move freely in the axial direction. This boundary condition is the clamped condition (Boundary Condition I) defined in Figure 2.19.

The effects of self-weight and variations in the hydrostatic pressure load with depth were investigated in the present study. The numerical results suggest that these factors can have an influence on the location of the first collapse, but have only a negligible impact on the predicted collapse pressure. As a result, we recommend these details be neglected in future analyses.

The element type utilized in the present study is the 4-noded quadrilateral shell based on the degenerate solid element formulation and enhanced by mixed interpolation of tensorial strain components (MITC4). The convergence studies performed in the present work suggest that for the long cylinders, which are designed to collapse in a overall buckling mode, at least seven elements should be used between stiffeners and 128 elements used along the circumference. For the short cylinders, which are designed to fail in an interframe buckling mode, finer meshes are required to accurately capture the more localized deformations. In this case, sixteen elements between stiffeners and 288 elements along the circumference are recommended. For both cylinder configurations, four elements along the web height and four elements across the flange width are sufficient. However, locally refined meshes are required in the areas of simulated corrosions to obtain an adequate representation of stress and strain gradients in those areas. Removal of the material at the shell-shell intersection does not result in a noticeable change in the nonlinear solutions and is unnecessary for future analyses.

The procedure in SubSAS for incorporating the measured out-of-circularity and thickness variations is both reliable and sufficiently accurate. This is proven by the good agreement between

the experimentally measured and numerically predicted strain histories and strain variations in the circumferential direction.

The orthogonal trajectory solution strategy was employed along with the Newton-Raphson method in all nonlinear analyses in the present work and no convergence problems were encountered. This solution method is a modification of the constant arc-length method, but is more stable numerically. This is because that the latter requires solution of a quadratic algebraic equation during equilibrium iterations to determine incremental load parameters and the desired root must be selected using a set of rules. In some cases, a wrong solution can be selected causing failure of the nonlinear solution.

In nonlinear analyses using the VAST code, an initial incremental load parameter must be specified to start the nonlinear run. The load increments for the subsequent solution steps are then computed fully automatically using a load step adjustment algorithm. Through the analyses performed in this work, we recommend to use 0.5 MPa as the initial load step, which has resulted in accurate and stable nonlinear solutions for all cylinder specimens.

Guidelines for future nonlinear FE analyses of similar ring-stiffened cylinders under external pressure may be suggested based on the above-mentioned conclusions. As such, it is recommended that the analyst: (1) use the overlay model with multi-linear stress-strain properties from the material tests in the circumferential direction; (2) use clamped boundary conditions and uniformly distributed end loads; (3) use sixteen elements between stiffeners and 288 elements along the circumference for the short cylinders and seven elements between stiffeners and 144 elements along the circumference for the long cylinders; (4) use the combined Fourier and spline method in SubSAS to incorporate out-of-circularity and thickness variations, (5) use the orthogonal trajectory solution method with an initial load step of 0.5MPa; (6) ignore the effects of the self-weight of cylinders, the variation of hydrostatic pressure with depth and the extra material in the finite element model at the shell-shell intersection. These recommendations will be tested in the analyses of the seven new cylinder specimens to be considered in Phase IV of the current contract.

5.0   REFERENCES

[1]   MACKAY, J.R., *Effect of In-service Damage and Repair on the Structural Integrity of Pressure Hulls–Phase 1: Experimental Results*, Technical Memorandum TM 2006-304, DRDC Atlantic, 2007.

[2]   TOBIN, S., WALLACE, J., JIANG, L., MACADAM, T. and NORWOOD, M., *Submarine Structure Modeling and Analysis for Life-Cycle Management, Phase 1 – Final Report*, Martec Technical Report # TR-07-42, Martec Limited, August 2007.

[3]   *Tensile Test Results*, March 2007, TNO.

[4]   PEGG, N.G. and SMITH, D.R., *PRHDEF-Stress and Stability Analysis of Ring Stiffened Submarine Pressure Hulls*, DREA Technical Memorandum 87/213. June 1987.

[5]   WILSON, L.B., DRA Program PD004B, Ministry of Defence, United Kingdom.

[6]   SMITH, M.J. and MACKAY, J.R., "Overall Elasto-Plastic Collapse of Ring Stiffened Cylinders with Corrosion Damage", *International Journal of Maritime Engineering*, 147 Part A1, pp. 53-61, 2005.

[7]   VALLIAPPAN, S., BOONLAULOHR, P. and LEE, I.K., "Nonlinear Analysis for Anisotropic Materials", *International Journal for Numerical Methods in Engineering*, Vol. 10 (3), pp.597-606, 1976.

[8]   OWEN, D.R.J. and FIQUEIRAS, J.A., "Elasto-Plastic Analysis of Anisotropic Plates and Shells by the Semiloof Element", *International Journal for Numerical Methods in Engineering*, Vol. 19 (4), pp.521-539, 1983.

[9]   OWEN, D.R.J. and LI, Z.H., "Elasto-Plastic Dynamic Analysis of Anisotropic Laminated Plates", *International Journal for Numerical Methods in Engineering*, Vol. 70 (3), pp.349-365, 1988.

This page intentionally left blank.

Distribution list

Document No.: DRDC Atlantic CR 2007-329

LIST PART 1 – Internal Distribution by Centre:

2   Scientific Authority (1 paper copy, 1 CD)
3   DRDC Atlantic Library (1 paper copy, 2 CDs)

5   TOTAL LIST PART I

LIST PART II: External Distribution by DRDKIM

1   NDHQ/DRDKIM 3 (1 CD)
1   Library and Archives Canada (1 CD)
        Attn: Military Archivist, Government Records Branch

2   TOTAL LIST PART II

7   TOTAL COPIES (2 paper copies, 5 CDs)

This page intentionally left blank.

1.	ORIGINATOR (The name and address of the organization preparing the document. Organizations for whom the document was prepared, e.g. Centre sponsoring a contractor's report, or tasking agency, are entered in section 8.) Martec Limited 1888 Brunswick Street, Suite 400 Halifax, Nova Scotia B3J 3J8		2. SECURITY CLASSIFICATION (Overall security classification of the document including special warning terms if applicable.) UNCLASSIFIED (NON-CONTROLLED GOODS) DMC A REVIEW: GCEC APRIL 2011	

3. TITLE (The complete document title as indicated on the title page. Its classification should be indicated by the appropriate abbreviation (S, C, R or U) in parentheses after the title.)

Submarine Structure Modeling and Analysis for Life-Cycle Management: Phase 2 Final Report

4. AUTHORS (last name, followed by initials – ranks, titles, etc. not to be used)

Jiang, L.; Wallace, J.

5.	DATE OF PUBLICATION (Month and year of publication of document.) February 2008	6a. NO. OF PAGES (Total containing information, including Annexes, Appendices, etc.) 146	6b. NO. OF REFS (Total cited in document.) 9

7. DESCRIPTIVE NOTES (The category of the document, e.g. technical report, technical note or memorandum. If appropriate, enter the type of report, e.g. interim, progress, summary, annual or final. Give the inclusive dates when a specific reporting period is covered.)

Contract Report

8. SPONSORING ACTIVITY (The name of the department project office or laboratory sponsoring the research and development – include address.)

Defence R&D Canada – Atlantic
9 Grove Street
P.O. Box 1012
Dartmouth, Nova Scotia B2Y 3Z7

9a. PROJECT OR GRANT NO. (If appropriate, the applicable research and development project or grant number under which the document was written. Please specify whether project or grant.) 20CM05-01, 20CM05-02	9b. CONTRACT NO. (If appropriate, the applicable number under which the document was written.) W7707-063569	

10a. ORIGINATOR'S DOCUMENT NUMBER (The official document number by which the document is identified by the originating activity. This number must be unique to this document.) Martec Technical Report TR-07-59	10b. OTHER DOCUMENT NO(s). (Any other numbers which may be assigned this document either by the originator or by the sponsor.) DRDC Atlantic CR 2007-329	

11. DOCUMENT AVAILABILITY (Any limitations on further dissemination of the document, other than those imposed by security classification.)

(X) Unlimited distribution
(   ) Defence departments and defence contractors; further distribution only as approved
(   ) Defence departments and Canadian defence contractors; further distribution only as approved
(   ) Government departments and agencies; further distribution only as approved
(   ) Defence departments; further distribution only as approved
(   ) Other (please specify):

12. DOCUMENT ANNOUNCEMENT (Any limitation to the bibliographic announcement of this document. This will normally correspond to the Document Availability (11). However, where further distribution (beyond the audience specified in (11) is possible, a wider announcement audience may be selected.))

Unlimited

13. ABSTRACT (A brief and factual summary of the document. It may also appear elsewhere in the body of the document itself. It is highly desirable that the abstract of classified documents be unclassified. Each paragraph of the abstract shall begin with an indication of the security classification of the information in the paragraph (unless the document itself is unclassified) represented as (S), (C), (R), or (U). It is not necessary to include here abstracts in both official languages unless the text is bilingual.)

This report presents results from the nonlinear structural analyses of six cylinder specimens in order to provide validation of the finite element methods of predicting collapse pressures and post collapse behaviour of stiffened cylindrical shells. The six cylinder specimens considered in the present study included a non-corroded short cylinder, two short cylinders with simulated center corrosion, a non-corroded long cylinder, a long cylinder with simulated corrosion in flange and a long cylinder with penetrations. The nonlinear calculations were performed using the VAST finite element (FE) code. In these nonlinear analyses, convergence studies were first conducted to determine the adequate mesh sizes for capturing nonlinear collapse behaviour of cylinders of different geometry. Other factors affecting the nonlinear responses of cylinders, such as material properties, geometric imperfections, boundary conditions, specimen's self weight and some meshing details, were also considered. In order to facilitate direct comparison between measured and predicted strain histories, a FORTRAN program was developed to automatically extract load-strain histories at all strain gauge locations from the FE solutions. FE meshes were produced using SubSAS, a submarine structural analysis program developed for DRDC Atlantic and the UK MoD. Tools for incorporating tapered regions and simulated corrosion were under development in SubSAS at the time of writing, and so specialized FORTRAN programs were written to incorporate these features into the FE models, and to generate shell element meshes for plate junctions that do not contain material overlaps. Very good agreement is obtained between the numerical and experimental results, indicating that the modeling approach and numerical analysis procedures described herein are capable of predicting the collapse behaviour of corroded stiffened cylindrical shells.

Le présent rapport présente les résultats d'analyses de structure non linéaires menées sur six éprouvettes cylindriques dans le but de valider les méthodes par éléments finis utilisées pour prédire les pressions d'écrasement et le comportement post-écrasement des coques cylindriques renforcées. Les six éprouvettes cylindriques en question étaient un cylindre court non corrodé, deux cylindres courts à corrosion simulée au centre, un cylindre long non corrodé, un cylindre long à corrosion simulée aux brides, ainsi qu'un cylindre long à corrosion pénétrante. Les calculs non linéaires ont été effectués à l'aide du code d'éléments finis VAST. Dans ces analyses non linéaires, des études de convergence ont d'abord été menées pour déterminer la taille des maillages apte à représenter le comportement d'écrasement non linéaire de cylindres présentant des géométries différentes. D'autres facteurs susceptibles de modifier les réponses non linéaires des cylindres, comme les propriétés des matériaux, les imperfections géométriques, les conditions limites, le poids propre des éprouvettes et certains détails de maillage, ont aussi été pris en considération. Pour qu'il soit plus facile de comparer directement l'évolution des contraintes mesurées avec l'évolution des contraintes prédites, un programme FORTRAN a été mis au point pour automatiquement extraire des solutions par éléments finis l'évolution des contraintes sous charge à tous les emplacements de jauges extensométriques. Un certain nombre d'autres programmes FORTRAN ont également été mis au point pour incorporer dans les modèles par éléments finis certaines caractéristiques telles que zones coniques et corrosions simulées, et pour générer des maillages d'éléments spéciaux de coque pour le cas de la jonction de plaque qui ne contiennent pas de chevauchements de matière. Une très bonne concordance est obtenue entre les résultats numériques et expérimentaux, ce qui indique que le programme VAST est capable de prédire le comportement d'écrasement non linéaire de coques cylindriques renforcées par raidisseurs corrodées.

14. KEYWORDS, DESCRIPTORS or IDENTIFIERS (Technically meaningful terms or short phrases that characterize a document and could be helpful in cataloguing the document. They should be selected so that no security classification is required. Identifiers, such as equipment model designation, trade name, military project code name, geographic location may also be included. If possible keywords should be selected from a published thesaurus, e.g. Thesaurus of Engineering and Scientific Terms (TEST) and that thesaurus identified. If it is not possible to select indexing terms which are Unclassified, the classification of each should be indicated as with the title.)

Submarine, finite element analysis, SubSAS, experiment, collapse

This page intentionally left blank.

Defence R&D Canada

Canada's leader in defence
and National Security
Science and Technology

R & D pour la défense Canada

Chef de file au Canada en matière
de science et de technologie pour
la défense et la sécurité nationale

DEFENCE **R&D** DÉFENSE

www.drdc-rddc.gc.ca